UNIVERSITY COLLEGE LONDON

Drop Coalescence with Liquid/Liquid Interfaces in the Presence of Surfactants

Teng Dong

Supervised by Prof. Panagiota Angeli

Submitted to the Department of Chemical Engineering

in partial fulfilment of the requirements for the degree of

Doctor of Philosophy in Chemical Engineering

at University College London

December 2019

"To see a world in a grain of sand. And a heaven in a wild flower, Hold infinity in the palm of your hand. And eternity in an hour."

William Blake

I, Teng Dong, confirm that the work presented in this thesis is my own. Where information has been derived from other sources, I confirm that this has been indicated in the thesis.

December 2019
London, United Kingdom

Abstract

The dissertation describes the experimental investigations on the effect of surfactants on drop coalescence with liquid/liquid interfaces. Different coalescence events are carried out in two unique-designed vessels at different dimensions. Optical methods including high-speed shadowgraphy and Particle Image Velocimetry (PIV) are applied to detect the drop surface behaviour and the drop inner dynamics. Planar Laser Induced Fluorescence (PLIF) is also utilized to detect the spatio-temporal distribution of surfactants on the coalescing drop surface. A novel flow channel is developed to investigate the surfing drops at moving liquid/liquid interfaces at last.

Initially, the total coalescence of drops with the liquid/liquid interfaces, both packed with surfactants at concentrations up to the Critical Micelle Concentration (CMC), are studied. It is found that the increase of the surfactant concentration promotes the deformation of the interface before the film that separates the drop from the interface drains and ruptures. After the film rupture, two counter-rotating vortices appear inside the drop, which move faster at low surfactant concentrations. The intensities of the two counter-rotating vortices significantly decrease at increasing surfactant concentration.

In the second part of the dissertation, the experimental results on the partial coalescence of drops are presented. The coalescence map based on the dimensionless numbers $Oh=\mu_d/(\rho_m\sigma D)^{1/2}$ and $Bo = \Delta\rho g D^2/\sigma$ is plotted to distinguish the partial coalescence region, which is found to reduce in the presence of surfactants. The size ratios of the daughter to the mother drop are measured and plotted against the *Bo* and *Oh* as well. In the gravity dominant regime, the surfactants have negligible effect on the drop ratio, while in the inertia-capillary regime the drop size ratio decreases with increasing surfactant concentration. The velocity fields inside the partial coalescing drop are acquired. In the surfactant-free system, it is found that the inward motion of

the fluids at the upper part of the drop favours the generation of a liquid cylinder in the early stages. The pressure gradient created by the downward stream at the bottom of the liquid cylinder is believed to cause the pinch-off of the cylinder and the formation of the secondary droplet. The surfactants tend to make the coalescence non-symmetric resulting in total coalescence.

The spatiotemporal distributions of surfactants on the merging interfaces are presented in the following part. It is found that when a drop rests on an interface, the surfactants that have been adsorbed on the interfaces are swept outwards by the draining liquid film between the drop and the flat interface and reach a peak value at about $0.75R$ away from the center, where R is the horizontal drop radius. After the film ruptures, the surfactant concentration at the tip of the retreating meniscus continues to increase. Once the film has retracted to the drop sides, the concentration of the surfactants peaks at the meniscus at the bottom of the drop. The variation of the surfactant concentration along the merging interfaces in the later stages is presented as well.

In the end, the delayed coalescence of drops with moving liquid-liquid interfaces is experimentally investigated. Drops are released onto the moving interfaces at velocities from 0 cm/s up to 3.4 cm/s. Drop coalescence is found to be largely delayed at increasing interface speed, which is attributed to the lubrication pressure developed in the draining film. Numerical simulations are conducted for a half-pendent drop levitating on a moving liquid-liquid interface. The results indicate that the minimum pressure appears at the front bottom of the moving drop, where most of the film ruptures are observed to take place. Also, the pressure in the film is calculated based on the local curvature of the drop surface and the tangential velocities on the drop surface and on the interface in the film region. It is found that the lubrication pressure increases with the interface speed. The PLIF technique is used to measure the drop shape and the film thickness between the drop and the interface. A dimple structure in the film is more likely to form at lower interface speeds, while the film tends to be flat when the interfaces move with high speed. During coalescence of drops with moving interfaces, in some cases when films are thicker, the liquid in the film cannot completely drain out but form drops-on-string resulting in the oil entrainment in the aqueous phase.

Impact Statement

In terms of scientific impact, the research outcomes included in the thesis provide new knowledge on the physics and the mechanism of the coalescence phenomenon of drops with liquid/liquid interfaces, either stationary or moving, in the presence of surfactants. The partial coalescence study reveals that the hydrodynamic pressure in the coalescing drop contributes to the generation of daughter droplets, in addition to the action of capillary waves along the drop surface (Ding et al., 2012). The PLIF studies on the distribution of surfactants during coalescence offer other researchers new experimental approaches to investigate coalescence and other interfacial phenomena.

In industry, the results of the work are expected to offer useful references for the processes where drop coalescence is encountered. For instance, the current findings that surfactants tend to resist the partial coalescence, can be used to predict the drop size distribution in emulsions in dairy products (Benjamins et al., 2009), and during dispersed flow in the long-distance transportation and separation of multiphase mixtures (Rommel et al., 1993). The experimental discoveries on the delayed coalescence of surfing drops on moving interfaces will be relevant to the fields of drop manipulation in microfluidic systems and in printing processes (Deng et al., 2016). In the fields of environment protection and climate change, the new findings on partial coalescence as well as on drop coalescence at moving interfaces will be relevant to the phenomena involved in the generation of the ocean mist (Deike et al., 2016), the transportation of airborne particles (Raes et al., 2000) and the droplet growth in clouds (Berry and Reinhardt, 1974).

Acknowledgements

First and foremost, I feel great pleasure to express my special appreciation and thanks to my supervisor Prof. Panagiota Angeli for recruiting me as a Ph.D. student and introducing me to such a fantastic research project. I really enjoy the scientific exploration over the past four years and I am really grateful for her encouragement during the difficult times. She is not only a good tutor in scientific research but also a great life mentor who inspired me to do continuous efforts in exploring the new horizons and never give up. It is obvious the thesis would not be the same without her professional guidance and valuable suggestions during my writing process. Thanks for her patience and expertise while cultivating me into a scientist.

I would like to express my gratitude to Dr. Weheliye H. Weheliye who provided insight and expertise that greatly assisted the research. I learned extensive experimental skills and technical knowledge from him during the past years. This dissertation was not able to achieve good quality without his useful comments that greatly improved the manuscript. I appreciate the time we spend together in attempting experimental approaches, discussing the new phenomena and exploring the world of the tiny drops.

I would like to thank Dr. Roumpea, Evangelia, Dr. Zainal Abidin, Dr. Lusheng Zhai, Mr Seng Hue, Miss Kalli, Maria and other members in the ThAMeS Multiphase group. Their enthusiasm to friends and passion for life enabled me to adapt myself to the new environment smoothly when I first joined the group. It was great and enjoyable to share the laboratory and office with them during the four years.

I generally appreciate Dr Fei Wang for his help on the numerical simulations. I would like to thank the help from Mr. Maney Adam and Albert Corredera, especially Mr. Smith Graeme for the design and manufacture of the experimental apparatus.

Finally and most importantly, I would like to express my gratitude to my family

who provides endless supported in all of my pursuits. Their earnest love, trust, and untiring encouragement make my journey wonderful and amazing.

I would like to acknowledge the Chinese Scholarship Council and the University College London for providing me with the UCL-CSC joint scholarship to study abroad.

Contents

Abstract v
Impact Statement vii
Acknowledgements ix
List of Figures xv
List of Tables xxiv
Nomenclature xxv
Introduction 1
1.1 Background and motivation 1
1.2 A guide through the thesis 2
Literature review 5
2.1 Surfactants and Marangoni effect 6
2.1.1 Surfactant properties 6
2.1.2 Marangoni effect 8
2.2 Drop rest phenomena 8
2.2.1 Drop rest time 8
2.2.2 Film draining 9
2.2.3 Lubrication flow 12
2.2.4 Theoretical predictions of the drop rest time 14
2.2.5 Distribution of surfactants in the film region 15
2.3 Neck growth 16
2.3.1 Neck growth regime 16
2.3.2 Neck expansion with surfactants 18
2.4 Dynamics of the liquid merging 20
2.4.1 Total coalescence 20
2.4.2 Partial coalescence 20
2.4.3 Partial coalescence mechanism 22

2.4.4 Criterion for partial coalescence 23
2.4.5 Pinch-off time 24
2.4.6 Drop ratio 26
2.5 Delayed coalescence at a moving fluid interface 28
2.5.1 Vibration induced non-coalescence 28
2.5.2 Thermocapillary induced non-coalescence 29
2.5.3 Drop levitation on a moving surface 30
2.6 Conclusions 34
Experimental methodologies and techniques 35
3.1 Experiments on total & partial coalescence 35
3.1.1 Experimental set-up and techniques 35
3.1.2 Materials 37
3.1.3 Drop shape tracking algorithm 41
3.2 Fluorescence visualization on surfactant distribution 43
3.2.1 Materials 43
3.2.2 Experimental set-up and techniques 44
3.2.3 Experimental methods 46
3.2.4 Fluorescent imaging and calibration 47
3.2.5 Image processing and limitations 50
3.3 Experimental set up for the study of delayed coalescence in moving interfaces 52
3.3.1 Experimental set-up and materials 52
3.3.2 Experimental methods 54
3.4 Conclusions 55
Surfactants effect on the total coalescence 57
4.1. Interfacial characteristic and droplet coalescence evolution 58
4.1.1 Rupture point locations 58
4.1.2 Drop height evolution 60
4.2. Generation of the vortices inside the drop 62
4.2.1 Spatial-temporal evolution of the vortices 62
4.2.2 Surfactant effects on the vortices strength 66
4.3. Kinetic energy per unit mass 68

4.4. Conclusions 71

Surfactants effect on the partial coalescence 73

5.1 Boundary between partial and total coalescence 74

5.2 Effect of surfactants on the drop ratio 78

5.3 Evolution of the drop surface during coalescence 80

5.3.1 Drop height evolution in surfactant-free system 80

5.3.2 Evolution of the drop surface during coalescence 84

5.4 Fluid dynamics in the drops 87

5.4.1. Evolution of Velocity fields 87

5.4.2. Vortices evolution 92

5.4.3 Pressure fields inside the coalescing drop 94

5.5 Conclusions 96

Fluorescence visualization of the surfactant distribution 99

6.1 Drop rest phenomenon 100

6.2 Neck growth 104

6.3 Distribution of surfactants along the drop surface 108

6.4 Conclusions 113

Delayed coalescence of drops at moving interfaces 115

7.1 Delayed coalescence and lubrication model 115

7.2 General Observations 118

7.2.1 Drop deformation during initial impact with the interface 118

7.2.2 Drop movement 119

7.2.3 Film thickness 120

7.2.4 Drop inner circulation 124

7.3 Lubrication flow in the film 125

7.3.1 Lubrication flow 125

7.3.2 Lubrication pressure 128

7.4 Drop coalescence 131

7.5 Oil entrainment 133

7.6 Conclusions 135

Conclusions and outlook 137

8.1 Conclusions 137
8.2 Recommendations for future work 139
Appendix A: Error analysis for the surface excess Γ 141
Appendix B: Pressure calculation based on 2D-PIV velocity 143
Appendix C: Acceleration of drops on the moving interface 151
Appendix D: Estimation of the pressure in the trapped film for a stationary drop 155
Scientific output 157
References 159

List of Figures

Figure 2.1 An illustration of the coalescence process after a drop hits the surface of its homophase. 5

Figure 2.2 A Schematic of the migration of surfactant molecules. The solid circle represents the hydrophilic part of the surfactant, the curve represents the hydrophobic part.....7

Figure 2.3 The silicone oil film trapped between two glycerol drops after the dimple forms (Chan et al., 2011). The experimental data shown in figure is obtained with the light interference technique.....11

Figure 2.4 The draining patterns of the thin film trapped between the drop and the bulk liquids; (a) rapid, uniform thinning to coalescence; (b) inflow to dimple, and draining to coalescence; (c) non-symmetrical draining, thinning to coalescence; (d) slow dimpled thinning (Hodgson and Woods, 1969). 12

Figure 2.5 A schematic showing the lubrication film when a drop approaches a flat liquid surface to a small distance. The schematic radial velocity profile $u(r;z)$ is plotted to help visualization. The distribution of the pressure $p(r)$ is relevant to the pressure of the surrounding liquids.....13

Figure 2.6 Marangoni flow induced from the uneven distribution of surfactant molecules during the film draining. 16

Figure 2.7 Growth of the neck radius r_n against time t. The data are plotted on a log-log scale. The crosses refer to the data acquired by Thoroddsen et al. (2005), the data of solid symbols from Aarts et al. (2005) and the pluses from Menchaca-Rocha et al. (2001). The rhombus with crosses are the results of Eri and Okumura (2010). The red dashed line (coefficient $k = 0.5$) show the scaling law in the inertial regime, while the black line ($k = 1$) indicated the trend in the viscous regime. 18

Figure 2.8 Growth of the neck radius r_n against the time t in the surfactant system. The stars refer to the data of drop-drop binary coalescence acquired by Nowak et al. (2016), where SLES is sodium lauryl ether sulfate. The data of circles and the pluses are from the coalescence of drops with the fluid interface by Nash et al. (2018); The ALS can CTAB refer to ammonium lauryl sulfate and cetyltrimethylammonium bromide, respectively. The squares are from the coalescence of drops at the fluid interface in a Hehe-Shaw cell by Chinaud et al. (2016). 19

Figure 2.9 Partial coalescence of a drop of pure water at the interface between 5 cSt Silicone oil and pure water. The time t starts at the moment of the film rupture. 21

Figure 2.10 The partial coalescence cascade for a drop of pure water at the interface between pure water and a 5 cSt silicone oil. Five coalescence events were observed in this cascade. As the size of the 6^{th} drop is quite small, the relevant image is not shown here..... 22

Figure 2.11 Partial coalescence region map based on the *Bo* and *Oh*. The solid line shows a rough boundary between the total and partial coalescence region. The pink shows the total coalescence data, and the blue color for the partial coalescence. 24

Figure 2.12 (a) A plot of the pinch-off time in different regimes. For the data of Thoroddsen and Takehara (2000) and Chen et al. (2006), the data in the gravity regime are plotted against *Bo*, while the data in inertia-capillary and viscous regimes are plotted against *Oh*. The data of Zhang et al. (2009) and Haldar et al. (2018) are plotted against *Oh*. (b) A plot of the pinch-off time for the coalescence of a bubble with a soap film (Aryafar and Kavehpour, 2006) and for the coalescence across a wide range of *Oh* (Aryafar and Kavehpour, 2006, Kavehpour, 2015). 25

Figure 2.13 Drop ratio ξ (for all the stage of the cascade) against *Oh*. The solid red line represents the predicted value of ξ by Kavehpour (2015). 27

Figure 2.14 The levitation of drops at different conditions; (a) drop resting at the hydraulic jump of a liquid film (Sreenivas et al., 1999); (b) drop floats at the inner surface of the rotating cylinder covered with a thin liquid film (Sawaguchi et al., 2019, Lhuissier et al., 2013, Castrejón-Pita et al., 2016); (c) drop levitated on a flat surface of the rotating plate covered with a thin liquid film (Gauthier et al., 2016). 32

Figure 3.1 (a) Experimental set up for the study of coalescence; (b) raw image obtained from the shadowgraphy observation; (c) raw image obtained with the PIV technique. 36

Figure 3.2 Interfacial tension of the interface between the 80% glycerol solution and the Exxsol D80 oil at different Span 80 concentrations. 39

Figure 3.3 Description of the steps of the detection algorithm of the droplet profile: (a) identification of laser reflections at the organic-aqueous interface; (b) region enclosed in the white rectangle to show three different positions in the estimation of σ_I; (c) variation of σ_I along a vertical height of the droplet; (d) raw profile of the droplet surface detected after the standard deviation analysis. 42

Figure 3.4 Interfacial tension of the 5 cSt silicone oil and the 46% glycerol solution, σ, for different concentrations of NBD-PC φ. The squares indicate the interfacial tension under various surfactant concentrations. The data were plotted against the bottom linear scale of φ. The dashed line is fitted to the experimental data. The continuous line is the prediction of the surfactant excess Γ on the interface based on the Langmuir adsorption model (Equation (3.4)). The data were plotted against the top log scale of φ. The calculation of the error bars of the red line is presented in Appendix A. 44

Figure 3.5 The PLIF experimental set-up. 45

Figure 3.6 Raw fluorescent images of a drop resting on the interface for (a) T = 0 min, (b) T = 60 min, and (c) T = 240 min. 47

Figure 3.7 Calibration of surfactant fluorescence intensity as a function of the surfactant concentration. The squares represent the averaged fluorescence intensity at each concentration, and the dashed line shows the fitting trend. The error bars show the standard deviation of the light intensity among the three measurements. 48

Figure 3.8 The average of the normalized surfactant concentration Γ^* along the drop surface for different surface ages T. Here, the normalization of concentration $\Gamma* = \Gamma/\Gamma max900$. The error bars show the variation of Γ^* along the drop surface. 50

Figure 3.9 (a) Schematic of the interfacial region detection and (b) intensity curves along the lines $L1$, $L2$, and $L3$. 51

Figure 3.10 Schematic of the Experimental Set-up for the studies on the delayed coalescence of drop with fluid interface. 53
Figure 3.11 (a) Raw image obtained from the moving PLIF measurement; (b) Raw image obtained from the moving PIV technique. 55
Figure 4.1 Time evolution of the drop before and after film rupture for $\phi=2\times10^{-5}$ and $\phi=5\times10^{-4}$ 58
Figure 4.2 The variation of the relative height from the drop upper surface to the equilibrium interface, h_s, with increasing receding meniscus time, t, for a single droplet coalescence event. The dashed line in the inset refers to the initially flat interface. ... 62
Figure 4.3 Time-resolved vector fields and contour plots of the vorticity, ω_z, in a single droplet for $\phi = 1\times10^{-4}$ and: (a) $t = 8$ ms; (b) $t = 16$ ms; (c) $t = 25$ ms; (d) $t = 35$ ms. .. 63
Figure 4.4 Time-resolved velocity fields and contour plots of the vorticity, ω_z, in a single droplet for $\phi = 2\times10^{-4}$ and: (a) $t = 8$ ms; (b) $t = 30$ ms; (c) $t = 45$ ms; (d) $t = 55$ ms; .. 64
Figure 4.5 Spatial evolution of the centers of the two vortices present on the left (×) and right (◦) hand side in a single droplet for: (a) $\phi =1\times10^{-4}$; (b) $\phi = 2\times10^{-4}$. 66
Figure 4.6 Time-resolved vector fields and contour plots of the vorticity, ω_z, in a single droplet for $\phi = 5\times10^{-4}$ and: (a) $t = 8$ ms; (b) $t = 70$ ms. 66
Figure 4.7 (a) Visualisation of the area, A_ω, over which the circulation ω_z has been estimated ($\phi = 2\times10^{-4}$); (b) Variation of the dimensional circulation, $\Gamma\omega z*$, with increasing t for both the right and left hand side vortices ($\phi =2\times10^{-4}$) in a single droplet; (c) Variation of the dimensional circulation, $\Gamma\omega z*$, with increasing t for different ϕ, averaged over 10 droplets. 68
Figure 4.8 Contour plots of the kinetic energy, k_{xy}, for: (a) $\phi = 1\times10^{-4}$ and $t = 8$ ms; (b) $\phi = 1\times10^{-4}$ and $t = 30$ ms; (c) $\phi = 2\times10^{-4}$ and $t = 8$ ms; (d) $\phi = 2\times10^{-4}$ and $t = 55$ ms. . 69
Figure 4.9 Variation of the dimensional space-averaged kinetic energy per unit mass, $kxy*$, in a single droplet with increasing t for different ϕ. 70
Figure 5.1 *Oh-Bo* map for coalescence in surfactant-free systems. The solid symbols represent the partial coalescence data with glycerol concentrations in the aqueous phase ranging from $\zeta = 0\%$ to $\zeta = 42.5\%$, the asterisks show the total coalescence data for all glycerol concentrations. The stars refer to the conditions investigated with PIV. The

dashed line is for reference only and shows the boundary between the partial and total coalescence regions. 75

Figure 5.2 *Oh-Bo* map for coalescence in surfactant-laden systems. The square symbols represent the partial coalescence data with different surfactant concentrations for ζ = 0%, the round symbols represent the partial coalescence data with different surfactant concentrations for ζ = 25%. The asterisks show the total coalescence data for all cases. The stars refer to the conditions investigated with PIV. The dashed lines are only for reference and show the boundary between the partial and the total coalescence regions for both surfactant-free and surfactant-laden systems. 77

Figure 5.3 Daughter to mother drop size ratio in different regimes for the systems with surfactants. 79

Figure 5.4 Partial coalescence of a single drop of water-glycerol (ζ = 33%) with its homophase within 0.65 cSt silicone oil. To aid imaging, Rhodamine 6G was dissolved in the drop liquid. In the above, a thin layer of the liquid under the interface was also dyed with a very small amount of Rhodamine 6G to show the shape of the interface. 80

Figure 5.5 (a) Change of the dimensionless height of the drop summit relative to the initial location during partial coalescence. The aqueous coalescing phase is a water/glycerol mixture at various concentrations and the surrounding organic phase is a 5 cSt silicone oil; (b) Change of the dimensionless height of the drop summit relative to the initial location during partial coalescence for organic phases with different viscosity. The aqueous coalescing phase is a water/glycerol mixture (ζ = 33 %)..... 82

Figure 5.6 Enhanced raw PIV images obtained for (a) partial, (b) boundary, and (c) total coalescence. 84

Figure 5.7 Drop surface evolution for (a) partial, (b) boundary, and (c) total coalescence. The visualization of the drop surface is stereoscopic. The drop profile at each time step is plotted in the *x*-*y* plane first, and then the figures are presented along the *t* axis..... 86

Figure 5.8 Variation of circulation level $\Gamma\omega z*$ against coalescence time. 88

Figure 5.9 The vertical and horizontal velocity fields in the coalescing drop for ϕ = 0. 90

Figure 5.10 The vertical and horizontal velocity fields inside the drop for $\phi = 1.3\times10^{-6}$. 91

Figure 5.11 Time-resolved streamlines and contour plots of vorticity ω_z for $\phi = 0$. ... 93

Figure 5.12 Time-resolved streamlines and contour plots of vorticity ω_z for $\phi = 1.3 \times 10^{-6}$. 94

Figure 5.13 Pressure distribution (Pa) in a partial coalescing drop (D = 3.6 mm) of the same case shown in Figure 5.9 for ϕ =0; 95

Figure 6.1 Surface concentration of surfactants Γ^* along the interface. The distance, indicating the distance from the center, is normalized by the horizontal drop radius R. The negative values of the distance indicate the area on the left, and the positive values indicate the area on the right from the center. 100

Figure 6.2 Typical structures of the thin film trapped between the drop and the bulk liquid at the initial stages of the rest phenomena for varying surface ages. The drop surface and the phase interface are highlighted with yellow and red lines, respectively, to help visualization. 103

Figure 6.3 Evolution of the local structure at the neck tip for different surface ages: (a) T = 0 min, (b) T = 240 min, and (c) T = 300 min. 105

Figure 6.4 The distribution of surfactant concentration Γ^* at the tip area during the neck growth for T = 0 min. 106

Figure 6.5 Surfactant concentration at the tip of the neck for coalescences under different surface ages. 107

Figure 6.6 Travel distance of the neck tip versus coalescence time for various drop surface ages. The travel length is defined as the distance of the tip away from its original location. 108

Figure 6.7 Surfactant concentration Γ^* along the coalescing drop surface for T = 720 min. 109

Figure 6.8 Surfactant distributions along the deforming surfaces and the related evolution of the drop surface. The hollow circles in the figure indicate the positions of the neck edges, while the full (red) dots indicate the positions with the maximum

surfactant concentration. ..... **错误!未定义书签。**

Figure 7.1 Probability distribution of drop rest time at the liquid-liquid interfaces with different speed. 116

Figure 7.2 (a) Variation of the drop deformation characterized by the diameter ratio D_h/D_v and the descend depth of the drop bottom from its initial position at t = 0 ms, when the drop contacts the interface.; and the impact (b) and rebound (c) of a single drop at the fluid interface of v = 3.4 cm/s; 119

Figure 7.3 Change of drop velocity with time (a) over the whole measuring period, and (b) during the initially impact and rebound period. The velocity values in the legend are determined by tracking the motion of the drops at the final stage when the velocity is same as that of the interface. 120

Figure 7.4 (a) Raw PLIF image showing the film shape; (b) the variation of the light intensity along the vertical dashed (yellow) line in Figure (a)..... 121

Figure 7.5 The variation of the film thickness during drop impact and rebound at (a) v = 1.0 cm/s (b) v = 2.1 cm/s and (c) v = 3.4 cm/s. The dotted (red) lines represent the locations with the maximum film thicknesses at the last time step of the measurement. 122

Figure 7.6 (a) Variation of the horizontal locations of the minimum film thickness against the time t. The initial values were taken at 5ms after the drop contacts the bulk interface (b) evolution of the film width; only the cases v = 1.0 cm/s and v = 3.4 cm/s are shown to help visualization. 123

Figure 7.7 Velocity fields (m/s) in both the drop and the bulk liquid at different locations away from the impact point for v = 2.1 cm/s. The velocity in the figure is the value relative to the translational speed of the drop, which is measured by detecting the trajectory of the centre point of the drop..... 125

Figure 7.8 (a) A pendant drop resting on the interface without coalescence. The origin of the axis is at the centre of the maximum width of the deformed drop, which is defined as 2R; (b) thickness of the film trapped between the drop surface and the liquid-liquid interface; The film thickness is averaged from 5 different times when drop levitate on

the interface, and the error bars show the standard deviation. (c) The magnitude of the velocity along both the drop surface and the interface. The spatial location is normalized by the drop 'radius' R..... 126
Figure 7.9 (a) the lubrication pressure along the film; (b) velocity profiles at different locations in the trapped film. 128
Figure 7.10 Comparison of the film pressure calculated by the local curvature of the drop surface with the numerically simulated pressure. The data shown in the figure is averaged from the pressures at five different time steps. The error bars show the standard deviation. 129
Figure 7.11 (a) relative lubrication pressure ΔP_l in the film region for v = 3.4 cm/s; (b) magnitude of the ΔP_l at different velocities. The pressure value is averaged over 5 different tests and the error bars show the standard deviation. 130
Figure 7.12 Distribution of rupture points for interface with different speeds. 131
Figure 7.13 Film thickness at two different locations L from the drop impact point for interfaces of different speeds. 133
Figure 7.14 Formation of the drops-on-string during the coalescence of drops with moving interfaces with speeds of (a) v =2.1 cm/s, L = 0.5 cm; (b) v = 3.4 cm/s, L = 1 cm; (c) Incomplete drop string formation for a coalescence event at v = 3.4 cm/s, L = 5 cm..... 134
Figure B.1 The one dimensional discretization grid. 144
Figure B.2 2D computational grids at times t(n) and t(n+1). 145
Figure B.3 Strategy for integration of pressure. 145
Figure B.4 Schematic of the integration scheme in the coalescing drop; the circles represent the grid points with known pressure. 145
Figure C.1 Defined variables of the drop geometries on the deformed interface. 152
Figure C.2 The variations of the total force F_{total} that the drops acquire for the acceleration, the estimated drag force F_{drag} from the surrounding liquids and the tangential force F_{film} from the film at the bottom of the drop 152
Figure D.1 Computational domain and details of the grid used around the drop and in the film region (total cells 128053)..... 156

Figure D.2 Contours of the pressure field (Pa) in the trapped film and in the surrounding area. 156

List of Tables

Table 2.1 Literature on drop rest time measurements..... 6

Table 2.2 The velocity profile and the corresponding lubrication force with different surface mobility. $m = (D/h_0)^{0.5}/\lambda$, D is the diameter of the drop, λ is the ratio of the drop viscosity, μ_d, to the viscosity of the surrounding liquid, μ_s; R_m is the average radius of the two drops; h_0 is the initial distance of the two interfaces; Δu refers to the approaching velocity of the two drops The velocity profile in the film is considered the sum of a uniform velocity u_t (to account for the mobility of the interfaces) and a parabolic part u_p (Davis et al., 1989). 13

Table 3.1 Fluid properties for the investigation on the total coalescence..... 38

Table 3.2 Fluid properties for the partial coalescence. The W and G represent the water and the glycerol, respectively; the SO refers to silicone oil and S80 refers to Span 80. 40

Nomenclature

Bo	Bond number;	
Ca	Capillary number;	
CMC	Critical Micelle Concentration;	
D	Horizontal diameter of the drop;	m
D_d	Horizontal diameter of the daughter drop;	m
F_{oil}	Drag forces from the surrounding oil phase;	N
F_{film}	Drag force from the film liquids;	N
I	Intensity of the PIV/PLIF image;	
K_L	Adsorption constant;	m^3/mol
M	Molecular weight;	g/mol
Ma	Marangoni number;	
N	Number of the drops do not coalescence in a specified time t;	
N_0	Number of the test drops in total;	
NBD-PC	Abbreviation of the fluorescence surfactants;	
Oh	Ohnesorge Number;	
Oh_c	Critical Oh number for the partial coalescence;	
Oh_d	Ohnesorge Number based on the drop liquids;	
Oh_s	Ohnesorge Number based on the surrounding liquids;	
P_{in}	Pressure on the drop surface from the drop inner liquids;	Pa
P_{out}	Pressure on the drop surface from the outside of the drop;	Pa
PIV	Particle Image Velocimetry;	
PLIF	Planar Laser Induced Fluorescence;	

Q_x	Volume flow rate in the trapped film;	m^3/s
R	Horizontal radius of the drop;	m
R_b	Radius of the barrier ring;	m
Re	Reynolds number;	
T	Drop surface (phase interface) age;	min
Γ	Surface concentration of surfactants ;	mol/m^2
Γ_∞	Saturated surfactant concentration at the interface;	mol/m^2
Γ^*	Normalized surface concentration;	
Γ_{tip}^*	Space averaged surfactant concentration at the film tip;	mol/m^2
Γ_{max}^{900}	Maximum surface concentration at the surface age of 900 min;	mol/m^2
$\Gamma_{\omega_z}^*$	Space-averaged vorticity in the drop;	
g	Gravitational acceleration	m/s^2
h_0	Initial distance between the drop surface and the interface before film drainage;	m
h_c	The critical thickness of the film when the rupture occurs;	m
k_{xy}	Kinetic energy per unit mass;	m^2/s^2
k^*_{xy}	Space averaged kinetic energy per unit mass ;	m^2/s^2
κ_b	Curvature of the bottom interface;	m^{-1}
n	Refractive index;	
σ	Interfacial tension;	N/m
σ_T	Temperature based interfacial tension ;	N/m
$p(r)$	Lubrication pressure in the film;	Pa
ρ_d	Density of the drop liquids ;	kg/m^3
ρ_s	Density of the surrounding phase;	kg/m^3
ρ_m	Average Density of the two phases;	kg/m^3
$\Delta\rho$	Density difference between the two phases;	kg/m^3
r_f	Radius of the trapped film in laser plane;	m
r_n	Radius of the expanding neck in laser plane;	m
r_c	the radius of the liquid cylinder;	m

γ	Amplitude of the vibration;	m
t_σ	Character time in the capillary regime;	s
u_t	Tangential velocity along the interface;	m/s
u_d	Tangential velocity along the drop surface;	m/s
u_f	Velocity in the trapped film;	m/s
u_b	Velocity along the interface of the bulk liquids;	m/s
μ_d	Dynamic viscosity of the drop liquids;	Pa·s
μs	Dynamic viscosity of the surrounding phase;	Pa·s
μ_m	Average viscosity of the two phases;	Pa·s
μ_a	Dynamic viscosity of air;	Pa·s
w_d	Approaching velocity of the drop surface;	s/s
w_b	Approaching velocity of the bottom interface;	m/s
ω_0	Frequency of the vibration;	
ω_z	Vorticity in the drop;	s^{-1}
λ	Ratio of the drop viscosity μ_d to the viscosity of the surrounding liquids μ_s;	
ξ	Drop ratio of diameter of the daughter drop to the mother drop;	
ϕ	Mass ratio of the surfactants to the base oil;	wt/wt
ζ	Volume concentration of glycerol;	vt/vt
φ	Surfactant concentration in the liquids ;	mol/m^3

Chapter 1

Introduction

1.1 Background and motivation

The coalescence of drops is often encountered in many industrial applications involving the processing of emulsions and dispersions. In some of the fields such as the oil transportation and milk production, drop coalescence rate plays a key role in controlling the stability of the emulsions (Yeo et al., 2003, Tcholakova et al., 2006, Gilet et al., 2007, Venkataraman et al., 2013, Kavehpour, 2015, Farhadi et al., 2016, Han et al., 2018). In other processes including drug encapsulation, ink-jet printing, drop manipulation in micro systems and liquid jet atomization, precise control of the drop size as a result of coalescence is required for high product quality (Andrade et al., 2015, Wang et al., 2016, Deng et al., 2016, Somwanshi et al., 2018, Wagoner et al., 2018).

Despite the widespread technical relevance and applications of drop coalescence in engineering, the mechanisms underpinning the phenomenon are still not fully understood, especially when surface active agents are presented. In many applications listed above, surfactants either exit naturally or are artificially introduced in the liquid systems to stabilize the liquid-liquid dispersions. Surfactants are found to affect the coalescence behaviour significantly. Previous studies have shown that the coalescence time is prolonged when surfactants are presented, and several theoretical models have been proposed to explain the mechanism underpinning. In almost all models, an uneven spreading of surfactants along the drop surface during coalescence is predicted, but so far these studies have not been experimentally validated.

As first reported by Mahajan (1930), a drop approaching its bulk homophase may not always merge with it but instead partial coalescence takes place, where a daughter

drop is generated. There is still no consensus in the literature on what causes partial coalescence. Some researchers attribute it to the convergence of the capillary waves along the drop surface (Ding et al., 2012), while others consider it mainly a result of the dynamics in the liquid inside the drop (Blanchette and Bigioni, 2006).

Most of the previous studies only focus on the coalescence of drops with a stationary interface. However, in engineering applications the majority of the coalescence events happen with moving interfaces. As recently reported, drops are able to levitate on the free surface of a bulk liquid for a long time before coalescence occurs when the liquid is flowing (Lhuissier et al., 2013, Sreenivas et al., 1999). This interesting phenomenon is expected to occur as well for drops over moving liquid/liquid interfaces. However, there is no related experimental work reported.

The motivation of the present study is to address the lack of detailed knowledge of the coalescence of drops with liquid-liquid interfaces, especially in the presence of surfactants for both complete and for partial coalescence. For this purpose, it is essential to track the rapidly evolving drop surface as well as the changes in the velocity field inside the drop. Previously employed measuring techniques such as high-speed shadowgraphy and high-speed Particle Image Velocimetry (PIV) (Mohamed-Kassim and Longmire, 2004), will be utilized in this work. To further investigate the effects of surfactants on the coalescence mechanism, a high-speed Planar Laser Induced Fluorescence (PLIF) technique will be applied to detect the distribution of the surfactants along the drop surface throughout the whole coalescence process. A novel flow set-up will, finally, be designed to study the coalescence phenomenon with moving liquid-liquid interfaces. The levitation of drops at the moving interfaces at different speeds will be investigated with the optical methods mentioned above.

1.2 A guide through the thesis

The thesis aims to explore the mechanisms underlying the coalescence of drops with liquid/liquid interfaces in the presence of surfactants. Initially, the widespread industrial applications of the coalescence process and the corresponding scientific problems are briefly outlined in this Chapter. In Chapter 2, the previous investigations

on various aspects of coalescence including the film drainage during the drop rest phenomena, the neck expansion after film rupture, the partial and total coalescence and the non-coalescence phenomena are reviewed. The experimental systems and the methodologies used to study the partial and the total coalescence, the spatiotemporal distribution of surfactants and the delayed coalescence on moving interfaces are described in Chapter 3. The techniques applied including high-speed shadowgraphy, PIV and PLIF are introduced as well.

Chapter 4 presents the experimental results on the total coalescence of drops with stationary liquid-liquid interfaces with and without surfactants. The drop surface evolution as well as the drop internal fluid dynamics are discussed. In Chapter 5, the effects of the surfactants on the drop/interface partial coalescence are presented. Phase maps are plotted to indicate the partial coalescence region as well as the variation of daughter to mother drop ratios during the coalescence cascade. The mechanism leading to the generation of daughter drops is analysed based on the velocity and pressure fields. To further discover how the surfactant-induced Marangoni effects impact on the coalescence process, PLIF studies are conducted to find the spatiotemporal distribution of fluorescent surfactants along the drop surface as well as the interface, and the results are shown in Chapter 6. Chapter 7 discusses the behaviour of the drops that surf along moving interfaces, including the initial acceleration of the drops, the shape of the film trapped between the drop and the interface, and the inner dynamics of the travelling drops. The lubrication pressure in the trapped film that delays the coalescence is calculated. The scientific conclusions from this study are summarized in Chapter 8.

Chapter 2

Literature review

When a drop suddenly impacts on an initially flat surface of its homophase through air or another immiscible liquid, the fluid between the drop bottom and the bulk is not able to escape completely but leaves a thin film behind. This film will gradually become thinner as it drains. After the film sufficiently thins to around 1000 Å, van der Walls force comes into effect to break it (Chen, 1985). Immediately after the film rupture, the neck connecting the drop and the bulk expands rapidly while the remaining of the film retreats. The liquid in the drop will then drain either partially (*partial coalescence*) or completely (*total coalescence*) into the bulk phase, as shown in Figure 2.1.

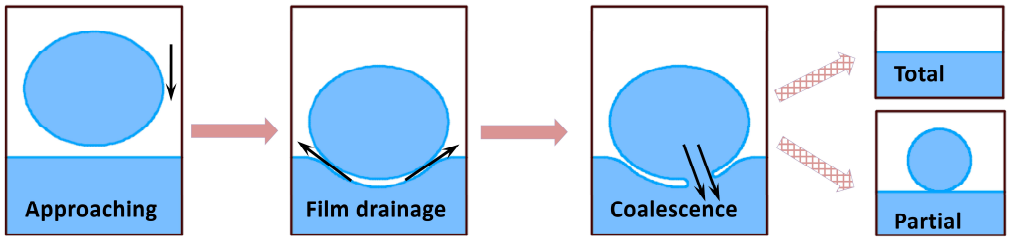

Figure 2.1 An illustration of the coalescence process after a drop hits the surface of its homophase.

In this Chapter, the previous experimental and theoretical studies on the coalescence phenomenon will be briefly summarized to provide a general knowledge of the research progress and the existing problems in this field. It is worth mentioning that this review will focus on, but will not be limited to, the coalescence of drops with a liquid/liquid interface; studies on other types of coalescence, including the coalescence of drops at air/liquid surfaces, the drop to drop coalescence, and the coalescence of bubbles will also be considered, as they share similar dynamics to those of drop coalescence with liquid-liquid interfaces. As the effects of surfactants on the drop/interface coalescence will be the main focus in this work, a general introduction

of the properties of surfactants will be presented.

The literature review is structured in the following five sub-sections to highlight the main results on the aspects which are most relevant to the coalescence events discussed in the thesis.

- Surfactants and Marangoni effect
- Drop rest phenomena
- Neck growth
- Dynamics of liquid merging
- Delayed coalescence at a moving liquid interface

2.1 Surfactants and Marangoni effect

In this section, the properties of the surfactants and their general effects on the interface dynamics will be introduced briefly.

2.1.1 Surfactant properties

For any general liquids, the molecules at the surface interact more strongly with the molecules inside the liquid than with the molecules of the air. Surface tension is generated due to the higher potential energy of the molecules at the surface than inside the liquid. By introducing surfactants into the system, the surface tension can be reduced. This unique property of surfactants is due to their amphiphilic structure which consists of both a hydrophilic group and a hydrophobic group. In the case that surfactants dissolved in aqueous phase, the hydrophobic group of the surfactants breaks hydrogen bonds between the water molecules and structure the water in the vicinity of the hydrophobic group. As a result, a part of the surfactant molecules is expelled to the interface which reduces the potential energy of the molecules at the surface and the surface tension.

Depending on the structure of the hydrophilic group, surfactants are generally classified as Anionic, Cationic, Zwitterionic and Nonionic (Milton, 2004). Surfactants are widely used in surface wetting, ore floating and emulsification in many industrial applications (Shah et al., 2013). In order to provide general guidelines that are helpful in the selection of surfactants in these fields, it is essential to understand their basic

properties, such as the adsorption speed of the surfactant molecules to the interface, the potential to reduce the surface tension, and the Critical Micelle Concentration (CMC).

When the surfactant concentration increases in the bulk liquid, the surfactant molecules are adsorbed at the surface until the surface is fully covered, after which with further increase of the surfactant concentration, micelles appear (Figure 2.2). The surfactant concentration corresponding to the onset of micelles formation is termed Critical Micelle Concentration (CMC value). The surface tension presents a decreasing trend during the adsorption until the CMC is reached. After CMC, the surface tension becomes virtually steady state even though the concentration continues to increase.

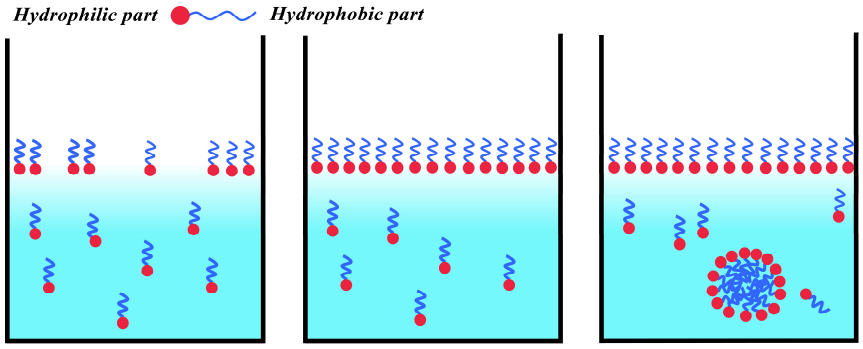

Figure 2.2 A Schematic of the migration of surfactant molecules. The solid circle represents the hydrophilic part of the surfactant, the curve represents the hydrophobic part.

The quantification of the surfactant concentration at the interfaces is very important for this study. Some advanced techniques like the Langmuir trough have been developed and applied to directly measure this value. However, these techniques were not used for the study of the liquid/liquid interface because it is challenging to effectively isolate the interfacial region from the bulk. Alternatively, a plot of the dynamic surface tension against the surfactant concentration in the bulk until equilibrium is reached, is generally applied to describe the surfactant adsorption. By fitting the data, the saturated surfactant concentration at the surface corrsponding to the concentration in the bulk can be predicted through the Gibbs adsorption equation (Milton, 2004). The surface tension measurement and the calculation of the concentration at the surface (interface) will be presented in Chapter 3 and Chapter 5 in combination with the description of the experimental results.

2.1.2 Marangoni effect

When an initially flat surface that is packed with surfactants is expanded or compressed, the surfactant concentration decreases or increases locally respectively. As described above, the accumulation of surfactant molecules at the surface results in a low surface tension while the area with fewer surfactant molecules has a high surface tension. Thus a surface tension variation inevitably appears at the interface (Weiß, 2004). The gradient of the surface tension exerts a tangential shear stress, $\partial\sigma/\partial t$, at the surface (interface), which causes convection, $\partial u_t/\partial n$, on the liquids at the vicinity:

$$\frac{\partial \sigma}{\partial t} = \mu \frac{\partial u_t}{\partial n} \tag{2.1}$$

where σ is the local surface tension, u_t is the velocity tangential to the surface, n and t denote the directions orthogonal and parallel to the surface, respectively. The displacement of the fluids induced by the surface tension gradient along the surface (interface) is called the Marangoni flow after the Italian physicist Carlo Marangoni, who first studied this phenomenon in 1865 (Marangoni, 1865). Obviously, the Marangoni effect can significantly influence coalescence when surfactants are present, as the drop surface evolves significantly during the process (Blanchette et al., 2009, Dai and Leal, 2008, Yeo et al., 2003). These effects will be introduced in the following sections.

2.2 Drop rest phenomena

2.2.1 Drop rest time

As discussed above, as a drop approaches an interface (or another drop) a thin film forms and coalescence will occur when the film breaks. Compared to the later stages of coalescence, the time that the drop rests on the interface before the film breaks is the longest. The rest time is generally defined as the interval from the arrival of the drop on the interface to the film rupture. It is an important indicator for the stability of emulsions in many industrial fields, such as oil/water separation (Mason et al., 1995), milk & coffee production (Klemaszewski et al., 1992) and liquid extraction (Ban et al., 2000).

Thus, many studies have focused on the prediction of the rest time.

It has been established that even under the same conditions the drop rest time is not a constant but presents a wide distribution. During the 1950s to 1980s, a number of pioneering works were conducted to directly measure the drop rest time in various conditions. A comprehensive list is provided in Table 2.1. Researchers found that an increase in temperature and the presence of sonic disturbances lead to a decrease of the rest time (Nielsen et al., 1958, Charles and Mason, 1960a, Lang and Wilke, 1971). While the increase of the drop size, the presence of mechanical disturbances, the increase of the elasticity of the liquids and the addition of surfactants result in an increase of the rest time (Hodgson and Woods, 1969, Dreher et al., 1999). In terms of the effect of drop size on the rest time, Dreher et al. (1999) concluded that the coalescence time increases almost linearly with the drop size for drops with diameter 0.3~2.5 mm. However, Nielsen et al. (1958) reported that the drop size can increase or decrease the rest time depending on fluids properties and on the presence of surfactants.

Initially, researchers attempted to build models that predict the rest times for the drops on a surface (interface) by fitting of the measured data. However, some of the models are not very accurate (Gillespie and Rideal, 1956), because of limited understanding of the draining behaviour of the film liquid. A full knowledge of the film structure and the dynamics of the liquids during the draining is essential, as the rest time is greatly determined by the film drainage.

2.2.2 Film draining

Due to gravity, as the drop approaches its homophase, it presses against the interface which takes a concave shape. In return, the drop will deform as well due to repulsive forces. The deformation of both the drop surface and the interface result in an uneven distribution of the film thickness, which significantly affects its drainage. It is challenging to measure the film thickness directly (e.g. with imaging) as the film is very thin (<μm). Instead, light interference technique is widely applied to obtain the thickness of the trapped film by recording the optical interference fringe patterns caused

Reference	Coalescence type	Fluids (Aqueous/organic)	Drop (bubble) phase	Drop diameter(cm)	Variables	Surfactants
Gillespie and Rideal (1956)	Drop/Interface	water/ benzene water/liquid paraffin	water	0.3-0.8	drop size; temperature;	--
Nielsen et al. (1958)	Drop/Interface	water(polyvinyl alcohol, carboxymethyl cellulose, gelatin)/ Benzene toluene, styrene, p-xylene, nujol, butyl chloride, methyl n-butyrate, 3 pentanone polystyrene,	benzene, toluene, styrene, p-xylene; butyl chloride, 3-Pentanone	0.068-0.307	temperature, interface curve, drop sizes, PH, interfacial viscosity	Saponin, sodium salt of sulfonated polystyrene, sodium salt of polyacrylic acid
Charles and Mason (1960a)	Drop/Interface	water(KCL)/ Benzene; water(KCL)/ carbon tetrachloride water(KCL)/ heptane	water, Carbon tetrachloride	0.082-0.578	drop size; temperature;	--
MacKay and Mason (1963)	Bubble/surface Drop/Interface	N_2/86% glycerol water/cinnamaldehyde water/diphenyl sulphide water/dibutyl phthalate	N_2/water	0.047-0.085	surface tension, viscosity	--
Jeffreys and Hawksley (1965)	Drop/Interface	water/ Benzene, water/liquid paraffin water/heptane	water	0.192-0.276	falling distance; temperature, drop size	--
Hodgson and Lee (1969)	Drop/Interface	water(KCL)/ toluene	Water; Toluene	0.084-0.42	drop size	sodium benzoate; sodium lauryl sulfate
Hodgson and Woods (1969)	Drop/Interface	water(KCL)/ toluene water(KCL)/ anisole	Anisole, toluene	0.156-0.306	surface tension	sodium lauryl sulfate
Lang and Wilke (1971)	Drop/Interface	water (glycerol)/bezene water (glycerol)/ tributyl phosphate water (glycerol)/anisole water/Aroclor 1248	Water(glycerol);	0.267,0.415	drop size, viscosity, surface tension, sonic disturbances	Span 80; Tween 81 sodium oleate
Burrill and Woods (1973b)	Drop/Interface	water(KCL)/toluene, water(KCL)/anisole cyclohexanol, cyclohexane-anisole (CA)	toluene,anisole, cyclohexanol, CA	0.124-0.363	drop size, viscosity, surface tension	sodium dodecyl sulfate

Table 2.1 Literature on drop rest time measurements.

by the refraction of the light passing through the film. (Hodgson and Woods, 1969, Burrill and Woods, 1973a, Chan et al., 2011). A representative example is shown in Figure 2.3, a dimpled film, which presents a thicker region in the centre and a thin area at the rim, is generally observed.

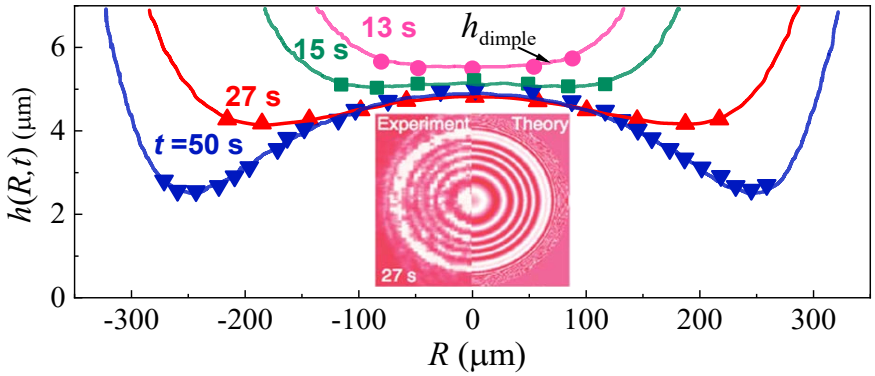

Figure 2.3 The silicone oil film trapped between two glycerol drops after the dimple forms (Chan et al., 2011). The experimental data shown in figure is obtained with the light interference technique.

As presented in Figure 2.3, the film thinning process is usually symmetrical for binary coalescence of drops, while various non-symmetrical draining patterns can be observed for the drop/interface coalescence (Hodgson and Woods, 1969, Burrill and Woods, 1973a). As described by Chan et al. (2011), the draining dynamics of the film is complex, which is determined by many factors such as the initial distance of the drop from the interface, the fluid viscosity, the surface tension and the electric double layer that forms in the area. In most of the cases, the thickness of the dimpled film decreases rapidly until its rupture (Figure 2.4 (a)), while a slow thinning behaviour of the dimple is also possible (Figure 2.4 (d)). Interestingly, it has been observed that the thickness at the centre region of the film gradually increases for a while before it gets thinner, see Figure 2.4(b). Non-symmetrical thinning has also been observed due to instabilities, as shown in Figure 2.4(c). It should be noted that all the cases shown in Figure 2.4 are with surfactants, which tend to make the film draining complex.

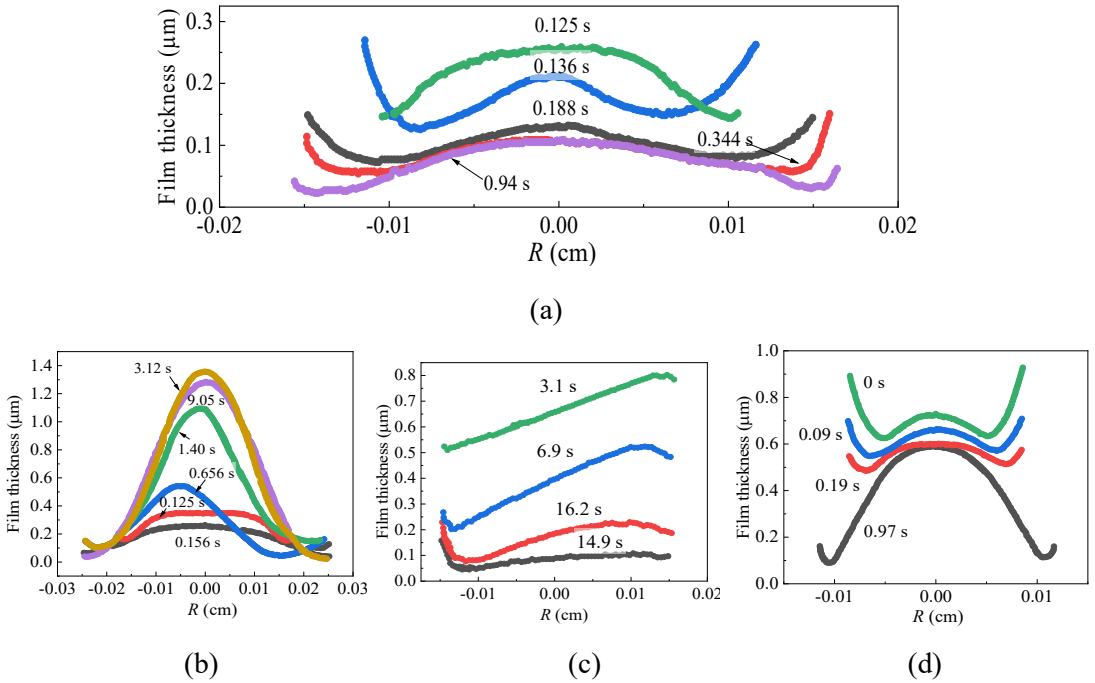

Figure 2.4 The draining patterns of the thin film trapped between the drop and the bulk liquids; (a) rapid, uniform thinning to coalescence; (b) inflow to dimple, and draining to coalescence; (c) non-symmetrical draining, thinning to coalescence; (d) slow dimpled thinning (Hodgson and Woods, 1969).

2.2.3 Lubrication flow

At later studies, supported by better understanding of the fluid mechanics in the film liquid, the lubrication theory was employed to predict the drainage of the film in a narrow gap between two drops or between a drop and its bulk homophase (Davis et al., 1989). In a bearing system, the hydrodynamic lubrication generates a disjoining pressure in the thin film to resist the contact of the shaft and bearing and limit friction (Hamrock et al., 2004). In analogy to the bearing lubrication, it is widely accepted that the thinning of the trapped film is controlled by the balance between the lubrication pressure that resists the drainage and the gravity force that pushes the drop to contact the interface. As shown in Figure 2.5, when the drop approaches a flat liquid surface to a small distance, the thickness of the film h is far less than that the length L. Under the circumstance, the Reynolds number $Re = \rho uh/\mu$ in the thin trapped film is much lower than 1(Sawaguchi et al., 2019), the inertia is neglected and the Navier-Stokes equations are:

$$\frac{\partial p}{\partial z} = 0 \tag{2.2}$$

$$\frac{\partial p}{\partial r} = \mu \frac{\partial^2 u}{\partial z^2} \tag{2.3}$$

where r and z are coordinates in the direction along the interface and perpendicular to the interface, u is the radial velocity. By substituting the boundary conditions into Equation (2.3), the pressure distribution through the entire film area is known. For the case of drop surface approaching an initially flat interface, where the tangential velocity of both the drop surface and liquid surface are 0, the pressure distribution is as shown in Figure 2.5. Due to the local low pressure, a minimum thickness is generated at the border area of the film giving rise to a global dimple structure.

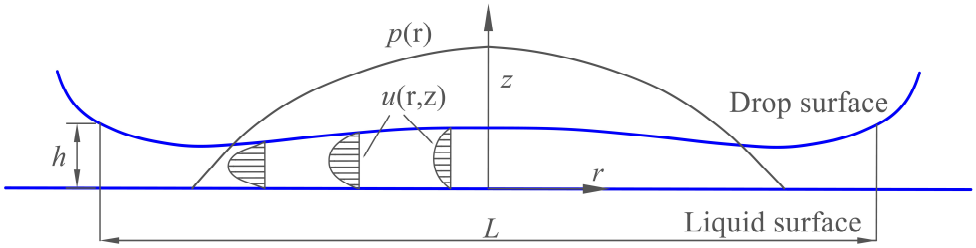

Figure 2.5 A schematic showing the lubrication film when a drop approaches a flat liquid surface to a small distance. The schematic radial velocity profile $u(r,z)$ is plotted to help visualization. The distribution of the pressure $p(r)$ is relevant to the pressure of the surrounding liquids.

The velocity profile plotted in Figure 2.5 is based on the assumption of immobile interface. Davis et al. (1989) took the mobility of the interface into consideration and calculated the repulsive lubrication force resisting the thinning of the film for the case of drop/drop binary coalescence, as shown in Table 2.2.

Surface mobility	m	Velocity profile	Lubrication force F
Nearly rigid	$m<<1$	$u_t=0$, $u_p>>u_t$;	$F/(6\pi\mu R_m^2\Delta u/h_0)=1-1.31m+1.78m^2$
Fully mobile	$m>>1$	$u_t=\Delta ur/h, u_p<<u_t$;	$F/(6\pi\mu R_m^2\Delta u/h_0)=0.876/m$
Partially mobile	$m=o(1)$	$u_t=o(u_p)$;	$F/(6\pi\mu R_m^2\Delta u/h_0)=(1+0.38m)/(1+1.69m+0.43m^2)$

Table 2.2 The velocity profile and the corresponding lubrication force with different surface mobility. $m=(D/h_0)^{0.5}/\lambda$, D is the diameter of the drop, λ is the ratio of the drop viscosity, μ_d, to the viscosity of the surrounding liquid, μ_s; R_m is the average radius of the two drops; h_0 is the initial distance of the two interfaces; Δu refers to the approaching velocity of the two drops The velocity profile in the film is considered the sum of a uniform velocity u_t (to account for the mobility of the interfaces) and a parabolic part u_p (Davis et al., 1989).

It is easy to find out that the coalescence could even be prevented if the overall force found from the integration of the pressure along the film area balances the drop gravity. The distribution of the pressure is related to the liquid flow in the film, which is affected by the surface velocity. Therefore, many researchers altered the velocity at both the surfaces to produce a non-coalescence phenomenon, which will be reviewed in Section 2.5.

2.2.4 Theoretical predictions of the drop rest time

Considering the drainage dynamics in the trapped film, a number of models were established to predict the coalescence time. Gillespie and Rideal (1956), who considered that a periodic disturbance at a frequency of f and an amplitude of A_0 on the interface leads to the rupture of the film, suggested the model shown in Equation (2.4):

$$\log(N/N_0) = -K(t - t_0)^{3/2} \tag{2.4}$$

where the coalescence constant $K = fC_0A_0(6\sigma/R\mu)$, N is the number of the drops that do not coalescence at t; N_0 is the total number of tested drops, t_0 is the time when the liquid draining starts; C_0 is a constant related to the environment influences (temperature and mechanical shocks), σ is the interfacial tension, R is the radius of the drop and μ is the viscosity of the film liquid. However, as C_0 is sensitive to the environments, the model is only accurate for drop radius at 0.15~0.45 cm.

Another model was proposed by Charles and Mason (1960a) based on the mass conservation of the liquids and the force balance in the thinning film. According to their study, the time for the film between a sphere of radius R and an unbounded interface drains to the critical value can be estimated by Equation (2.5),

$$t = \frac{6\pi\mu R^2}{F}\ln\frac{h_o}{h_c} \tag{2.5}$$

where F is the force acting on the sphere, h_0 and h_c refer to the initial thickness of the film before the draining and the thickness when the rupture occurs. However, the model assumes that the interface is rigid, therefore it leads to large errors for liquid/liquid systems, where the tangential force along the interface induces inner circulation in the

drop. Taking the circulation into account, Jeelani and Hartland (1994) derived a new equation to predict the rest time according to lubrication theory:

$$t = \frac{3\pi\mu n^2 r_f^4}{16Fh_c^2} \tag{2.6}$$

where n is relevant to the mobility of the interface and r_f refers to the radius of the film area. It is worth noting that the film thickness in this model was assumed uniform, which is inconsistent with the actual case.

As many factors like the drop size, the fluids viscosity, the environmental temperature, and the mechanical or sonic perturbations can affect drop coalescence, there is no existing model that achieves high accuracy for all cases. Thus, the assumptions of the models should be considered when they are applied.

2.2.5 Distribution of surfactants in the film region

The drop rest time is largely prolonged when surfactants are presented. Several researchers (Wasan, 1992, Cristini et al., 1998, Dai and Leal, 2008) attributed the increased stability of the drops to the surfactant induced Marangoni effect. As shown in Figure 2.6, the draining of the liquids may sweep the surfactants that have initially been adsorbed along the drop surface and the interface towards the edge of the film forming a barrier ring. The varying surface tension resulted from the non-uniform distribution of surfactants produces a force along the interface that opposes the film draining flow, and increases the rest time.

Based on the theory, several numerical studies were conducted to predict the film drainage with surfactants. For the cases with high surfactants concentration along the interface, Chesters and Bazhlekov (2000) found that the Marangoni effect is able to refill the dimple region and make the film thicker, which was not observed by Yeo et al. (2003) whose simulation was carried at lower surfactant concentration. Ghosh and Juvekar (2002) further pointed out that the Marangoni force is not sufficient to refill the film; the only effect is to resist the inner circulation of the drop and increase the interface rigidity. As the migration of the surfactants along the interface in the film region differs in the various numerical analyses, experiments are needed to validate the

simulations.

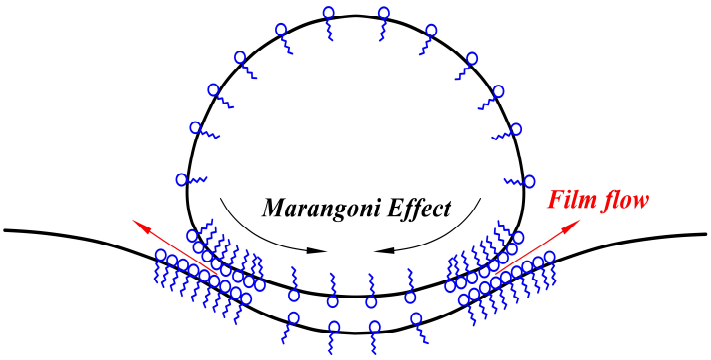

Figure 2.6 Marangoni flow induced from the uneven distribution of surfactant molecules during the film draining.

2.3 Neck growth

2.3.1 Neck growth regime

Once the film rupture occurs, a neck is formed connecting the droplet and the bulk liquid (or the other droplet). High capillary forces are generated at the sharp edges of the neck as a result of the large curvature. They promote the retraction of the film as well as the growth of the neck. Understanding the dynamics of the neck growth is essential in fields such as printing, sintering and liquid spray, because they affect phenomena such as distribution of the drop size and mixing quality in multiphase systems (Aarts and Lekkerkerker, 2008, Scherer, 1984).

Two main regimes have been identified to describe the neck growth, namely the viscous regime and the inertial regime, depending on whether the viscous or the inertia forces are dominant in resisting the capillary forces. It was found that the neck growth initially falls in the viscous regime, where the rupture process is dominated by the balance of viscous and surface tension forces. After a short time, the viscous regime gives way to the inertial regime as the inertial forces become large and overtake the viscous forces to resist the neck expansion (Eggers et al., 1999, Paulsen et al., 2011, Kavehpour, 2015).

In each regime the neck expansion is commonly characterized by the growth of the neck radius r_n against time t. Through dimensional analysis, the capillary number Ca =

$\mu v/\sigma$, which indicates the relative importance between viscous and surface tension forces, was found to describe the process in the viscous regime, where $v = r_n/t$ refers to the speed of the neck radius expansion. By setting the *Ca* number to unity, the growth of the neck radius over time obeys a linear relationship (Eggers et al., 1999, Thoroddsen et al., 2005, Aarts et al., 2005):

$$r_n \propto \frac{\sigma}{\mu_d} t \tag{2.7}$$

where μ_d is the viscosity of the drop liquid. However, in this scaling law the effect of the droplet radius R was not taken into consideration. Eggers et al. (1999) further concluded that the growth of the neck radius obeys the law of:

$$r_n = -\frac{\sigma}{\pi\mu_d} t \ln\left(\frac{\sigma}{\mu_d R} t\right) \tag{2.8}$$

which indicates a logarithmic correlation between the neck radius and the time. Thoroddsen et al. (2005) pointed out that this is only valid when the r_n/R is less than 0.03.

The $Re \sim \rho\sigma r_n/\mu^2$ has been used to indicate if the neck growth occurs in the viscous regime ($Re < 1$) or the inertial regime ($Re > 1$). In the inertial regime, the scaling law of the neck radius as a function of time is predicted by equating the capillary force to the inertial force (Aarts et al., 2005):

$$r_n \propto \left(\frac{\sigma R_d}{\rho}\right)^{0.25} t^{0.5} \tag{2.9}$$

According to Eggers et al. (1999), the viscous regime would end at around 0.7 ns. However, Paulsen et al. (2011) stated that the inertial forces became dominant at a much later time than what was suggested by Eggers et al. (1999). The duration of each regime is influenced by the properties of fluids both inside and outside the drop. As pointed by Aarts et al. (2005), the viscous regime for general liquids can be quite short (10^{-10} s for water drops). Thus, it is challenging to acquire the data in this period even with high speed imaging.

Some representative data extracted from previous experiments showing the neck growth against time are presented in Figure 2.7. In the system with low viscous liquids, a large range of the data fall in the inertial regime with a scaling law shown in Equation

(2.9) (k = 0.5). When the fluids are very viscous, the majority of the data falls in the viscous regime with a linear correlation (k = 1) between the neck radius and the time.

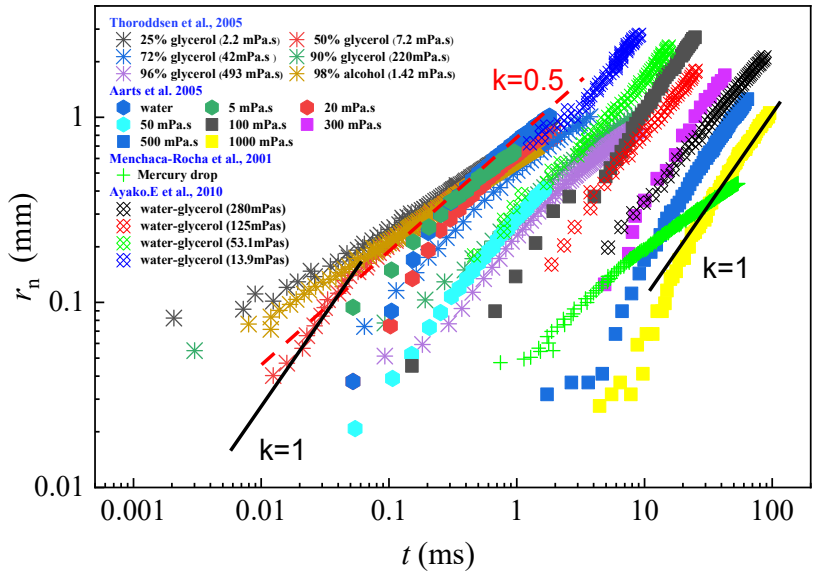

Figure 2.7 Growth of the neck radius r_n against time t. The data are plotted on a log-log scale. The crosses refer to the data acquired by Thoroddsen et al. (2005), the data of solid symbols from Aarts et al. (2005) and the pluses from Menchaca-Rocha et al. (2001). The rhombus with crosses are the results of Eri and Okumura (2010). The red dashed line (coefficient k = 0.5) show the scaling law in the inertial regime, while the black line (k = 1) indicated the trend in the viscous regime.

In Figure 2.7, only the data of Eri and Okumura (2010) is based on drop/interface coalescence, while the rest were obtained from the drop/drop coalescence experiments. Thus, it can be seen that the growth of the neck during the drop/interface coalescence obeys the same rule as the drop/drop coalescence.

2.3.2 Neck expansion with surfactants

Some of the previous experimental data on the neck growth for coalescence in the presence of surfactants are summarized in Figure 2.8. As Chinaud et al. (2016) conducted the experiments in a confined set-up, a Hele-Shaw cell, the growth of the neck has a significantly lower speed than in other cases due to the resistance from the wall.

The addition of surfactants in the fluids leads to a decrease of the interfacial tension, which subsequently decreases the driving force for the neck expansion. Thus, the

expansion speed of the neck reduces as presented in Figure 2.8. However, the surfactants do not significantly affect the scaling law, which was still $r_n \sim kt^{1/2}$ against the coalescence time t.

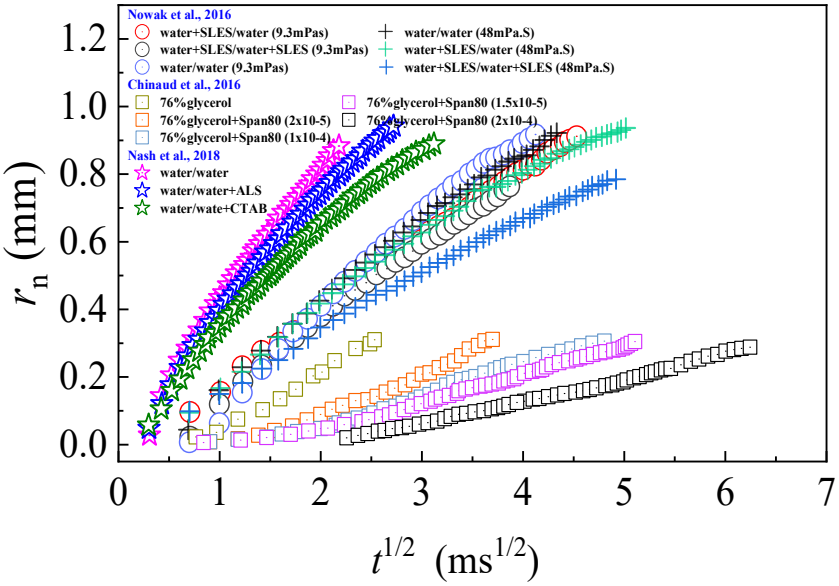

Figure 2.8 Growth of the neck radius r_n against the time t in the surfactant system. The stars refer to the data of drop-drop binary coalescence acquired by Nowak et al. (2016), where SLES is sodium lauryl ether sulfate. The data of circles and the pluses are from the coalescence of drops with the fluid interface by Nash et al. (2018); The ALS can CTAB refer to ammonium lauryl sulfate and cetyltrimethylammonium bromide, respectively. The squares are from the coalescence of drops at the fluid interface in a Hehe-Shaw cell by Chinaud et al. (2016).

Apart from the effect of decreasing the surface tension, the surfactants produce Marangoni flow along the interface, which influences the neck growth as well. Nowak et al. (2016) pointed out that for the coalescence between a pure drop and the surfactant laden drop, the Marangoni flow tends to reduce the neck expansion speed, as the transfer of surfactants reduces the effective interfacial tension. The non-uniform spread of the surfactants during coalescence that leads to Marangoni flows has yet to be directly visualized, due to limitations of the experimental techniques. Recently, simulations were conducted by Martin and Blanchette (2015) to show how the surfactants distribute on the interfaces during coalescence. From the results, a large number of the surfactant molecules was found to accumulate at the tip of the neck due to the local area reduction resulting from the film retreat. Chinaud et al. (2016) further estimated from experimental observations that the surfactant concentration at the

meniscus of the neck is two times of that in the bulk.

2.4 Dynamics of the liquid merging

While the neck expands, the drop liquid starts to merge with the bulk (or the other drop) after the film breakage. After the completion of the neck growth, a large downward flux of the drop liquid results in the reduction of the drop volume. In this section, the previous investigations on this process will be briefly discussed.

2.4.1 Total coalescence

Driven by the surface tension, the drop surface rapidly shrinks and pushes the inner liquid into the bulk. For drops of high viscous liquids or with large diameter, the liquids are able to completely merge with the bulk resulting to a total coalescence. This is frequently encountered in many micro-scale processes such as the preparation of dispersions in a microchannel (Jose and Cubaud, 2012) and the drug encapsulation (Chen et al., 2011), where the merging speed of the liquids significantly affects the quality of products.

As the total coalescence takes place rapidly and finishes in microseconds, it is challenging to experimentally acquire the inner dynamics of the drop liquids. Most of the previous results only present the evolution of the drop surface, which reveals mainly collapse of the drop and the development of capillary waves on the drop surface (MacKay and Mason, 1963, Anilkumar et al., 1991). To the best of the author's knowledge, Mohamed-Kassim and Longmire (2004) were the first who investigated the velocity fields of the liquids during coalescence with a two dimensional PIV technique. Two vortices were observed near the neck edge in the coalescing drop when the film is receding. The vortices continued to move upwards along the collapsing drop surface until they converged. It was also found that the evolution speed of the vortices was reduced when the surrounding liquids had high viscosity.

2.4.2 Partial coalescence

Under some conditions, the drop surface can pinch off at the neck region before the

drop liquid complete drains out, which leaves a daughter drop on the interface (Figure 2.9). The procedure is repeated with the daughter drop, after it has bounced and rests on the interface. This partial coalescence phenomenon is common in daily life and can be seen on raindrops impacting on a pond and in the generation of the ocean mist (Raes et al., 2000, Thoroddsen and Takehara, 2000). In industrial applications, the increase of the entire coalescence time and the formation of a range of drop sizes caused by partial coalescence can decrease the separation efficiency in liquid-liquid coalescers. On the other hand, the small drops created by partial coalescence can improve the perception of fat-related sensory attributes in the food industry (Rommel et al., 1993).

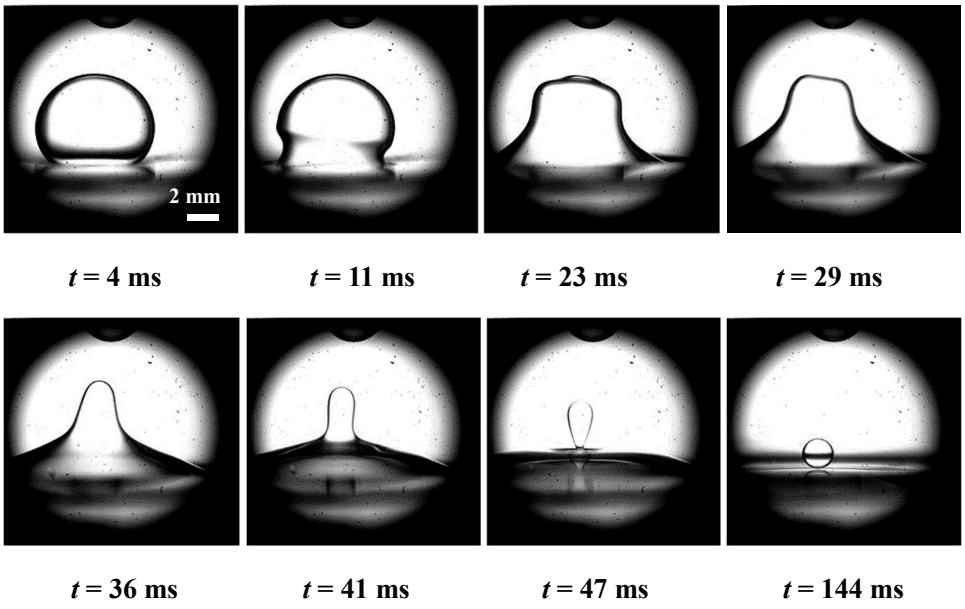

Figure 2.9 Partial coalescence of a drop of pure water at the interface between 5cSt Silicone oil and pure water. The time *t* starts at the moment of the film rupture.

A cascade phenomenon is produced where the daughter drops undergo partial coalescence for many times until the last drop completely joins the bulk, (Figure 2.10). Because of the properties of the fluid, the cascade exhibits different stages. Mar and Mason (1968) found that the coalescence of a drop with a liquid/liquid interface had more stages than that with an air/liquid interface. The experimental results of Nikolov and Wasan (1995) indicated that the stages of partial coalescence were reduced when surfactant was present. Charles and Mason (1960b) compared the rest times of the drops at different coalescence stages. The results showed that the primary drop had the longest rest time, while the rest time for the drop in the last stage was the shortest.

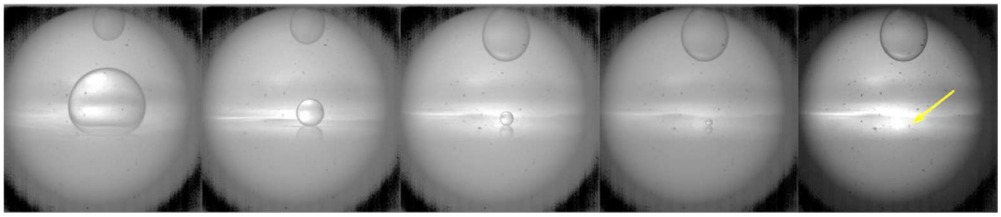

Figure 2.10 The partial coalescence cascade for a drop of pure water at the interface between pure water and a 5cSt silicone oil. Five coalescence events were observed in this cascade. As the size of the 6th drop is quite small, the relevant image is not shown here.

2.4.3 Partial coalescence mechanism

Following the first study on partial coalescence by Mahajan (1930), subsequent researchers have attempted to explain the mechanism of partial coalescence. Charles and Mason (1960b) systematically investigated the partial coalescence of drops with liquid/liquid interfaces and suggested that it resulted from a Rayleigh-Plateau instability. According to the theory, the daughter droplet is generated through two stages: (1) the volume of the mother drop reduces after the film rupture until it takes the shape of a cylinder (t = 4 ms to t = 41 ms in Figure 2.9); (2) when the height, h, of this liquid cylinder becomes $h > 2\pi r_c$, where r_c is the radius of the cylinder, the top of the cylinder pinches off due to the Rayleigh instability and a daughter drop forms (t = 41 ms to t = 47 ms in Figure 2.9). However, Blanchette and Bigioni (2006a) found from the simulations of drops coalescing at air/liquid interfaces that the pinch-off did not result from the Rayleigh-Plateau instability. To show this, they paused their simulation when the cylinder was fully stretched and restarted it by setting all velocities to 0. This procedure did not lead to pinch-off. It should be noted, however, that the column length h in the simulations did not reach $h > 2\pi r_c$. Instead, Blanchette and Bigioni (2006a) proposed that the pinch-off was controlled by the competition between the horizontal collapse (as shown in Figure 2.9 from t = 4 ms to t = 41 ms) and vertical collapse of the droplet surface induced by surface tension. From simulations in liquid-liquid systems, Ray et al. (2010) plotted the u- and v-velocity contours around the drop surface for both the dispersed and the continuous phases and reached the same conclusion. Some other researchers analyzed the phenomenon from an energy balance point of view. Yue et al. (2006) found from numerical simulations that the surface area of the drop increased

when the neck edges approached each other during pinch-off. The additional interfacial energy associated with the increased drop surface area presented an energy barrier that should be overcome for partial coalescence to occur. Viscous dissipation in the liquids around the interface determined whether the energy barrier could be overcome. Zhang et al. (2009) found that during partial coalescence capillary waves carried momentum upwards and at the same time they caused an inward motion of the neck. The upward capillary waves and the drainage rate of the drop liquid were both suppressed in highly viscous systems. They showed, in addition, that pinch-off depended on the geometry of the neck and in particular the relative values of the axial and the azimuthal curvatures.

2.4.4 Criterion for partial coalescence

As the distribution of the drop sizes produced from the partial coalescence largely affects the stability of the dispersions, a number of criteria have been proposed for the conditions necessary for its occurrence. Blanchette and Bigioni (2006a) pointed out that partial coalescence happens when the vertical collapse of the drop was prevented by the convergence of the capillary waves, which were mainly dominated by the interfacial tension and the viscosity of the surrounding liquids. Through a simple dimensional analysis, the *Oh* and *Bo* number are usually considered to characterize the transition between partial and total coalescence (Gilet et al., 2007, Chen et al., 2006, Blanchette and Bigioni, 2006a).

In Figure 2.11 the previous results on coalescence, summarized in a phase map based on the $Bo = (\rho_d-\rho_s)gD^2/\sigma$ and $Oh = \mu_d/(\rho_m D\sigma)^{1/2}$ as coordinates, suggest a boundary between total and partial coalescence. Here, ρ_d and ρ_s refer to the density of the drop and the surrounding phase, D is the diameter of the drop, μ_d for the dynamic viscosity of the drop liquid, ρ_m is the arithmetic mean value of the densities of the two phases. For small $Bo < 5$, the effect of gravity on the drop collapse is negligible and the *Oh* number dominates the partial coalescence. For large *Bo* number, Mohamed-Kassim and Longmire (2004) proposed that partial coalescence would occur when $Bo \cdot Oh <$ 0.02-0.03, where *Oh* was defined using the arithmetic average of the viscosities of the two phases (dashed red line shown in Figure 2.11). Gilet et al. (2007) took the influence

of the viscosities of both phases into consideration and suggested that partial coalescence would take place when $Oh_d + 0.057Oh_s < 0.02$ for $Bo < 0.1$. It is worth noting that the total coalescence data of Gilet et al. (2007) falls into the partial coalescence area designated by other researchers. Therefore, the boundary between partial and total coalescence should be a region rather than a clear line, as the coalescence phenomenon is complex. For instance, the points where the rupture happens can vary a lot even under the same *Bo* or *Oh* number. The effect of the surfactants on the partial coalescence region has not been reported in the literature.

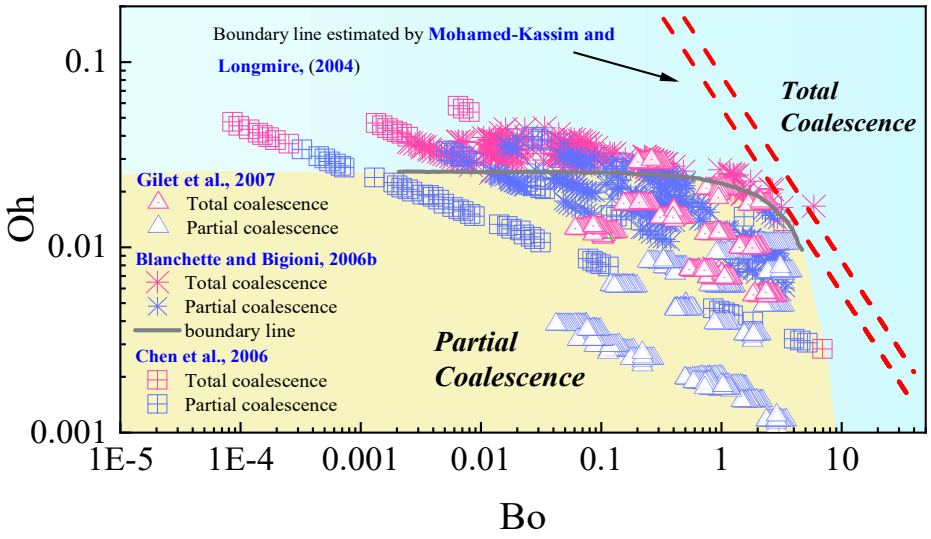

Figure 2.11 Partial coalescence region map based on the *Bo* and *Oh*. The solid line shows a rough boundary between the total and partial coalescence region. The pink shows the total coalescence data, and the blue color for the partial coalescence.

2.4.5 Pinch-off time

The previous studies on the pinch-off time, which is defined as the interval between the film rupture to the pinch-off of the daughter drop in partial coalescence are listed here. The pinch-off time characterized by capillary time $t_\sigma = (\rho_d D^3/\sigma)^{1/2}$ at each regime is shown in Figure 2.12, where $Bo = (\rho_d-\rho_s)gD^2/\sigma$ and $Oh = \mu_d/[(\rho_d+\rho_s)D\sigma]^{1/2}$. Chen et al. (2006) categorized the occurrence of pinch-off into three regimes. For large drops (on the left of the graph), the gravity effect cannot be ignored and *Bo* dominates the drop evolution (gravity regime). For medium size drops which are always produced in self-similar stages, the dynamics of the pinch-off are controlled by both capillarity and inertia (inertia-capillary regime). For drops small enough, the *Oh* increases and *Bo*

decreases, and viscous effects become significant (viscous regime). It was found that the pinch-off time was independent of the drop size in the inertia-capillary regime, but in both the gravity and viscous regimes, it decreased with the increase of the droplet size (Chen et al., 2006). As stated by Kinoshita et al. (1994), the viscosity of the cylinder liquid had more effect on the pinch-off phenomena than that of the surrounding liquid. Yue et al. (2006) plotted the pinch-off time against the average Oh_m number based on an average viscosity $\mu_m = (\mu_d + \mu_s)/2$ and a specific Oh_0 defined using $\mu_0 = (3\mu_d + \mu_s)/4$. Here, μ_d and μ_s refer to the viscosity of the droplet and the surrounding phase. The results indicated that it was inappropriate to solely discuss which viscosity contributes more to the pinch-off time without considering the complex flow in and surrounding the liquid cylinder.

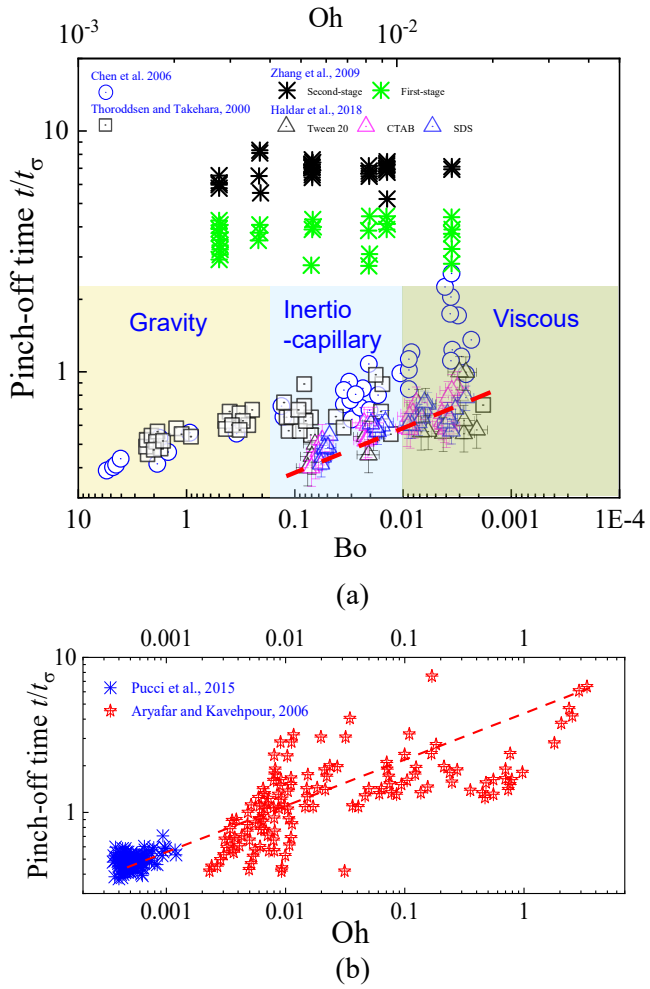

Figure 2.12 (a) A plot of the pinch-off time in different regimes. For the data of Thoroddsen and Takehara (2000) and Chen et al. (2006), the data in the gravity regime are plotted against *Bo*, while the data in inertia-capillary and viscous regimes are plotted against *Oh*. The data of Zhang et al. (2009) and Haldar et al. (2018) are plotted against *Oh*. (b) A plot of the pinch-off time for

the coalescence of a bubble with a soap film (Aryafar and Kavehpour, 2006) and for the coalescence across a wide range of *Oh* (Aryafar and Kavehpour, 2006, Kavehpour, 2015).

Zhang et al. (2009) investigated the pinch-off time for the case of drop/drop coalescence. As the crosses shown in Figure 2.12 suggest, a larger pinch-off time is observed for drop/drop coalescence than that for drop/interface coalescence. They also reported that when the diameter ratio of the two mother droplets increased, the pinch-off time decreased for the first stage, while the pinch-off time of the second stage was unaffected. Recently, Haldar et al. (2018) measured the pinch-off time in a surfactant system. The results presented a linear relation between the dimensionless pinch-off time and the *Oh* number, as the dashed line shows in Figure 2.12(a).

The partial coalescence of a soap bubble with a film of the same liquid was studied by Pucci et al. (2015). The pinch-off time is plotted in Figure 2.12(b) against *Oh* as the gravity effect is negligible. Also, the pinch-off times at a wide range of *Oh* were measured by Aryafar and Kavehpour (2006) and Kavehpour (2015). From these data, it was found that the pinch-off time presents an approximately linear increase with the increase of *Oh*.

2.4.6 Drop ratio

The ratio of the daughter droplet to mother drop diameter, $\xi = D_d/D$, is often used to characterize the degree of partial coalescence. A summary of the drop ratio against $Oh = \mu_d/(\rho_m D\sigma)$ acquired from previous investigations is shown in Figure 2.13. Charles and Mason (1960b) measured the drop ratio in partial coalescence with various fluid pairs. The drop ratio varied with the viscosity ratio $\lambda = \mu_d/\mu_s$, where μ_d and μ_s are the viscosities of the drop (aqueous phase) and of the surrounding liquid (organic phase), respectively. Partial coalescence was not observed when $\lambda < 0.2$ or $\lambda > 11$, and the drop ratio reached a maximum value at $\lambda = 1$. However, Yue et al. (2006) found numerically that the drop ratio kept increasing when λ increased from 0.1 to 10.

The drop ratio changes as well in different coalescence regimes. In the inertia-capillary regime, the drop ratio is independent of the drop size, and it decreases as the drop size increases in the gravity regime; in the viscous regime it also decreases before

reducing rapidly to zero (Chen et al., 2006).

The effect of *Bo* and *Oh* on the drop ratio ξ was separately analyzed by Yue et al. (2006). The drop ratio was found to be independent of *Bo* when $Bo < 0.1$. Also, ξ remained constant for $Oh < 0.1$ when *Bo* was negligible. However, ξ decreased significantly when gravity became significant at large *Bo*. As shown in Figure 2.13, most of the data in the pink region were acquired from the first stage of the cascade, where the big size of the drop leads to a large *Bo*. in this region the value of ξ is much lower.

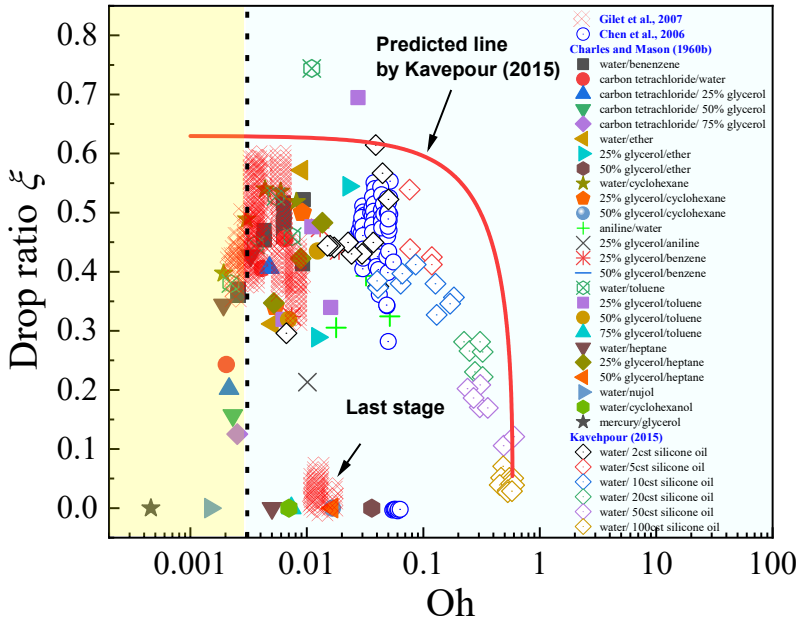

Figure 2.13 Drop ratio ξ (for all the stage of the cascade) against Oh. The solid red line represents the predicted value of ξ by Kavehpour (2015).

To predict the drop ratio, Charles and Mason (1960b) consider that the Rayleigh-Plateau instability causes partial coalescence and pinches off the liquid cylinder. They assumed that the volume of the daughter droplet is the same as the volume of the liquid cylinder formed in the previous step. The ratio was found to be equal to $\xi = (2Z_0^2/3)^{1/3}$, where Z_0 is a non-dimensional parameter which represents the ratio of the wavelength of disturbance to the diameter of the liquid column. The estimation is not very accurate as Blanchette and Bigioni (2006a) argue that the pinch-off is not only due to the Rayleigh-Plateau instability. Recently, Kavehpour (2015) suggested that $\xi = (1-3(Oh+(Oh^2+4)^{1/2})/8)^{1/3}$ by fitting a large number of experimental data with good

accuracy in both inertia-capillary regime and the viscous regime, as the red solid line shows in Figure 2.13.

Only a few studies have been reported on partial coalescence with surfactants. Martin and Blanchette (2015) found numerically that pinch-off and partial coalescence are inhibited in the presence of surfactants. The few studies available only report qualitative results on the effect of surfactants on partial coalescence. There is no quantitative information on the changes of the partial coalescence boundary or the ratio of drop sizes when surfactants are added in two-phase systems. In addition, the effects of surfactants on the drop velocity fields during partial coalescence have not been investigated.

2.5 Delayed coalescence at a moving fluid interface

The non-coalescence of drops floating on a liquid surface has attracted attention for a long time. In as early as 1881, Reynolds discussed the phenomenon and indicated that the impurity of the surface might lead to coalescence (Reynolds, 1881). Obviously, this conclusion is not entirely correct, later researchers found an increase in the floating time when detergents or surfactants are added (Dong et al., 2019, Dong et al., 2017). Instead, non-coalescence of drops can be achieved through many physical approaches like vibrations of the surface, creating thermal induced Marangoni convection, and creating velocity difference between the two interfaces.

2.5.1 Vibration induced non-coalescence

The non-coalescence of drops at a fluid surface under vibration has been investigated for a long time. Early in the last century, Raymond, as mentioned in the paper of Walker (1978), discovered that with mechanical vibrations the drops could survive at the liquid surface for as long as 18 mins. In a similar experiment, Walker (1978) tested the delayed coalescence of drops on an oscillating plate at 10~150 Hz, and found that oscillations in the middle of the amplitude range resulted in the longest drop rest time, while a smaller or larger amplitude reduced the drop life. When a drop approaches the interface of its homophase with air, a thin film of air is trapped and

coalescence occurs when the thin film drains out. Accordingly, Walker (1978) attributed the delay of coalescence to the refill of the air film as a result of the vibrations. The refill mainly happens with small drops (Couder et al., 2005). For large drop, the vibrations becomes less obvious than that of the small drop under the same driven force from the interface. As the large drop rests deeper in the interface than the small drop, the drainage of the air film becomes slow. Thus for large drops the delay of the coalescence is mainly due to the slow draining of the film fluid rather than the refill of the film. Vibrating interfaces have recently been used to delay coalescence of drops (Couder et al., 2005, Damiano et al., 2016, Sáenz et al., 2018, Pucci et al., 2018). Moláček and Bush (2013) combined the properties of the fluids and the vibration parameters of the interface based on $\omega_0/(\sigma\rho R^3)^{1/2}$ and γ/g as the coordinates in a map of drop behaviour which included coalescence, bounce, walk and chaotic behaviour. Here, ω_0 and γ refer to the frequency and the amplitude of the vibration, σ is the surface tension, ρ is the density of the liquid, R is the radius of the drop. Sáenz et al. (2018) recently discovered a statistically well-defined pattern of the speed of the floating drops on vibrating surfaces. More specifically, they found that, under their experimental conditions, the velocity distribution of the floating drops on the liquid surface resembled a series of concentric annuli.

2.5.2 Thermocapillary induced non-coalescence

Apart from the vibration induced non-coalescence, a temperature difference between the drop surface and the interface can delay coalescence as well. For example, a temperature difference of $\Delta T = 30$ °C between two drops of a 5 cSt silicone oil is able to delay coalescence for 1 hour until ΔT diminishes below a critical $\Delta T_c = 3.0 \pm 1.0$ °C (Dell'Aversana et al., 1996). Geri et al. (2017) further stated that the drop residence time increased monotonically with the initial temperature difference ΔT_0. The thermal induced Marangoni convection was considered to be responsible in this case (Napolitano et al., 1986). When two liquid bodies with different temperature meet with each other, the fluids move from the region of high to the region of low temperature creating a Marangoni surface flow that resists the drainage of the trapped film. Geri et

al. (2017) derived a Marangoni number $Ma = |\sigma_T \Delta T_0| R/\mu_0 \alpha_0$ to characterize the relative importance of the thermal capillary flow and the thermal diffusion. Here, α is the thermal diffusivity. The magnitude of the Marangoni flow could be estimated by the velocity $v_m = \sigma_T \Delta T/\mu$ (Dell'Aversana et al., 1996, Savino et al., 2003), where σ_T is the interfacial tension corresponding to temperature T. According to the lubrication theory introduced in Section 2.2.3, the velocity profile in the film is affected by the Marangoni flow that refills the film with air. As a result, the magnitude of the increased lubrication pressure in the film is predicted as:

$$\Delta P = \frac{\mu_a}{\mu_p} \frac{\sigma_T R}{h^2} \Delta T \tag{2.10}$$

where μ_a and μ_p refer to the viscosity of the air and the pool liquid and h is the thickness of the film (Savino et al., 2003). By equating the pressure over the drop to the weight of the drop, Davanlou (2016) correlated the film thickness at equilibrium to the temperature gradient for the drop to float upon a liquid pool, as shown in Equation (2.11):

$$h = \sqrt{\frac{3\sigma_T \mu_a}{16 \rho_a g \mu_p} \Delta T} \tag{2.11}$$

According to the equation, an increase in the temperature difference leads to a thicker air film and to delay coalescence.

2.5.3 Drop levitation on a moving surface

As the lubrication pressure in the trapped film between a drop and an interface resists its draining, Dell'Aversana et al. (1996) suggested that the main reason for the delay in coalescence is the tangential velocities along the drop surface and the interface that increase the lubrication pressure and prevent the contact of the drop with its bulk homophase. To test the assumption, they deposited a drop on a moving liquid surface. They found that a drop can float on a moving surface in the absence of temperature gradient. The phenomenon was confirmed by subsequent works (Sreenivas et al., 1999, Lhuissier et al., 2013, Gauthier et al., 2016). Sreenivas et al. (1999) investigated the non-coalescence phenomena of drops at the hydraulic jump of a flowing film (Figure

2.14(a)). The velocity of the drop surface caused by the shear stress from the air film was predicted to be $u_d = u_f/(1+K)$, where $K=h\mu_d/H\mu_a$. In the expression, u_d, and u_f refer to the velocity of the drop surface and the film surface, h and H are the thickness of the trapped air film and the height of the drop, respectively; μ_d and μ_a are the viscosity of the drop liquid and the air. Researchers subsequently reported that in this case the drops do not always stay at the hydraulic jump steadily but exhibit an oscillation (Pirat et al., 2010), which is not conducive to investigating the dynamics of the trapped film beneath. As shown in Figure 2.14(b), relatively steady drop floating was achieved by releasing drops on the inner surface of a rotating cylinder coated with a thin layer of the same liquid as in the drop (Davis et al., 1980, Sawaguchi et al., 2019, Lhuissier et al., 2013). Whether the drops levitate on the surface or not depends a lot on the drop release and impact conditions. Splashing, smooth coalescence, the lamella jetting can be observed as well. A phase map was plotted by Castrejón-Pita et al. (2016) to indicate the different patterns using $WeRe^{1/2}$ and $v_t/(v_nRe^{1/2})$ as coordinates, where v_t and v_n are the velocity of the surface and the impact velocity of the drop. Drop levitation was observed on the liquid surface at large values of $v_t/(v_nRe^{1/2})$, which requires a high viscosity of the liquid, a low impact velocity and a large rotation speed. Through direct observation, Davis et al. (1980) found the shape of the floating drop is affected by the rotation speed; a higher speed produces a flatter bottom of the drop. Recently, the levitation of a single drop on a rotating disk was realized by Gauthier et al. (2016) who were able to track the horizontal motion of drops on the plate and the drag forces acting on them, see Figure 2.14(c).

The rest time of drops on a moving liquid surface depends on two parameters, the thickness and the pressure in the film which separates the drop from the interface. Lhuissier et al. (2013) used interferometry and found that when drops were levitated at the inner surface of a cylinder the distribution of the film thickness was uneven. Using lubrication theory, the air film thickness was estimated, and was found to be partially in agreement with the measurements. For large drops, the film thickness $h \sim Ca^{2/3}\kappa_b^{-1}$, while for small drops $h \sim Ca^{4/5}(a\kappa_b)^{4/5}\kappa_b^{-1}$, where the capillary number Ca is based on the velocity of the air film, κ_b is the surface curvature at the bottom of the drop and a =

$(\sigma/\rho g)^{1/2}$ is the capillary length. According to the prediction, the film thickness increases exponentially with the speed of the air film for small drops. Sawaguchi et al. (2019) measured the film thickness for the same cases. They further described that the thickness of the air film was evenly distributed at the bottom of the low-viscous drops, while a large change of the film shape was observed for highly-viscous drops. Gauthier et al. (2016) measured the film thickness for the floating drop on a rotating disk. The thickness of the air film was found to be $h \sim 0.3D\mathrm{Ca}^{2/3}$, where D is the diameter of the drop.

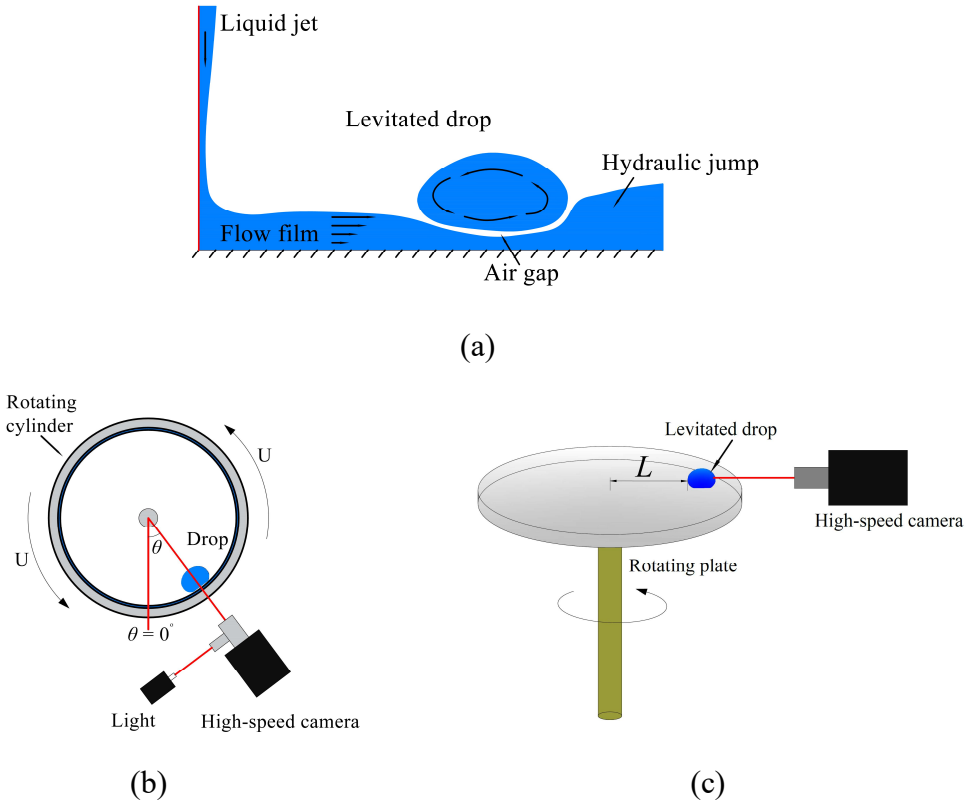

Figure 2.14 The levitation of drops at different conditions; (a) drop resting at the hydraulic jump of a liquid film (Sreenivas et al., 1999); (b) drop floats at the inner surface of the rotating cylinder covered with a thin liquid film (Sawaguchi et al., 2019, Lhuissier et al., 2013, Castrejón-Pita et al., 2016); (c) drop levitated on a flat surface of the rotating plate covered with a thin liquid film (Gauthier et al., 2016).

There are few papers reporting the pressure in the trapped film or the resulted lift force that leads to drop levitation. Sreenivas et al. (1999) who studied the levitation of drops at the hydraulic jump, as shown in Figure 2.14(a), suggested that the force needed to balance the weight of the drop was:

$$W = f_L \mu_a U L_y \frac{L_x^2}{h^2} \tag{2.12}$$

where, L_x and L_y refer to the length and width of the deformed drop, f_L is related to the shape L_x/L_y and inclination of the drop. However, Sreenivas et al. (1999) only discussed qualitatively the formula and did not conduct any calculations. According to the lubrication theory, Sawaguchi et al. (2019) found that the 2D pressure distribution in the trapped film for a steadily floating drop shown in Figure 2.14(b) was:

$$\frac{\partial}{\partial x}\left(\frac{h^3}{\mu}\frac{\partial p}{\partial x}\right) + \frac{\partial y}{\partial x}\left(\frac{h^3}{\mu}\frac{\partial p}{\partial y}\right) = 6U\frac{\partial h}{\partial x} \tag{2.13}$$

The local pressure in the film was calculated by substituting the variation of the thickness h in Equation (2.13). As the drop shape is controlled by the balance between the inner pressure of the drop and the outer pressure plus the Laplace force, Sawaguchi et al. (2019) also calculated the film pressure based on the drop surface curvature. The results obtained from the two methods were comparable.

It is not difficult to see from the above that the previous investigations only focus on the phenomena of drops at a liquid surface. In many industrial applications where the drop is levitated over a liquid-liquid interface, including oil petroleum transportation and oil-water separation (Rommel et al., 1993), the drops are surrounded by another liquid and the fluid interface is significantly deformed when the drop approaches it because of gravity. In most of the previous investigations, drops were generated in air and approached the interfaces of liquid films with air (Lhuissier et al., 2013, Gauthier et al., 2016, Castrejón-Pita et al., 2016, Sawaguchi et al., 2019). In such cases, drop levitation can only be realized with high speed of the interfaces and with high viscosity liquids. In addition, as the liquid films were thin and close to the bottom wall, the interfaces were not significantly deformed as the drops approached them. For the other investigations such as drops levitated at the hydraulic jump of a film flow (Sreenivas et al., 1999), wakes were observed at the vicinity of the drops while the drops were oscillating during the levitation (Pirat et al., 2010). Recently, Hale and Akers (2016) investigated drop deceleration on a stationary liquid surface. However, in this case surfactants were used, and the delayed coalescence could be due either to the presence of the surfactants or to the tangential velocity in the interface. In this thesis, a

new case of delayed coalescence of drops with a liquid/liquid interface will be reported in Chapter 7.

2.6 Conclusions

In this Chapter, the previous studies on the entire coalescence process from the drop resting on the interface, to the film breakage, the neck expansion and the final liquid merging are presented. The models predicting the drop rest time and the neck expansion, the maps showing the partial coalescence region, and the mechanisms of various types of drop levitation are summarized. The literature survey reveals that there are still many unresolved research questions, especially for coalescence in the presence of surfactants. In this work, the effect of surfactants on both total and partial coalescence, the distribution of surfactants along the coalescing drop surface and the delayed coalescence of drops with moving liquid-liquid interfaces will be investigated. To this end, in the next Chapter, the experimental set ups developed to study coalescence, the applied materials, the advanced techniques employed for the measurements and the experimental methodologies will be presented.

Chapter 3

Experimental methodologies and techniques

This Chapter describes the experimental set-ups as well as the techniques applied to study coalescence. Three groups of experiments are conducted: (1) studies of both total and partial coalescence with PIV approaches; (2) observation of the surfactant distribution on the coalescing interfaces with PLIF; (3) the investigation on the delayed coalescence at a moving interface. The experimental apparatuses and the methods corresponding to each group of experiments are described in detail below [1].

3.1 Experiments on total & partial coalescence

3.1.1 Experimental set-up and techniques

The dynamics of total and partial coalescence of drops with an initially flat liquid/liquid interface were investigated first. As shown in Figure 3.1(a), the coalescence tests were carried out in a transparent acrylic vessel of 5 cm square section width and 15 cm height. The bottom of the vessel was filled with the aqueous phase, and the organic phase was added on top, forming a liquid/liquid interface. To prevent the variation of the drop impact location, the aqueous droplets were generated through stainless steel nozzles located at 1 cm above the interface. For the observation of the total coalescence, only the nozzle with 2 mm internal diameter was used. For the partial

[1] Part of the contents presented in this chapter are included in:
WEHELIYE, W. H., DONG, T. & ANGELI, P. 2017. On the effect of surfactants on drop coalescence at liquid/liquid interfaces. *Chemical Engineering Science,* 161**,** 215-227.
DONG, T., WEHELIYE, W. H., CHAUSSET, P. & ANGELI, P. 2017. An experimental study on the drop/interface partial coalescence with surfactants. *Physics of Fluids,* 29**,** 102101.

coalescence studies, different sizes of the droplets were generated for the determining of the partial coalescence criterion. This was realized by using nozzles with different internal diameters equal to 0.5 mm, 1 mm, and 2 mm. The nozzles were connected to a syringe mounted on an Aladdin® syringe pump that was operated at a constant flow rate of 0.2 ml/min.

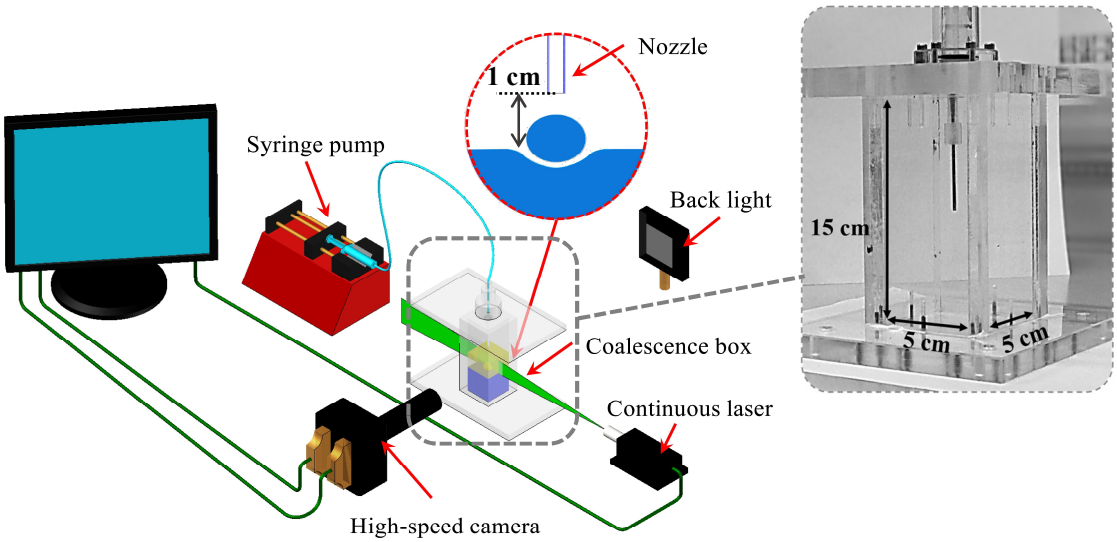

(a)

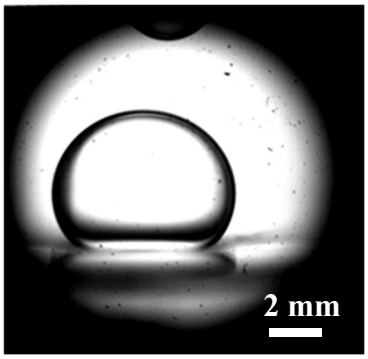

(b)

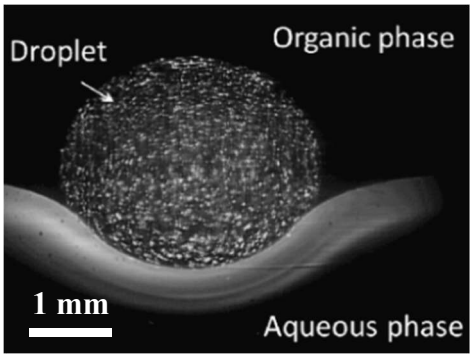

(c)

Figure 3.1 (a) Experimental set up for the study of coalescence; (b) raw image obtained from the shadowgraphy observation; (c) raw image obtained with the PIV technique.

Two techniques, high-speed shadowgraph and Particle Image Velocimetry (PIV), were used to study the evolution of the drop surface and the flow fields inside the coalescing drops. In shadowgraphy, the observation area was lit by a backlight, which was located at around 15 cm behind the vessel, as shown in Figure 3.1(a). The images of drop coalescence were captured by a high-speed camera set with roughly 15 cm in

front of the vessel, which was equipped with a mono-zoom Nikon lens giving a field of view of 9 × 9 mm^2. The camera was inclined at 5° downwards to view the drop bottom. An example of a raw image is presented in Figure 3.1(b).

The velocity fields inside the drops were studied with a 2-dimensional PIV (2D-PIV) technique. As shown in Figure 3.1(a), the PIV set-up was similar to that of the shadowgraphy. The difference was that the backlight was removed and the observation area was illuminated by a Laserglow® continuous diode laser (300 mW) with a wavelength of 532 nm and 4 mm beam size. A cylindrical lens was mounted in front of the laser creating a laser sheet of approximately 1 mm thickness. The relative position between the laser and the coalescence box was adjusted to ensure the laser sheet illuminates the middle plane of the drop. For the observation of the velocity fields in the plane, the drops were seeded with 1 μm Rhodamine coated tracer particles. After each coalescence test, the particles were removed from the interface with a suction pump. In addition, to improve the interface imaging, the bulk aqueous phase near the interface was dyed with a small amount of the Rhodamine 6G. The motion of the tracer particles during the coalescence process was captured by the high-speed camera. A relatively lower frame rate of 1000 fps was used for the total coalescence, which evolves at a lower speed than the partial coalescence. For the partial coalescence cases, the frame rate was increased to 5400 fps to acquire adequate information in the flow fields. A PIV raw image of a resting drop at the fluid interface is shown in Figure 3.1(c).

The images obtained from the camera were treated by the open source freeware JPIV® where an adaptive correlation tracking of the full image was applied with a final interrogation window of 32 × 32 pixels. A 50% window overlap was used for a final resolution of 16 × 16 pixels, corresponding to an area of 0.14 × 0.14 mm^2.

The experimental devices for both shadowgraph and PIV technique were fixed on an optical table to avoid any vibrations from the background environment.

3.1.2 Materials

3.1.2.1 Total Coalescence

The total coalescence was investigated with 2D-PIV technique at first. Exxsol D80

oil was selected as the organic phase. To remove optical distortion and improve the quality of the PIV images close to the interface, the refractive indices of the organic and the aqueous phases were matched. The refractive index of Exxsol D80 oil is high at 20 °C with $n_{Exxsol80} = 1.443$, while the refractive index of water is only $n_{water} = 1.333$. By adding glycerol into the water, the refractive index can be increased. After checking the properties of the glycerol (Association, 1963), the refractive index of the glycerol solution at a volume concentration of 78% was found equal to the value of the Exxsol D80 oil. Refractive indices were measured with an Abbe 5® refractometer.

An non-ionic surfactant Span 80 (density ρ = 990 kg/m^3, molecular weight M = 428.6 g/mol) was applied to investigate the effects of surfactants on total coalescence. The HLB index of Span 80 is 4.3 making it soluble in the oil phase. A detailed description of the properties of Span 80 under similar conditions can be found elsewhere (Benmekhbi et al., 2014) and are only briefly summarized here. Five different concentrations of surfactants were tested, with mass ratios of surfactant to organic phase at $\phi = 0$, $\phi = 2\times10^{-5}$, $\phi = 1\times10^{-4}$, $\phi = 2\times10^{-4}$, $\phi = 5\times10^{-4}$. It is quite difficult to directly prepare the liquids at low surfactant concentrations as big measuring errors might be introduced if the small amount of the highly viscous Span80 is directly taken and dissolved in the liquids. Thus the liquids at a concentration of $\phi = 5\times10^{-4}$ were prepared at first. Then the liquids in lower concentrations were prepared by diluting the initial dense liquid. Ultrasound at 45 kHz was used to ensure homogenous mixing of the surfactant in the aqueous phase. The refractive index of the Exxsol D80 oil with different concentrations of Span80 was measured. No difference was found compared to that of the pure Exxsol D80 oil. More properties of the fluids are shown in Table 3.1.

Liquids	Surfactant concentration ϕ (wt/wt)	Density ρ (kg/m^3)	Dynamic viscosity μ (mPa.s)	Interface tension σ (μN/m)
80% Glycerol	-	1210	54	-
Exxsol/Span80	0	804	1.57	26.73 ± 0.14
	2×10^{-5}			23.43 ± 0.25
	1×10^{-4}			13 ± 0.07
	2×10^{-4}			7.8 ± 0.15
	5×10^{-4}			2.16 ± 0.21

Table 3.1 Fluid properties for the investigation on the total coalescence.

The equilibrium interfacial tensions of different liquid pairs were measured with the Du Noüy ring method using Krüss K100®. At least three measurements were conducted for each concentration and the averaged value (standard deviation less than 5%) is shown in Figure 3.2. It is found that the interfacial tension decreases with increasing concentration but changes less when ϕ is close to the CMC value, which was around $\phi = 8\times10^{-4}$. It should be noted that the adsorption of Span 80 at the interface was fast for the liquids used, thus the interfacial tension measurements were taken shortly after the liquid pairs were prepared. The results shown in Figure 3.2 were in good agreement with the data of Voulgaropoulos (2018) who let the liquids rest for 12 hours before the measurement.

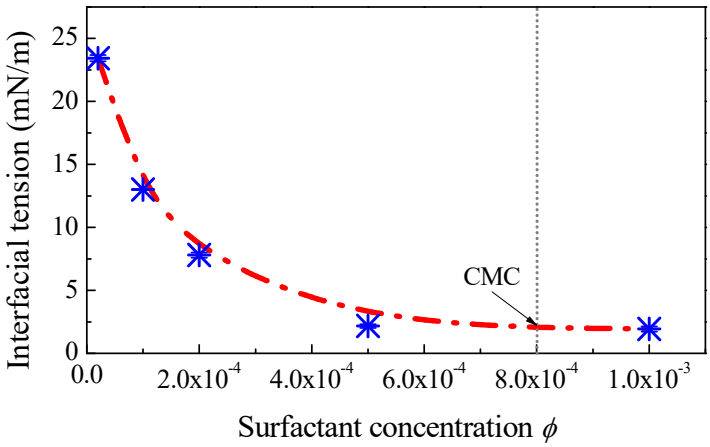

Figure 3.2 Interfacial tension of the interface between the 80% glycerol solution and the Exxsol D80 oil at different Span 80 concentrations.

3.1.2.2 Partial Coalescence

Both the shadowgraphy and the PIV techniques were applied for the study of partial coalescence. The boundary between the partial and total coalescence regions as well as the effect of surfactants on the drop ratio during the coalescence cascade were studied first with shadowgraphy. To this end, fluids with a wide range of properties were chosen.

The shadowgraphy experiments were carried out both without and with surfactants. The organic phase was a 5 cSt silicone oil and the aqueous phase was a glycerol-water solution with different volume concentrations, ζ. By varying the concentration of the glycerol, the viscosity of the aqueous phase is changed. The interfacial tension also decreases with the increase of the fraction of the glycerol. The variation of the viscosity

and the interfacial tension produces a wide range in the phase map. For the experiments with surfactants, oil-soluble Span 80 was added in the oil phase at $\phi = 0$, $\phi = 2\times10^{-5}$, $\phi = 5\times10^{-5}$, $\phi = 1\times10^{-4}$, and $\phi = 2\times10^{-4}$. It was found previously that a high surfactant concentration tends to produce total coalescence. Therefore, the liquids at high surfactant concentration close to the CMC value were not tested, as the main purpose of these experiments was to find the boundary between partial and total coalescence.

Liquid			ρ_a (kg/m^3)	ρ_o (kg/m^3)	μ_a (mPa·s)	μ_o (mPa·s)	σ (mN/m)
	Aqueous	organic					
Shadow -graph tests	100%W	5cst Silicone Oil	1000	914	1.00	4.57	39.7
	75%W+25%G		1059		1.97		32.3
	65%W+35%G		1085		2.85		30.7
	57.5%W+42.5%G		1105		3.99		30.0
	100%W	5SO+2×10^{-5} S80	1000	914	1.00	4.57	33.8
		5SO+5×10^{-5} S80					26.7
		5SO+1×10^{-4} S80					21.4
		5SO+2×10^{-4} S80					15.5
	75%W+25%G	5SO+2×10^{-5} S80	1059	914	1.97	4.57	27.8
		5SO+5×10^{-5} S80					24.2
		5SO+1×10^{-4} S80					19.2
PIV Tests	67%W+33%G	0.65cst Silicone Oil	1080	761	2.599	0.49	20.20
		0.65SO+1.3×10^{-6} S80					11.88
		0.65SO+1.3×10^{-4} S80					1.97

Table 3.2 Fluid properties for the partial coalescence. The W and G represent the water and the glycerol, respectively; the SO refers to silicone oil and S80 refers to Span 80.

A better understanding of the partial coalescence mechanism can be obtained with the velocity data from the PIV. However, the PIV technique limits the properties of the fluids that can be used, as the refractive indices of the liquids need to be matched. If the 5 cSt silicone oil ($n_{5cst} = 1.396$) is applied in the PIV tests, the corresponding concentration of the glycerol solution has to be $\zeta = 46$ % to match the refractive index. The shadowgraphy observations indicated that partial coalescence hardly occurred in such a high viscosity system. Thus, the organic phase was replaced by a less viscous 0.65 cSt silicone oil ($n_{0.65cst} = 1.372$ at 20 °C). It was found that glycerol solution at a concentration of $\zeta = 33$ % matched the refractive index of the 0.65 cst silicone oil within 0.01%. Thus, the 0.65 cSt silicone oil and the 33% glycerol solution were selected as test liquids for the PIV measurements. To test the effect of surfactants on the flow fields during coalescence, two surfactant concentrations, $\phi = 1.3\times10^{-6}$ and $\phi = 1.3\times10^{-4}$, were

used. The properties of the fluids are shown in Table 3.2.

3.1.3 Drop shape tracking algorithm

In the experiments, a proper detection of the drop surface and the interface is necessary for accurately describing the evolution of the drop shape in both total and partial coalescence. An image analysis algorithm comprising of three steps was developed to identify the profile of the drop shape at a given time instant. In the first step, the bottom part of the PIV image, at the bulk of the aqueous phase, was made uniform, by removing any reflections of the laser light at the interface. In this case, every pixel with a light intensity $I > 0.5$ (where an intensity value $I = 1$ indicates white) was converted to an intensity value of 0 (i.e. black). In the second step, the coordinates of the points positioned on the edge of the droplet were determined by exploiting the differences in illumination of points inside and outside the droplet. A close up of the white rectangular region of Figure 3.3(a) is shown in Figure 3.3(b) where three points above, on and below the droplet are denoted as A, B, and C, respectively. It is evident that points A and C are located in regions with a more uniform illumination texture, while the presence of seeding particles makes the image inhomogeneous within the droplet (i.e. point B).

The homogeneity of the local illumination texture in a window of 3 × 3 pixels surrounding each pixel of the image and the corresponding deviation, s_I, of the light intensity in the interrogation window was calculated using Equation (3.1):

$$s_I = \sqrt{\frac{1}{N_w}\sum_{1}^{N_w}(I_k - I_m)^2} \tag{3.1}$$

where N_w is the number of points in the interrogation window of 3×3 pixels, I_m is the mean value of the light intensity in the window and I_k is the light intensity of the k^{th} point of the window. The variation of the standard deviation along the vertical direction, y, at a location x is shown in Figure 3.3(c) as a representative. The original point is located on the upper left side.

From Figure 3.3 (c) it is observed that the value of the standard deviation, s_I, is zero at small values of y in the area outside the drop where the local illumination texture is

uniform as shown in Figure 3.3(b) and point A. When the interrogation window is crossing the upper edge of the droplet, there is a sharp increase of s_I. For $y > 150$ and $y < 460$, the interrogation window is completely inside the seeded droplet region and the standard deviation varies around a value of 20, because of the light inhomogeneity due to the presence of the seeding particles. A decrease of the value of s_I occurs when the

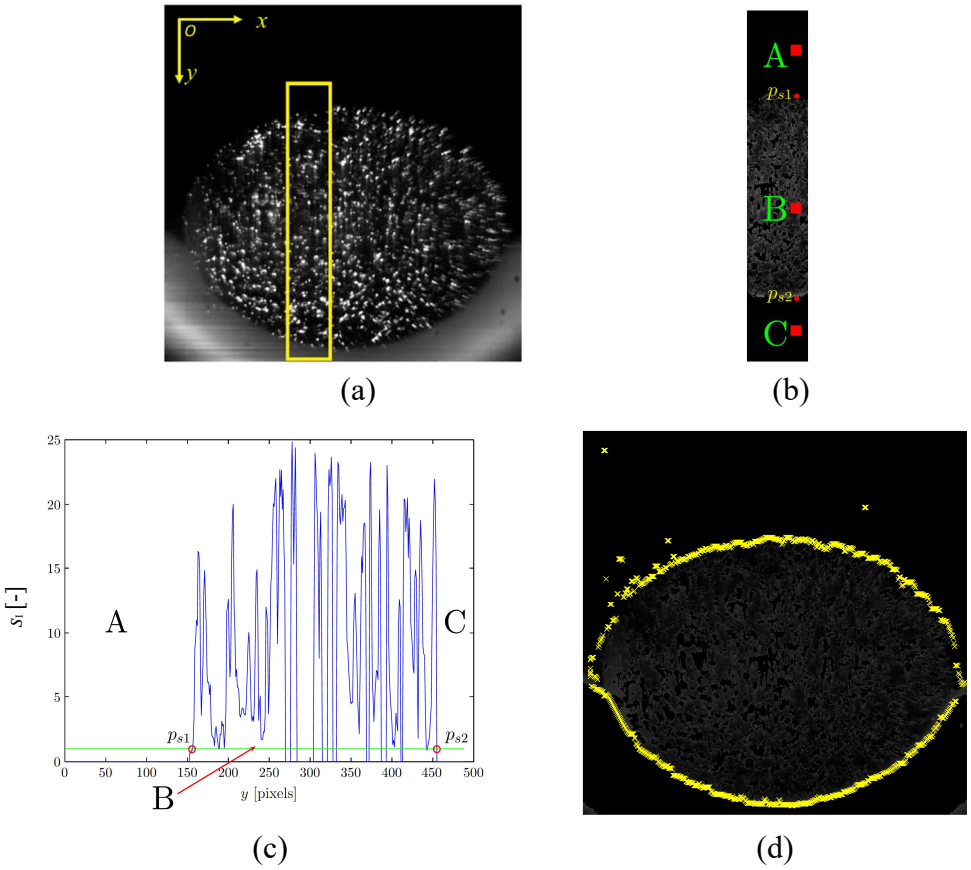

Figure 3.3 Description of the steps of the detection algorithm of the droplet profile: (a) identification of laser reflections at the organic-aqueous interface; (b) region enclosed in the white rectangle to show three different positions in the estimation of s_I; (c) variation of s_I along a vertical direction; (d) raw profile of the droplet surface detected after the standard deviation analysis.

interrogation window crosses the bottom edge of the droplet at $y > 460$ (lower part of the image, point C). The presence of the first and last peak of s_I together with the pronounced noisy texture in between, allows the identification of the edges of the upper (p_{s1}) and the lower surface (p_{s2}) of the droplet, respectively. The same procedure was repeated for all horizontal coordinates x until the entire droplet profile at a given time instant was determined, as illustrated in Figure 3.3(d). A local regression was conducted in the following step to smoothen the detected droplet profile, as well as to identify and

discard those outliers whose distance from the droplet was greater than a fixed threshold. A mask was then applied to each raw image and the values of all pixels outside the droplet profile were converted into 0 (black).

3.2 Fluorescence visualization on surfactant distribution [2]

To further understand the effect of surfactants on the coalescence behaviour, the spatiotemporal distribution of surfactants on the merging interfaces during the coalescence of drops with a flat liquid/liquid interface was studied with Planar Laser Induced Fluorescence (PLIF) technique. In this section, the properties of the applied fluids, the experimental methodology, and the data processing involved in the experiments will be described.

3.2.1 Materials

For all the PLIF tests the organic phase was a 5 cSt silicone oil (density ρ_s = 914 kg/m^3, viscosity μ_s = 4.57 mPa.s), and the aqueous phase was a water-glycerol mixture. The volume concentration of the glycerol in the aqueous phase was set at ζ = 46 % to match the refractive index of the oil (n_{5cst} = 1.3925 at 20 °C) and avoid any light distortions at the interface when the laser illumination was used. The density and viscosity of the 46% glycerol solution were ρ_d = 1150 kg/m^3 and μ_d = 4.35 mPa.s, respectively.

For the experiments, a fluorescently tagged surfactant NBD-PC (1-palmitoyl-2-12-[(7-nitro-2-1,3-benzoxadiazol-4-yl) amino] lauroyl-sn-glycero-3-phosphocholine) with molecular weight equal to M = 856.038 g/mol was dissolved in the aqueous phase. The surfactant absorbs at 464 nm and emits at 531 nm. Ultrasound was used to help the surfactant distribute uniformly in the aqueous phase. The dynamic interfacial tensions of the 5 cSt silicone oil with the aqueous solutions that had different concentrations of NBD-PC were measured until the final equilibrium level with the Du Noüy ring method

[2] Most of the results presented in this section are included in:
DONG, T., WEHELIYE, W. H. & ANGELI, P. 2019. Laser induced fluorescence studies on the distribution of surfactants during drop/interface coalescence. Ibid.31**,** 012106.

(Krüss K100® tensiometer). The interfacial tensions under the same surfactant concentration were reproducible with a relative standard deviation of less than 5%. The equilibrium interfacial tension is presented in Figure 3.4 for different surfactant concentrations in the aqueous phase. As can be seen, NBD-PC is able to lower the interfacial tension by around 0.020 N/m from φ = 0 mol/m^3 to the CMC, which is reached at a surfactant concentration $\varphi \approx 0.013$ mol/m^3. For the coalescence experiments, the concentration of the surfactant in the aqueous solution was set at φ = 0.001 mol/m^3. This concentration was selected because it lowers sufficiently the interfacial tension, has adequate fluorescence for the PLIF experiments, while it prevents the formation of surfactant micelles in the aqueous phase that can interfere with the PLIF experiments.

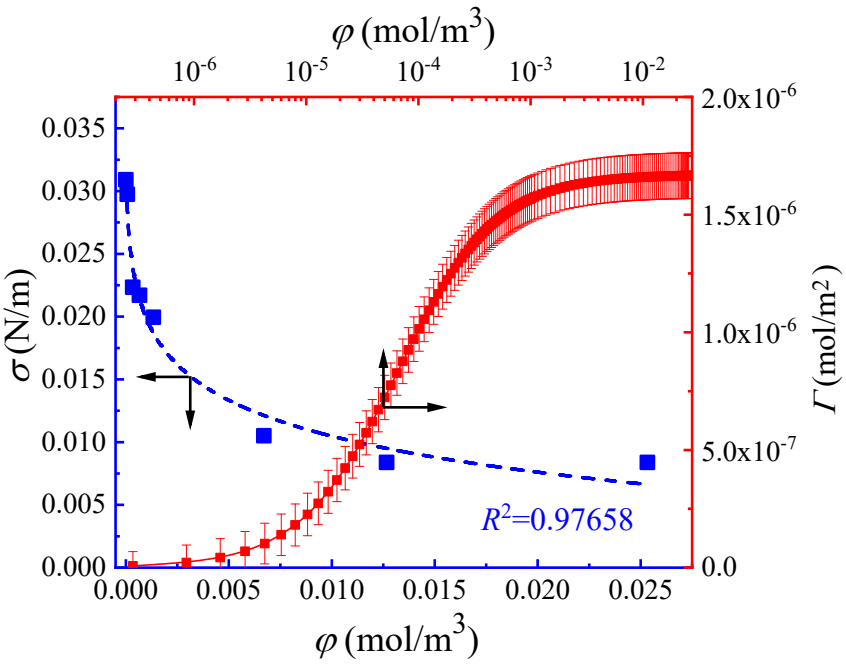

Figure 3.4 Interfacial tension of the 5 cSt silicone oil and the 46% glycerol solution, σ, for different concentrations of NBD-PC φ. The squares indicate the interfacial tension under various surfactant concentrations. The data were plotted against the bottom linear scale of φ. The dashed line is fitted to the experimental data with R^2= 0.97658. The continuous line is the prediction of the surfactant excess Γ on the interface based on the Langmuir adsorption model (Equation (3.4)). The data were plotted against the top log scale of φ. The calculation of the error bars of the red line is presented in Appendix A.

3.2.2 Experimental set-up and techniques

As shown in Figure 3.5, the experimental set-up for the PLIF study is similar to the

PIV set-up described in Section 3.1.1. The coalescence events were carried out in the same acrylic box as described above. The drops were created through a flat-ended nozzle (inner diameter ID = 2 mm) that connects to the syringe pump. The flow rate of the syringe pump was set at 0.2 ml/min for better control of the drop sizes, which were 5.90 ± 0.14 mm in horizontal diameter for all the experimental conditions.

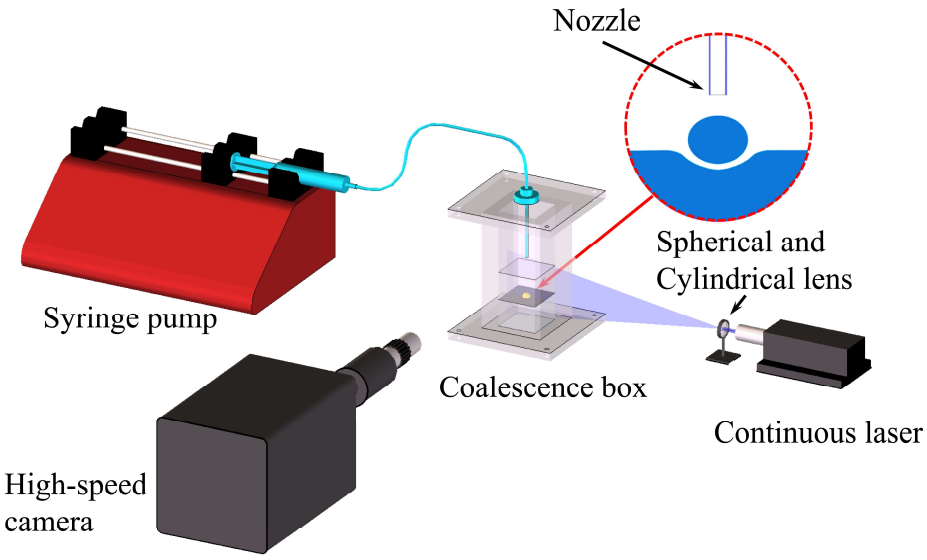

Figure 3.5 The PLIF experimental set-up.

In the PLIF studies, the middle plane of the drop was illuminated by a laser sheet. As the fluorescent surfactant absorbs at 464 nm and emits at 531 nm, the continuous laser applied to the PIV tests in Section 3.1 is no longer appropriate. A laser with a peak wavelength close to 464 nm is needed to effectively excite the fluorescent component of the surfactants. Thus, a Laserglow5® continuous laser (473 nm, 300 mW) connecting to a spherical and a cylindrical lens in series was employed to create a 1 mm laser sheet. The laser along with the optical lenses was mounted on a mobile stage at around 2 cm away from the acrylic box on the right-hand side. The laser sheet was adjusted to bisect the centre plane of the drop. In all experiments, the output power of the laser was kept constant to prevent any energy deviations. For better visualization and consistent comparisons, only the coalescence events where the film rupture points are on the laser plane were considered. A Phantom® high-speed camera, equipped with a mono-zoom Nikon lens, which gave a spatial resolution of 13 μm/pixel, was placed perpendicular to the laser sheet to capture the process of coalescence. The distance between the acrylic

box and the head of the lens was kept at 13 cm for all the tests. A green filter was connected to the lens to eliminate reflections. To capture the very fast film rupture and the liquid merging steps, the camera was operated at a high frame rate of 2000 fps.

The whole setup was mounted on an optical table, and the relative spatial locations among the high-speed camera, the continuous laser, and the coalescence vessel were fixed to avoid any mismatch between runs. During each experiment, the temperature was kept constant in the lab. As the drops were generated in the organic phase and the whole coalescence process occurred within the liquid system, the effect of the environmental humidity was considered negligible.

3.2.3 Experimental methods

As pointed out by Eastoe and Dalton (2000), the adsorption of the surfactant molecules from the bulk liquids to the interface can be slow depending on the properties of the fluids and the environmental conditions. For the surfactant used in this work, it takes hours for the interfacial tension to reach the final equilibrium value. To account for this, the coalescence experiments were carried out for different ages of the drop surface and the interface. Here, the drop surface (or the interface) age T refers to the time from when the drop contacts the surrounding organic phase (or the organic phase contacts the bulk aqueous phase) to the time when the coalescence experiment starts. Drop surface ages from $T = 0$ min to $T = 900$ min were studied. In the fresh system ($T = 0$ min), the interface was generated by adding the liquids in the vessel, while the drop was formed in the oil and immediately after it was deposited on the interface. For the experiments carried out at different ages, the drop was generated within the oil and was kept attached to the nozzle for the required age T, before it was released to approach the interface to start the coalescence process; the bulk oil and water phases were also kept in contact for the same time T. The initial sizes of the pending drops for all the tests were kept constant by the syringe pump. Since the drop surface age and the interface age are equal in the experiments, the surface age T will be used in the rest of the paper to represent both ages. Typical fluorescent images of drops resting on the interface for various drop surface ages are shown in Figure 3.6. As can be seen, for $T =$

0 min, the drop surface has similar brightness as the rest of the liquid inside the drop. The part at the bottom of the drop appears brighter because it is the location where both interfaces, the drop and the liquid-liquid one, meet. At longer ages, the brightness of the drop surface is higher than that inside the drop, which indicates that the surfactant is adsorbing to the drop surface.

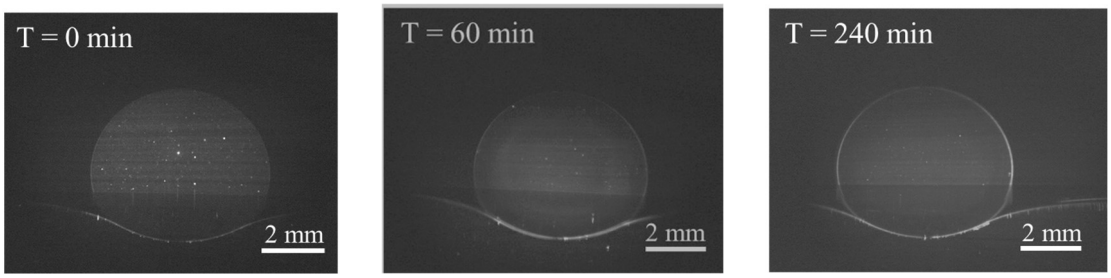

(a) (b) (c)

Figure 3.6 Raw fluorescent images of a drop resting on the interface for (a) $T = 0$ min, (b) $T = 60$ min, and (c) $T = 240$ min.

3.2.4 Fluorescent imaging and calibration

In the PLIF measurements, the concentration of the surfactants is estimated by detecting the fluorescence intensity in the recorded images. To generate the calibration curve, various concentrations of NBD-PC from 0 to 0.0078 mol/m^3 were dissolved in the bulk 46% glycerol solution and the corresponding intensity was measured. For each concentration, more than 200 images were captured to produce the average fluorescent intensity. To avoid the effect of the adsorption of surfactants on the surface on the calibration results, the bulk liquid at each concentration was mixed well and measurements were taken immediately after. To account for any changes in the fluorescence intensity because of the chemical stability of the surfactant, the calibration was repeated three times with a 24 hours difference between each test. Between experiments, the liquids were stored in a dark environment to prevent photo-dissociation.

The fluorescence intensity as a function of the surfactant concentration is shown in Figure 3.7. As can be seen, the fluorescence intensity increases exponentially with the surfactant concentration in the range of the measurements. By fitting the data, the following correlation was found that links the fluorescence intensity, I, to the

corresponding surfactant concentration:

$$\varphi = I^{2.27} \tag{3.2}$$

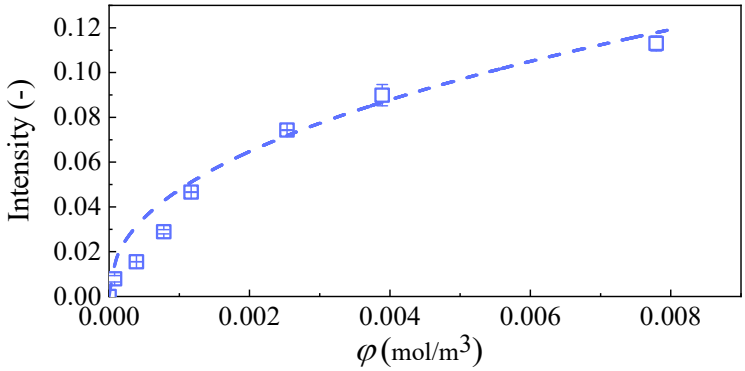

Figure 3.7 Calibration of surfactant fluorescence intensity as a function of the surfactant concentration. The squares represent the averaged fluorescence intensity at each concentration, and the dashed line shows the fitting trend. The error bars show the standard deviation of the light intensity among the three measurements.

From the volume concentration φ calculated in Equation (3.2), the surface concentration, Γ, was calculated, which is generally used to describe the surface excess of surfactants (Ghosh and Juvekar, 2002, Giribabu and Ghosh, 2007, Fallest et al., 2010, Strickland et al., 2015). For an interface with a given thickness, the surface excess can be obtained by integrating the volume concentration φ along the surface thickness h, which could be regarded as constant (Hodgson and Lee, 1969).

The theoretical surface excess of the NBD-PC on the interface between the 5 cSt silicone oil and the 46% glycerol solution was also calculated to validate the calibration results. According to the Szyszkowski-Langmuir Equation (3.3), the surfactant concentration at the interface can be estimated if the data of the interfacial tension is known (Ravera et al., 2000, Giribabu and Ghosh, 2007, Jin et al., 2017).

$$\sigma = \sigma_0 - RT\Gamma_\infty \ln(1 + K_L\varphi) \tag{3.3}$$

where σ_0 is the interfacial tension for the system without surfactant, R is the universal gas constant, T is the temperature, Γ_∞ is the surfactant concentration at the saturated interface, φ is the surfactant concentration in the bulk liquids, and K_L is the equilibrium constant, which indicates the ratio of the rates of surfactant adsorption and desorption. Since the equilibrium interfacial tensions under various surfactant concentrations in the

bulk are known, the values of Γ_∞ and K_L can be calculated by fitting the data. Then the surface excess related to each bulk concentration can be calculated through the Langmuir isotherm (Equation (3.4)).

$$\Gamma = \frac{\Gamma_\infty K_L \varphi}{1 + K_L \varphi} \tag{3.4}$$

According to the Langmuir isotherm, the surface excess of the surfactant on an interface can be calculated if the two parameters Γ_∞ and K_L are known. By fitting the measured interfacial tension points at various surfactant concentrations (dashed line shown in Figure 3.4), it was found that $\Gamma_\infty = 1.67\times10^{-6}$ mol/m^2 and $K_L = 15249$ m^3/mol. When these values are substituted into Equation (3.4), the surface excess corresponding to the bulk surfactant concentration can be calculated, as shown in Figure 3.4 by the continuous (red) line. For the current system, the surface excess at the flat liquid/liquid interface is in the order of $\Gamma = 0 \sim 1.67\times10^{-6}$ mol/m^2 depending on the age of the interface. The error analysis for the calculation of the surface excess is shown in Appendix A.

The surface concentration Γ obtained through the calibration curve, from Equation (3.2), using the average intensity at the interface was in reasonable agreement with the values estimated from the Langmuir adsorption model. However, deviations could not be avoided as the calibration was not directly based on the intensity from the interface. As reported by Fallest et al. (2010), a similar fluorescent surfactant, NBD-PC, was employed on a thin liquid layer, and the concentrations measured at the interface were found to be linear with the intensity of the emitted light. Therefore, for the rest of this study, a linear relationship is assumed between the surface concentration and the fluorescent intensities emitted at the interface. The surface concentration Γ was normalized with the maximum surfactant concentration at the drop surface at $T = 900$ min, i.e., $\Gamma^* = \Gamma/\Gamma_{max}^{900}$. The normalized surfactant concentration Γ^* along the drop surface was extracted for different surface ages T. As shown in Figure 3.8, with the drop surface aging, the surfactant concentration Γ^* was increased.

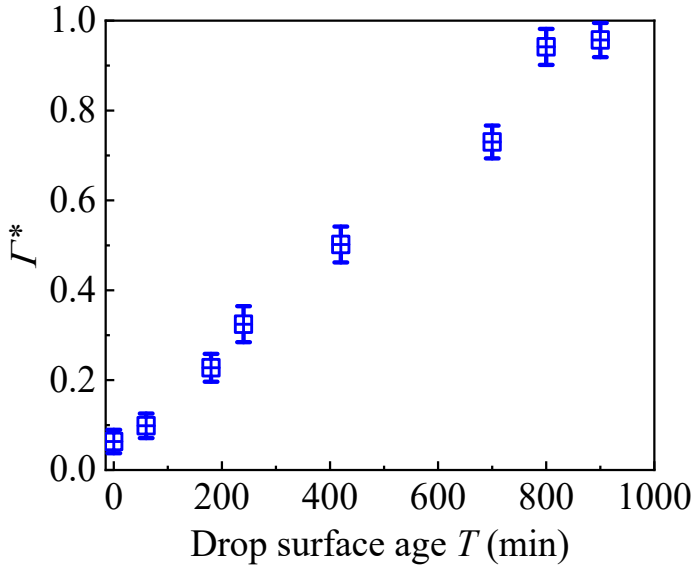

Figure 3.8 The average of the normalized surfactant concentration Γ^* along the drop surface for different surface ages T. Here, the normalization of concentration $\Gamma^* = \Gamma/\Gamma_{max}^{900}$. The error bars show the variation of Γ^* along the drop surface.

3.2.5 Image processing and limitations

In this section, the image processing methodology and the challenges encountered in the experiments will be outlined. First, it is necessary to properly detect the interface region for the subsequent calculations of the surfactant concentration. This is shown below for the interface at the bottom of the drop as a representative example. Initially the intensities along vertical lines in the image (e.g., $L1$, $L2$, and $L3$ in Figure 3.9(a)) are plotted, as shown in Figure 3.9(b). When the interface region is crossed, the intensity increases sharply. The location of the peak point was then defined as a y value. Intensities were recorded every 5 vertical columns, and the data were smoothened by cubic smoothing spline functions to produce a continuous interface curve.

The thickness of the interface was then calculated by measuring the bandwidth of the sharp increase in the intensity curve, as shown in Figure 3.9 (b), between the dashed lines. This interface thickness was thin (0.026 mm) for the drop surface at T = 0 min, while it reached around 0.1 mm for T = 900 min.

However, it should be noted that the thickness of the interface shown in the images can be much larger than the thickness of the real interface (Xu et al., 2013) because of the curvature of the drop surface and the light diffraction. The effect of the curvature of

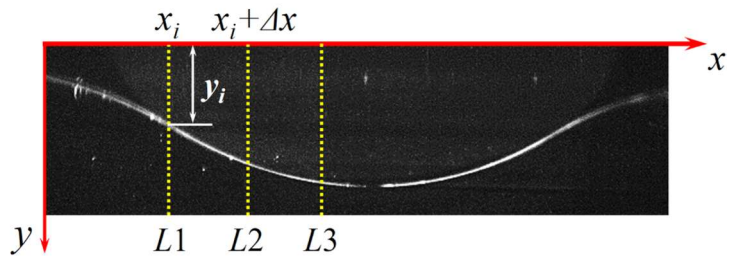

(a)

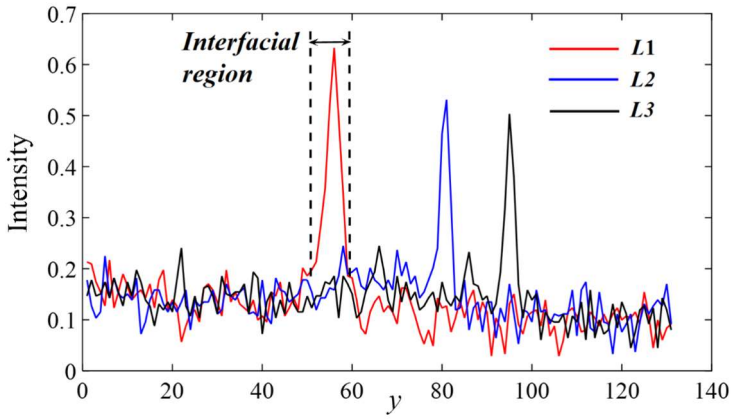

(b)

Figure 3.9 (a) Schematic of the interfacial region detection and (b) intensity curves along the lines *L*1, *L*2, and *L*3.

the drop surface can be eliminated by generating drops with a diameter much larger than the laser sheet thickness. In this work, the thickness of the laser sheet was 1 mm and the monozoom Nikon lens connected to the camera gave a depth of field (DOF) approximately equal to 0.5 mm. The effect of the curvature of the drop surface could become significant when the drop diameter was close to 1 mm. In the current study, the drops were about 6 mm in diameter and the curvature effect is negligible.

Light diffraction can also affect the calculation of the interface thickness. To estimate this, the averaged surfactant concentrations were calculated from two different approaches. The first approach was to calculate the average surfactant concentration Γ_1 considering the maximum value at the peak and the values at 2 neighboring points, while the second approach was to average the surfactant concentration Γ_2 among all the values in the interfacial region (within the dashed lines in Figure 3.9(b)). It was found that for the drop surface, the averaged surfactant concentration $\Gamma_1 = (1.1 \pm 0.04)\ \Gamma_2$ depending on the interface aging time. For the interface region that combines the drop

surface and the phase interface, $\Gamma_1 = (1.2 \pm 0.052)\ \Gamma_2$. It appears that the interfacial thickness does not significantly affect the results on surfactant concentration. The first approach was used below to calculate the surfactant concentration at the interface at different aging times.

3.3 Experimental set up for the study of delayed coalescence in moving interfaces

3.3.1 Experimental set-up and materials

The experimental set-up for the investigation of the delayed coalescence of drops with a liquid interface is shown in Figure 3.10. A rectangular flow channel with a 5 cm × 5 cm cross-section and 1 m length was built for the tests. The flow channel was connected to an inlet chamber and an outlet chamber through two openings at 5 mm above the bottom wall. Initially, an aqueous phase of 78% glycerol solution in water (density $\rho_d = 1210$ kg/m^3, viscosity $\mu = 54$ mPa·s) was introduced into the channel by a Cole-Parmer® magnetic drive centrifugal pump. The pump was stopped and the valves were closed to hold the liquid in the channel with a surface height approximately equal to 15 mm from the bottom of the tank. The organic phase (Exxsol D80 oil; density $\rho_o =$ 804 kg/m^3, viscosity $\mu = 1.75$ mPa·s) was then added in the channel through an oil inlet at 10 cm away from the outlet. The thickness of the oil film was set at around 20 mm. A flat stationary interface (interfacial tension $\sigma = 26.73$ mN/m) formed in the flow channel. Subsequently, the valves were opened and the pump was restarted to circulate the 78% glycerol solution in the channel. Because of the motion of the water phase, the interface was also set in motion. As shown in Figure 3.10(b), a baffle was placed opposite the aqueous phase inlet to dampen any disturbances on the flat interface. In addition, the bottom of the wall that separated the inlet chamber from the main channel had a smooth shape to reduce any waves at the interface. In the outlet chamber, a cross-shaped obstacle was placed in the drain hole to prevent any vortices forming, see Figure 3.10(c). In the experiments, the interface speed was varied by changing the flow rate of the aqueous phase through the centrifugal pump. A rotameter with a maximum flow

rate at 1 *L*/min with 5% accuracy was installed in the inlet tube to monitor the flow rate.

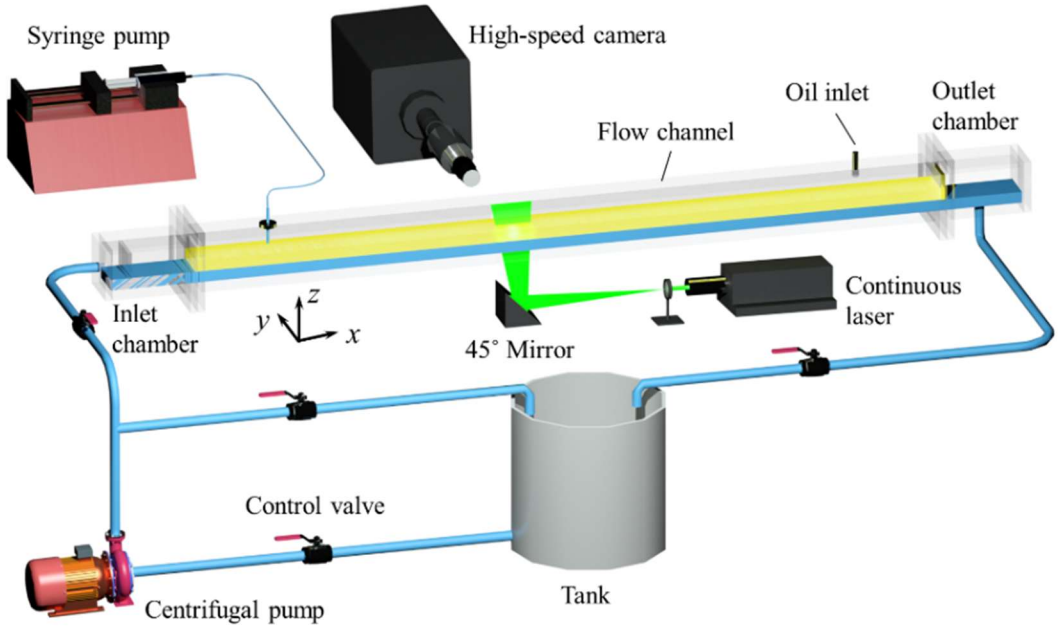

(a)

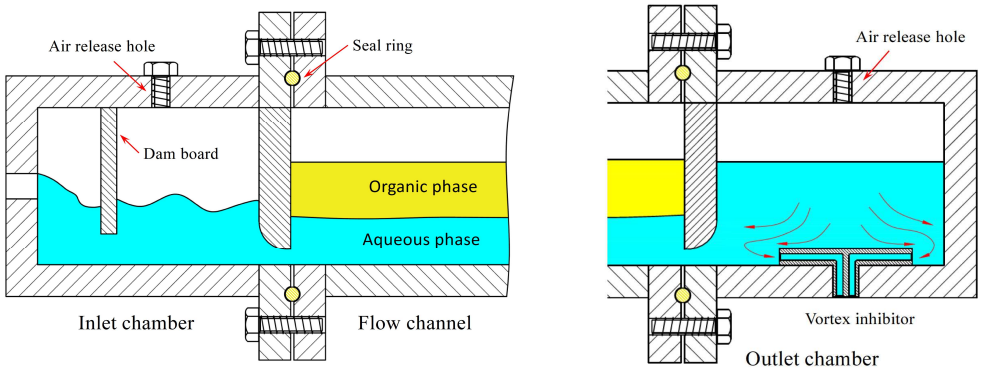

(b) (c)

Figure 3.10 Schematic of the Experimental Set-up for the studies on the delayed coalescence of drop with fluid interface.

As shown in Figure 3.10(a), the aqueous phase drops were generated by supplying the fluid from a syringe to a flat-ended nozzle which was located 20 cm away from the inlet. The flow rate in the nozzle was controlled by a programmable Aladdin® syringe pump and was set at 0.2 ml/min. The inner diameter of the nozzle is 2 mm which produces drops of an average size of (5 ± 0.15) mm. As mentioned by Klyuzhin et al. (2010), the drop rest time, which is the difference between the time that the drop contacts the interface and the coalescence time, could be affected by the height of the nozzle from the interface. Thus, the height of the nozzle was set at 10 mm above the

interface for all tests. From simulations it was found that the oil phase has a weak recirculation, with a backward flow at the top of the channel. Placing the nozzle at 10 mm above the interface avoids the effect of the backflow on the droplets.

3.3.2 Experimental methods

The rest times of the drops on the interface moving at different speeds were initially measured to evaluate the delay in coalescence. The falling time of the drops from the nozzle to the interface at the beginning and the coalescence time in the end were neglected as they were very short compared to the drop rest period. A stopwatch with an accuracy of 0.01s was used to measure the rest times. It was previously found that about 50 runs were sufficient to capture the distribution of the rest times of the drops with a stationary interface. In the current experiments, around 200 runs were conducted for each set of conditions to reduce uncertainties caused by the moving interface.

A high-speed Planar Laser Induced Fluorescence (PLIF) was then utilized to visualize the motion of the drop and the shape of the film as was also shown by Oldenziel et al. (2012), As shown in Figure 3.10(a), the PLIF system consists a Laserglow® continuous laser (532 nm, 3 W) at the bottom of the flow channel, which emits a laser beam of 4 mm in diameter. A spherical and a cylindrical lens were connected to the head of the laser in series to create a 1 mm thickness laser sheet, which was directed to the flow channel by a 45˚ angle mirror. As the drop was generated in the middle of the channel in the *y* direction and no appreciable deviation from the centre was observed when it travelled with the interface along the *x* direction (see Figure 3.10(a)), the middle plane of the drop could be illuminated when it went through the laser plane. A small amount of the fluorescent dye Rhodamine 6G was dissolved into both the drop and the aqueous film to help distinguish the interfaces and the structure of the oil film trapped between the drop and the interface. A Phantom® high-speed camera, equipped with a mono-zoom Nikkon lens, which gave a spatial resolution of 14 μm/pixel, was placed perpendicular to the laser sheet to capture the whole process. Since it was quite challenging to track the motion of the drops by moving the high-speed PLIF system, the laser plane and the high-speed camera were located at different

distances up to 20 cm away from the location of the drop impact to the interface. A raw PLIF image which clearly reveals the film shape is shown in Figure 3.11(a).

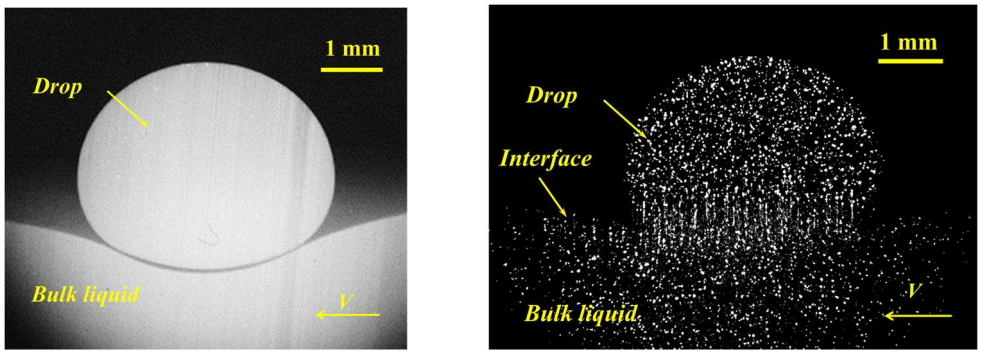

(a) (b)

Figure 3.11 (a) Raw image obtained from the moving PLIF measurement; (b) Raw image obtained from the moving PIV technique.

The Particle Image Velocimetry (PIV) technique was also applied to investigate the fluid dynamics inside the surfing drop. The drops were seeded with 1 μm Rhodamine coated spherical particles in order to show the velocity fields. As previously reported, some particles might affect the drop rest time depending on their properties (hydrophilic or hydrophobic) (Stancik et al., 2004, Mohamed-Kassim and Longmire, 2004); however the Rhodamine coated particles applied in the current study were not found to have an effect. A typical PIV raw image of a drop immersed in a pool of liquid is shown in Figure 3.11(b). An open source freeware JPIV was subsequently used to process the images obtained from the camera through the adaptive correlation tracking of the full image with a final interrogation window of 32 × 32 pixels. A 50% window overlap was used for a final resolution of 16 × 16 pixels, corresponding to an area of 0.2 × 0.2 mm^2.

3.4 Conclusions

In this Chapter, the experimental apparatuses used to investigate the different aspects of the drop coalescence phenomena are presented. The applied optical methods, including high-speed shadowgraphy, PIV and PLIF are introduced as well. For the investigations of both the total and the partial coalescence of drops with liquid interfaces, high-speed PIV, which has previously been employed by (Mohamed-Kassim and Longmire, 2004), was utilized to detect the fluid dynamics of the coalescing drops.

The innovation of the current experiments compared to the previous studies is the introduction of surfactants. The effects of surfactants on both the total and the partial coalescence are presented in Chapter 4 and in Chapter 5, respectively. To realize the visualization of the surfactants distribution on the coalescing interfaces, a pioneering experiment was conducted using PLIF to detect the surface concentration of the fluorescent surfactant NBD-PC throughout the whole coalescence process. The relevant results and discussion are presented in Chapter 6. At last, a novel flow channel was designed to study the coalescence of drops at moving liquid interfaces, which are usually encountered in the actual practice. The results are presented in Chapter 7.

Chapter 4

Surfactants effect on the total coalescence

Total coalescence of drops with liquid interfaces tends to occur when the drop liquid or the surrounding phase have high viscosity, which is often seen in dispersed flow in the petroleum industries. Commonly, surfactants are also presented either naturally or added to stabilize the dispersions in the liquid/liquid mixture. In this Chapter, the effect of surfactants on the total coalescence behaviour is considered [3]. As described in Section 3.1, the coalescence tests are carried out in an acrylic 3D cell. And both high-speed shadowgraph and Particle Image Velocimetry (PIV) are applied to investigate the surface morphology and the inner dynamics of coalescing drops. In Section 4.1, the evolution of the interfacial characteristics and droplet coalescence is discussed. Section 4.2 compares the evolution of the velocity and vorticity fields inside the coalescing drops at different surfactant concentrations. Furthermore, this section provides an estimation of the circulation and the position of the centre of the two counter-rotating vortices forming inside the drop during coalescence. Subsequently, the kinetic energy per unit mass inside the droplet for varying surfactant concentrations is investigated, see Section 4.3.

[3] Most of the results presented in this chapter are included in:
WEHELIYE, W. H., DONG, T. & ANGELI, P. 2017. On the effect of surfactants on drop coalescence at liquid/liquid interfaces. *Chemical Engineering Science,* 161**,** 215-227.

4.1. Interfacial characteristic and droplet coalescence evolution

4.1.1 Rupture point locations

The film rupture behaviour at different surfactant concentrations is first analysed. The aqueous phase drops generated from the nozzle initially rest on the aqueous-organic interface before the film ruptures. From the PIV images, it can be seen that during this resting period, the liquid inside the droplet is motionless prior to the rupture. When rupture occurs, the tracer particles close to the rupture point start to move. This instant is defined as the starting point of the rupture, while the moment when the interface returns to the initial quiescent level is recognized as the end of the coalescence. Figure 4.1 shows the rupture processes for two different surfactant concentrations, $\phi = 2\times10^{-5}$ and $\phi = 5\times10^{-4}$, where the dot on each sketch indicates the initial rupture point. The solid lines indicate the interface while the dashed ones outline the volume of the fluid from the drop that is now in the bulk phase; it was possible to identify this volume because the liquid in the drop was seeded with the PIV tracer particles and could be distinguished from the liquid in the bulk homophase.

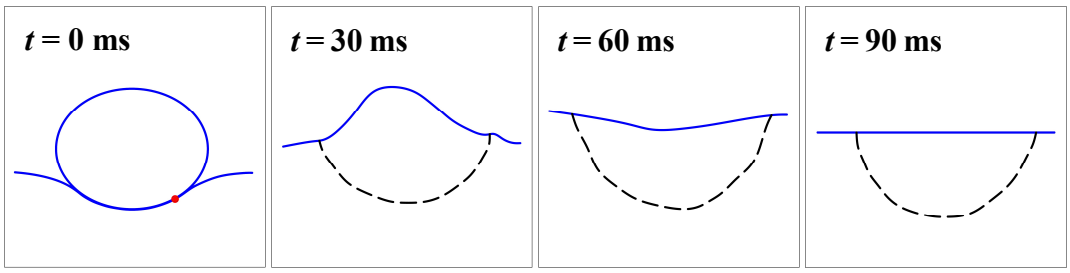

(a) ϕ=2×10^{-5}

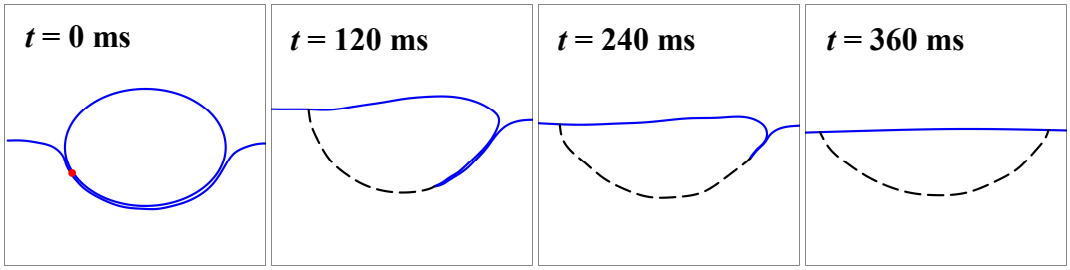

(b) ϕ=5×10^{-4}

Figure 4.1 Time evolution of the drop before and after film rupture for $\phi = 2\times10^{-5}$ and $\phi = 5\times10^{-4}$. The red dots indicate the initial rupture points.

For $\phi = 2\times10^{-5}$, the rupture and neck expansion proceeded quickly and ended in a short time (before 30 ms) as shown in the top row of Figure 4.1. In this case, the originally flat interface does not deform significantly when the drop rests on it, and the thin film trapped between the drop and the bulk phases retracts rapidly to let the droplet merge with the bulk. During the process, the drop top surface quickly moves below the equilibrium interface and eventually reaches the quiescent state smoothly. For a mass ratio of surfactant to organic phase equal to $\phi = 5\times10^{-4}$, it takes longer for the droplet to coalesce with the bulk liquid, as shown in the bottom row of Figure 4.1. In this case, the interface is significantly deformed when the drop rests on it. After the initial breakage, it takes longer for the neck to retract outwards, especially when asymmetrical rupture occurs. The upper part of the droplet does not pass through the equilibrium interface, but approaches slowly the final interface position.

The rupture time variation for different surfactant concentrations is attributed to two factors. High surfactant concentration promotes the deformation of the initially flat interface, which takes the shape of a hemisphere, and increases the length of the oil film trapped between the drop and the interface. This increases the time needed for the film to drain compared to low surfactant concentration. In addition, high surfactant concentration decreases the surface tension force that drives the expansion of the neck between the drop and the bulk fluid and the film drainage after rupture. Also, Marangoni effects tend to resist the drainage of the film due to the uneven distribution of surfactants along the drop surface and the interface. This behaviour is analogous to that reported by Yeo et al. (2003) and Nowak et al. (2016) who have shown that the presence of surfactants can have a significant effect on the drainage and stability of the organic phase film and thus on the coalescence time of drops. They reported that increased surfactant concentration slows down the film retraction and increases the coalescence time. The Marangoni effect will be discussed in Chapter 6 in combination with the results obtained from PLIF.

It was also found that the position of the initial rupture point varied. Chi and Leal (1989) investigated the film geometry (in particular the thickness of the film), using a boundary integral method, for various viscosity ratios, λ = 0.1, 1 and 10. For a low

viscosity ratio, λ = 0.1, the film is thinnest at the centre, and the rupture occurs at the centre of the droplet, while for a high viscosity ratio, λ = 10, the film has minimum thickness at an off-axis location, where rupture would occur. Other investigators have also observed off-axis rupture on an initial flat interface, experimentally. Mohamed-Kassim and Longmire (2004) reported for *Bo* number equal to 6, the location of the rupture point did not change for viscosity ratios 0.14 and 0.33. Ortiz-Dueñas et al. (2010) found that for a viscosity ratio equal to λ = 0.14 the rupture point varied with increasing Bond number. In the current work the Bond number is varied from 2.38 in the system without surfactant to 29.5 at the highest surfactant concentration system, while the viscosity ratio is constant and equal to λ = 31. For all the surfactant concentrations, tested off-axis rupture was observed and, for increasing Bond number, rupture occurred further away from the on-axis location as shown in Figure 4.1. Also, for each surfactant concentration, rupture occurred at approximately the same off-axis location. It should be noted that in the current work *Bo* was varied by decreasing interfacial tension σ (i.e. increasing surfactant concentration). At this point, it is uncertain why the increase of the surfactant concentration causes the rupture point to be further away from the on-axis location. It is possibly due to the uneven distribution of the surfactant along the deformed interface. As reported by Ghosh and Juvekar (2002) during the drainage process, the surfactant molecules will be swept outwards by the draining film and form a ring at a distance away from the on-axis location. Therefore, the rupture location would be likely associated to the area where the surfactant molecules have the highest concentration (i.e. the lowest σ point). This will be discussed in detail in Chapter 6 as well.

4.1.2 Drop height evolution

The variation of the relative height $h_s = h/D$ with increasing meniscus receding time, t, from the point of rupture for four different surfactant concentrations and for the case of no surfactant is shown in Figure 4.2. As show in the inset of Figure 4.2, h is the distance between the top of the drop to the equilibrium interface, D refers to the drop vertical diameter. For t = 0 ms, the value of h_s reduces with increasing surfactant

concentration in the organic phase. As the surfactant concentration increases, the interfacial tension decreases which leads to larger deformation of the interface where the droplet is resting and reduces h_s. As the surfactant concentration approaches the CMC value, however, the rate of reduction of interfacial tension and of the interface deformation decreases. As a result, at higher surfactant concentrations the initial height h_s does not vary as much.

Immediately after the film rupture, h_s reduces quickly at a rate that is higher for the lower surfactant concentrations. For $\phi = 0$ and the two lowest surfactant concentrations, h_s acquires negative values which shows that the top of the drop is below the initial flat interface level. The height reaches a minimum after which it gradually approaches the equilibrium interface level. For $\phi = 0$, $\phi = 2\times10^{-5}$ and $\phi = 1\times10^{-4}$ the upper part of the drop surface deflects at around $t = 50$ ms, $t = 55$ ms and $t = 80$ ms, respectively. It is worth mentioning the maximum deflection values of the interface decreased for increasing surfactant concentration. For the higher two surfactant concentrations, the top of the drop approaches the equilibrium interface level slowly and remains positive. The time taken to reach the equilibrium interface height is much longer than in the lower surfactant concentration systems. At these high surfactant concentrations, because of the interface deformation, the film trapped between the drop and the interface takes longer to drain. In addition, the low interfacial tension reduces the surface forces which drive the expansion of the neck, which again reduces the coalescence rate.

In the current experiments, no partial coalescence was observed. As discussed in the literature, three dimensionless numbers determine the appearance of partial coalescence, Oh_d; Oh_s and Bo_R. In the current investigation, the Ohnesorge number of the aqueous phase was $0.19 < Oh_d < 0.68$, and for the organic phase, $0.01 < Oh_s < 0.03$, while the Bond number based on the drop radius was $0.6 < Bo_R < 7.38$. The Oh_d is outside the range of critical Oh_d for partial coalescence proposed by Gilet et al. (2007) which explains why partial coalescence does not occur. In the following Chapter, the criterion of the partial coalescence will be discussed systematically.

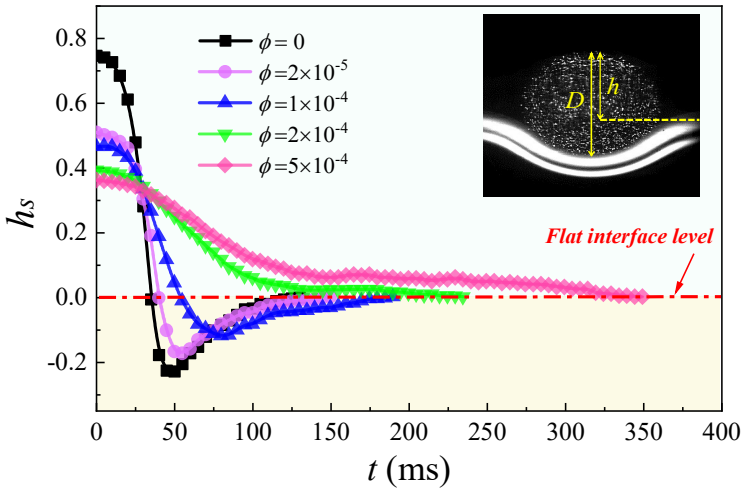

Figure 4.2 The variation of the relative height from the drop upper surface to the equilibrium interface, h_s, with increasing receding meniscus time, t, for a single droplet coalescence event. The yellow dashed line in the inset refers to the initially flat interface.

4.2. Generation of the vortices inside the drop

4.2.1 Spatial-temporal evolution of the vortices

At the beginning of the coalescence, two vortices are observed at the bottom of the drop and then develop inside the drop. The evolution of the 2D time-resolved velocity fields and the contour plots of the vorticity, ω_z, after film rupture are presented for three different surfactant concentrations in this section. It is worth noting that the applied PIV system has a maximum sampling frequency 1000 fps. Therefore, the time difference between two consecutive images is 1 ms, which limited the investigation of the high magnitude velocities occurring at the early stages of coalescence in the systems for no surfactant present or for mass ratio of surfactant to organic phase equal to $\phi = 2\times10^{-5}$. For the rest of the discussion, image analysis of the coalescence process was carried out for the whole range of surfactant concentrations while velocity fields were obtained for mass ratio of surfactant to organic phase, $\phi = 1\times10^{-4}$, $\phi = 2\times10^{-4}$ and $\phi = 5\times10^{-4}$. The results presented here are from a single droplet unless otherwise stated.

In Figure 4.3 the results are shown at four different time steps for $\phi = 1\times10^{-4}$ (σ = 18.34 mN/m). The sketch above the plots indicates the position where rupture happened. In the figure, the solid line encloses the volume of the drop (volume with tracer particles) during the coalescence and should not be confused with the interface between the drop

and the bulk phase. At a small time step, two counter-rotating vortices are observed close to the bottom of the drop (Figure 4.3(a)). The intensity of the two vortical structures is similar to each other in magnitude with absolute vorticity levels varying in the range of $|\omega_z| = 0 \sim 80\ s^{-1}$. Furthermore, for $t = 16$ ms and $t = 25$ ms (Figure 4.3 (b) and (c)), the two counter-rotating vortices start to move to the upper part of the droplet and their intensity increases in magnitude, with the maximum vorticity almost doubling ($|\omega_z| = 80 \sim 150\ s^{-1}$). During these times (Figure 4.3(b) and (c)), the droplet shape changes from spherical to elliptical while sharp angles start to appear on either side of the droplet.

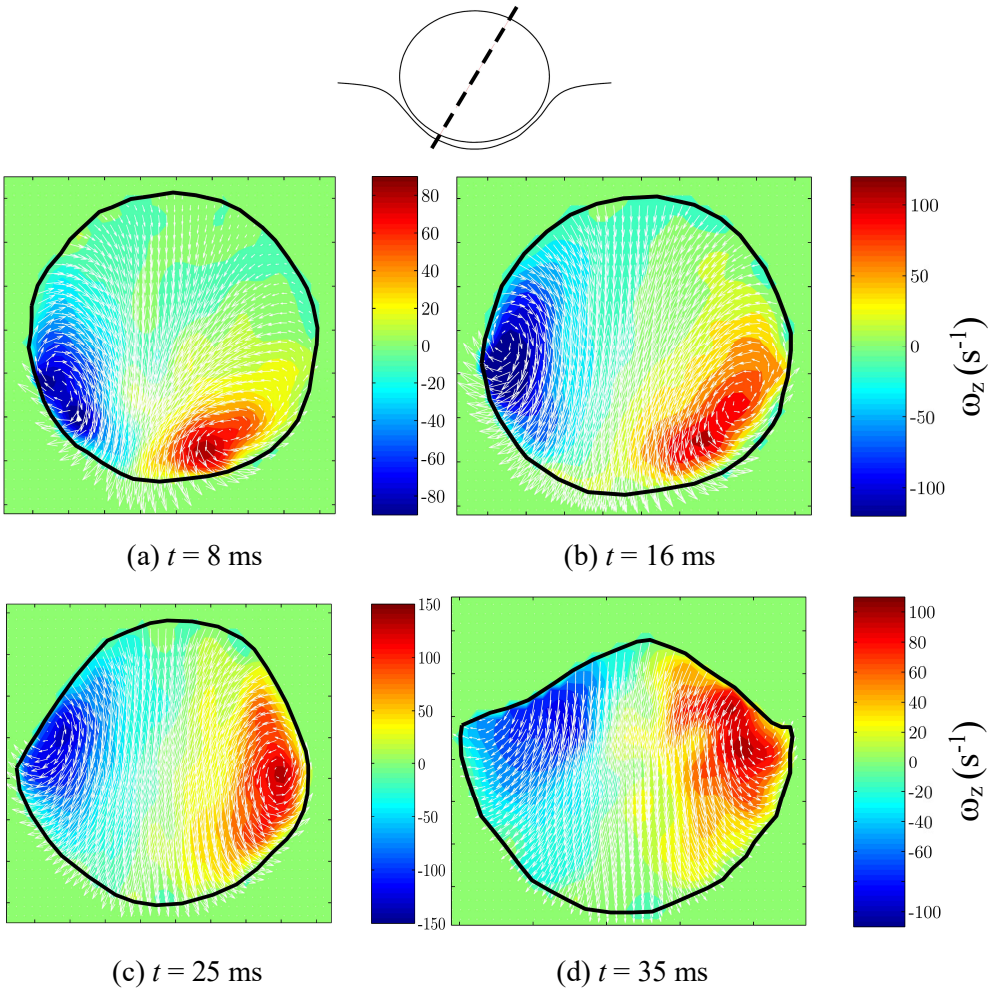

(a) $t = 8$ ms (b) $t = 16$ ms

(c) $t = 25$ ms (d) $t = 35$ ms

Figure 4.3 Time-resolved vector fields and contour plots of the vorticity, ω_z, in a single droplet for $\phi = 1\times10^{-4}$ and: (a) $t = 8$ ms; (b) $t = 16$ ms; (c) $t = 25$ ms; (d) $t = 35$ ms.

For $t = 35$ ms (Figure 4.3(d)), a transition occurs in the velocity vector field, and a downward axial motion dominates the flow dynamics inside the droplet. Despite the presence of this strong downward axial motion, the two vortical structures, in the upper

part of the droplet, are still identifiable. In addition, the areas occupied by the two counter-rotating vortices are of similar magnitude throughout the coalescence process. The results are consistent with the findings of Mohamed-Kassim and Longmire (2004) who have shown from vorticity counter plots for varying viscosity ratio $\lambda = \mu_d/\mu_s = 0.14$ & 0.33 and constant interfacial tension $\sigma = 29$ mN/m, that two counter-rotating vortices first appeared at the bottom of the droplet which stayed attached to the sides and moved to the upper part of the droplet as coalescence progressed.

The velocity field and vorticity contour plots for mass ratio $\phi = 2\times10^{-4}$ ($\sigma = 9.56$ mN/m) are shown in Figure 4.4(a)~(d). Similar to the previous case, two counter-rotating vortices can be distinguished in all the plots. As t increases (Figure 4.4(a)~(d)), the two counter-rotating vortices move from the bottom of the drop to the upper part

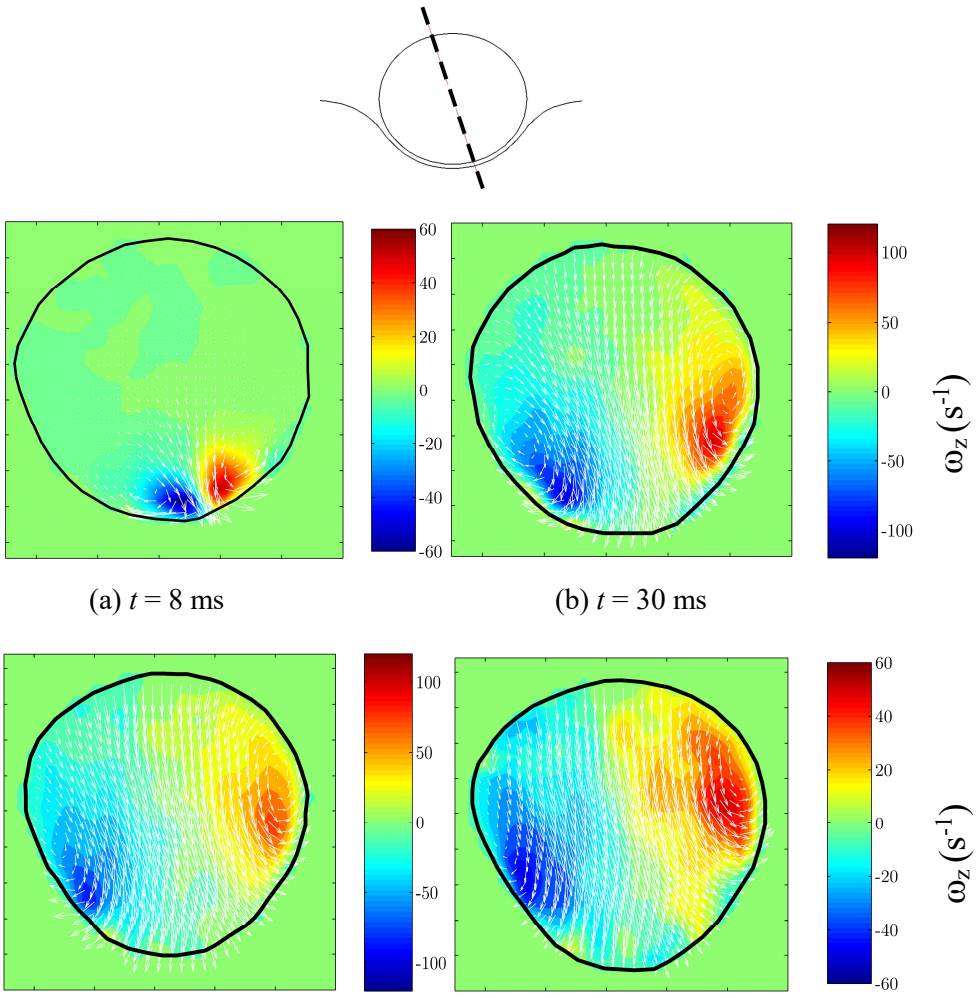

Figure 4.4 Time-resolved velocity fields and contour plots of the vorticity, ω_z, in a single droplet for $\phi = 2\times10^{-4}$ and: (a) t = 8 ms; (b) t = 30 ms; (c) t = 45 ms; (d) t = 55 ms;

and their intensity increases in magnitude, with the maximum dimensional vorticity increasing more than tenfold ($|\omega_z|$ = 10~110 s^{-1}). While in the beginning the two vortices only occupy a small part of the drop, at t = 30 ms and 45 ms, they extend over the entire drop (Figure 4.4(b) and (c)) and completely control the flow dynamics inside it. At time t = 55 ms, a transition occurs and a downward axial motion dominates the flow dynamics inside the droplet (Figure 4.4 (d)). Compared to $\phi = 1\times10^{-4}$, the flow transition occurred at a later time for $\phi = 2\times10^{-4}$, while the droplet shape remained almost spherical during the whole time. As was discussed before, the presence of surfactants increases the coalescence time.

The motion and trajectory of the two counter-rotating vortices are summarized in Figure 4.5 for the two surfactant concentrations, where the x and y coordinates of the vortex centres are tracked over time. Due to the resolution of the velocity field, the cores of the vortices cannot be observed until t = 3 ms. When the vortices move close to the upper surface of the droplet, they are suppressed and their full shape cannot be recognized. At this time the recording is terminated (for $\phi = 1\times10^{-4}$, t = 25 ms and for $\phi = 2\times10^{-4}$, t = 48 ms). The solid lines show the shape of the drop when the two counter-rotating vortices first appear, while the dashed lines indicate the shape of the drop when the vortices have disappeared. It is evident from the schematic diagrams in Figure 4.5(a) and (b) that the cores of the vortices originate from the film rupture point at the bottom of the droplet. For increasing receding time, t, the centres of the vortices stay attached to the sides of the droplet. For low surfactant concentration, $\phi = 1\times10^{-4}$, the vortices propagate faster to the upper part of the droplet.

The velocity vector and vorticity fields for the high mass ratio of surfactant to organic phase $\phi = 5\times10^{-4}$ are shown in Figure 4.6. Similar to the lower surfactant concentrations, at short times (Figure 4.6(a), t = 8 ms) two counter rotating vortices of similar magnitude appear on each side of the rupture point. However, at longer times (Figure 4.6(b), t = 70 ms) a significant change is observed and the vortical structures become asymmetric. This difference is attributed to the location of the rupture point. For this concentration, the film rupture occurred off-centre and near the equilibrium interface height, while for $\phi = 1\times10^{-4}$ and $\phi = 2\times10^{-4}$ rupture occurred near the centre of

the deformed interface. When asymmetric rupture occurs, such as the one shown in Figure 4.6 , it takes longer for the oil film to retract outwards on one side of the droplet compared to the side closest to the equilibrium interface height, which causes the difference in the flow pattern within the drop.

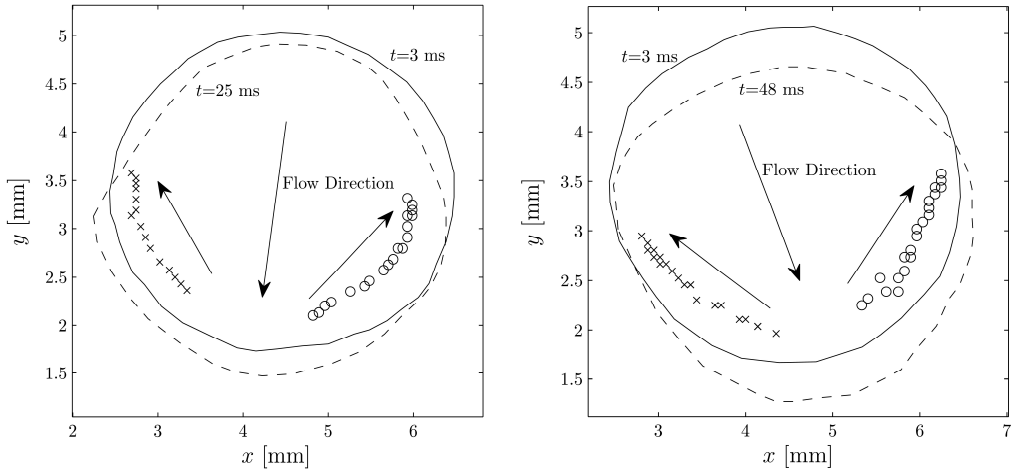

(a) (b)

Figure 4.5 Spatial evolution of the centers of the two vortices present on the left (×) and right (◦) hand side in a single droplet for: (a) $\phi = 1\times10^{-4}$; (b) $\phi = 2\times10^{-4}$.

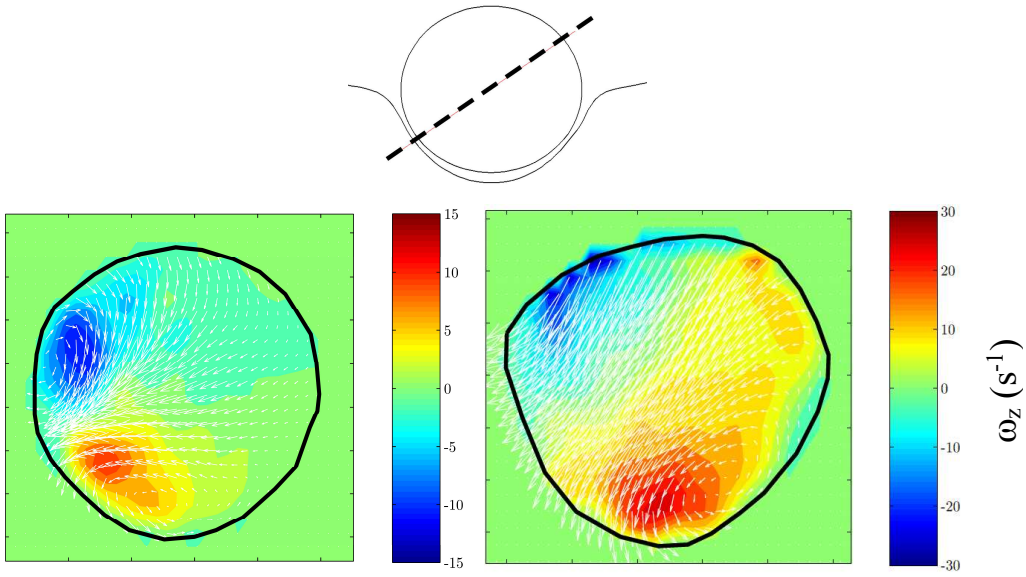

(a) (b)

Figure 4.6 Time-resolved vector fields and contour plots of the vorticity, ω_z, in a single droplet for $\phi = 5\times10^{-4}$ and: (a) t = 8 ms; (b) t = 70 ms.

4.2.2 Surfactant effects on the vortices strength

A further analysis was carried out to assess how the circulation of the two counter-rotating vortices varied with the receding time, t. The circulation, $\Gamma^*_{\omega_z}$, was estimated

from Equation (4.1) where the integral was carried out over the area, A_ω, which corresponds to a vorticity level $\omega_z > 10$ s^{-1}. A visualization of the areas $A_{\omega R}$ and $A_{\omega L}$ for the right and left hand side vortices, respectively, is shown in Figure 4.7 (a).

$$\Gamma^*_{\omega_z} = \frac{\int_{A_\omega} |\omega_Z| dA_\omega}{A_\omega} \tag{4.1}$$

The circulation, $\Gamma^*_{\omega_z}$, for $\phi = 2\times10^{-4}$ of the right and left hand side vortices is shown in Figure 4.7(b) for a single droplet coalescence event. As can be seen the circulations of the two vortices at either side of the rupture point are of comparable magnitude for the whole time studied. It can also be noted that the greatest circulation, $\Gamma^*_{\omega_z}$, is observed for 14 ms < t < 30 ms, where the intensity of the vorticity is high and the vortices occupy most of the droplet. For t < 14 ms the vortices have just started forming and are restricted to the lower part of the drop, while for t > 30 ms the flow inside the drop becomes dominated by the downward axial motion. The effect of surfactant concentration on $\Gamma^*_{\omega_z}$ averaged over 10 drop coalescence events is shown in Figure 4.7(c) for ϕ =1×10^{-4}, ϕ = 2×10^{-4} and ϕ = 5×10^{-4}. It should be noted that the rupture points chosen for averaging $\Gamma^*_{\omega_z}$ were of the same proximity from the center point of the deformed interface in order to obtain comparable flow fields. Since in all cases the two counter-rotating vortices are symmetrical, the circulations of only one of the vortical structures is presented. Again the calculations were carried out for iso-vorticity levels $\omega_z > 10$ s^{-1}. The iso-vorticity contour $\omega_z > 10$ s^{-1} was selected because it can capture the vortices from the beginning of the coalescence. For example, the minimum iso-vorticity contour observed for ϕ = 1×10^{-4} at t = 1 ms is ω_z = 10 s^{-1}, while for ϕ = 5×10^{-4} an iso-vorticity contour, ω_z = 10 s^{-1}, is observed at t = 7 ms. As can be seen $\Gamma^*_{\omega_z}$ increases with decreasing ϕ. For t < 14 ms similar circulation levels are observed for ϕ = 1×10^{-4} and ϕ = 2×10^{-4}, while for 14 ms < t < 30 ms the circulation levels for ϕ = 1×10^{-4} ($\Gamma^{*max}_{\omega_z}$ = 48 s^{-1}) are higher than those for ϕ = 2×10^{-4} ($\Gamma^{*max}_{\omega_z}$= 35 s^{-1}) and ϕ =5×10^{-4} ($\Gamma^{*max}_{\omega_z}$= 16 s^{-1}). For all the ϕ investigated, a plateau of the $\Gamma^*_{\omega_z}$ is reached, which indicates that the counter-rotating vortices have extended over the entire droplet when their intensities have reached a maximum. The plateau extends to longer times as the surfactant concentration increases, indicating that for high ϕ the counter-rotating vortices spread

over the entire droplet over a longer period compared to a low ϕ. For $\phi = 1\times10^{-4}$ and $\phi = 2\times10^{-4}$ the $\Gamma^*_{\omega_z}$ decreases after times t = 30 ms and t = 40 ms, respectively. Beyond these times a transition occurs in the flow pattern and a downward axial motion dominates the flow dynamics inside the droplet. At the high surfactant concentration, $\Gamma^*_{\omega_z}$ increases slightly and then remains almost constant which agrees with the slow dynamics of the neck evolution that result in low intensity vortices.

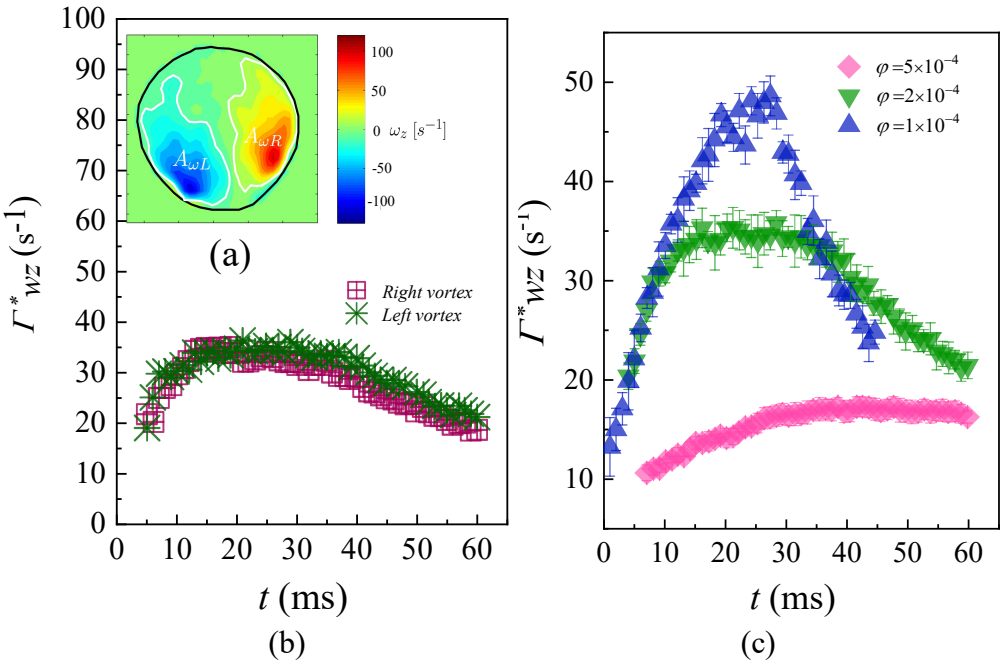

Figure 4.7 (a) Visualisation of the area, A_ω, over which the circulation ω_z has been estimated ($\phi = 2\times10^{-4}$); (b) Variation of the dimensional circulation, $\Gamma^*_{\omega_z}$, with increasing t for both the right and left hand side vortices ($\phi = 2\times10^{-4}$) in a single droplet; (c) Variation of the dimensional circulation, $\Gamma^*_{\omega_z}$, with increasing t for different ϕ, averaged over 10 droplets.

4.3. Kinetic energy per unit mass

The kinetic energy per unit mass contour plots of Figure 4.8 allow a quantitative comparison of the velocity dynamics inside the droplet for different mass ratio of surfactant to organic phase and at different time instants during the coalescence. The kinetic energy per unit mass of Figure 4.8 has been estimated according to the two dimensional approximation of Equation (4.2), where the indices x and y refer to the velocity components measured in the plane considered, while the third component contribution is estimated as the average of the other two (i.e. $\omega^2=(u^2+v^2)/2$)

$$k_{xy} = \frac{3}{4}(u^2 + v^2) \tag{4.2}$$

The kinetic energy per unit mass, k_{xy}, inside the drop for $\phi = 1\times10^{-4}$ and $\phi = 2\times10^{-4}$, is shown in Figure 4.8 (a, b) and (c, d), respectively, for different time steps. At the initial stages of coalescence, k_{xy} is mainly distributed near the bottom of the drop (see Figure 4.8(a) and (c)). Prior to rupture, the fluid inside the droplet is motionless. Once the film separating the drop and the interface reaches a critical thickness (Chen, 1985), rupture occurs at the lower part of the drop. All the fluid situated near the bottom of the drop rushes through the rupture point as shown in the kinetic energy per unit mass distribution. At the later stages of coalescence, the k_{xy} is mainly distributed near the top of the drop (Figure 4.8(b) and (d)). At these stages a combination of gravity and interfacial tension forces push the fluid at the top of the drop downwards, generating a strong axial flow (see also Figure 4.3(d) and Figure 4.4(d)). It should be noted that at high ϕ the interfacial tension is reduced, and the intensity of k_{xy} inside the drop is also reduced as shown in Figure 4.8 (c) and (d). Furthermore, the patterns of the two counter-rotating vortices described previously in Section 4.2, are a result of the high momentum

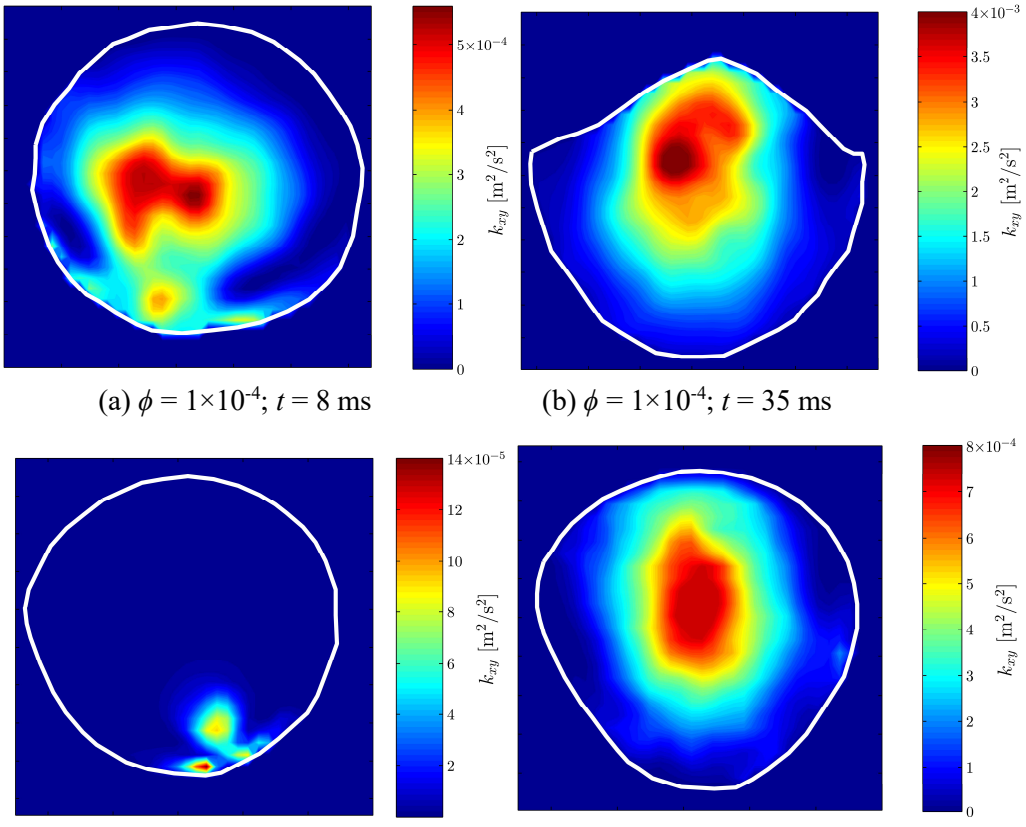

(a) $\phi = 1\times10^{-4}$; $t = 8$ ms (b) $\phi = 1\times10^{-4}$; $t = 35$ ms

(c) $\phi = 2\times10^{-4}$; $t = 8$ ms (d) $\phi = 2\times10^{-4}$; $t = 55$ ms

Figure 4.8 Contour plots of the kinetic energy, k_{xy}, for: (a) $\phi = 1\times10^{-4}$ and $t = 8$ ms; (b) $\phi = 1\times10^{-4}$ and $t = 30$ ms; (c) $\phi = 2\times10^{-4}$ and $t = 8$ ms; (d) $\phi = 2\times10^{-4}$ and $t = 55$ ms.

imparted to the fluid by the fast downward motion of the drop in conjunction with the rapidly growing neck. These two effects force the fluid to follow a circular motion along a closed loop inside the drop (see Figure 4.3(a)~(c)). For low ϕ, a fast growth of the neck is expected (Aarts et al., 2005, Lu and Corvalan, 2012, Chinaud et al., 2016) which, in combination with high k_{xy} (see Figure 4.8(a) and (b)) in the centre of the drop, results in high intensity vortical structures. At high ϕ, or low interfacial tension force, k_{xy} and the velocity of the neck growth of the drop are reduced and, therefore, decrease the intensity of the vortices inside the drop.

The variation of the space-averaged kinetic energy per unit mass over the measurement plane in the drop, k_{xy}^*, with receding time, t, is calculated from Equation (4.3):

$$k_{xy}^* = \frac{1}{A}\int_A k_{xy} dA \tag{4.3}$$

The results are shown in Figure 4.9 for $\phi = 1\times10^{-4}$, $\phi = 2\times10^{-4}$ and $\phi = 5\times10^{-4}$. As already discussed, at a receding time $t = 0$ ms, the fluid inside the drop is motionless and k_{xy}^* has its lowest value. As t increases k_{xy}^* gradually increases and peaks at $t = 28$ ms for $\phi = 1\times10^{-4}$ ($k_{xy}^* = 8.8 \times 10^{-4}$ m^{2}s^{-2}), $t = 39$ ms for $\phi = 2\times10^{-4}$ ($k_{xy}^* = 2.9 \times 10^{-4}$ m^{2}s^{-2}) and $t = 56$ ms for $\phi = 5\times10^{-4}$ ($k_{xy}^* = 9 \times 10^{-5}$ m^{2}s^{-2}). After the peaks, k_{xy}^* decreases for all the ϕ investigated. For $\phi = 1\times10^{-4}$, k_{xy}^* reaches a value of zero at $t = 80$ ms and it

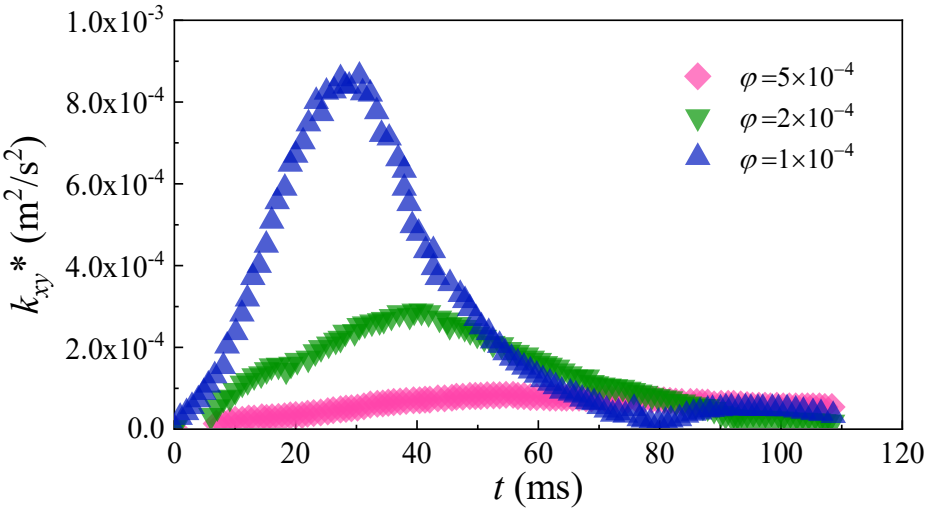

Figure 4.9 Variation of the dimensional space-averaged kinetic energy per unit mass, k_{xy}^*, in a single droplet with increasing t for different ϕ.

increases again thereafter. This is related to the behavior of the interface for this surfactant concentration. As shown in Figure 4.2, the interface reaches its maximum downward deflection at this time and then moves upwards to its equilibrium position. Conversely, for $\phi = 2\times10^{-4}$ and $\phi = 5\times10^{-4}$ the values of k_{xy}^{*} decrease to zero when complete coalescence of the droplet occurs.

4.4. Conclusions

This Chapter presents the investigations on the effect of an oil soluble surfactant on the total coalescence of a drop with a liquid/liquid interface. The shape of the interface while the drop rested on it was studied with a PIV system before the thin film that separated the drop from the interface ruptured. It was found that prior to rupture the interface under the drop deformed while the deformation increased with increasing surfactant concentration. In addition, as the surfactant concentration increased, the time needed for the film to drain and rupture to occur also increased. The interface behaviour during coalescence was similar to that observed in previous experiments on drops rupturing at liquid/liquid interfaces (Mohamed-Kassim and Longmire, 2004). A key difference, however, is that in the current experiments, no deflection of the interface was observed during coalescence at high surfactant concentrations in the organic phase. Under all the conditions considered, no partial coalescence was observed.

The high-speed PIV system was also utilized to obtain the velocity fields, the evolution of the vortices and the kinetic energy per unit mass distribution inside the droplet after the film rupture. Immediately after rupture, two counter-rotating vortices appeared at the bottom of the drop on either side of the rupture point, which then moved towards the upper part of the droplet while their corresponding intensities increased. At a later stage, a transition occurred and the dynamics in the drop were no longer dominated by the two counter-rotating vortices but by a downward axial motion. After the transition, the intensities of the vortices decreased with time. With increasing surfactant concentration, the intensity of the two counter rotating vortices decreased. The kinetic energy per unit mass, k_{xy}, distribution inside the droplets for different surfactant concentrations was calculated from the velocity fields. At the early stages of

coalescence, k_{xy} was mainly distributed near the bottom part of the droplet, while in the later stages of the coalescence it was distributed near the upper part of the droplet.

Chapter 5

Surfactants effect on the partial coalescence

As introduced in Chapter 2, the conditions under which partial coalescence will occur, as well as the approximate size of the daughter drops formed, are well documented for systems without surfactants. However, in various industrial applications surfactants are present in liquid/liquid systems either naturally or artificially. Only a few studies have been conducted on partial coalescence with surfactants. Martin and Blanchette (2015) found numerically that pinch-off and partial coalescence are inhibited in the presence of surfactants. Their results were partly validated by Pucci et al. (2015) who studied experimentally the partial coalescence of bubbles with soap films when surfactants were present. The few studies available only report qualitative results on the effect of surfactants on partial coalescence. There is no quantitative information, however, on the changes of the partial coalescence boundary or the ratio of drop sizes when surfactants are added in two-phase systems. In addition, the effects of surfactants on the drop velocity fields during partial coalescence have not been investigated. To address these questions, the coalescence between a drop and a liquid-liquid interface in the presence of surfactants is experimentally investigated in this Chapter[4]. The experimental set-up and the techniques on the partial coalescence has been introduced in Chapter 3.

[4] Most of the results presented in this chapter are included in:
Dong T, Weheliye W H, Chausset P, et al. An experimental study on the drop/interface partial coalescence with surfactants[J]. Physics of Fluids, 2017, 29(10): 102101.

5.1 Boundary between partial and total coalescence

In this section, the criterion for partial coalescence will be discussed based on dimensionless analysis. It is well acknowledged that partial coalescence involves 7 independent parameters, namely, the viscosities, μ_d and μ_s, and the densities, ρ_d and ρ_s, of the aqueous and the organic phases respectively, the diameter of the mother droplet D, the interfacial tension σ, and the gravitational acceleration g. Four dimensionless groups are thus formed, the Bond number $Bo = \rho g D^2/\sigma$, the Ohnesorge number $Oh=\mu/(\rho\sigma D)^{1/2}$, the viscosity ratio $\lambda = \mu_d/\mu_s$, and the density ratio $\eta = \rho_d/\rho_s$. To account for both gravity and buoyancy, the Bond number is written as $Bo = \Delta\rho g D^2/\sigma$, where $\Delta\rho$ is the density difference between the aqueous and the organic phases and D is the initial horizontal diameter of the mother drop. The occurrence of partial coalescence is closely related to the pinch-off phenomenon at the upper part of the drop, which depends on the competition between the liquid draining from the drop to its bulk homophase and the speed that the neck contracts at pinch-off. When Bo is large, gravity dominates the coalescence process and the drop liquid drains much faster than the contracting speed of the neck. As a result, the drop ratio ξ is monotonically decreasing with Bo, and a critical Bond number Bo_c exists above which there is no partial coalescence (Gilet et al., 2007). When Bo is small, mainly the viscous forces resist the surface tension forces and the Oh number is used instead to describe partial coalescence. For large Oh, the viscosity forces become significant and dampen the capillary waves thus allowing more time for the liquid in the drop to drain out before pinch-off generates a secondary drop (Thoroddsen and Takehara, 2000, Chen et al., 2006). Above a critical Oh_c number, there is no partial coalescence. In the literature, there is no general consensus on whether the viscosity of the drop or of the surrounding liquid is more important for partial coalescence and different forms of the Oh number have been suggested. Investigators have used the higher of the two viscosities (Kavehpour, 2015), or the viscosity of the drop phase only (Blanchette and Bigioni, 2006, Chen et al., 2006, Yue et al., 2006), to calculate the Oh number, or have considered more than one Oh numbers based on the drop liquid Oh_d and on the surrounding liquid Oh_s (Gilet et al., 2007, Ray et al., 2010).

In the current study, only the drop liquids are varied to extend the range of the viscosity while the organic phase was kept constant, thus only the drop viscosity is considered for the estimation of the *Oh* number for a more convenient comparison with previous studies (Yue et al., 2006, Chen et al., 2006, Blanchette and Bigioni, 2006). In addition, the density is taken equal to the arithmetic mean of the densities of the two phases, $\rho_m=(\rho_d+\rho_s)/2$. The *Oh* number is then calculated as follows: $Oh=\mu_d/(\rho_m\sigma D)^{1/2}$. Based on the above, a coalescence map with the boundary between partial and total coalescence is plotted with *Bo* and *Oh* as coordinates.

The coalescence map for the non-surfactant systems is shown in Figure 5.1. The values of the *Bo* and the *Oh* numbers were changed by varying the glycerol concentration ζ in water (0%, 25%, 35%, and 42.5%) and the size of the mother drops. As shown in Figure 5.1, there exists a critical Oh_c number for partial coalescence when

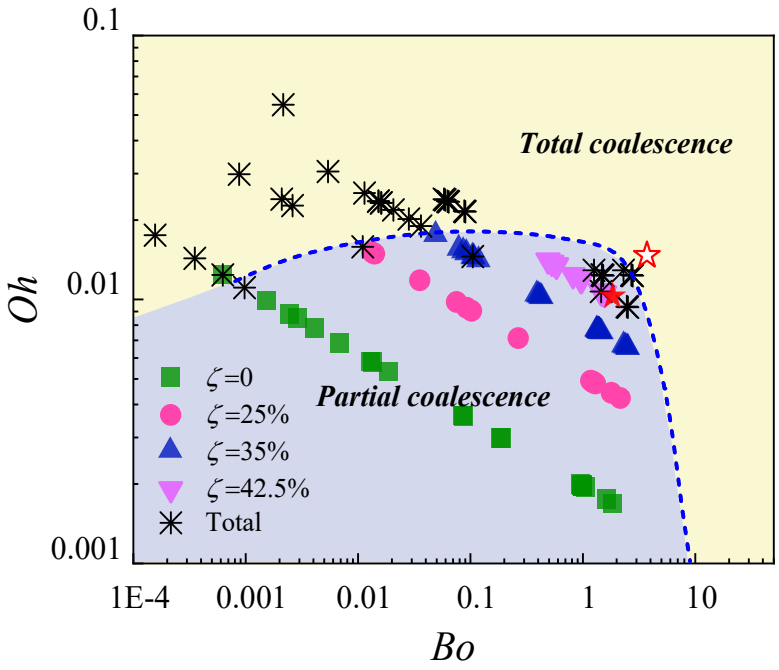

Figure 5.1 *Oh-Bo* map for coalescence in surfactant-free systems. The solid symbols represent the partial coalescence data with glycerol concentrations in the aqueous phase ranging from ζ = 0% to ζ = 42.5%, the asterisks show the total coalescence data for all glycerol concentrations. The stars refer to the conditions investigated with PIV. The dashed line is for reference only and shows the boundary between the partial and total coalescence regions.

Bo < 1, which increases slightly as the glycerol concentration increases from 0% to 35%. A similar increase was also observed by Chen et al. (2006). According to Yue et al. (2006) and Zhang et al. (2015), increasing the viscosity of the liquid in the drop delays its drainage and favours partial coalescence. For ζ > 35%, where the corresponding Bo number is large, the effect of viscosity is diminished and the Oh_c number does not continue to increase.

The Oh_c number in the current experiments increases from 0.01 to 0.02, while it increased from 0.02 to 0.03 in the experiment by Chen et al. (2006) for similar aqueous phases. In the experiments by Chen et al. (2006) the organic surrounding phase was decane with 1 mPa s viscosity, which is about 1/5 of the viscosity of the silicone oil in this work. As the viscosity of the surrounding liquid increases, the contracting speed of the neck is inhibited and the transition to total coalescence happens at a reduced drop based Oh_c. The effect of the viscosity ratio $\lambda = \mu_d/\mu_s$ on the critical Oh_c number was discussed by Yue et al. (2006). The results show that the critical Oh_c number increases linearly with the viscosity ratio when Bo is very small. For $0.22 < \lambda < 0.88$, which is the range of the current experiments, Oh_c increases from 0.01 to 0.02. When λ varies from 1 to 3.4, as in the experiments by Chen et al. (2006), the Oh_c number is larger and varies from 0.02 to 0.03.

Figure 5.2 shows the partial and total coalescence regions when surfactant is introduced into the oil at concentrations varying from $\phi = 2\times10^{-5}$ to $\phi = 2\times10^{-4}$. As can be seen, the partial coalescence region is largely reduced when surfactant is present. According to Martin and Blanchette (2015), the decrease of critical Oh_c can be attributed to the uneven distribution of surfactants along the interface. Just after the film breakage, the edges of the meniscus between the drop and the bulk homophase retract outwards rapidly, with speed higher than the rate of surfactant redistribution at the interface (Fallest et al., 2010). Therefore, the surfactant accumulates at the neck. Initially, capillary waves move upwards to the top of the drop. The top surface is stretched by the momentum of the capillary waves while the increase in area decreases the local concentration of the surfactants in this region. As a result, a surface tension gradient builds between the top and the bottom of the drop, which creates large

tangential forces that promote the contraction of the interface and drive the liquid out of the drop. The surfactant concentration remains high locally at the neck, even at the later stages. Under the circumstance, the Marangoni force generated by the surface tension gradient between the neck and the global area at the interface tends to resist the contraction of the neck edges and prevent the pinch-off. In addition, the sharp curvature at the neck creates a large Laplace pressure that also resists pinch-off because of the non-symmetrical contraction of the droplet, which will be shown in the following Section 5.4. The combined action of the two effects prevents pinch-off and partial coalescence. (The experimental observation of the distribution of the surfactants will be described in detail in Chapter 6.)

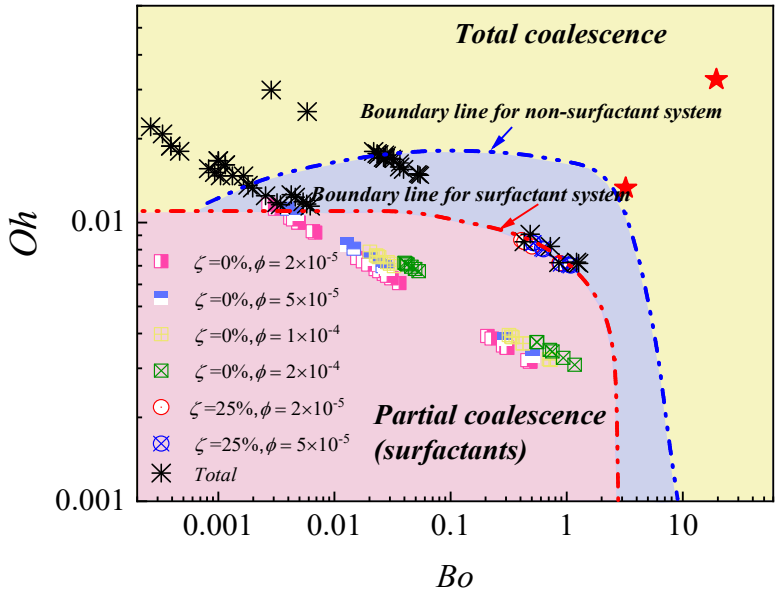

Figure 5.2 *Oh-Bo* map for coalescence in surfactant-laden systems. The square symbols represent the partial coalescence data with different surfactant concentrations for $\zeta = 0\%$, the round symbols represent the partial coalescence data with different surfactant concentrations for $\zeta = 25\%$. The asterisks show the total coalescence data for all cases. The stars refer to the conditions investigated with PIV. The dashed lines are only for reference and show the boundary between the partial and the total coalescence regions for both surfactant-free and surfactant-laden systems.

It was also observed that for pure water, the critical Oh_c number for the partial coalescence slightly decreases when the surfactant concentration increases from $\phi = 0$ to $\phi = 2\times10^{-4}$. While for the glycerol solution with $\zeta = 25\%$, the critical Oh_c number reduces significantly even with a small amount of surfactant. The trend agrees well with

the numerical data of Martin and Blanchette (2015) which reveal that the critical Oh_c number decreases fast with the addition of surfactant for highly viscous drop liquids. An increased viscosity not only dampens the motion of the capillary waves but also resists the movement of the surfactant molecules along the interface and favours total coalescence. For pure water, it is relatively easy for the surfactant molecules to relocate along the interface. In the 25% glycerol solution, which has viscosity two times larger than that of pure water, it is more difficult for the surfactant molecules to spread.

5.2 Effect of surfactants on the drop ratio

In this section, the effect of the surfactants on the drop size ratio ξ is analyzed. Thoroddsen and Takehara (2000) identified a narrow regime for a drop coalescing with an air/liquid interface where both the viscous and gravitational forces are negligible and a constant drop ratio $\xi \approx 0.5$ is found for all steps of partial coalescence. Chen et al. (2006) stated that partial coalescence can be extended to all three regimes, i.e., the gravity, the inertio-capillary regime, and the viscous regime. The drop ratio in each regime is plotted for different surfactant concentrations in Figure 5.3, with the data taken from all stages of the partial coalescence cascade. The solid lines are drawn to show the trends in the drop ratio at different concentrations. The drop size ratio data were plotted in the gravity regime against the *Bo* number, which indicates the relative importance of the gravitational and the surface tension forces while in both the inertio-capillary and the viscous regimes it was plotted against the *Oh* number. As discussed by Chen et al. (2006) , $Bo = 0.1$ can be taken as the boundary between the gravity and the inertio-capillary regimes. In the gravity regime, the drop ratio for all the surfactant concentrations studied $\phi = 0$, $\phi = 2\times10^{-5}$, $\phi = 5\times10^{-5}$, and $\phi = 1\times10^{-4}$, does not change significantly. This is expected since the addition of the surfactants only slightly affects the density of the aqueous phase which is important in this regime. Chen et al. (2006) also found that in this regime, the drop ratios were around 0.25 for $Bo \approx 1$. The variations in drop ratio ξ are attributed to daughter drops that may form displaced from the focus plane of observation.

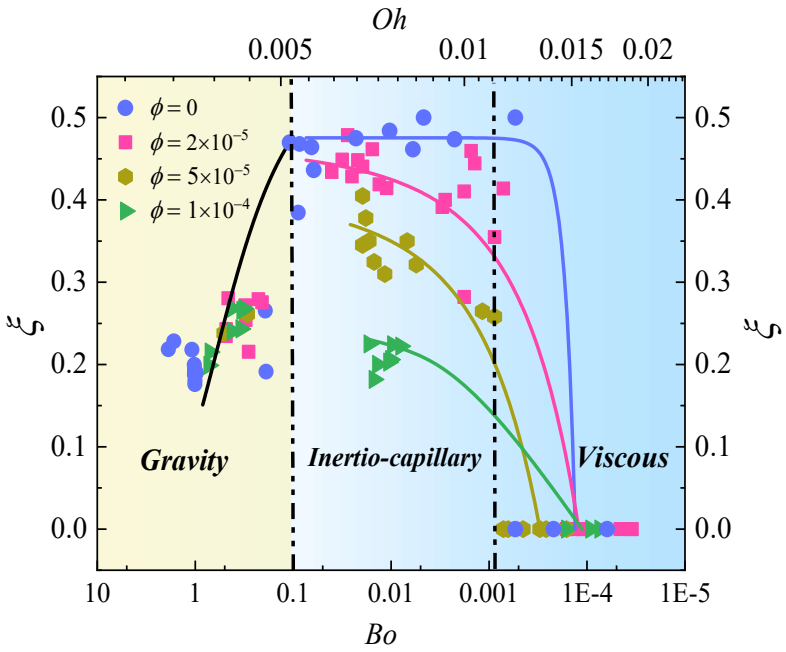

Figure 5.3 Daughter to mother drop size ratio in different regimes for the systems with surfactants.

Conversely, the presence of surfactants has a great effect on the drop size ratio in the inertio-capillary and the viscous regimes. For ϕ = 0, the drop size ratio at each coalescence stage is almost constant and around 0.5 in the inertio-capillary regime between $Oh \approx 0.005$ and $Oh \approx 0.012$. The drop size ratio decreases rapidly to zero when Oh increases further. This trend is in agreement with the results by Chen et al. (2006) and the boundary between the inertio-capillary and the viscous regimes is set at Oh = 0.01 for the non-surfactant system (see Figure 5.3). When surfactants are present, the drop size ratio in the inertio-capillary regime decreases. For $\phi = 2\times10^{-5}$ and $\phi = 5\times10^{-5}$ the value of ξ decreases to around 0.45 and 0.35, respectively, at the boundary with the gravity regime, while for $\varphi = 1\times10^{-4}$, the ratio becomes as low as ~0.22, which is less than half of the value for φ = 0. Interestingly, in the presence of surfactants, in the inertia-capillary regime the drop ratio does not remain constant any more but decreases with increasing Oh. According to (Martin and Blanchette, 2015), the concentration of surfactants along the surface of the daughter droplet is higher than that of the previous mother drop. Therefore, the drop ratio will decrease in every coalescence step, as a result of the corresponding lower interfacial tension. However, the distribution of the

surfactants along the surface of the droplets in every stage needs to be confirmed experimentally.

5.3 Evolution of the drop surface during coalescence

5.3.1 Drop height evolution in surfactant-free system

Once the film that separates the drop from the flat surface is broken and coalescence has started, capillary waves form at the bottom of the drop which travel upwards. This is not obvious for the cases of total coalescence in Chapter 4 as the system has high viscosity. It is stated in the literature that the convergence of the capillary waves on the upper part of the drop creates a liquid cylinder and favours the pinch off of a secondary droplet. The change of the drop surface shape for a typical partial coalescence process is shown in Figure 5.4 for a drop (D = 3.6 mm) of glycerol/water solution (ζ = 33%) in a 0.65 cSt silicone oil continuous phase. The coalescence time was scaled with the capillary time $t_\sigma = (\rho_m R^3/\sigma)^{1/2}$, where ρ_m is the average value of the density of the drop

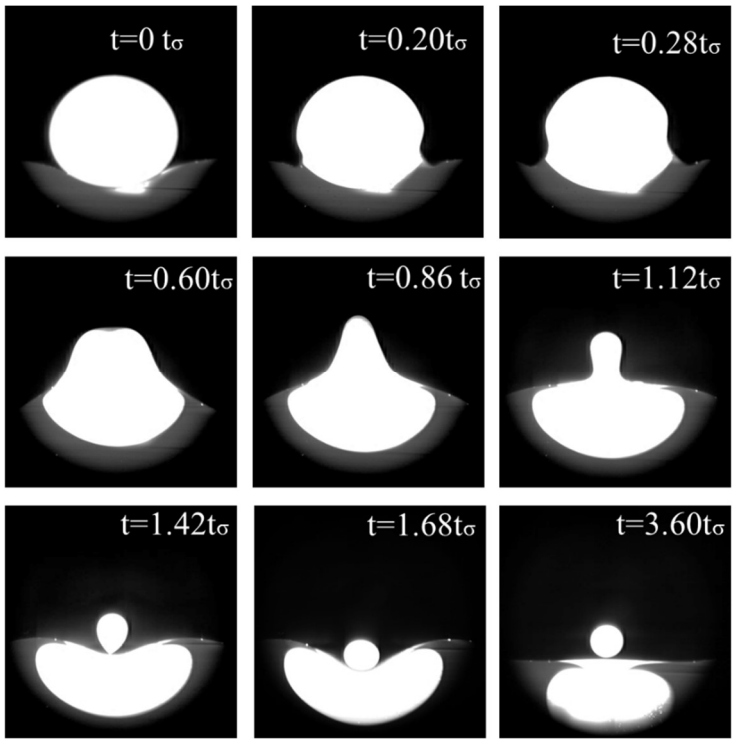

Figure 5.4 Partial coalescence of a single drop of water-glycerol (ζ = 33%) with its homophase within 0.65 cSt silicone oil. To aid imaging, Rhodamine 6G was dissolved in the drop liquid. In the above, a thin layer of the liquid under the interface was also dyed with a very small amount of Rhodamine 6G to show the shape of the interface.

and the surrounding liquid and R is the drop radius. It is found that once rupture occurs, the sudden retraction of the thin film creates capillary waves which propagate along the drop surface as the neck expands from $t = 0t_\sigma$ to $t = 0.6t_\sigma$, as shown in Figure 5.4. The drop surface is perturbed by the capillary waves, and a small dimple is observed on the top at $t = 0.6t_\sigma$. Afterwards, the liquid at the top of the drop is raised up when large capillary waves reach the summit, and a liquid cylinder appears ($t = 1.12t_\sigma$) which is then pinched off ($t = 1.42t_\sigma$) to create a secondary droplet (partial coalescence).

The convergence of the capillary waves is widely considered to delay the vertical collapse of the drop into the bulk homophase and to favour partial coalescence (Thoroddsen and Takehara, 2000, Blanchette and Bigioni, 2006, Chen et al., 2006, Zhang et al., 2009). To further study this behaviour, the movements of the drop summit for various conditions were tracked and plotted in Figure 5.5(a) and (b). The coalescence of drops of various glycerol concentrations surrounded by the same 5 cSt silicone oil are shown in Figure 5.5(a). Initially, the drop summit slightly decreases for all cases studied ($\zeta = 0$ % to $\zeta = 42.5$ %). When the capillary waves climb up to the top part of the drop, the surface of the drop is squeezed upwards and the height of the summit increases. After a certain time, the height of the drop summit starts to decrease with increasing speed driven mainly by gravity until the pinch-off. Interestingly, the dimensionless time where the drop summit starts to move upwards is similar at all conditions studied ($t = 0.80t_\sigma$), while the maximum height is reached at $t \approx 1.0t_\sigma$, which is consistent with the results of Gilet et al. (2007). This suggests that the increase in the height of the top of the drop is mainly controlled by the convergence of the capillary waves, as the dimensionless time t_σ represents the time that capillary waves travel along a distance equal to the radius of the drop R.

Before the significant increase in the height, a slight fluctuation on the top of the drop surface is observed for $\zeta = 0\%$ as shown in the magnified square in Figure 5.5(a). According to Gilet et al. (2007), the propagation speed of the capillary waves along the drop surface is proportional to $l^{1/2}$, where l is the mode of the capillary waves. The fluctuations on the drop summit are caused by capillary waves with higher modes than

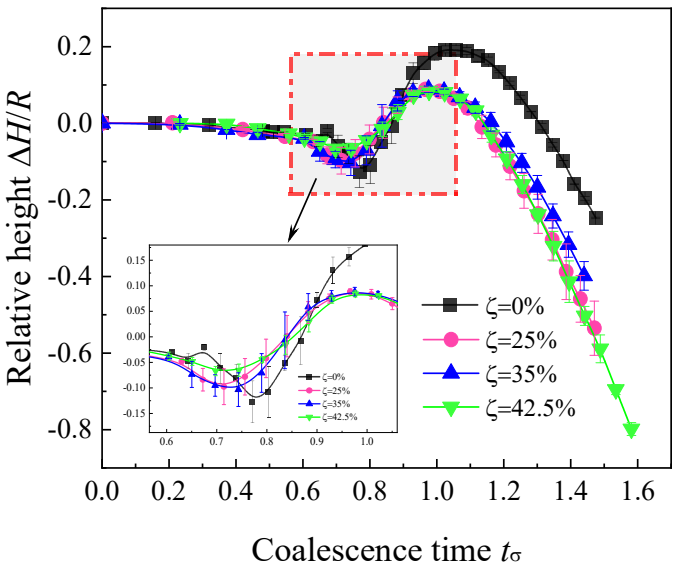

(a)

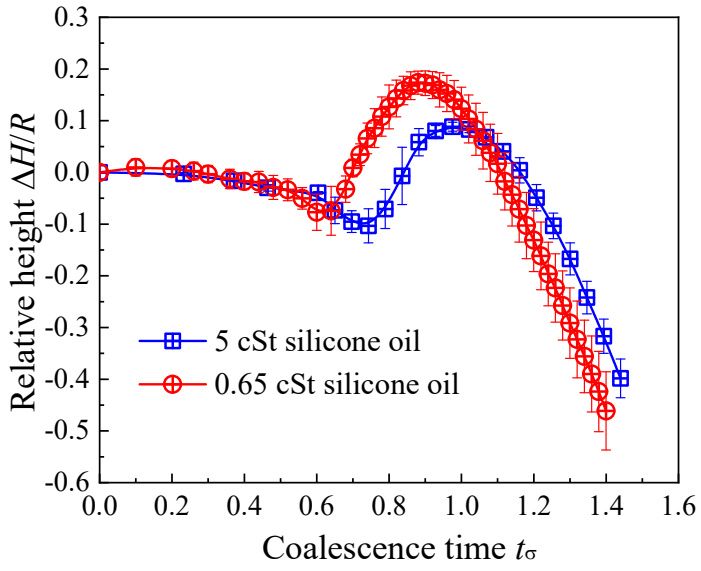

(b)

Figure 5.5 (a) Change of the dimensionless height of the drop summit relative to the initial location during partial coalescence. The aqueous coalescing phase is a water/glycerol mixture at various concentrations and the surrounding organic phase is a 5 cSt silicone oil; (b) Change of the dimensionless height of the drop summit relative to the initial location during partial coalescence for organic phases with different viscosity. The aqueous coalescing phase is a water/glycerol mixture (ζ = 33 %).

the dominant capillary waves ($l \approx 11$), which reach the summit later. Similar fluctuations are also observed for larger ζ. At high ζ, however, the capillary waves are not as large and are dissipated by the drop viscosity. The dominant capillary waves are dampened by the drop viscosity as well. As a result, the height that the drop summit

reaches is reduced at high ζ. This is in good agreement with the observations by Ray et al. (2010) that a coalescing drop is not elongated to take a column shape in high viscosity systems. As can be seen, the height that the drop summit reaches, is reduced when the fraction of glycerol in water increases from $\zeta = 0$ % to $\zeta = 25$ % and the viscosity increases, but remains almost the same when the fraction of glycerol is further increased at $\zeta > 25\%$. As discussed by Yue et al. (2006), the viscosity does not only dampen the capillary waves, but also reduces the drop drainage velocity. It seems that with increasing viscosity of the drop, the reduction of the capillary waves that extend the drop upwards is balanced by the reduction in the drop drainage rate which tends to reduce its height. As a result the maximum height that the drop summit can reach remains almost constant above a certain viscosity.

The effect of the viscosity of the surrounding liquid on the drop surface evolution was investigated as well. In these measurements, the glycerol concentration was kept constant at $\zeta \approx 35$ % and different silicone oils (0.65 cSt silicone oil and 5 cSt silicone oil) were used to change the viscosity of the organic phase. As shown in Figure 5.5(b), the evolution of the drop surface shape is similar to that shown in Figure 5.5(a). For the low viscosity 0.65 cSt oil the drop summit reaches a higher level compared to the 5 cSt oil indicating that the capillary waves are dampened by the viscosity of the outer phase as well. In addition, as can be seen from Figure 5.5(a), the maximum dimensionless height decreases from 0.19 to 0.08 when the drop viscosity slightly increases from 1 mPa.s ($\zeta = 0$ %) to 1.97 mPa.s ($\zeta = 25$ %). However, a similar height decrease is obtained for an increase of the outer phase viscosity of about 9 times, as shown in Figure 5.5(b). Thus, the drop viscosity seems to be more efficient than the viscosity of the outer phase in dampening the capillary waves, which agrees with the findings by Gilet et al. (2007).

Even though the capillary waves seem to play an important role in raising up the drop surface and create the liquid cylinder, partial coalescence is still observed in the absence of the waves in many occasions, mostly for drop coalescence with liquid/liquid interfaces (Gilet et al., 2007, Dong et al., 2017). Based on numerical studies, Yue et al. (2006) suggested that the low pressure area at the neck drove the drop surface inwards and promoted partial coalescence. Thus, a clear understanding of the changes in the

velocity fields as well as in the pressure distribution in the drop during partial coalescence are important for understanding the phenomenon.

5.3.2 Evolution of the drop surface during coalescence

The effects of surfactants on the evolution of the drop surface in both partial and total coalescence are analysed in this section. The raw PIV images for indicative partial, boundary, and total coalescence cases are present in Figure 5.6. From these images, the drop surface profiles at different time steps under each condition were extracted manually by detecting the boundary between the particle area and non-particle area and are shown in Figure 5.7. The continuous blue lines at the upper part of the drop indicate the real drop surface, while the dashed red lines at the bottom part distinguish the fluid with particles, originating from the drop, from the bulk liquid at the lower part of the tank. In Figure 5.7, the profile of the drop and the dashed line were plotted in the plane of *x*-*y*, and then the figures at different time steps were allocated along the *t* axis. The time interval is scaled with the capillary time t_σ as well.

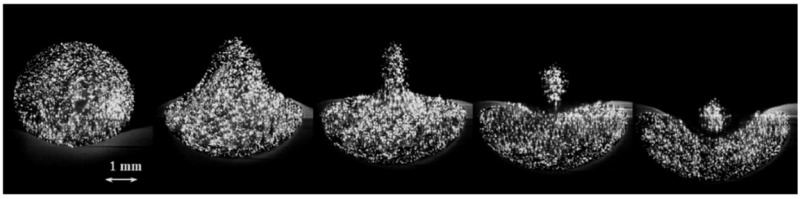

(a) Partial coalescence, $\phi = 0$;

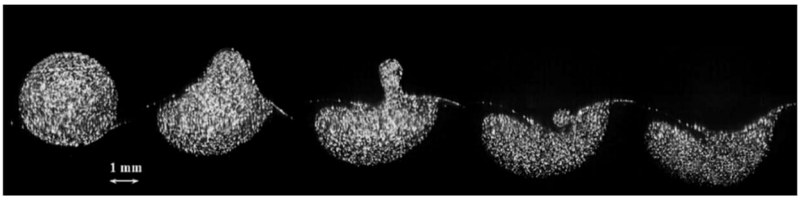

(b) Boundary coalescence, $\phi = 1.3\times10^{-6}$;

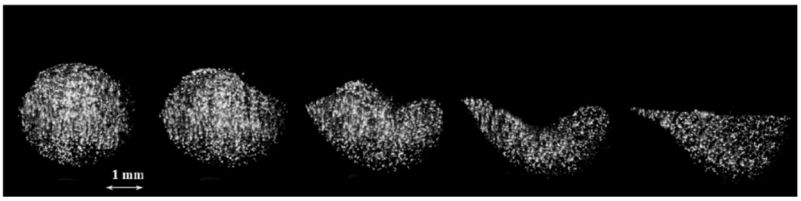

(c) Total coalescence, $\phi = 1.3\times10^{-4}$;

Figure 5.6 Enhanced raw PIV images obtained for (a) partial, (b) boundary, and (c) total coalescence.

In Figure 5.7 (a), the shape evolution is shown for partial coalescence with 0.65 cst silicone oil and 33 % glycerol/water mixture. The droplet has horizontal diameter equal to D = 3.33 mm. It can be observed that the droplet rests at the interface and deforms it significantly prior to the film rupture. Once rupture occurs, the sudden retraction of the film creates capillary waves at the bottom of the droplet. At the initial stages, the capillary waves are clearly observed climbing upwards the drop surface. In a short time, the waves reach the summit of the drop where they converge and distort it. From t = 0.1 to $t = 0.95t_\sigma$, the drop top surface is squeezed upwards, which causes a small amount of liquid to rise higher than the level of the initial top of the drop. Blanchette and Bigioni (2006) found that in air-water systems, the liquid could rise above the initial drop top level by as high as 30 % of the initial drop diameter. In the current experiments, the rise was about 4% ~ 10% of the initial drop diameter. The viscosity of the surrounding organic phase seems to reduce this increase in drop height. After about t = 0.95 t_σ, the height of the top of the drop starts to decrease, while the sides of the drop move inwards until a cylinder is formed at $t = 1.13t_\sigma$. The height to diameter ratio of the cylinder for all experiments was found to be much smaller than π, which means that the Raleigh-Plateau instability is not activated (Charles and Mason, 1960). After t = 1.13 t_σ, the bottom part of the liquid cylinder continues to contract and is finally pinched off at t = 1.37 t_σ. The liquid cylinder breaks away and a daughter drop is formed. As the surface curvature at the bottom of the daughter drop is much higher than at the top, the droplet tends to recover its spherical shape because of the Laplace pressure. This reduces the downward speed of the droplet, which becomes less than that of the interface. The bulk interface under the inertia of the draining liquids moves downwards and reaches a minimum height at t = 1.54 t_σ. Accordingly, the separation between the droplet and the interface increases between t = 1.37 t_σ and t = 1.54 t_σ. Once the droplet becomes almost spherical, it starts moving downwards and contacts the rising interface at t = 2.05 t_σ. The droplet and the interface finally move to the quiescent level at t = 4.80 t_σ.

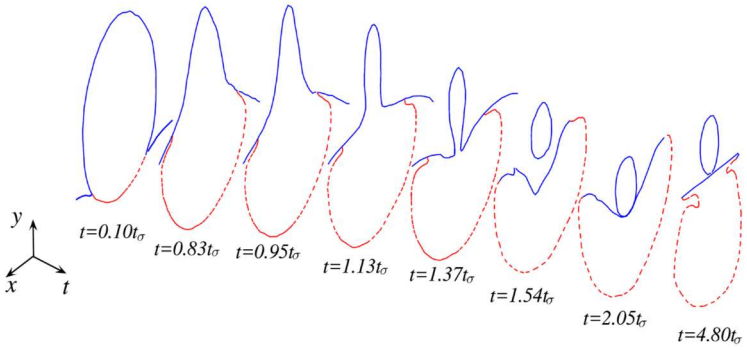

(a) Complete pinch-off, $\phi = 0$.

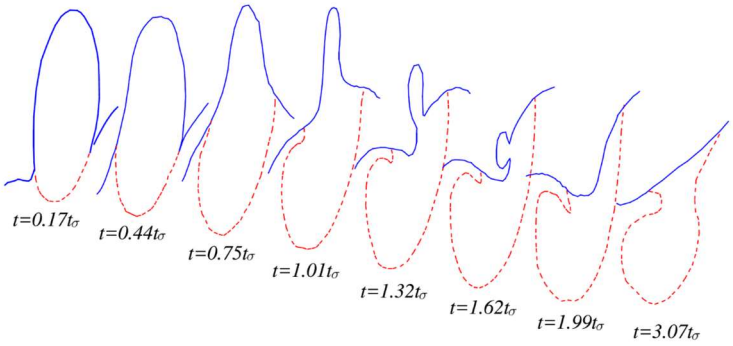

(b) Failed pinch-off, $\phi = 1.3\times10^{-6}$.

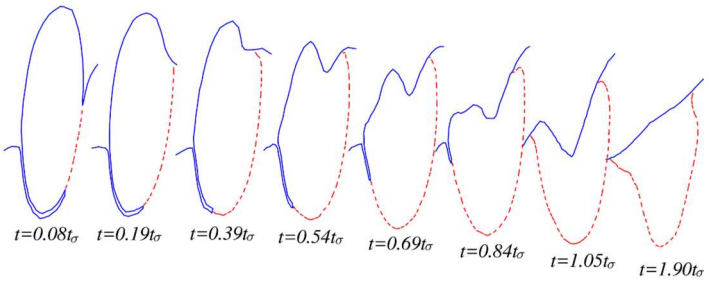

(c) Total coalescence, $\phi = 1.3\times10^{-4}$.

Figure 5.7 Drop surface evolution for (a) partial, (b) boundary, and (c) total coalescence. The visualization of the drop surface is stereoscopic. The drop profile at each time step is plotted in the *x*-*y* plane first, and then the figures are presented along the *t* axis.

The droplet surface evolutions for the same fluids and two different surfactant concentrations are shown in Figure 5.7 (b) and Figure 5.7 (c) for $\phi = 1.3\times10^{-6}$ and $\phi = 1.3\times10^{-4}$, respectively. The corresponding drop sizes are $D = 3.29$ mm and $D = 2.99$ mm. It is clearly observed that the initial deformation of the interface is increased with the surfactant concentration. The increase of the surfactant concentration also shifts the rupture points off-axis, as discussed as well in Chapter 4. For $\phi = 0$, the rupture points are close to the centre axis of the drop and the average horizontal distance between the

rupture point and the central axis over 15 coalescence events is (0.24 ± 0.06)D. This distance increases to (0.36 ± 0.03)D for $\phi = 1.3\times10^{-6}$. At the low surfactant concentration at $t = 0.44t_\sigma$, the oil film takes longer to retract outwards on the right-hand side of the rupture point, while on the left-hand side, the film drainage has already finished. A cylinder is again formed from the shrinking coalescing drop but the left bottom side of the cylinder is much lower than the right one as shown at $t = 1.32t_\sigma$. Under the inertia of the liquids, the left edge of the neck continues to move downwards to the right, while the right edge of the neck is dragged upwards by the Laplace force. Thus, the cylinder is leaning to the left and continues to reduce in size until the interface becomes smooth under the action of surface tension at $1.99t_\sigma$. Pinch-off in this case has failed. This type of coalescence was assigned at the boundary between coalescence regimes. When the surfactant concentration increases to $\phi = 1.3 \times 10^{-4}$, the interface deforms significantly and nearly half of the drop is under the initial flat interface height. On this occasion, the rupture occurs close to the periphery of the drop, even further away from the on-axis location than for $\phi = 1.3\times10^{-6}$. At $t = 0.08t_\sigma$, the film has already drained on the right while on the left there is still film with a large curvature. The left edge of the neck reaches the flat interface at $t = 1.05t_\sigma$ while most of the liquid in the drop has already mixed with the bulk homophase. In this case, no cylinder is formed. The drop surface approaches the final flat interface position for total coalescence, which is similar to our previous observations (Chapter 4) and the observations by Mohamed-Kassim and Longmire (2004).

5.4 Fluid dynamics in the drops

5.4.1. Evolution of Velocity fields

In this section, the 2D time-resolved velocity fields inside the droplet during partial coalescence as well as in the boundary case are discussed (the total coalescence was discussed in the previous chapter). The results presented here are from a single case as representatives. To check the repeatability of the PIV results, the average circulation level $\Gamma^*_{\omega z}$ inside a coalescing droplet, over 10 tests, was plotted for $\phi = 0$ and $\phi = 1.3 \times$

10^{-6}. The circulation, $\Gamma^*_{\omega z}$, was estimated from Equation (4.1) in section 4.2.2. The integral was carried out over the area, A_ω, which corresponds to a vorticity level $\omega_z >$ 10 s^{-1}. The film rupture point is close to the central axis when there is no surfactant, while it is away from the centre in the presence of surfactants; in the latter case, the two vortices generated at the bottom of the droplet after the film rupture might travel over different path lengths. As the evolution of circulation levels $\Gamma^*_{\omega z}$ depends on the paths that the vortices follow, the vortices along the longer paths were considered. As shown in Figure 5.8, $\Gamma^*_{\omega z}$ for different coalescence events under the same conditions evolve in a similar trajectory. The errors in $\Gamma^*_{\omega z}$ are acceptable, except for few points in the high surfactant concentration.

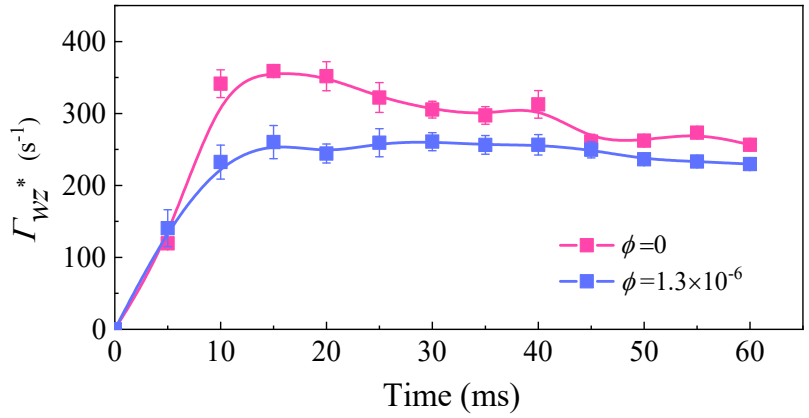

Figure 5.8 Variation of circulation level $\Gamma^*_{\omega z}$ against coalescence time.

The velocity field evolution for partial coalescence without surfactant is presented in Figure 5.9, with the vertical velocity (v-velocity) fields in the left column and the horizontal velocity (u-velocity) fields in the right column. The solid line in each figure shows the interface of the bulk and of the drop, while the dashed line shows the area with tracer particles after the film rupture. The time steps are similar to those plotted in Figure 5.7. In the beginning ($t = 0.10\ t_\sigma$), the top part of the drop is not moving and only the liquid at the bottom starts to flow downwards with a relatively low speed. At the same time, the retracting thin film (along the dashed line) generates an outflow of the liquid near the bottom interface. In the area near the interface just above the neck, the curved drop surface induces a Laplace pressure that pushes the liquid inwards. Thus, a pair of horizontal velocity components with opposite directions forms near the neck

(region A). Similar horizontal velocity pairs were also observed in the numerical simulations by Blanchette and Bigioni (2006) of a drop coalescing with an air/liquid interface. They reported that the velocity pairs were coupled with the upward capillary waves on the drop upper surface. However, this is not seen here, probably because the viscosity of the surrounding liquid suppresses the interfacial capillary waves.

At $t = 0.83t_\sigma$, the u-velocity (right column) contour plot shows a large area of the liquids which approaches the middle of the drop with an average velocity of around 0.04 m/s (region B). Meanwhile, in the middle of the drop, there is also a large area of gravity-driven downstream flow (v-velocity). At $t = 0.95t_\sigma$, the inward horizontal velocities cause the liquid column to shrink. At longer times, $t = 0.95t_\sigma \sim 1.37t_\sigma$, the radius of the neck decreases and the outward Laplace forces increase which resist the pinch-off; as a result the u-velocities decrease. However, the edges of the neck continue to approach driven by the inertia of the liquid. When the liquid cylinder is formed at $t = 1.13t_\sigma$, the fluid at the bottom of the cylinder has higher v-velocity and accordingly lower pressure compared to the surrounding area (Region C). This low-pressure area has also been reported in the numerical studies by Ding et al. (2012) and Martin and Blanchette (2015). The reduced pressure drives the edges of the neck to contact with each other and causes the pinch-off at $t = 1.37t_\sigma$.

When surfactant is present at $\phi = 1.3\times10^{-6}$, the film drainage is not symmetrical and the film rupture occurs at an off-axis location (Figure 5.10). The liquid at the bottom of the drop has a distinct u-velocity at $t = 0.17t_\sigma \sim 0.44t_\sigma$. At the left side, the retracting film carries the fluid outwards and causes the collapse of the drop left surface. At $t = 0.17t_\sigma$, the liquid near the left surface has a small velocity towards the right driven by the collapsing surface (region D); a similar velocity is not observed at the right side. At a later stage ($t = 0.44t_\sigma$), most of the liquid inside the drop starts to move downwards. However, the average v-velocity is about 0.05 m/s, which is much lower than that at $\phi = 0$ (0.15 m/s). The drop surface on the right-hand side also begins to collapse, and the liquid near the upper right surface starts to move towards the left driven by the collapsing surface. At $t = 0.44t_\sigma$, the horizontal negative streams from the top-right and

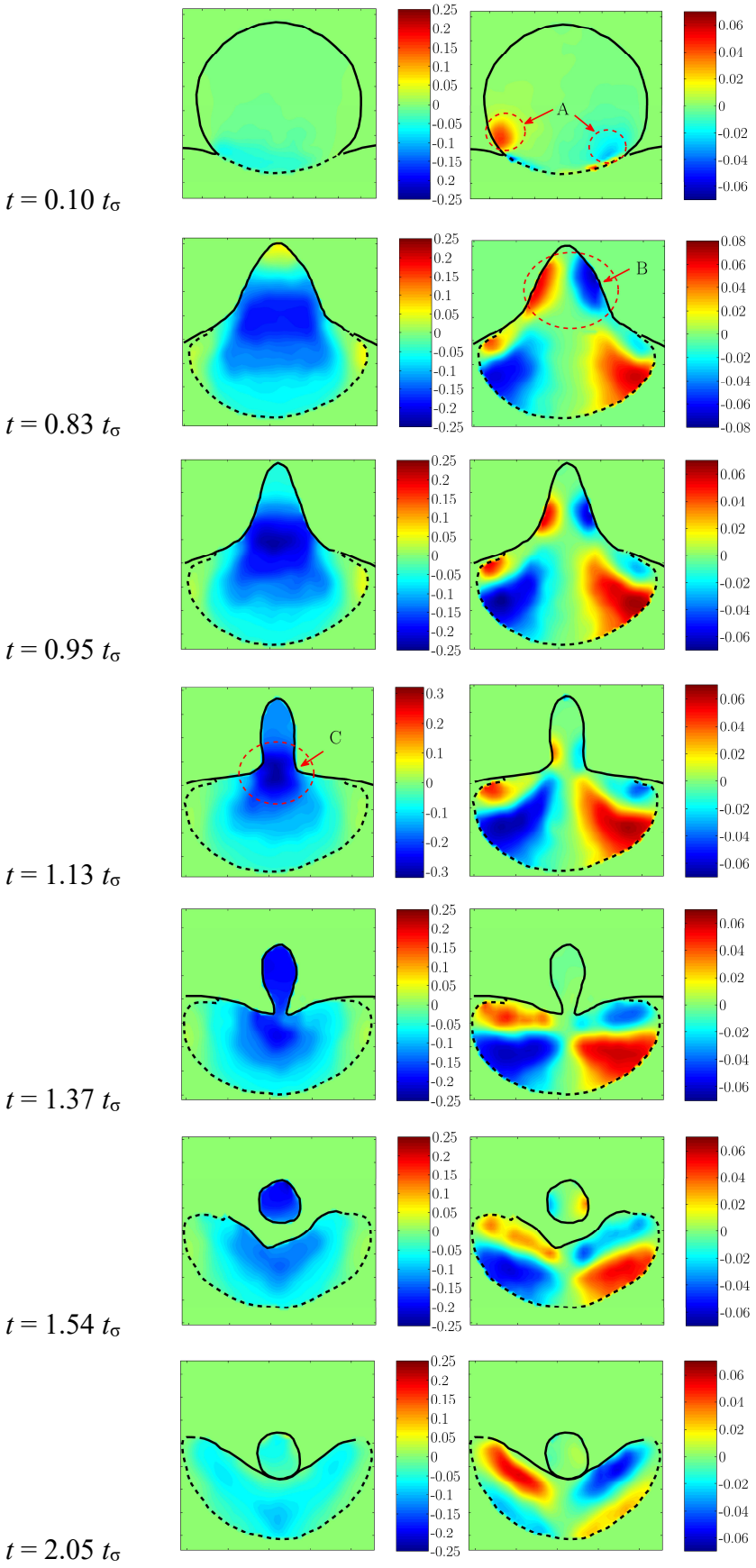

Figure 5.9 The vertical and horizontal velocity fields in the coalescing drop for $\phi = 0$.

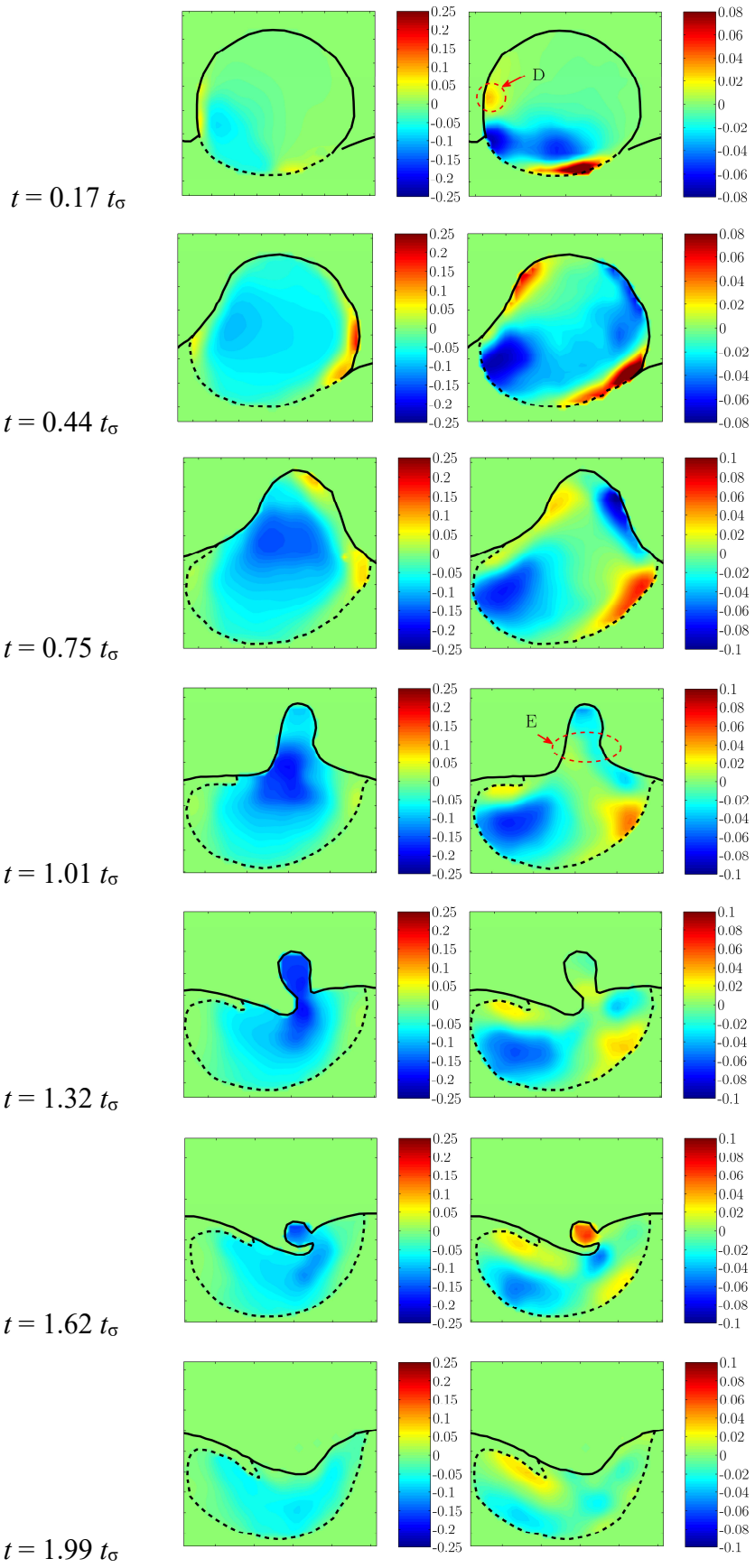

Figure 5.10 The vertical and horizontal velocity fields inside the drop for ϕ=1.3×10^{-6}.

the bottom-left parts of the drop join and occupy a large area. Because of the flow asymmetry, at $t = 0.75t_\sigma$, the horizontal velocity on the right side has a high value and occupies a large area, which drives the interface on the right to a concave shape while the left is flat (region E). Similar to the case of $\phi = 0$, the downward stream at the bottom of the liquid cylinder reduces the pressure at this region and helps the pinch-off of the interface at $t = 1.01t_\sigma$. As the velocity difference for $\phi = 1.3\times10^{-6}$ is lower compared to $\phi = 0$, the corresponding pressure gradient that drives the pinch-off is less. In addition, the flow asymmetry makes the liquid cylinder inclined to the left when the pinch-off is about to happen which increases the local curvature of the interface ($t = 1.62t_\sigma$). As Zhang et al. (2009) discussed, the pinch-off is prevented because of the local large curvature of the neck. The interface finally becomes flat under the effect of the Laplace force and no secondary drop forms. When the surfactant concentration increases to $\phi = 1.3\times10^{-4}$, a typical total coalescence is observed which was discussed previously in Chapter 4.

5.4.2. Vortices evolution

As previously discussed (in Chapter 4 for total coalescence), two counter-rotating vortices are created near the bottom of the droplet just after the film breaks up, which then expand inside the droplet during coalescence. In partial coalescence, Gilet et al. (2007) reported that the evolution of the vortices inside the drop may help the interface pinch-off and the formation of a secondary droplet. The evolution of the vortices ω_z (s^{-1}) inside the droplet for $\phi = 0$ is presented in Figure 5.11. Two counter-rotating vortices are observed at the bottom of the drop immediately after the film rupture, with intensities that are similar in magnitude and absolute vorticity levels varying in the range $|\omega_z| = 0 \sim 750\ s^{-1}$.

Until $t = 0.83t_\sigma$, the cores of the vortices move outwards and upwards along with the edges of the neck in a symmetrical way. As the edges continue to retract, the top of the drop acquires a conical shape and the peak value of $|\omega_z|$ decreases to 450 s^{-1} at $t = 0.83t_\sigma$. At the same time, the vortical structures acquire a tadpole shape. Two tail areas with high $|\omega_z|$ are observed connected to the cores of the vortices. As the flow changes

from a horizontal to a downward direction in the tail area, the vorticity reaches a value of $|\omega_z|$ = 550 s^{-1}, larger than that in the core of the vortices ($|\omega_z|$ = 330 s^{-1}). From t = 0.83t_σ to t = 1.37t_σ, the edges of the neck converge and lead to pinch-off, the high vorticity tail areas are pushed downwards and the cores of the vortices continue to move outwards in the bulk phase. ω_z of the tail area is decreased to 350 s^{-1} at t = 1.37t_σ. After the pinch-off, the highly curved interface tends to return to the flat level under the effect of surface tension, while the liquid beneath the interface continues to move downwards due to inertial effects. Symmetrical vortices form beneath the interface from t = 1.54t_σ to t = 2.05t_σ. Eventually the vortices move towards the centre and their strength diminishes. In partial coalescence, the vortices do not enter the liquid cylinder region and just remain below the interface. It can therefore be assumed that the vortices do not affect both the formation of the liquid cylinder and the pinch-off.

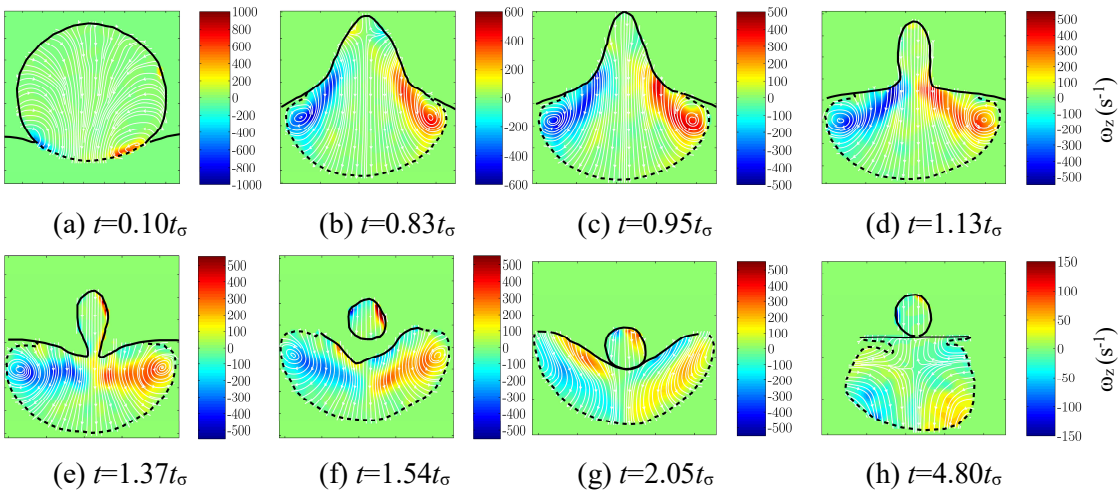

Figure 5.11 Time-resolved streamlines and contour plots of vorticity ω_z for ϕ = 0.

The evolution of vorticity for ϕ = 1.3×10^{-6} is presented in Figure 5.12. At the early stages, two counter-rotating vortices are created at the bottom of the droplet near the edges of the neck with absolute values of $|\omega_z|$ up to 700 s^{-1}. At t= 0.17t_σ, the core of the left vortex has moved above the edge of the neck while the core of the right vortex is still below the edge. The intensity of the right vortex has slightly increased driven by the draining film. The downward motion in the central part of the drop increases the area occupied by the vortices and elongates them. Two long tails with high ω_z are

created as a result of the changing flow direction from horizontal to vertical at $t = 0.75t_\sigma$. Contrary to $\phi = 0$, the vorticity tails are able to reach the top part of the droplet in this case. The core of the left vortex is below the neck edge and its tail becomes suppressed when the interface moves inwards at $t = 1.01t_\sigma$. At the same time, the tail of the right vortex is also dampened by the inward motion of the drop surface on the right side. A liquid cylinder is formed at $t = 1.32t_\sigma$ and two asymmetric vortical areas are observed below the cylinder. From $t = 1.32t_\sigma$ to $t = 1.99t_\sigma$, the locations of the two cores are less affected by the irregular motion of the interface and they do not change location until the interface becomes smooth. When the surfactant concentration increases to $\varphi = 1.3\times10^{-4}$, total coalescence is observed and the evolution of the vortices was similar to what discussed in Chapter 4.

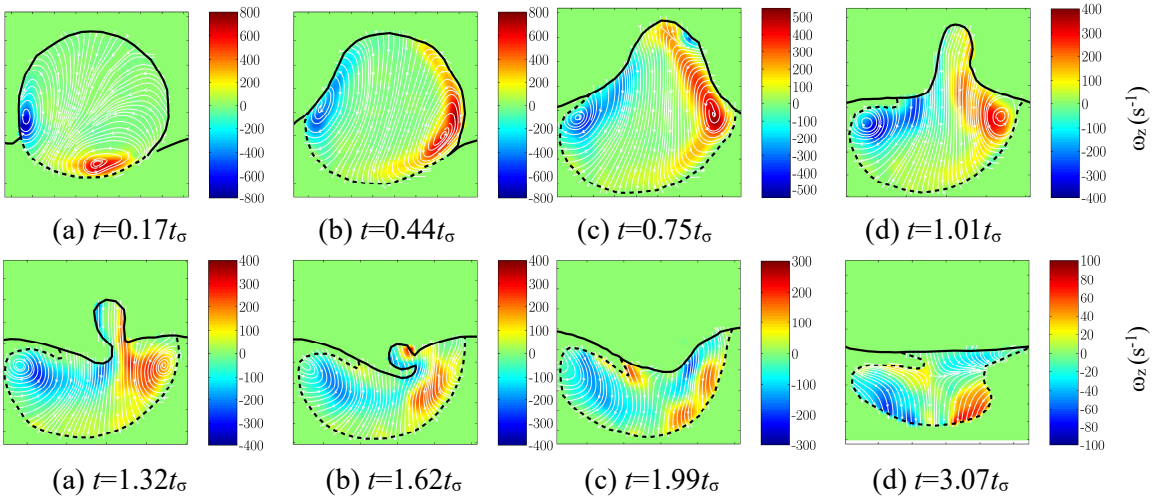

Figure 5.12 Time-resolved streamlines and contour plots of vorticity ω_z for $\phi = 1.3\times10^{-6}$.

5.4.3 Pressure fields inside the coalescing drop

As discussed in Section 5.4.1, the pressure gradient in the drop tends to favour the occurrence of the partial coalescence, especially during the period of the pinch-off. Therefore, a knowledge of the pressure distribution inside the drop during coalescence would help to better understand the development of the phenomenon. Calculation of pressure fields from PIV velocity field data has been presented for a number of different applications including flow over a foil (Tronchin et al., 2015, Violato et al., 2011), standing waves (Jakobsen et al., 1997), lid-driven cavity flow (Liu and Katz, 2006), vortex shedding in the flow after a cylinder (McClure and Yarusevych, 2017) flow

around a bubble (Hosokawa et al., 2003) and in boundary flows (Ghaemi et al., 2012). In this section, the pressure fields extracted from the 2D-PIV velocity data are presented. The methodology for the pressure calculation is outlined in Appendix B. Since the approach is based on the assumption that the whole coalescence process is axisymmetric, only the case of $\phi = 0$ is analysed.

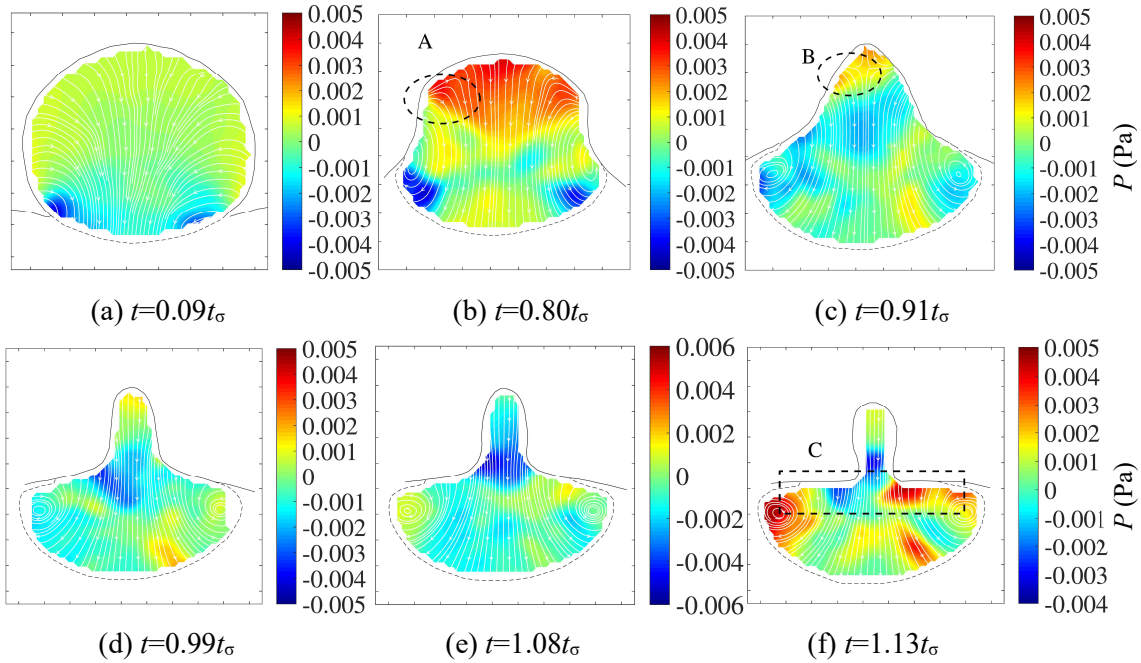

Figure 5.13 Pressure distribution (Pa) in a partial coalescing drop (D=3.6 mm) of the same case shown in Figure 5.9 for ϕ =0;

The pressure distribution and the velocity streamlines within a partially coalescing drop (D = 3.6 mm) for ϕ = 0 are shown in Figure 5.13 at different times. The negative values of the pressure mean that pressure is lower than the reference point. As can be seen, the film rupture creates a vortex ring in the drop which expands outwards in agreement with previous findings (San Lee et al., 2015, Blanchette et al., 2009, Dooley et al., 1997). The vortices have largely reduced pressure in their cores (Jeong and Hussain, 1995), and as a result the area near the meniscus has low pressure at $t = 0.09t_\sigma$, just after the film rupture. As the meniscus expands, the low pressure areas move to the sides (t = 0.80t_σ). The neck expansion provides a larger channel for the liquid in the drop to drain out, while the vertical collapse of the upper part of the drop is resisted by the capillary waves. Thus, a large pressure difference is established between the top and the bottom of the drop with a boundary which is at about the same level as the

deformation of the interface caused by the dominant capillary waves (area A in Figure 5.13). The pressure distribution at this time step ($t = 0.80t_\sigma$) is in good agreement with previous simulation results (Martin and Blanchette, 2015, Ding et al., 2012). It is suggested that the outward expansion of the drop surface is resisted by the low pressure area at the low part of the drop. At a later time, $0.91t_\sigma$, the capillary waves continue to move upwards, as shown by the velocity streamlines, and the drop summit increases in height (as discussed in Section 5.4). At the same time, the liquid at the lower part of the drop flows downwards with large vertical velocity, which maintains the low pressure in that area. The vortices have however, largely dissipated and the cores have higher pressure than at the initial stages. A pressure difference still exists between the top and the bottom of the drop, but the boundary between high and low pressure areas has moved towards the top following the movement of the capillary waves (area B). The liquid cylinder created at $t = 0.99t_\sigma$ has lower pressure at the bottom than the surrounding liquid. This low-pressure area tends to drive the drop surface to converge at this region, while the thinner flow passage increases locally the vertical velocity. Pressure is, therefore, further reduced ($t = 1.08t_\sigma$). The local low pressure reduces the column width even more and leads to pinch off. Afterwards at $t = 1.13t_\sigma$, the area in the center of the bulk phase has lower pressure (because of the large vertical velocities) than the area of vortex ring (area C). This pressure difference causes the vortices to converge at the center.

5.5 Conclusions

This Chapter discusses the results on the partial coalescence of aqueous drops with organic-aqueous interfaces and the effect of surfactants on it. The evolution of the interface shape and the velocity fields inside the drop were investigated with shadowgraphy and with high speed PIV, respectively. A critical Oh_c number is found for the partial coalescence for small *Bo*. When surfactants are introduced into the organic phase, the partial coalescence region in the *Oh-Bo* map is found to reduce. In addition, the drop size ratio, ξ, of the daughter to mother drop size, decreased in the inertio-capillary regime with increasing surfactant concentration. As the daughter drop

is considered to have higher concentration of surfactants on its surface than the mother drop (Martin and Blanchette, 2015), the drop ratio reduces at the later stages of the partial coalescence.

While the rupture of the film, which separates the drop from the interface, occurs close to the central vertical axis when there are no surfactants, in the presence of surfactants, the rupture occurs off-axis. After rupture and at the early stages of coalescence, the inward movement of the liquid in the upper part of the drop creates a liquid cylinder. The strong downward flow of the fluid inside the droplet creates a low-pressure area at the bottom of the liquid cylinder in the subsequent stages. In a system without surfactants, this low pressure aids the pinch-off of a daughter drop and leads to partial coalescence. However, in the presence of surfactants, the liquid cylinder is not symmetric and does not pinch off. It is also found that vortices developing inside the droplet do not have a significant effect on partial coalescence.

Partial coalescence may be affected by the structure of the surfactants. Further studies of the velocity fields during coalescence with different types of surfactants are therefore needed. These should be complemented by investigation of the changes in pressure inside the drop to further elucidate the partial coalescence mechanism. In addition, the distribution of surfactants along the interface during drop coalescence has only been obtained from numerical simulations. Experimental work in this area is therefore needed, which will be discussed in the next Chapter.

Chapter 6

Fluorescence visualization of the surfactant distribution

It can be seen from the previous Chapters that surfactants have significant effects on both the complete and the partial coalescence. The available experimental studies mainly focus on the evolution of the drop shape but do not consider the surfactant distribution which is critical for revealing how surfactants alter the coalescence behaviour. Some numerical studies have been done to show the distribution of surfactants along the interface during coalescence. A number of phenomena are expected to occur, such as: (1) surfactants can accumulate at the film barrier ring area during drop rest (Giribabu and Ghosh, 2007, Yeo et al., 2003, Yeo et al., 2001); (2) the surfactant concentration at the meniscus tip can be higher than that in the rest of the film during the retraction of the meniscus (Chinaud et al., 2016, Martin and Blanchette, 2015); (3) the distribution of surfactants along the drop surface as the drop merges with its bulk homophase is uneven (Martin and Blanchette, 2015). However, the numerical results have not been validated experimentally. As described in Section 3.2, a novel experimental technique, high speed planar laser induced fluorescence, combined with a fluorescent surfactant is used to study the spatiotemporal distribution of surfactants during coalescence. The main results throughout the coalescence phenomenon, namely, film thinning, meniscus rupture, and final drop merging with the homophase are presented in this Chapter[5].

[5] Most of the results presented in this Chapter are included in:
DONG, T., WEHELIYE, W. H. & ANGELI, P. 2019. Laser induced fluorescence studies on the distribution of surfactants during drop/interface coalescence. *Physics of Fluids,* 31**,** 012106.

6.1 Drop rest phenomenon

Previous studies have shown that Marangoni stresses resulting from the uneven distribution of the surfactants along the interface largely affect the film drainage process (Yeo et al., 2003, Giribabu and Ghosh, 2007, Brenner, 2013). However, this phenomenon has not been observed experimentally previously. In this section, the normalized surfactant concentration Γ^* along the interface where the drop contacts the bulk phase for different surface ages T, is shown in Figure 6.1.

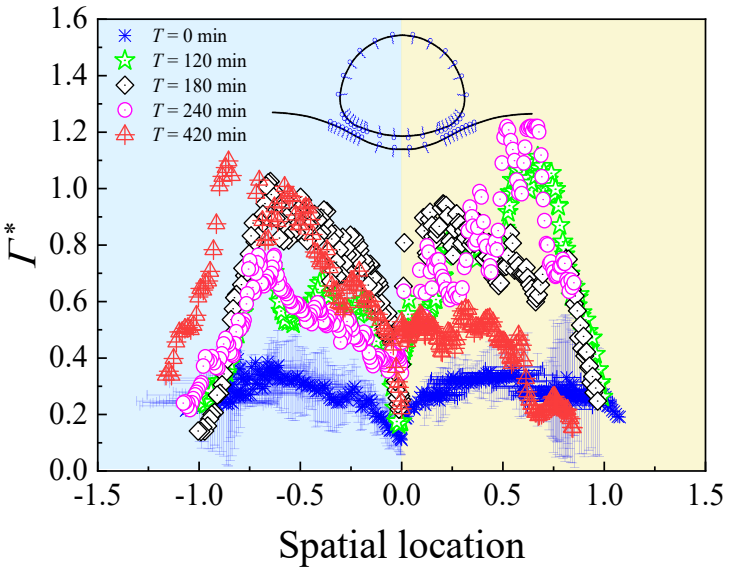

Figure 6.1 Surface concentration of surfactants Γ^* along the interface. The distance, indicating the distance from the center, is normalized by the horizontal drop radius R. The negative values of the distance indicate the area on the left, and the positive values indicate the area on the right from the center.

As described in Section 3.2, T refers to the time from when the drop contacts the surrounding organic phase (or the organic phase contacts the bulk aqueous phase) to the time when the coalescence experiment starts. The surface concentration Γ^* was normalized with the maximum surfactant concentration at the drop surface at T = 900 min, i.e., $\Gamma^* = \Gamma/\Gamma_{max}^{900}$. For consistency, all measurements were taken at the last time step just before the onset of the film rupture. The surfactant concentration Γ^* was averaged over 5 tests for the fresh system with T = 0 min. When the surface is aged to T > 60 min, the drop rest times are long and in some cases can exceed the sampling time of the high-speed camera. Therefore, the results shown for large T are from single representative tests since it was difficult to capture and repeat exactly the coalescence

events. As the thickness of the trapped film between the drop and the bulk liquid is less than a micrometer at the final moments just before film rupture (Morokuma and Utaka, 2016, Langevin, 2015), it is not possible to distinguish the drop surface from the phase interface. Thus, the combined surfactant concentrations from both the drop surface and the interface were evaluated and plotted.

For the fresh system at T = 0 min, the surfactants have little time to adsorb to the interface, and the surface concentration along the interface is much lower than the saturated concentration, as shown in Figure 6.1. During the draining process, the surfactants at the interface are driven outwards by the film liquids. As a result, the surface concentration Γ^* is low at the centre and gradually increases towards the outside until a maximum value is reached at around $0.7 \sim 0.75R$, where R refers to the horizontal drop radius. The area with the highest surfactant concentration is generally considered to be at the barrier ring, where the film is at its thinnest (Yang et al., 2018, Giribabu and Ghosh, 2007, Yeo et al., 2001). Hodgson and Woods (1969) reported that the barrier ring diameter is expanding during the drainage process. In the current experiments where both the drop and the interface are deformable, the radius of the barrier ring, R_b, just before rupture can be estimated from the work of Princen (1963).

$$R_b = 2R^2\sqrt{\frac{\Delta\rho g}{3\sigma}} \tag{6.1}$$

According to Equation (6.1), the radius of the barrier ring for a 5.9 mm drop is around $0.68R$. From Figure 6.1, the radius of the circumference where surfactants accumulate is around $0.7R$. Thus, the radius of the location of the maximum surfactant concentration is found to be close to the barrier ring.

As the surface age T increases, there is more time for the surfactant to adsorb to the interface. The film drainage time also increases after the drop contacts the interface (Giribabu and Ghosh, 2007), and more time is allowed for the fluid in the film to sweep the surfactant molecules toward the barrier ring area. The related maximum surfactant concentration resulting from the accumulation can reach to around $1\Gamma_{max}^{900} \sim 1.2\Gamma_{max}^{900}$ for $T >$ 120 min, which is much larger than that of the centre area. The increase in the surfactant concentration from the centre toward the barrier area is in good agreement

with the theoretical estimations by Burrill and Woods (1973). Interestingly, the maximum surfactant concentration stays at about $1\Gamma_{max}^{900} \sim 1.2\Gamma_{max}^{900}$ and does not increase with the surface age. This is attributed to Marangoni flows. As more surfactants are concentrated on the interface, more molecules are swept outwards during the film drainage; the increased surfactant concentration gradient along the interface can create significant Marangoni surface flows that resist further outward movement of the surfactants. A dynamic balance between the film flow and the Marangoni backflow is established that keeps the surfactant distribution constant.

The distribution of the surfactants is relatively symmetrical on both sides of the interface for T = 0 min, as shown in Figure 6.1. However, at larger surface ages, the distribution is not symmetrical anymore. The asymmetry is reflected in both the concentration of the surfactant along the interface and the location of the area with the highest concentration. For T = 120 min and 240 min, a distinct peak of the surfactant concentration is observed at 0.75R away from the centre on the right, while the interface on the left has a lower surfactant concentration. For T = 420 min, the opposite is observed. For T = 180 min, the peak value of the surfactant concentration is closer to the centre on the right than on the left side. The non-symmetrical distribution of surfactants along the contact interface is mainly attributed to the variations from the irregular draining of the thin film. As discussed by Chan et al. (2011), the film thinning is affected by a number of factors including the initial separation between the drop and the interface, the approaching manner of the drop, the film viscosity, the interface mobility, and the surface tension. Different types of thinning behaviour were observed accordingly (Oldenziel et al., 2012, Hodgson and Woods, 1969), including symmetrical draining, left side faster draining, and right side faster draining.

At the early stages of coalescence just after the drop has contacted the interface, a dimple appears in the film, which drains out subsequently to bring the drop surface close to the interface leading finally to rupture (Chan et al., 2011, Joye et al., 1992, Chen et al., 1984). The structures of the thin film at the initial stages of the drop rest for different surface ages are shown in Figure 6.2. For most tests with the fresh system of T = 0 min, the thickness of the thin film is small and the dimple structure is not obvious.

For some cases at T = 240 min and T = 900 min, a dimple-shaped film with a thinner part at the barrier ring and a thicker part at the centre is observed. As was mentioned before, non-symmetrical dimpled films can appear as well, as shown in Figure 6.2(c) for T = 800 min. As more surfactants are accumulated at the circumference at long surface age T, it has been suggested that the dimple is created by the strong Marangoni backflow which suppresses the outward lubrication flow (Wasan, 1992, Yeo et al., 2001, Bławzdziewicz et al., 1999, Cristini et al., 1998). Ghosh and Juvekar (2002) however, considered that the Marangoni flow decreases only the mobility of the drop surface and is too weak to resist the lubrication flow that drains the film. This explanation seems to agree better with the experimental results here which showed that the film drainage was still fast even for T = 800 min when a significant surfactant concentration gradient along the interface exists.

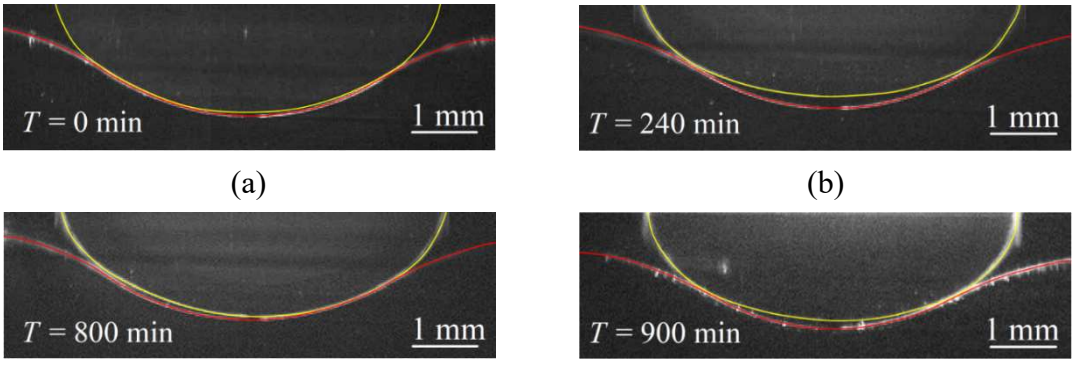

Figure 6.2 Typical structures of the thin film trapped between the drop and the bulk liquid at the initial stages of the rest phenomena for varying surface ages. The drop surface and the phase interface are highlighted with yellow and red lines, respectively, to help visualization.

The film drainage patterns seem to affect the distribution of the surfactants shown in Figure 6.1. For T = 0 min, where the film drains symmetrically, the distribution of surfactants is also symmetrical. As the trapped film and the dimple structure become thicker at large age drop surfaces, the liquid drainage time is increased and loses its symmetry (Figure 6.2(b)~(d)). This will affect the distribution of the surfactants as well and may give rise to instabilities. As a result, it is more likely to observe the non-symmetrical distribution of surfactants for longer age drops.

6.2 Neck growth

When the film rupture occurs, the meniscus (or neck) which links the drop and the bulk phase grows rapidly. It should be noted that in all cases reported here, the rupture points occurred in the laser plane. It was observed from the images that the drop surface folded up if the rupture points occurred out of the view plane. As has been discussed in Chapter 4 and Chapter 5, the rupture locations could be affected by the surfactant concentration. When the surfactant concentration in the bulk is increased close to the critical micelle concentration, the interface can be significantly deformed and the rupture points are shifted further away from the centre point. However, as the surfactant concentration in the bulk used here was 0.001 mol/m^3, which was far less than the critical micelle concentration, the location of the rupture points was not significantly affected. Also, the aging times had negligible effect on the location of the rupture point in this study. Numerically it has been found that the meniscus at the initial stages of retraction has a bulge structure (Weiss and Yarin, 1999, Eggers et al., 1999). As the tip is accelerated by the huge local curvature of the meniscus, its velocity is much higher than that of the liquid in the film which is gradually collected in the growing toroidal body. The findings have been confirmed by many experimental observations in the absence of surfactants (Wang et al., 2016, Kavehpour, 2015, Aryafar and Kavehpour, 2006).

The local structure of the meniscus tip and the surfactant concentration in this region are shown in Figure 6.3 for different surface ages. The coalescence time t in the figure refers to the time after the rupture of the thin film. Due to the instability of the expanding rim, a series of tendrils are created and detached from the rim to form tiny drops (Kavehpour, 2015), shown as bright spots in the images. The bright bulge at the edges of the meniscus cannot be seen for all the surface ages in the viscous regime from t = 1 ms to t = 2 ms because of two main reasons. First, the radius of the initial bulge r_b is theoretically in the order of $r_m^{2/3}$, where r_m is the radius of the neck (Eggers et al., 1999). At the viscous regime, the neck radius r_m is very small, and the related bulge cannot be seen accordingly. Second, the interfacial tension is largely reduced when

surfactants are present and the meniscus retracts at a lower speed than in the surfactant-free system. When the neck growth advances in the inertial regime from t = 4 ms to t = 9 ms, the bulge size increases in varying degrees for different surface age T. For T = 0 min, the bulge is small, while it becomes larger when the drop surface has aged to T = 240 min and 300 min, as shown in Figure 6.3. For an aged surface with large T, dimple structures form at the film; a large amount of the fluids is collected there which increases the size of the bulge as the meniscus advances through this thick part of the film.

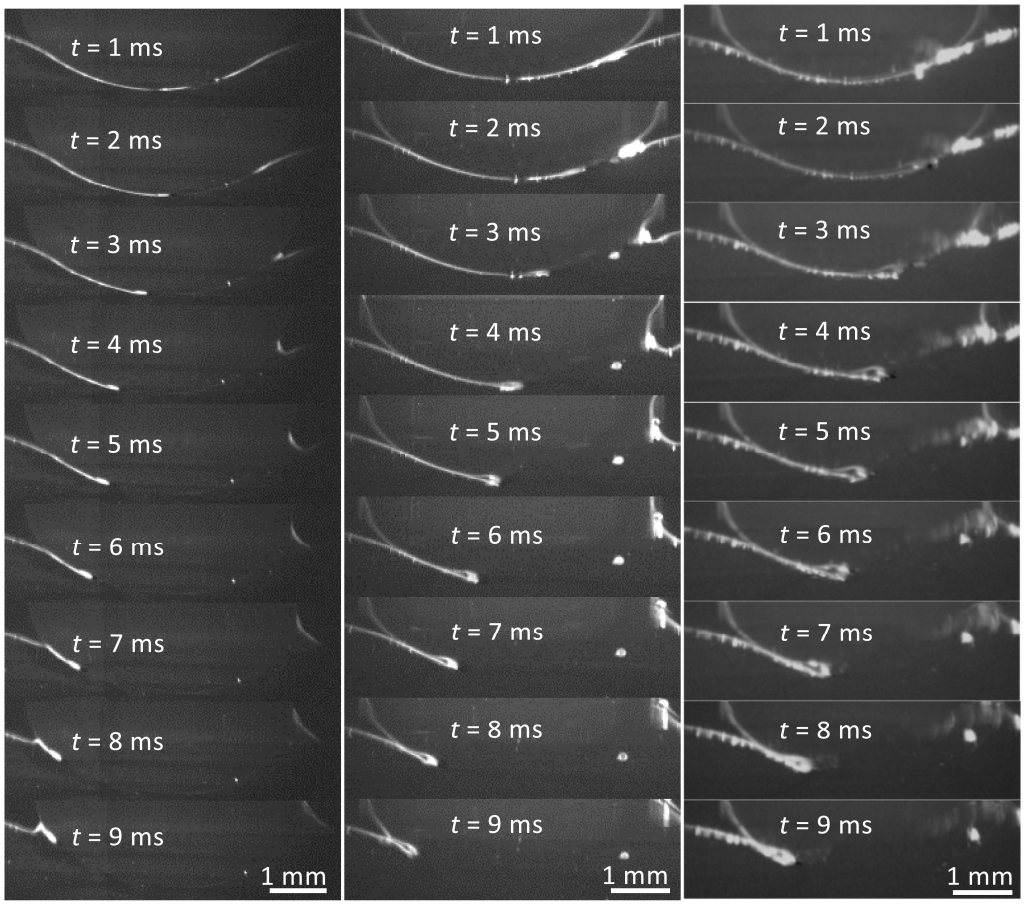

Figure 6.3 Evolution of the local structure at the neck tip for different surface ages: (a) T = 0 min, (b) T = 240 min, and (c) T = 300 min.

The distribution of the surfactant concentration along the interface for the surface age of T = 0 min is shown in Figure 6.4 as a representative example. Only the left tip which travels over a longer distance is plotted. When the film rupture happens, the rapid retraction of the tip reduces the interfacial area. In addition, there is not enough time

for the surfactants to diffuse or desorb from the interface. Thus, the surfactants are accumulated at the tip and increase the local concentration.

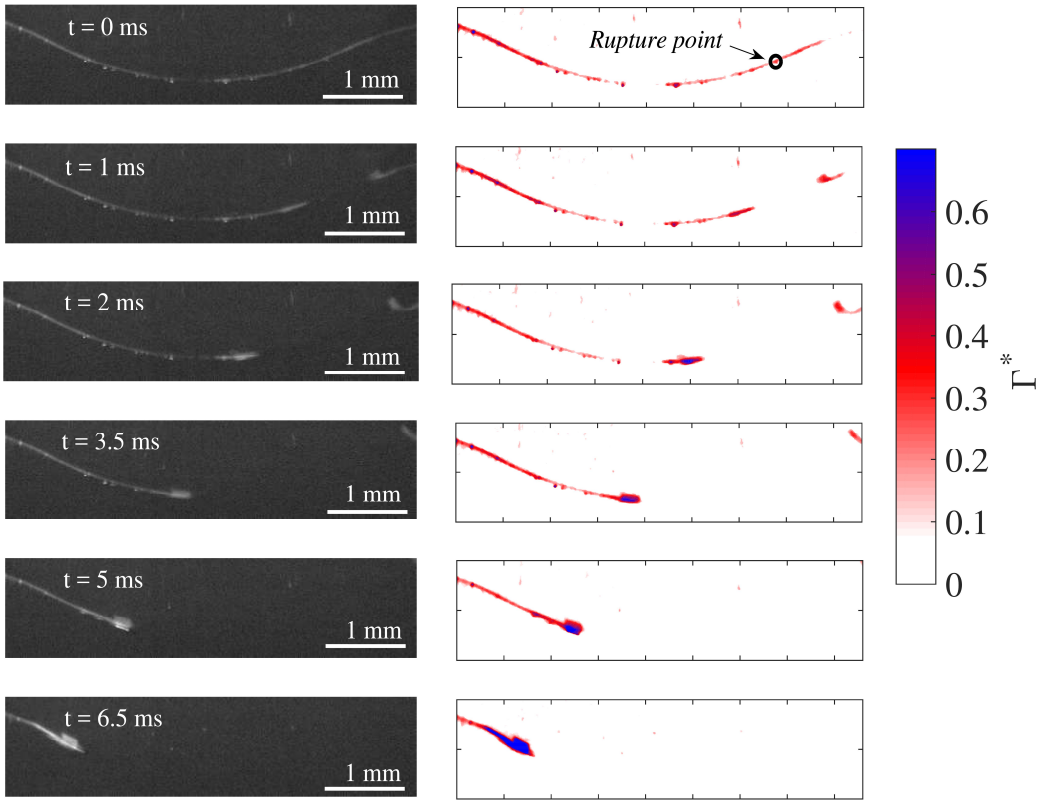

Figure 6.4 The distribution of surfactant concentration Γ^* at the tip area during the neck growth for $T = 0$ min.

To quantitatively investigate the accumulation of the surfactants at the neck tip, the space averaged surfactant concentration Γ^*_{tip} at the tip area is calculated according to Equation (6.2):

$$\Gamma^*_{tip} = \frac{\int \Gamma^* \, dA}{A_{tip}} \tag{6.2}$$

The area of the tip A_{tip} is found from subtraction of two consecutive images. For consistency, only the side of the neck that travels longer is considered for all the cases. The evolution of the surfactant concentration at the tip area is plotted in Figure 6.5 for different surfactant ages. The data are averaged over 5 tests for surface ages $T = 0$ min and 60 min, while for $T = 240$ min and 420 min, only representative data are plotted from one test. The accuracy in determining the onset of the rupture is 0.5 ms for all the tests as the frame rate of the high-speed camera is 2000 fps.

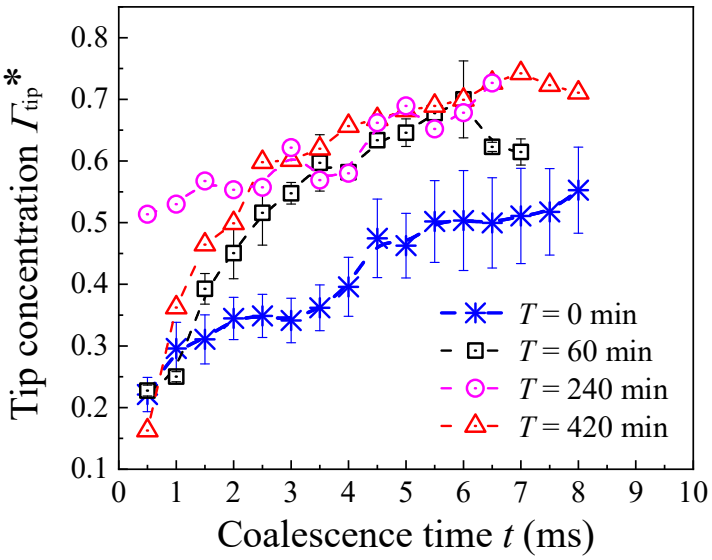

Figure 6.5 Surfactant concentration at the tip of the neck for coalescences under different surface ages.

For T = 0 min, the increase in the tip concentration is small compared to the other three cases, which is mainly due to the fewer surfactant molecules present at the interface. As Figure 6.1 shows, the initial surfactant concentration at the phase interface is much lower for T = 0 min than for the other cases. The retraction of the tip in this case does not accumulate enough surfactant molecules. In addition, the neck tip moves faster for T = 0 min than for the other ages (see Figure 6.5), and the area A_{tip} is relatively larger. For T = 60 min, a large increase in the tip concentration can be seen as more surfactants are initially packed on the interface. For drop ages above 60 min, the increase in the tip concentration is not as high as would be expected and remains similar to that for T = 60 min. This is mainly attributed to a similar surfactant distribution along the interface for larger surface ages during the drop rest before the film rupture (see Figure 6.1). In addition, as is shown in Figure 6.6, the travel speeds of the tips for surface ages above 60 min are close. As a result, the changes in the tip concentration for cases above 60 min do not vary a lot.

A different behaviour is observed for T = 240 min where the surfactant concentration becomes very high in the initial stages of the neck growth. This could be attributed to the initial uneven distribution of the surfactants along the interface before the rupture of the thin film. For T = 240 min, a large amount of surfactants is swept to the circumference to produce a high surfactant concentration on the right side, as shown

in Figure 6.1. When rupture occurs, a large amount of surfactant molecules has already been packed at the tip which gives the high tip concentration at the initial stages.

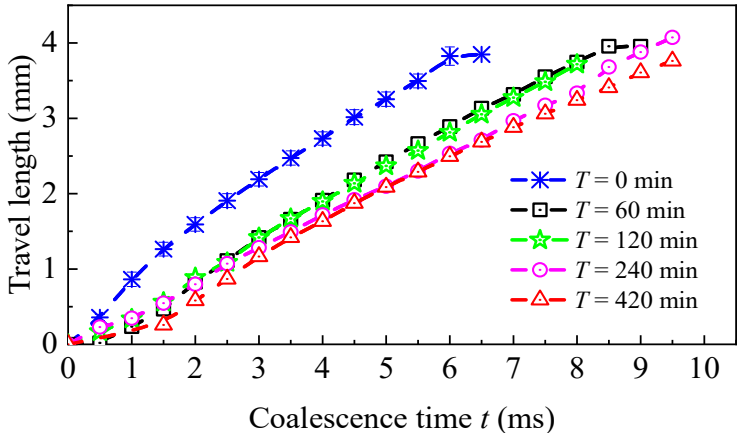

Figure 6.6 Travel distance of the neck tip versus coalescence time for various drop surface ages. The travel length is defined as the distance of the tip away from its original location.

6.3 Distribution of surfactants along the drop surface

When surfactants are present, the reduction in the drop surface as it merges with the continuous bulk phase at the final stages of coalescence becomes slow and partial coalescence can be prevented (Weheliye et al., 2017, Dong et al., 2017). This is attributed to the uneven distribution of surfactants on the drop surface (Martin and Blanchette, 2015). The surfactant concentration along the coalescing surfaces is discussed in this section.

The concentration of surfactants along the surface of a coalescing drop for T = 720 min is shown in Figure 6.7 as a representative example. The initial neck growth process was discussed in Section 6.2, and the results are shown here for the later stages of the drop merging with the bulk liquid. Previous studies including the results in Chapter 5 have shown that a liquid cylinder forms in the later stages of coalescence (Chen et al., 2006, Ray et al., 2010, Yue et al., 2006, Blanchette and Bigioni, 2006). From t = 20 ms to t = 36 ms, the top of the drop surface is stretched upwards by the convergence of the capillary waves initially formed after the meniscus rupture (Blanchette et al., 2009, Gilet et al., 2007). The surfactant concentration at the sides of the drop is higher compared to the top of the drop. The interface with the lower surfactant concentration on the top of the drop tends to pull the interface with the higher concentration at the

bottom due to tangential Marangoni stresses (Blanchette et al., 2009, Nowak et al., 2016, Nowak et al., 2017, van Capelleveen et al., 2017), as the arrows show in Figure 6.7(a). On the other hand, the area at the phase interface away from the neck also has a low surfactant concentration and the resulting Marangoni stress drives the spreading of the surfactant along the phase interface away from the drop, as the arrows show in Figure 6.7(b). At $t = 39.5$ ms when the liquid cylinder is created, the area with a high surfactant concentration is close to the summit of the drop. The distribution of surfactants agrees with the numerical findings by Martin and Blanchette (2015). Afterwards, the drop surface shrinks significantly until the liquid cylinder is about to pinch off at $t = 45.5$ ms. The average surfactant concentration in the drop increases because of the reduction in the area, especially at the top. As the Marangoni forces resist the convergence of the neck as the arrows show in Figure 6.7(d), partial coalescence does not occur in this case (Martin and Blanchette, 2015). In addition, it shows clearly that the daughter droplet tends to have higher surfactants concentration on its surface if the pinch-off occurs at t=45.5ms. Accordingly, the drop ratio at the later stage of the partial coalescence cascade tends to be lower than the former one, as discussed in Section 5.2.

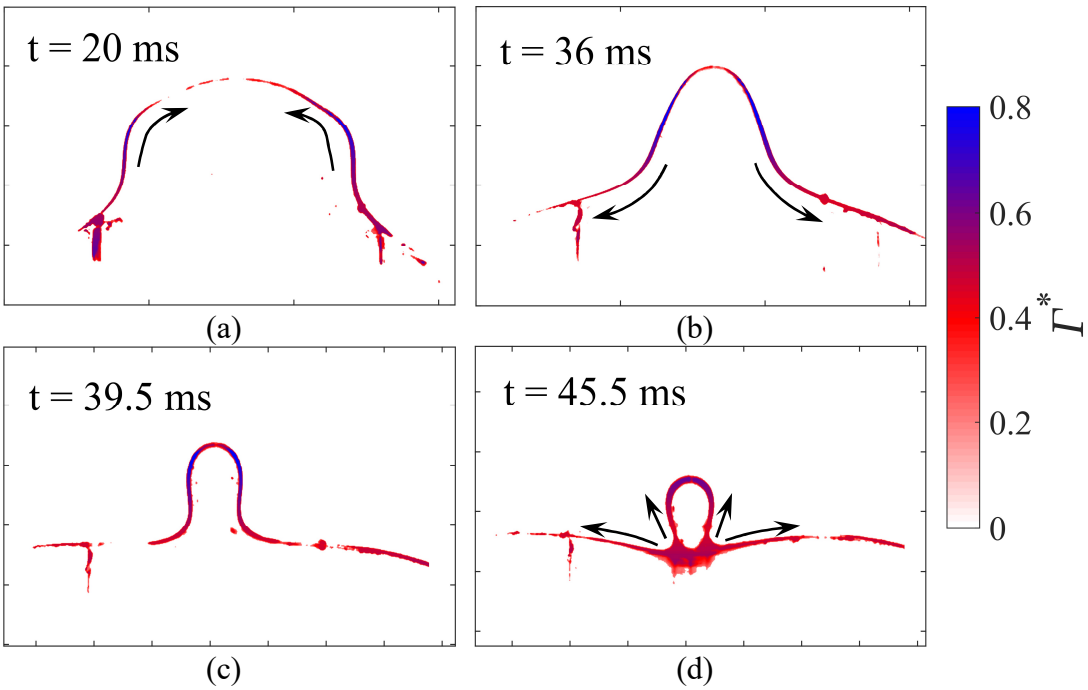

Figure 6.7 Surfactant concentration Γ^* along the coalescing drop surface for $T = 720$ min. The arrows indicate the direction of Marangoni stress.

To study the effect of surface age on the distribution of surfactants during the merging process, the surfactant concentration along the evolving surfaces was calculated at different T, as shown in Figure 6.8. The figures on the right represent the corresponding evolution of the drop surface during coalescence. The profile of the drop surface is found by detecting the boundary between the bright drop that has surfactant and the dark area in the surrounding liquid. As shown in the inset in Figure 6.8(b), the surfactant concentration Γ^* along the arc was extracted following the method described in Section 3.2. The arc length L, which was normalized by the horizontal diameter of the drop D, started at the drop summit O and terminated at the phase interface. The open points in the figure refer to the location of the neck edge. The locations with the highest surfactant concentration are denoted with the filled (red) points.

For $T = 0$ min, the peak of the surfactant concentration at $t = 6.5$ ms from the film rupture is observed at the bottom near the neck (corresponding arc length $L = 0.95D$), while the surfactant concentration is very low at the drop surface above the neck. This forms a boundary between the drop surface and the phase interphase, as plotted by the dashed line in Figure 6.8(a). During the drop merging, the boundary may shift and not be so clear anymore; for this reason, only the boundary at the initial stage is plotted here to help visualization. From $t = 20.0$ ms to $t = 32.0$ ms, the drop surface is largely shrinking except from the top area which is being stretched by the capillary waves to create the liquid cylinder (Figure 6.8(b)). Over this process, the surfactant concentration at the drop sides above the neck is increased. After $t = 32.0$ ms, the top area of the drop stops expanding and starts to contract. Thus the surface concentration Γ^* at the top with $L < 0.2D$ increases between $t = 32.0$ ms and $t = 36.5$ ms.

The peak value of Γ^* does not change too much at the bottom of the drop for $L > 0.7D$. At the early stages of coalescence, the peak concentration value slightly reduces from $t = 6.5$ ms to $t = 25.0$ ms but increases afterwards between $t = 25.0$ ms and $t = 36.5$ ms. This behaviour was shown as well by Martin and Blanchette (2015) through simulation. The local variation of the surfactant concentration over the drop surface is controlled by two factors, the changes in the local surface area and the Marangoni forces

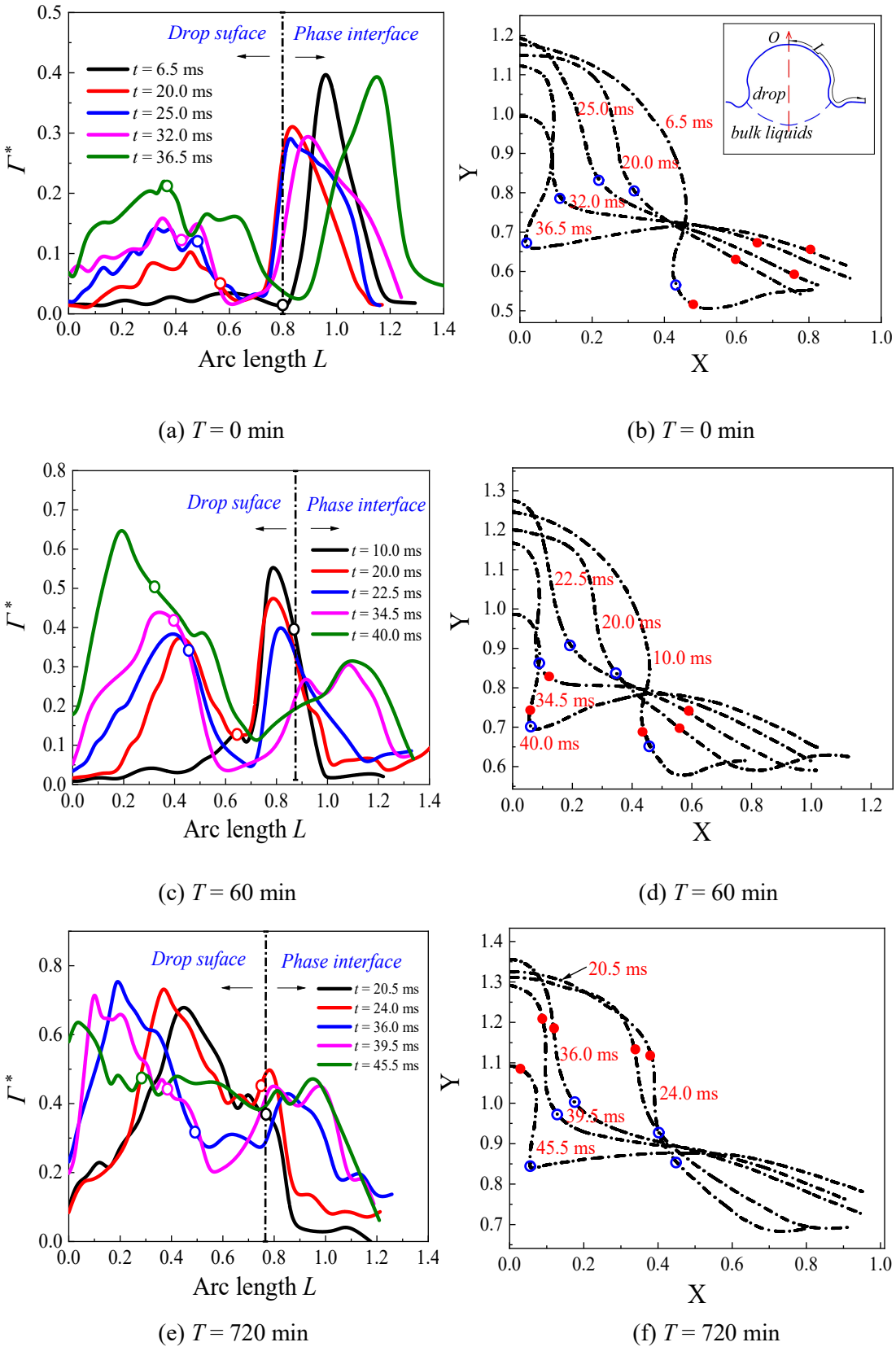

(a) $T = 0$ min (b) $T = 0$ min

(c) $T = 60$ min (d) $T = 60$ min

(e) $T = 720$ min (f) $T = 720$ min

Figure 6.8 Surfactant distributions along the deforming surfaces and the related evolution of the drop surface. The hollow circles in the figure indicate the positions of the neck edges, while the full (red) dots indicate the positions with the maximum surfactant concentration.

along the drop surface. The Marangoni stresses tend to smooth out the uneven of surfactant molecules along the interface, which is reflected in the decrease in the concentration peak from t = 6.5 ms to t = 25.0 ms. The contraction of the local surface area where the peak is located, on the other hand, may increase the concentration, which is seen from t = 25.0 ms to t = 36.5 ms. The concentration peak is located initially close to the neck edge (t = 6.5 ms) and then shifts away toward the phase interface, as shown in (Figure 6.8(b)). As the global surfactant concentration gradually increases along the drop surface due to the surface contraction at $L < 0.7D$, the corresponding surface tension is lower than that of the phase interface on the right side of the peak. The resulting Marangoni stress between the peak and the drop surface is, therefore, weaker than that between the peak and the phase interface on the right side. In addition, the propagation of the waves that was initially created by the receding neck tends to shift the peak location outwards along the interface (Fallest et al., 2010, Swanson et al., 2015). Therefore, the peak location gradually shifts away from the neck edge.

As the surface tension decreases when the drop surface is aged to T = 60 min, the evolution of the drop surface during coalescence is slower than at T = 0 min, as shown in Figure 6.8(d). In addition, the increase in the surfactant concentration on the drop surface, resulting from the surface contraction, is significant. This large increase in the concentration decreases the Marangoni forces acting on the left side of the peak concentration (filled red dot) and increases the importance of the Marangoni forces between the peak location and the phase interface on the right. As a result, the concentration peak is slightly smoothened out forming plateaus towards the phase interface between t = 10.0 ms and t = 40.0 ms. Similar to T = 0 min, the location of the peak is on the phase interface and shifts away from the neck from t = 10.0 ms to t = 22.5 ms. However, from t = 34.5 ms, the concentration increases significantly at the drop and the peak is now found close to the neck again. At T = 720 min, the surfactant concentration on the drop surface is high. Thus, the increase in surfactant concentration caused by the drop contraction is larger at $L < 0.7D$ compared to both T = 0 min and T = 60 min. The peak location appears directly at the drop surface and on the left of the neck edge, in contrast to T = 0 min and T = 60 min where the concentration peaks

appeared at the phase interface.

6.4 Conclusions

This Chapter presents in detail the PLIF experimental results on the local surfactant concentration along the interfaces during the drop/interface coalescence. When the drop rests on the interface, the surfactants are found to accumulate at a barrier ring and increase locally the concentration in the film. These findings for the first time verify previous theoretical predictions (Giribabu and Ghosh, 2007, Yeo et al., 2003, Burrill and Woods, 1973). The surfactant concentration at the ring increases as the interface age increases (higher initial surfactant concentration at the interfaces).

During the neck expansion after the rupture of the film, a bulge forms at the tip of the neck where the surfactant concentration is high compared to the rest of the area of the film. This confirms previous numerical findings and assumptions (Chinaud et al., 2016, Martin and Blanchette, 2015). The surfactant concentration at the tip area is not constant but increases during the neck growth, which is more significant when the initial surfactant concentration at the interface is higher.

After the film has retracted, a peak in the surfactant concentration is observed at the meniscus at the bottom of the drop; the peak is smoothened by the action of Marangoni forces along the interface. In these final stages of coalescence, a liquid cylinder is formed as the drop surface is stretched upwards by capillary waves. The top of the cylinder has a low surfactant concentration. Gradually the concentration in the cylinder is increased as the cylinder shrinks from the combined action of the reduction in the interfacial area and upward Marangoni forces.

Chapter 7

Delayed coalescence of drops at moving interfaces

In this Chapter, the experimental investigations on the drops surfing on moving liquid/liquid interfaces are presented. As noted in Chapter 2, the surfing and the delayed coalescence of drops had only been investigated on liquid interfaces with air in the previous studies. In many applications, however, drops coalesce with liquid-liquid interfaces, and their surfing has not been studied. For the investigations, a novel flow channel was designed which allowed an oil-water interface to move at different speeds as an aqueous drop was released on it. High-speed Planar Laser Induced Fluorescence (PLIF) and Particle Image Velocimetry (PIV) are used to obtain the shapes of the drop and the interface, the shape and thickness of the film trapped between the drop and the interface and the velocities of the drop surface and the interface bounding the film. The rest times of the drop on the interfaces are measured and the mechanism of delayed coalescence is discussed based on the lubrication pressure in the film and its dependence on the film shape and on the velocities of the drop bottom surface and of the interface. The changes of the drop shape at the initial stages of drop impact and rebound on the interface, as well as the acceleration of the drop immediately after the impact with the interface are analysed. Lastly, new observations on the shape of the ruptured film and on entrainment of oil in the water phase are presented.

7.1 Delayed coalescence and lubrication model

In this section, the results on the drop rest times are presented, while the phenomena that lead to the change in the drop rest times at interfaces with different velocity are discussed based on the lubrication theory. The experiments showed that drop

coalescence is significantly delayed when the oil-water interface is moving. Figure 7.1 shows the probability distribution of the drop rest times at interfaces of different speed. When the interface is stationary, most of the drops break in less than 10 s with a peak coalescence time at around 4 s. When the interface is moving, however, an increase of the drop rest time is observed. At interface speed of v = 0.4 cm/s, the drop rest time presents an almost normal distribution while no drop was found to coalescence in less than 10 s. Compared to the distribution with stationary interfaces, the peak shifts to around 20 s. When the speed of the interface reaches v = 1.0 cm/s, the distribution of the drop rest time becomes wider than the former two at v = 0 and v = 0.4 cm/s; some of the drops survive until 60 s, while a few breaks in less than 10 s. At v = 1.3 cm/s, the rest time shows a multimodal distribution, with three peak values located at various times. Despite this, however, the rest time is largely increased compared to that of v = 1.0 cm/s. For many of the drops at v = 1.3 cm/s, coalescence does not happen within the channel. As these cases are not included, a sharp decrease is seen after the peak.

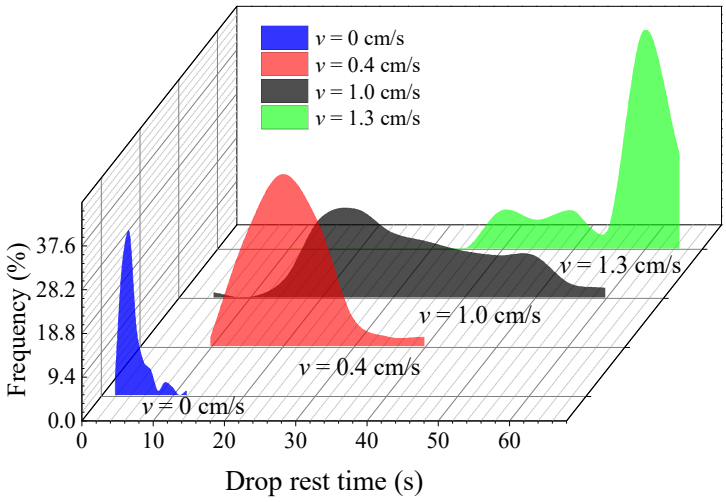

Figure 7.1 Probability distribution of drop rest time at the liquid-liquid interfaces with different speed.

Coalescence of drops with liquid/liquid interfaces is complex and can be affected by many factors (Chan et al., 2011), which explain the deviations of the rest time distributions from the normal one. Figure 7.1 clearly shows that coalescence is significantly delayed when the interface speed is increased. This is attributed to the

lubrication pressure that develops in the film between the drop and the interface which resists the settling of the drop (Hamrock et al., 2004). In the current experiments, the Reynolds number of the draining film is lower than 1, and the inertial term in the Navier-Stokes equations can be considered negligible (Sawaguchi et al., 2019, Nakayama, 2018, Geri et al., 2017) . The corresponding 2-dimensional momentum equation for the lubrication film is then reduced to:

$$\frac{\partial \mathrm{p}}{\partial \mathrm{x}} = \mu \frac{\partial^2 \mathrm{u}}{\partial \mathrm{z}^2} \tag{7.1}$$

By integrating Equation (7.1) with the boundary conditions $z = 0$, $u = u_b$ at the bulk interface and $z = h$, $u = u_d$ at the drop surface, the velocity in the film is equal to:

$$u = -\mathrm{z}\left(\frac{z-h}{2\mu}\right)\frac{\partial p}{\partial x} + u_b\left(\frac{h-z}{h}\right) + u_d\frac{z}{h} \tag{7.2}$$

where u_d and u_b are, respectively, the velocity along the drop surface and along the interface in the film region, while h is the film thickness. According to the continuity equation, the local variation of the film thickness resulting from the mass flow can be written as:

$$-\frac{\partial \rho Q_X}{\partial x} = \frac{\mathrm{d}}{\mathrm{dt}}(\rho h) \tag{7.3}$$

where Q_x is the volume flow rate per unit width $Q_X = \int_0^h u dz$. In the current experiments, the film liquid is incompressible and the density ρ is constant. Assuming that the bulk interface is flat, the right side of Equation (7.3) can be written as:

$$\frac{\partial h}{\partial t} = (w_d - w_b) - \frac{\partial h}{\partial x}u_d \tag{7.4}$$

where w_d is the vertical velocity of the drop surface approaching the interface, w_b is the vertical velocity of the interface and the positive direction is taken upwards. In Equation (7.4), the first term on the righthand side (w_d-w_b) refers to the thickness decrease caused by the approaching of the two surfaces, the second term refers to the change of the thickness caused by the horizontal motion of the drop surface along the x direction. See (Hamrock et al., 2004) for more details. By substituting Equation (7.4) into Equation (7.3), the pressure distribution in the film is:

$$\frac{\partial}{\partial x}\left(\frac{h^3}{12\mu}\frac{\partial p}{\partial x}\right)=\frac{\partial}{\partial x}\left(\frac{h(u_d+u_b)}{2}\right)+(w_d-w_b)-u_d\frac{\partial h}{\partial x} \qquad (7.5)$$

According to Equation (7.5), the lubrication pressure in the film can be generated by (i) the variation of film thickness, (ii) the drop surface and the interface velocity along the flow direction, and (iii) the approaching speed of the two interfaces. For the coalescence at a stationary interface, the tangential velocities along the drop surface and the interface u_d, u_b are zero. Without considering the film thickness variation (this is not the case at the very beginning of film drainage, while at the later stages, the film variation in the film region is quite small), only the second term on the right side of Equation (7.5) contributes to the pressure. As (w_d-w_b) reduces quickly in the current experiments, the resulting lubrication pressure is not able to resist coalescence for a long time. Therefore, the drop coalesces with the bulk interface fast. When the interface is moving, the other two terms on the right-hand side come into effect and increase the lubrication pressure, thus delaying coalescence. The dynamics of lubrication flow and the resulting distribution of pressure for a drop resting on a moving interface will be analysed in detail in Section 7.3.

7.2 General Observations

7.2.1 Drop deformation during initial impact with the interface

After their release from the nozzle, the drops initially impact on the interface and rebound. Figure 7.2(a) shows the changes in the drop and interface shape during the impact and rebound period. The drop shape is characterized by the ratio of the horizontal to the vertical diameter, D_h/D_v. As it can be seen, the changes in the drop shape are similar for all interface velocities. A typical case is presented in Figure 7.2 (b) and Figure 7.2 (c) for an interface of v = 3.4 cm/s.

At the initial impact period between t = 0 ms (when the drop starts to press against the interface) to around t = 30 ms, there is large resistance to the downward movement to the bottom of the drop from the interface, while the top of the drop still moves downwards from the effect of gravity. As a result, the drop extends horizontally at around t = 25 ms to a maximum D_h/D_v of about 1.7. This is followed by the contraction

of the drop and a reduction in D_h/D_v, driven by surface tension. The energy released from the drop contraction and the effect of gravity cause the drop to further descend until the interface reached a minimum height at $t = 50$ ms. As is shown in Figure 7.2(b), during the drop contraction from $t = 26$ ms to $t = 46$ ms, the height of the bottom surface of the drop decreases while the height of the upper surface of the drop slightly increases. The Laplace force from the deformed interface starts to push the drop upwards. This causes the drop to deform again and extend horizontally. However, the increase of the diameter ratio D_h/D_v and the drop deformation is far less than the one in the impact period, as can also be seen when the drop shapes in Figure 7.2(c) are compared against those in Figure 7.2(b).

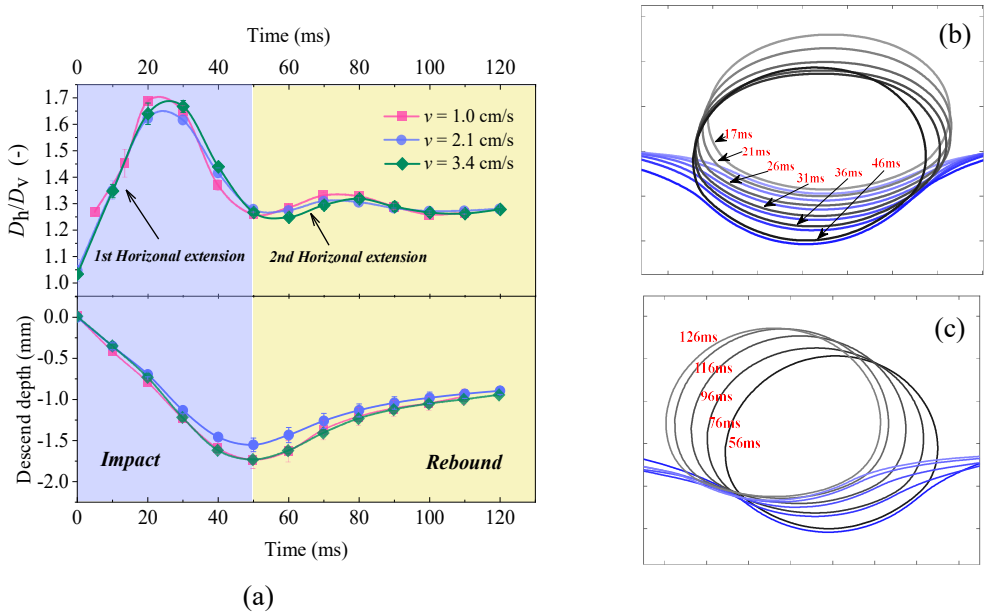

Figure 7.2 (a) Variation of the drop deformation characterized by the diameter ratio D_h/D_v and the descend depth of the drop bottom from its initial position at $t = 0$ ms, when the drop contacts the interface.; and the impact (b) and the rebound (c) of a single drop at the fluid interface of $v = 3.4$ cm/s;

7.2.2 Drop movement

The velocity of a drop surfing along the moving interface is measured from the images by tracking the displacement of the drop central point in the horizontal x direction. As can be seen in Figure 7.3(a), the drop speed increases fast initially during the impact and the rebound period (shaded area) for all interface velocity cases. This

fast increase is shown more clearly in Figure 7.3(b). For the cases of low velocity (v = 1.0 cm/s), the drops reach almost the velocity of the interface at the end of this period. For the faster interfaces, the drop speed continues to increase after the initial period but at a low rate until it reaches the velocity of the interface. The acceleration of the drops is believed to be caused by the drag force from the surrounding liquid both in the film region and in the outside area. A rough estimate, however, reveals that the drag force alone is not able to give this acceleration to the drop (See Appendix C). Possibly, the uneven distribution of the force acting normally on the drop surface due to lubrication pressure in the film generates a horizontal force component that contributes to the drop acceleration.

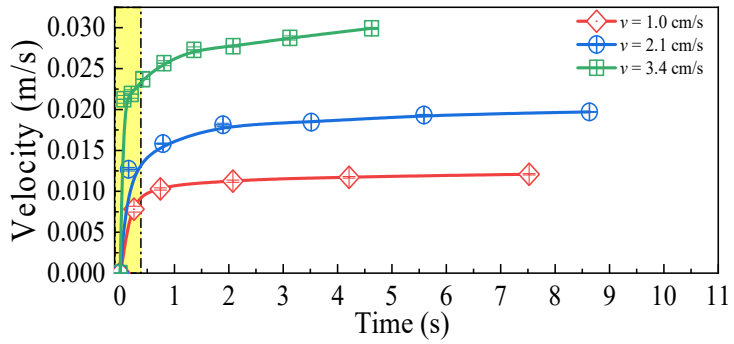

(a)

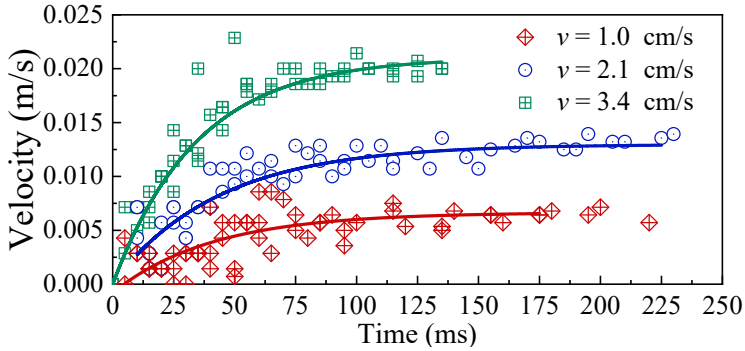

(b)

Figure 7.3 Change of drop velocity with time (a) over the whole measuring period, and (b) during the initially impact and rebound period. The velocity values in the legend are determined by tracking the motion of the drops at the final stage when the velocity is same as that of the interface.

7.2.3 Film thickness

The evolution of the film structure during the drop impact and rebound periods is discussed here. A typical PLIF image showing the shape of the film trapped between

the drop and the oil-water interface is presented in Figure 7.4(a). The fluorescent intensity along the vertical dotted line in the image is shown in Figure 7.4(b). As can be seen, the light intensity is significantly reduced across the film region. The film thickness is calculated by measuring the distance between the two z-points with maximum light gradient as proposed by Oldenziel et al. (2012).

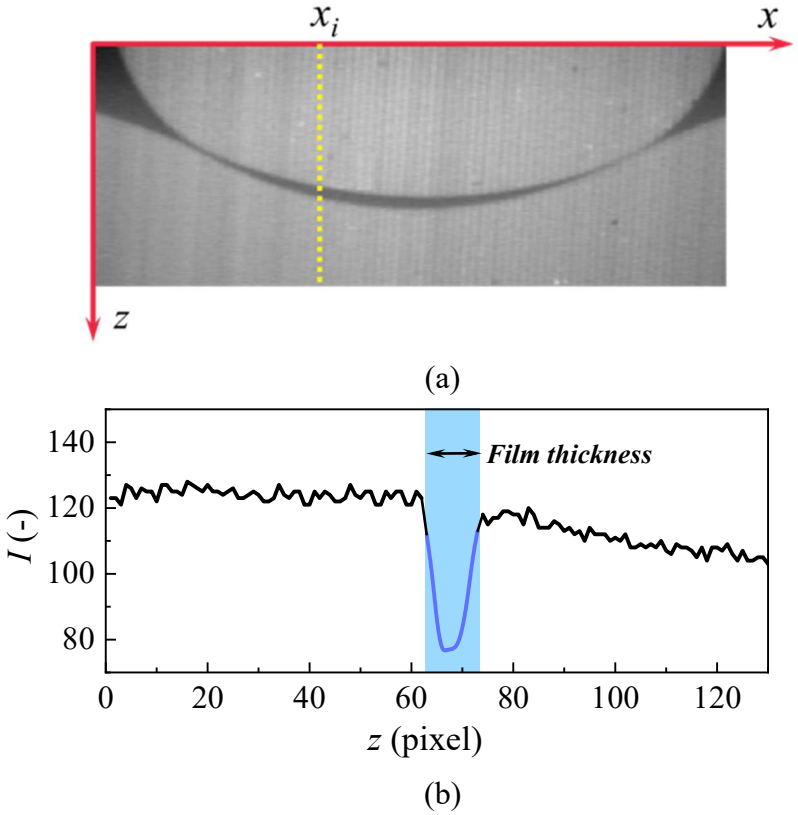

Figure 7.4 (a) Raw PLIF image showing the film shape; (b) the variation of the light intensity along the vertical dashed (yellow) line in Figure (a).

For interface speed equal to v = 1 cm/s, a decrease of the film thickness along the flow direction is observed when the drop approaches the interface (see Figure 7.5(a) from t = 8 ms to t = 13 ms). As the phase interface at this time is not deformed significantly, the structure of the film is similar to the cases of a drop resting on a thin air film (Sawaguchi et al., 2019, Gauthier et al., 2016, Lhuissier et al., 2013). From t = 13 ms to t = 23 ms, the film thickness continues to decrease. At this stage, the film has a dimple shape with a thicker area at the centre and a thinner area at the border, which is commonly seen in the coalescence of drops with stationary interfaces (Klaseboer et al., 2000). According to Equation (7.5) while the drop is approaching the interface, the tangential velocity of the interface is low, and the velocity difference (w_d-w_b) is the

dominant term in the calculation of the film lubrication pressure. It has been shown that the lubrication pressure resulting from a drop approaching a flat interface has an approximately concave shape with a peak near the centre (Yiantsios and Davis, 1990). The film, therefore thins slower at the centre than at the border and acquires a dimpled shape.

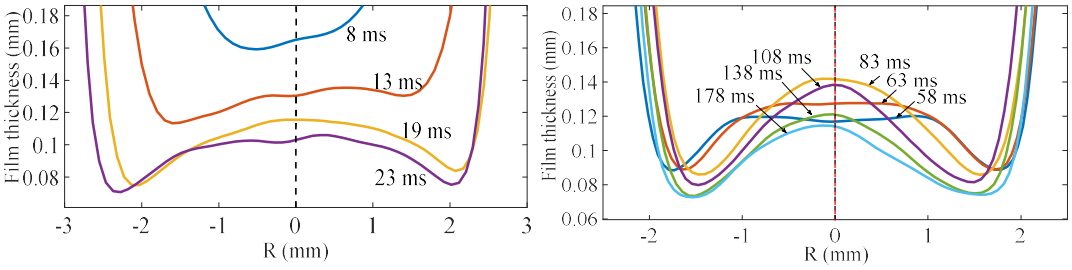

(a) v = 1.0 cm/s

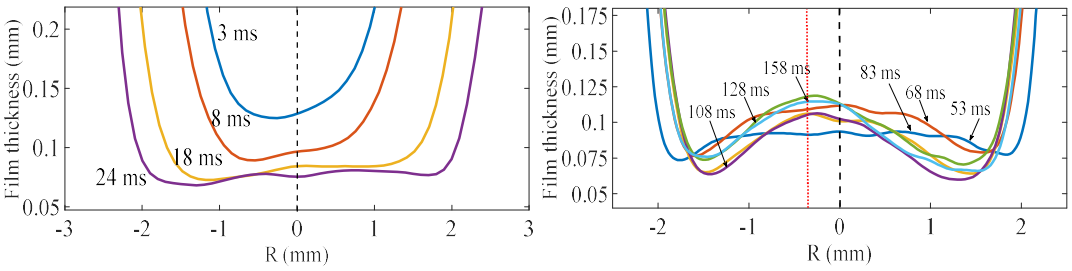

(b) v =2.1 cm/s

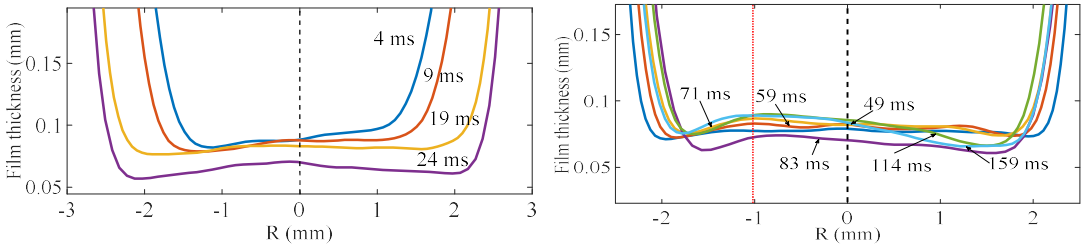

(c) v = 3.4 cm/s

Figure 7.5 The variation of the film thickness during drop impact and rebound at (a) v = 1.0 cm/s (b) v = 2.1 cm/s and (c) v = 3.4 cm/s. The dotted (red) lines represent the locations with the maximum film thicknesses at the last time step of the measurement.

During the drop rebound period, after t = 58 ms, the film thickness should continue to decrease as the liquid in the film is still draining. However, the central part of the film seems to refill and form a peak from t = 58 ms to t = 83 ms, as shown in Figure 7.5(a). It is believed, that it is not only the uneven distribution of the pressure in the film that causes the formation of the peak but also the horizontal shrinkage of the film. Figure 7.6(a) illustrates the change of the horizontal locations of the minimum film thickness

points over time. The distance between the two points, regarded as the film width, is shown in Figure 7.6(b). For interface speed of v = 1.0 cm/s, the film has expanded to a maximum width at around t = 30 ms, after which the width starts to decrease until a minimum value is reached at t = 100 ms. This horizontal film contraction is believed to accumulate the liquid in the centre and generate the peak. As the width of the film slightly increases after 100 ms (Figure 7.6(b)), the refill of the film stops and the film continues to thin while preserving its dimpled shape. The effect of the interface speed is low for this case, and the peak of the film thickness is located at the centre.

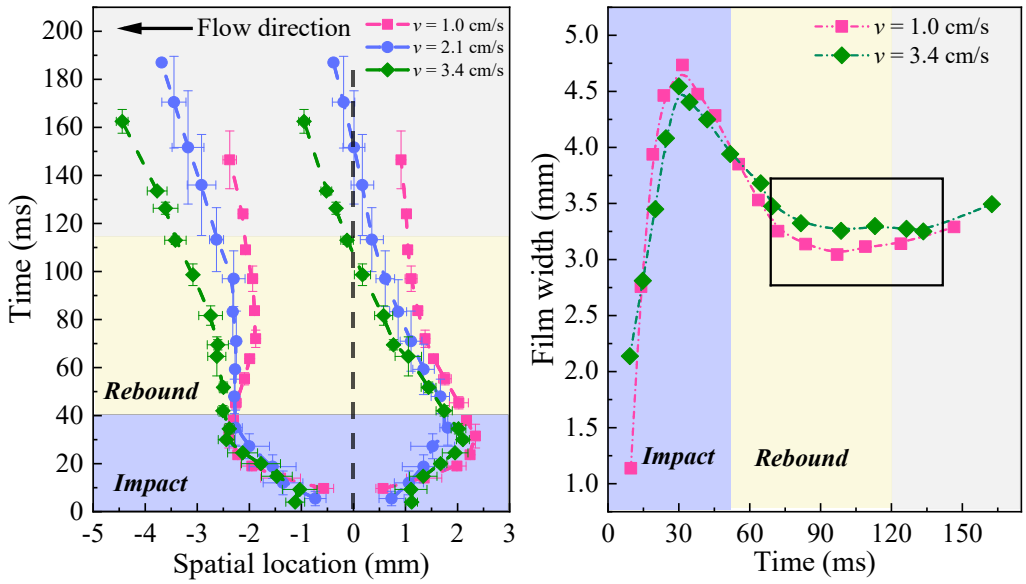

(a) (b)

Figure 7.6 (a) Variation of the horizontal locations of the minimum film thickness against the time t. The initial values were taken at 5ms after the drop contacts the bulk interface (b) evolution of the film width; only the cases v = 1.0 cm/s and v = 3.4 cm/s are shown to help visualization.

For the higher interface speed of v = 2.1 cm/s, the tangential velocity along the interface is also contributing to the lubrication pressure in addition to the drop approaching velocity. As will be discussed in Section 7.3, the pressure tends to be uniformly distributed in the film in this case and the dimpled structure is not as obvious as in v =1 cm/s, as shown in Figure 7.5(b) during the drop impact from t = 3 ms to t = 24 ms. During the drop rebound, the film also refills and a peak is formed. At t = 53 ms, the film forms a plateau around the centre line. Between t = 53 ms and t = 100 ms (see Figure 7.6(a)) the thin part of the film upstream moves faster than the one downstream.

As a result, the film peak is slightly shifted downstream. When the interface speed increases to v = 3.4 cm/s, the interface velocity contribution to the lubrication pressure is further increased and the dimple structure is less obvious. During the rebound, the film width does not contract as much as in the lower interface velocities (Figure 7.5(c)) and the refill is not obvious. In addition, the peak is shifted further away from the centre compared to v = 2.1 cm/s.

7.2.4 Drop inner circulation

The velocity of the liquid inside the drop was measured with PIV. This is shown for a moving interface of v = 2.1 cm/s in Figure 7.7. To observe the circulation patterns and isolate the circulation from the horizontal motion of the drop, the horizontal translational speed of the mass centre of the drop was subtracted from the local velocity. During the initial impact and rebound period, no circulation is seen as the drop undergoes a large deformation. Shortly after, recirculation appears in the drop, as shown in Figure 7.7 (a). At this time, the drop rotates like a rigid body with the rotation centre coinciding with the centre of mass, which is similar to what was previously observed for drops resting at hydraulic film jump (Sreenivas et al., 1999) and on a steady air film (Sawaguchi et al., 2019). But unlike those cases, as the drop accelerates to the velocity of the interface, the inner circulation decays.

When the drop travels to L = 0.5 cm away from the impact point, the velocity at the lower part of the drop becomes comparable to that in the bulk interface. The shear force acting on the bottom surface of the drop decreases. On the other hand, the average speed of the drop becomes higher than in the surrounding oil phase. The shear force on the upper surface of the drop from the surrounding oil contributes to the circulation inside the drop and a backflow with large velocity in the top area of the drop is observed. This is not balanced by the shear force at the bottom of the drop and the rotation centre does not coincide with the mass centre anymore. At L = 1 cm, the rotation centre covers a wide area close to the bottom of the drop, which indicates that the shear force at the bottom surface is small. At L = 2 cm, only the liquid in the upper part of the drop has a backward flow, while the rest of the drop liquid travels with the same velocity as the

average drop speed. The backward flow seen in Figure 7.7 (c) and Figure 7.7 (d) at the

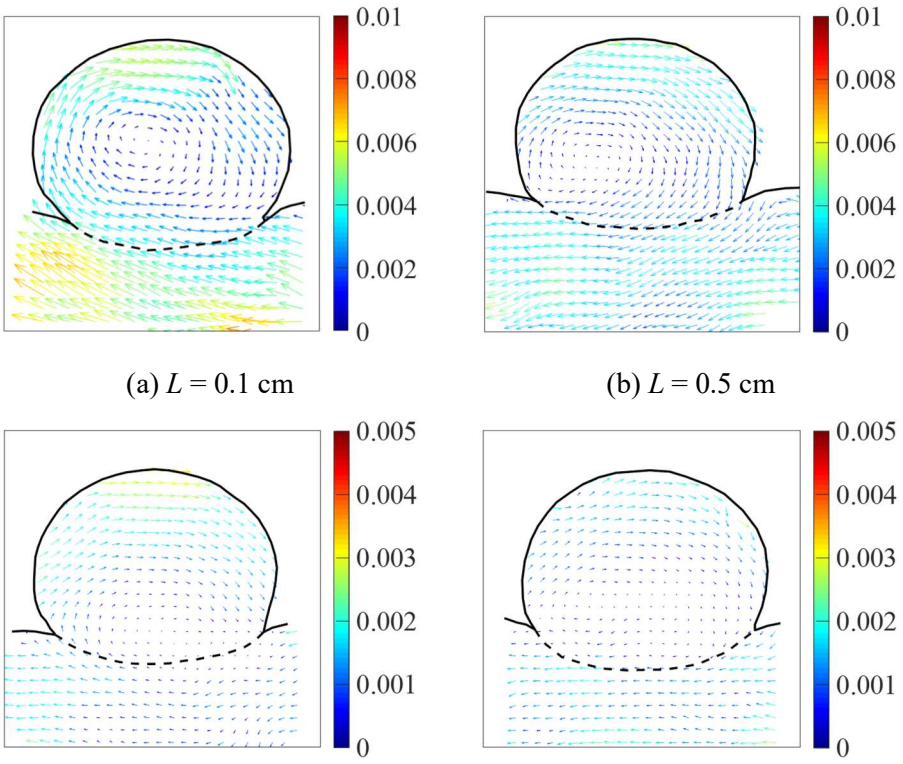

(a) L = 0.1 cm (b) L = 0.5 cm

(c) L = 1 cm (d) L = 2 cm

Figure 7.7 Velocity fields (m/s) in both the drop and the bulk liquid at different locations away from the impact point for v = 2.1 cm/s. The velocity in the figure is the value relative to the translational speed of the drop, which is measured by detecting the trajectory of the centre point of the drop.

top of the drop is not balanced by an equivalent forward flow near the bottom of the drop and suggests that there is no mass conservation of the liquid in the drop. Both Sreenivas et al. (1999) and Sawaguchi et al. (2019) commended that the internal flow in a drop on a moving surface is complicated. Some of their results have shown that secondary flows appear at the bottom of the drop with direction out of the measuring plane. To qualitatively analyse these phenomena three-dimensional velocity profiles would be needed.

7.3 Lubrication flow in the film

7.3.1 Lubrication flow

As was discussed above, the lubrication pressure in the film is considered responsible for the delayed coalescence of the drop with the interface. However, the

film thickness is not uniform, while both the drop interface and the oil-water interface are moving, which would make simulations challenging. Instead, a simplified approach was followed here to explore the lubrication pressure variation in the film. It was found that a drop, pendant from the nozzle, did not coalesce with a moving interface for a very long time (see Figure 7.8(a)). In a similar case (Dell'Aversana et al., 1996) of a drop contacting a moving liquid surface, a wake was observed on the interface after the drop had passed. In the current system, no wake was seen, perhaps because the thickness of the bulk liquid is large, about 15 cm, and there is no effect from the bottom wall on the interface flow, as was seen by (Dell'Aversana et al., 1996).

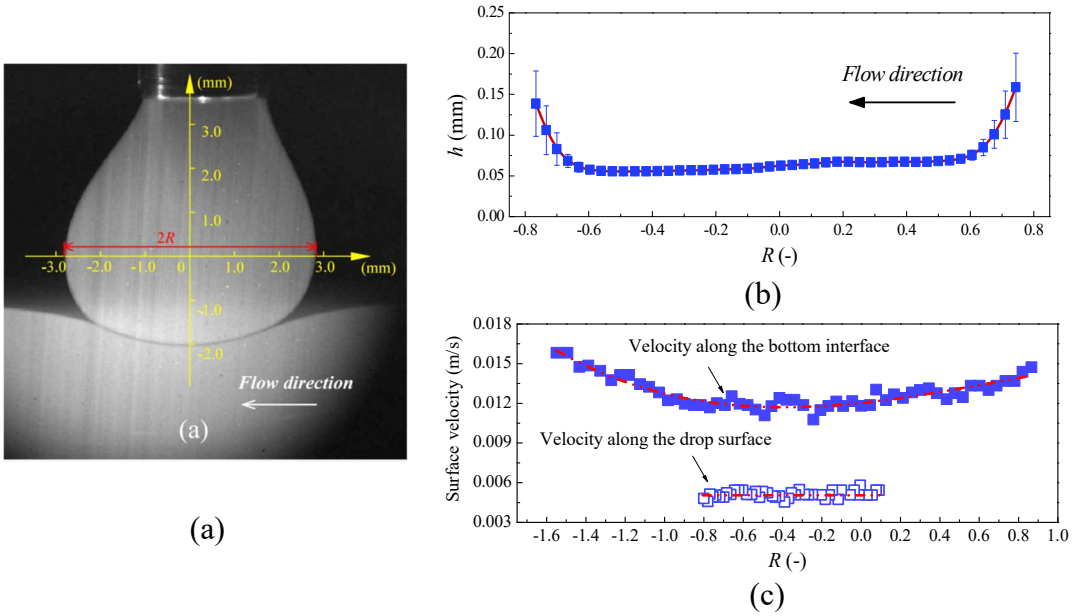

Figure 7.8 (a) A pendant drop resting on the interface without coalescence. The origin of the axis is at the centre of the maximum width of the deformed drop, which is defined as $2R$; (b) thickness of the film trapped between the drop surface and the liquid-liquid interface; The film thickness is averaged from 5 different times when drop levitate on the interface, and the error bars show the standard deviation. (c) The magnitude of the velocity along both the drop surface and the interface. The spatial location is normalized by the drop 'radius' R.

The thicknesses of the film trapped between the drop and the bulk homophase at various time steps was measured. As shown in Figure 7.8(b), the film thickness slightly decreases along the flow direction while the film structure does not change significantly with time. Therefore, the case can be regarded as a quasi-steady state process. To

investigate the lubrication pressure in the film, a numerical simulation is set where the drop surface and the bulk interface are regarded as solid boundaries with a given tangential velocity. These velocities are taken from the experimental data. The velocity at the bottom interface is found to decrease along the flow direction until a minimum value is reached roughly at the centre point. Afterwards, the velocity increases further downstream. The velocity along the drop bottom surface is almost constant in the region of the thin film (see Figure 7.8(c)). The velocities along the bottom interface and the drop surface are measured by tracking the motion of the particles at the vicinity of the interface. The methods and the details of the simulation are given in Appendix D.

Figure 7.9 (a) shows the simulated pressure in the trapped film. As can be seen, the pressure is positive in the majority of the film region. This pressure resists the contact of the drop surface with the oil-water interface. In the current experiments as the drop approaches, the oil-water interface deforms more than in the cases reported in the literature of drops levitated over a thin layer of air (Sawaguchi et al., 2019). As a result, the pressure distribution calculated here is slightly different from the former cases. In the experiments of Sawaguchi et al. (2019), the pressure in the film region is almost constant except from a sharp decrease at both the entrance and the exit sides of the film. In the current work, the pressure increases along the flow direction from the film entrance to the centre where a peak is observed. Downstream from the centre, the pressure decreases until a minimum value is reached at the exit of the film. As discussed by (Sawaguchi et al., 2019), the negative pressure in the film, which tends to pull the interfaces together, is balanced by the Laplace force created by the local surface deformation. Thus, coalescence is effectively prevented. Once the drop surface curvature is not able to balance the low pressure, the film breaks and coalescence is observed in the corresponding location. The variation of the lubrication pressure in the trapped film also affects the velocity profile. As shown in Figure 7.9(b), from the film entrance at Location 1 along to the approximately central position at Location 3, the velocity has a concave shape along the cross-section of the film. Downstream of the central point, the velocity profile acquires a convex shape. The variation of the velocity profile in the film agrees well with the profiles in oil lubrication films in classical

bearing theory (Hamrock et al., 2004).

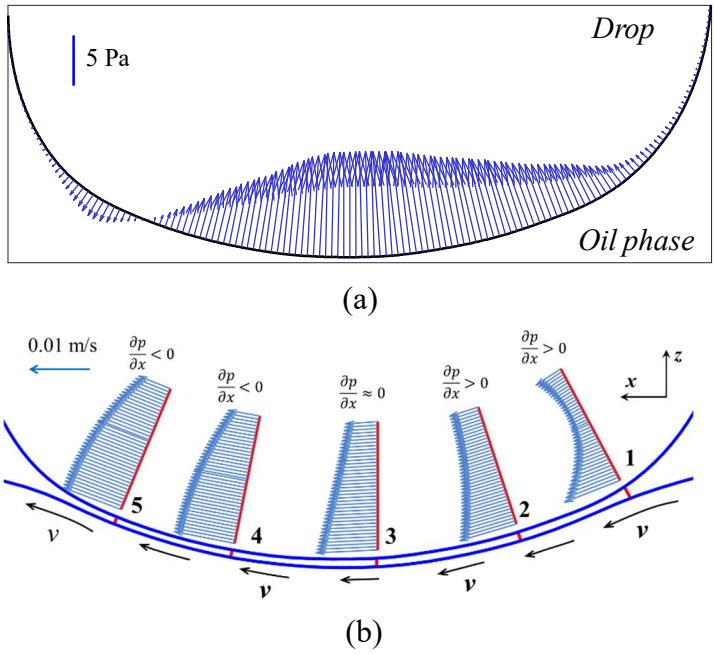

Figure 7.9 (a) the lubrication pressure along the film; (b) velocity profiles at different locations in the trapped film.

7.3.2 Lubrication pressure

At any point at the drop surface, the internal pressure in the drop is balanced by the external pressure in the film and the Laplace pressure resulting from the interface curvature:

$$P_{in} = P_{out} + \sigma(\kappa_r + \kappa_z) \tag{7.6}$$

here P_{in} and P_{out} refer to the pressure inside the drop and in the film respectively; κ_r is the main curvature of the surface and κ_z is the curvature normal to κ_r. Applying Equation (7.6) in the film flow, the lubrication pressure can be estimated if the local curvature of the drop surface and the drop internal pressure are known. For an accurate estimation of the pressure, the two components of the curvature κ_r and κ_z should be known. However, in the current experiments, where only the 2-dimensional profile of the drop is acquired, the azimuthal component of the curvature is unknown. As the drop bottom in the film region is relatively flat under the resistant pressure from the bulk interface, the azimuthal component of the curvature is considered small and is neglected (Lhuissier et al., 2013, Duchemin et al., 2005). The pressure variation was estimated with the PIV velocity data according to the methods explained by (Van Oudheusden,

2013). Inside the drop it was found that the pressure variation induced by the internal flow is much lower than the hydrostatic pressure. Thus, only the hydrostatic pressure is considered. The lubrication pressure in the film relative to the pressure P_0 at the film exit, where the curvature is maximum, is calculated as follows:

$$\Delta P_l = (\rho_d - \rho_s)gH + \sigma(\kappa_0 - \kappa_i) \tag{7.7}$$

where κ_0 and κ_i are the curvature at the reference point, 0, at the film exit and at a point, i, in the film region.

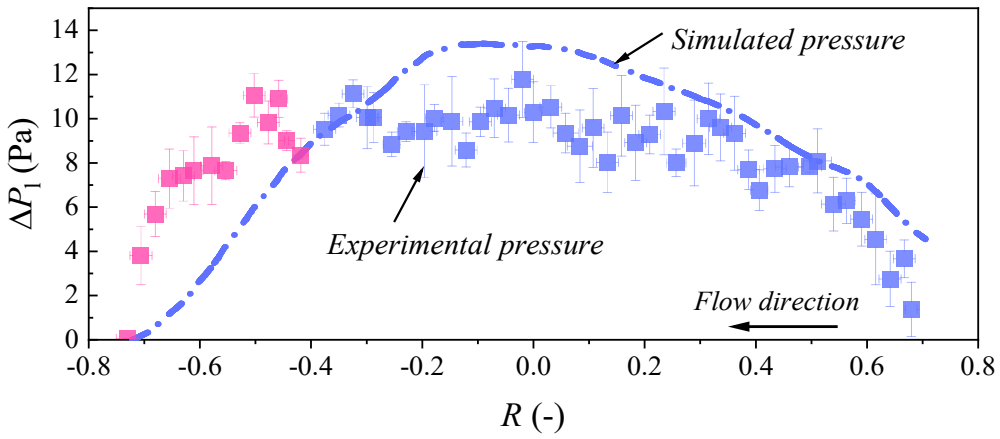

Figure 7.10 Comparison of the film pressure calculated by the local curvature of the drop surface with the numerically simulated pressure. The data shown in the figure is averaged from the pressures at five different time steps. The error bars show the standard deviation.

The variation of the pressure for the case discussed in Section 7.3.1 (see Figure 7.9) is shown in Figure 7.10. It is seen that the pressure values calculated from Equation (7.7) are slightly lower than the simulated ones in most of the film region. As previously discussed by (Smith and Neitzel, 2006, Lhuissier et al., 2013) in the experiments flow can also occur in the film in a direction lateral to the main flow. In the 2D simulations, however, there is no lateral flow and all the liquid entering the film flows in one direction and contributes to the lubrication pressure. The pressure values calculated from Equation (7.7) are higher than the simulated ones in the area near the film exit. A similar discrepancy was also observed by Lhuissier et al. (2013) who, based on a similar approach, found that the calculated air film shape differs a lot from the measured shape in the region near the film exit. The error is attributed to the effects of the azimuthal component of the curvature that is not taken into account in the calculation.

Equation (7.7) is then used to calculate the lubrication pressure in the film in the

different cases studied. As the shape of the film evolves over time, the corresponding lubrication pressure changes as well. For all the interface speeds studied, the lubrication pressure is calculated when the drop recovers to a steady shape and constant speed at t = 130 ms after the drop impacts the interface (see Figure 7.2 and Figure 7.3). Figure 7.11(a) illustrates the variation of the surface curvature at the bottom of the drop, as well as the corresponding pressure distribution at v = 3.4 cm/s, as an example. The relative pressure in the film at different interface speeds is shown in Figure 7.11(b).

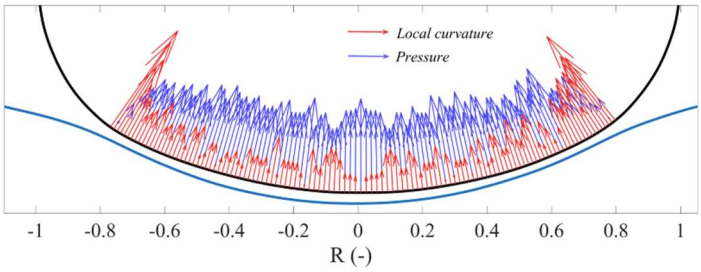

(a)

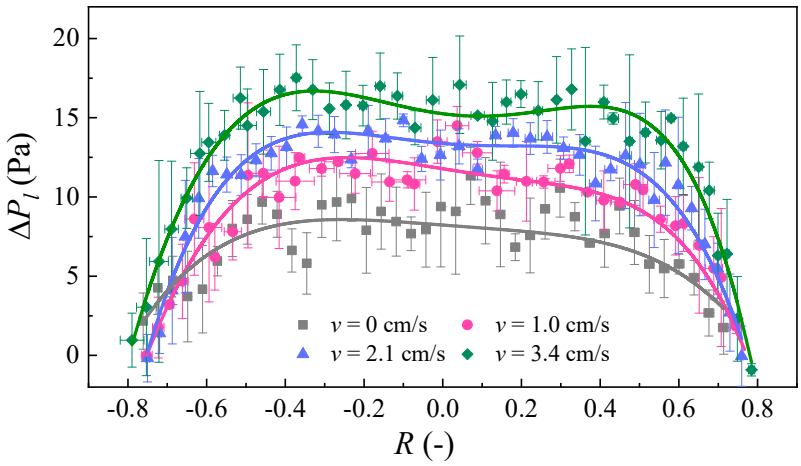

(b)

Figure 7.11 (a) relative lubrication pressure ΔP_l in the film region for v = 3.4 cm/s; (b) magnitude of the ΔP_l at different velocities. The pressure value is averaged over 5 different tests and the error bars show the standard deviation.

As can be seen, after the drop rebound, there is high lubrication pressure in the film region which resists the coalescence of the drop with the bulk interface. Consistently with what is predicted by Equation (7.5), the pressure magnitude increases with the interface speed. The pressures shown in Figure 7.11(b) are positive throughout the film region, because their magnitudes are relative to a minimum pressure at the film exit. When the absolute pressures are considered, then negative values are found at the film

exit for all the cases investigated, similar to what is shown in Figure 7.9(a). As discussed in Section 7.3.1, once the negative pressure exceeds the magnitude that the Laplace pressure is able to resist, the two interfaces will be pushed together, resulting in the film rupture (Sawaguchi et al., 2019).

7.4 Drop coalescence

Coalescence occurs when the film separating the drop from the interface thins sufficiently for the van Der Waals forces to become significant and cause its rupture (Hahn et al., 1985). At the location of the film rupture, the liquid in the drop moves rapidly and helps locate the rupture point on the drop surface with high speed imaging. Figure 7.12 shows the rupture points for all the coalescence events observed in the experiments. For the stationary interface, the rupture points are distributed equally around the drop middle point. The rupture rarely occurs near the centre, which is in good agreement to previous findings that the rupture points occur near the rim where the film is thinnest (Mohamed-Kassim and Longmire, 2004, Oldenziel et al., 2012).

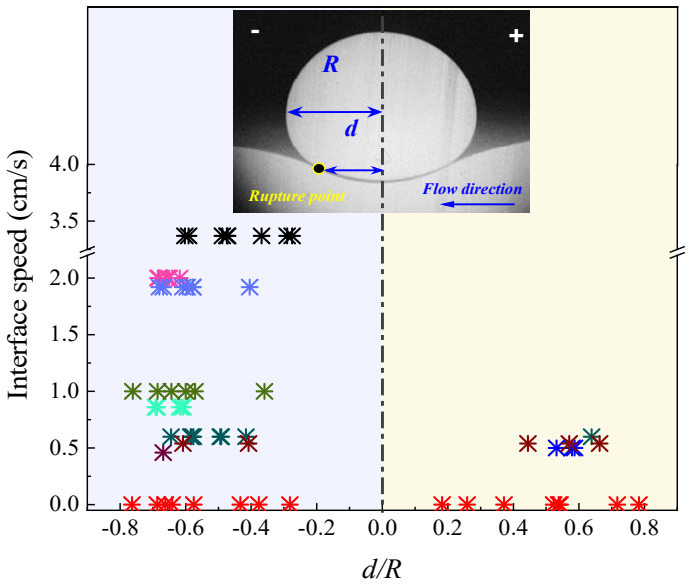

Figure 7.12 Distribution of rupture points for interface with different speeds.

At an interface speed of v = 0.5 cm/s, more of the rupture points are in the front of the drop centre than at the back. Interestingly, most of the rupture events at the back are observed shortly after the impact due to instabilities. In contrast, the rupture events at the front usually occur after the drops have travelled some distances (L > 5 cm). At

higher interface speeds, all rupture points are located at the front part of the film. It has been shown that when a drop travels along a stationary interface (Hale and Akers, 2016), the rupture points also tend to appear on the front part of the drop, in the direction of the flow, than at the back.

It is suggested that the locations of the rupture points are closely related to the spatial distribution of the lubrication pressure in the trapped film. For most of the cases where drops levitate on a moving liquid surface, the trapped air film thickness has a monotonic decrease from the upstream to the downstream location (Sawaguchi et al., 2019, Davanlou, 2016, Lhuissier et al., 2013, Sreenivas et al., 1999). According to the classical lubrication theory, the generated pressure in the air film is able to make the drops levitate. As it was shown in Section 7.2.3, the variation of the film shape for drops approaching a liquid/liquid interface is more complex than in the case of drops approaching an air-liquid surface. After the drop rebounds, the film still has a dimpled shape. The film thickness continues to evolve as the drop is travelling along the interface, as shown in Figure 7.13 for two different locations. As the film thickness is close to the spatial resolution of the high-speed camera at distances larger than L = 2 cm, only film thicknesses for shorter distances are measured. As can be seen, between the drop rebound location (as shown in Figure 7.5) and a distance L = 1 cm, the film thickness decreases significantly in the upstream part of the drop and is almost uniform (right half of the film shown in Figure 7.13) for all interface speeds. At the downstream part of the drop, the dimple structure survives and the film is thicker. The thinning of the film in the upstream location increases locally the lubrication pressure (Sreenivas et al., 1999), which prevents the drop from further approaching the interface. As a result, the rupture is less likely to happen in the upstream part of the drop, even though the film is thinner there than in the downstream location.

When the drops travel further downstream, the film thickness at the upstream part does not change a lot while it decreases at the front but still remains larger than at the back. As discussed previously, the expansion of the film in the dimple results in a low lubrication pressure in the corresponding area. The low pressure in this region is considered to be responsible for the rupture points to occur in the front part of the film,

as shown in Figure 7.12.

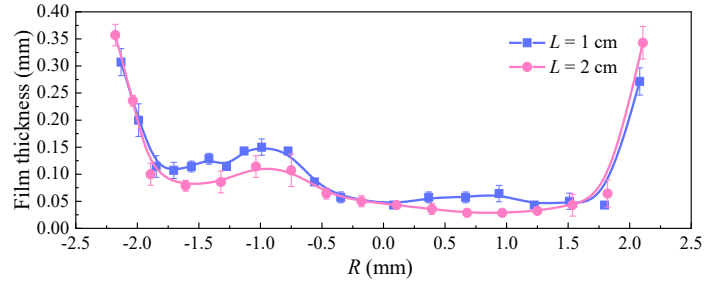

(a) v = 1.0 cm/s

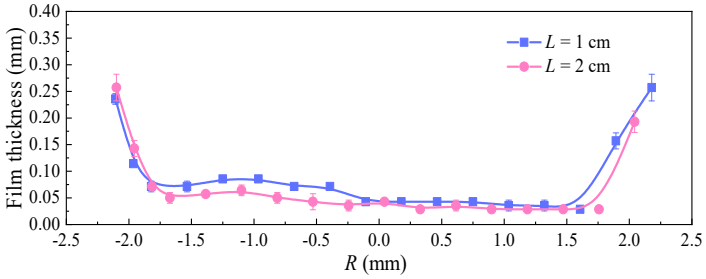

(b) v = 2.1 cm/s

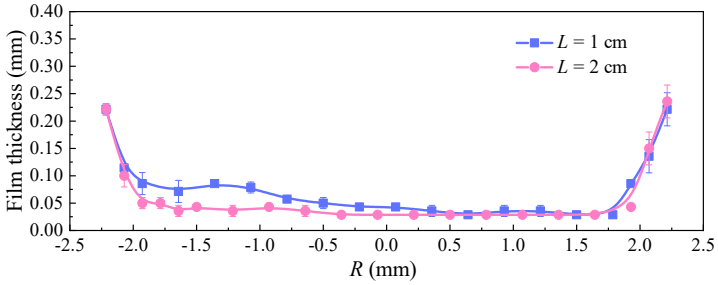

(c) v = 3.4 cm/s

Figure 7.13 Film thickness at two different locations L from the drop impact point for interfaces of different speeds.

7.5 Oil entrainment

When a drop coalesces with a stationary interface, a meniscus is created immediately after the film rupture which expands rapidly until the liquid in the drop completely merges with the bulk homophase. The expansion of the meniscus is resisted by the viscosity of the fluids at the initial stages, and later by the inertia of the liquids (Dong et al., 2019, Murano and Okumura, 2018, Aarts and Lekkerkerker, 2008). It was found, however, that when drops coalesce with moving interfaces, the trapped film, before it fully drains, can break in drop strings where different size drops form connected with thin threads. The breakage of the film in drops observed here is different to what was found previously for a drop coalescing with a moving air-liquid interface.

In the experiments of (Hale and Akers, 2016), the air film breaks into scattered bubbles resulting in a Mesler entrainment (Esmailizadeh and Mesler, 1986). However, in the current experiments, the satellite drops produced by the breakage of the film remain connected to each other with oil phase threads.

The breakage of the trapped film and the spatial evolution of the drop-string in the case of a drop coalescing with interfaces moving at v = 2.1 cm/s and v = 3.4 cm/s is presented in Figure 7.14. The drop strings shown in Figure 7.14(a) and Figure 7.14(b)

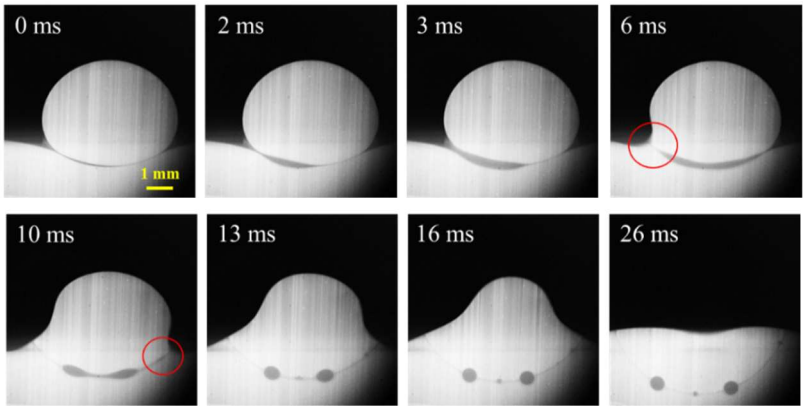

(a) v = 2.1 cm/s; L = 0.5 cm

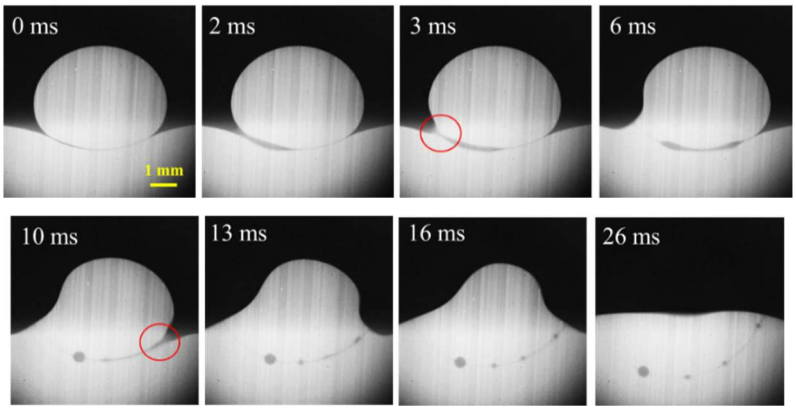

(b) v = 3.4 cm/s; L = 1 cm

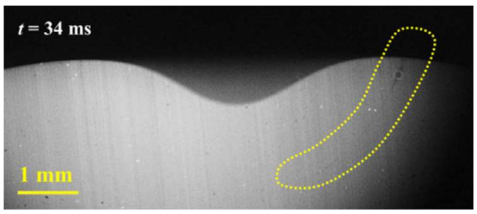

(c) v=3.4 cm/s; L= 5 cm

Figure 7.14 Formation of the drops-on-string during the coalescence of drops with moving interfaces with speeds of (a) v =2.1 cm/s, L = 0.5 cm; (b) v = 3.4 cm/s, L = 1 cm; (c) Incomplete drop string formation for a coalescence event at v = 3.4 cm/s, L = 5 cm.

are obtained with relatively thicker films. If the trapped film is thin at the moment of rupture, the resulting drop string is not fully linked with the left and right interfaces. Instead, only a tendril linking the drop to the oil phase is observed (see Figure 7.14(c)), which is similar to what was shown previously (Oldenziel et al., 2012, Aryafar and Kavehpour, 2008). The drop strings produced here are similar to the breakage of a viscoelastic filament (Bhat et al., 2010). As the drop strings were not seen to form in the case of a drop coalescing with a stationary interface with the same liquids, it is believed that the phenomenon is not caused by contamination that may change the interfacial properties of the fluids.

When a drop coalesces with a stationary interface, the meniscus that forms after rupture increases and the film can drain from all sides of the drop until it is completely drained. However, when the coalescence is with a moving interface, it was found that before the film can completely drain another coalescence event appears at the side of the drop leading to oil entrained in the bulk water phase. Subsequently, the entrained oil film starts to form drops under the influence of interfacial tension resulting in the drops-on-string structure. The capillary waves, initially created at the onset of the film rupture may further hinder the trapped oil to contract to a liquid body, favouring the generation of the drops-on-string (Charles and Mason, 1960a).

7.6 Conclusions

Surfing of drops and delayed coalescence on moving liquid/liquid interfaces is relevant to many industrial applications but has not been studied previously. The behaviour of travelling water drops on moving oil-water interfaces was studied here. Studies were carried out in a novel flow channel, using a combination of PLIF and PIV techniques to obtain the evolution of the shapes of the drops, of the film thickness and of the tangential velocities at the drop surface and the liquid-liquid interface, as the drops impact on the interface and move along. It was found that the drop coalescence is delayed by the moving interface, while the delay increases with the interface speed. The delay is attributed to the lubrication pressure in the film trapped between the drop and the interface. This pressure was calculated based on the local curvature of the drop

surface and the tangential velocities on the drop surface and on the interface in the film region. For the case of a stationary drop, the results were also compared with numerical simulations with good agreement. The results reveal that the lubrication pressure is high along most of the film, preventing the drop from approaching the interface, and increases with the interface velocity. The film has a dimple shape, with increased thickness close to the exits, which locally decrease the lubrication pressure. The reduced pressure in the dimple regions allows the drop to approach the interface and will eventually lead to the film rupture. As the interface velocity increases, the dimple shape becomes less obvious, especially at the upstream part of the drop. As a result, with increasing interface velocity, the film rupture occurs at the downstream part of the drop, where the film retains its dimple shape.

The current findings will be relevant to studies of dispersed flows and their separation (Rommel et al., 1993), drop manipulation in microfluidic systems (Deng et al., 2016) and in printing applications (Fathi et al., 2010). Further work is needed to understand the delayed coalescence. Previous studies by Sawaguchi et al. (2019) have shown that the circulation inside the drop is complex and three dimensional, while the results shown here only describe the circulation in the 2-D laser plane. The flow and characteristics of the film were also only observed in a two-dimensional plane. Volumetric PIV approaches will elucidate the flows in the drop and in the film. In addition, it is still unclear how the film breaks into the drops-in-string configuration and this would merit further studies.

Chapter 8

Conclusions and outlook

In this dissertation, the coalescence of a drop with an interface is investigated under various conditions. The effects of surfactants on the different steps of the coalescence process including drop rest phenomenon, film rupture and final liquid merging are analyzed in detail. In this Chapter, the main findings of the current research and the relevant impacts are reviewed. Recommendation for future work are finally suggested.

8.1 Conclusions

In this study, the total coalescence, the partial coalescence and the delayed coalescence of drops on either stationary or the moving liquid/liquid interfaces are studied by optical methods including the high-speed Shadowgraph and the PIV technique. The PLIF technology is applied to visualize the distribution of the surfactants along the coalescing surface.

The total coalescence between drops and initially flat interfaces was studied in Chapter 4. The surfactants are found to extend the drop rest time as well as increase the interface deformation prior to film rupture. Once the coalescence occurs, the top surface of the drop is able to descend to a level below the initial flat interface location in the surfactant-free system. This deflection of the surface is not observed for high surfactant concentration. The PIV results show that two counter-rotating vortices appear at the bottom of the drop straight after the film rupture. These vortices expand with their cores moving upwards. The strength of the vortices is increasing during the process until they meet the falling drop surface. Due to the block effect from the surface, the strength decreases subsequently. The presence of the surfactants tends to make the evolution of vortices non-symmetrical as well as slow down the evolution.

The experimental results on the drop/interface partial coalescence are presented subsequently (Chapter 5). The *Oh-Bo* based maps are plotted to show the conditions the where partial coalescence occurs. The surfactants are found to reduce the partial coalescence region in the map. In addition, the size ratios of the daughter drop to that of the mother drop, ξ, during the partial coalescence cascade are plotted as well in three regimes in the *Oh-Bo* map. In the gravity regime, ξ does not change a lot with the increase of surfactant concentration. However, surfactants decrease the drop ratio significantly in the inertia-capillary regime. The mechanism of the partial coalescence is discussed based on the 2D-PIV velocity fields. In the early stages of the coalescence, the inward motion of the sides at the upper part of the drop is believed to favour the generation of a liquid cylinder. Subsequently, the large vertical flux at the bottom of the liquid cylinder creates a low pressure in this region which causes the pinch-off leading to partial coalescence. It is seen that the existence of the surfactants prevents the occurrence of partial coalescence, which is partially due to the Marangoni effect induced by the uneven distribution of the surfactants along the drop surface. The spatial evolution of the vortices in the partial coalescing drop is described as well. As the vortices do not enter the liquid cylinder during the whole process, they do not seem to contribute to the pinch-off of the drop surface.

In Chapter 6, the spatiotemporal distribution of surfactants along the coalescing interface are presented. When drops rest on the interface, surfactants are found accumulated at a barrier ring at $0.7R$ away from the centre of the film. Once the rupture occurs, the retreating film collects the surfactant molecules and their concentration reaches a peak at the tip of the meniscus; the concentration at the tip continues to increase during the film retraction. The uneven distributions of the surfactants along the evolving drop surface in the following merging process is analyzed as well. Marangoni effects are believed to help drain the drop liquids and eventually prevent partial coalescence.

In Chapter 7, the delayed coalescence of the drop surf along the moving interface is investigated. The measured distributions of the rest times of the drops indicate that the drop coalescence is delayed drastically by the moving interface. Generally, a larger

velocity on the interface produces longer rest times. The film thickness between the surfing drop and the bottom interface is measured with high-speed PLIF in the early stages of the drop motion on the interface. The film presents a dimple when the drop rests on interfaces with low speed, but the dimple becomes less obvious with the increase of the interface speed. Numerical simulations are conducted for the case of a half-pendent drop levitating on the moving liquid-liquid interface. The results reveal that the minimum pressure appears at the vicinity of the film in a downstream location, which reasonably explains the phenomena observed in the experiments that the film always ruptures at the front bottom of the moving drop. The lubrication pressure in the trapped film is calculated based on the local curvature of the drop surface. A higher lubrication pressure is found at larger interface speeds. After the rupture, the trapped film is not able to completely drain out but leaves the drops-on-string structure in the bulk phase leading to the oil entrainment.

8.2 Recommendations for future work

The work presented in the thesis has addressed some questions regarding the various coalescence behaviour under specific conditions. The results are expected to provide reference for processes where coalescence is involved, including petroleum transportation (Farhadi et al., 2016), drug encapsulation (Andrade et al., 2015), liquid spray formation (Wagoner et al., 2018) and manipulation of drops in microfluidic devices (Deng et al., 2016). However, the current experiments cannot cover all conditions encountered in industrial fields. Besides, some new phenomena were observed in the experiments, which would need to be further investigated in the future.

For the partial coalescence, previous studies reported that the convergence of the capillary waves along the drop surface should be responsible for the occurrence of partial coalescence (Zhang et al., 2015, Ding et al., 2012). The way that capillary waves disturb the fluid dynamics near the drop surface has not been investigated yet. It is seen in the PIV tests that series of vortices appear near the drop surface, where the capillary waves pass. However, the phenomenon is not obvious due to the low resolution of the

PIV technique. Approaches such as the high-resolution Spatiotemporal Filter Velocimetry (SFV) technique, which has been successfully applied by Hosokawa et al. (2017) to obtain velocity fields at the vicinity of the drop surface, would be needed to investigate the interaction between the drop liquids and the capillary waves. In addition, Charles and Mason (1960b) point out that the liquid cylinder forming as the drop merges with the interface in partial coalescence is pinched off by the Rayleigh-Plateau instability if the height of the cylinder exceeds its circumference. However, partial coalescence is still observed without satisfying this criterion. When there is a surface tension gradient along the drop surface, the generated cylinder was found to be much higher than the circumference. The pinch-off in such conditions is more likely to produce several drops instead of a single secondary drop. This is worth exploring in the future to fully reveal the partial coalescence mechanism.

For the delayed coalescence and the surfing of drops on moving interface, the film thickness in the later stages of the drop movement cannot be measured due to the limitations of the PLIF technique. Thus in the future, a high-resolution interferometric method should be used to detect the thickness of the thin film (Sawaguchi et al., 2019). It is also worth investigating the circulation of the fluids inside the drop. As Sawaguchi et al. (2019) stated, the inner circulation of the moving drop is complicated, while the current experiments only describe the circulation in the laser plane. In addition, it is still unclear how the surrounding phase breaks the film into a filament to produce the drops-on-string after the film rupture. Thus, a 3D observation or PIV on the film breakage is necessary to further explore these processes.

Appendix A: Error analysis for the surface excess *Γ*

In this appendix, the factors affect the accuracy of the surface excess Γ described in Section 3.2.4 and the relevant error analysis are provide.

According to Equation (3.4), the stand error of surface excess, ε_Γ is mainly from the parameter Γ_∞ and K_L that were determined by fitting the surface tension data. The standard error of Γ_∞ and K_L are $\varepsilon_{\Gamma_\infty} = 1.95\times10^{-7}$ mol/m^2, $\varepsilon_{KL} = 1096$ m^3/mol, respectively. According to the propagation error equation:

$$\varepsilon_\Gamma = \sqrt{\left(\frac{\partial\Gamma}{\partial\Gamma_\infty}\right)^2 \varepsilon_{\Gamma_\infty}^2 + \left(\frac{\partial\Gamma}{\partial K_L}\right)^2 \varepsilon_{K_L}^2}$$

The stand error of the surface excess ε_Γ can be obtained.

Appendix B: Pressure calculation based on 2D-PIV velocity

In this appendix, the calculation of the pressure field based on the 2D-PIV velocity data is presented. Although three dimensional velocity field information would be required to fully characterize the coalescence process, this is difficult to obtain in practice experimentally. Therefore, most of the experimental studies have been conducted in 2D and the coalescence process is often described on a plane (Mohamed-Kassim and Longmire, 2004, Kim and Longmire, 2009, Weheliye et al., 2017, Shen et al., 2017, Dong et al., 2017). The estimation of the planar pressure in a 2D flow is briefly introduced below. The corresponding planar Navier-Stokes equations for an unsteady flow of incompressible liquids is given by:

$$\frac{\partial(\rho u)}{\partial t}+\frac{\partial(\rho uu)}{\partial x}+\frac{\partial(\rho vu)}{\partial y}=-\frac{\partial p}{\partial x}+\mu\left(\frac{\partial^2 u}{\partial x^2}+\frac{\partial^2 u}{\partial y^2}\right) \tag{B.1}$$

$$\frac{\partial(\rho v)}{\partial t}+\frac{\partial(\rho uv)}{\partial x}+\frac{\partial(\rho vv)}{\partial y}=-\frac{\partial p}{\partial y}+\mu\left(\frac{\partial^2 v}{\partial x^2}+\frac{\partial^2 v}{\partial y^2}\right) \tag{B.2}$$

Here, the x and y represent the horizontal and the vertical direction, respectively, and u, v are the velocities along the x and y direction respectively; p refers to the pressure in the measured plane. The body force and the Laplace force terms were not included since the generalized pressure was considered (Van Oudheusden, 2013). From the velocity fields obtained with the high-speed PIV, then the pressure gradient along x and y direction can be calculated as follows:

$$\frac{\partial p}{\partial x}=-\rho\left(\frac{\partial u}{\partial t}+u\frac{\partial u}{\partial x}+v\frac{\partial u}{\partial y}\right)+\mu\left(\frac{\partial^2 u}{\partial x^2}+\frac{\partial^2 u}{\partial y^2}\right) \tag{B.3}$$

$$\frac{\partial p}{\partial y}=-\rho\left(\frac{\partial v}{\partial t}+u\frac{\partial v}{\partial x}+v\frac{\partial v}{\partial y}\right)+\mu\left(\frac{\partial^2 v}{\partial x^2}+\frac{\partial^2 v}{\partial y^2}\right) \tag{B.4}$$

The central-difference method was applied for the discretization of the governing equations that has improved accuracy compared to the backward or forward difference

schemes (Van Oudheusden, 2013). Following a Taylor series expansion, the discretization of the first and second order of the partial differential terms for a given continuous function ψ(x,n) can be written as:

$$\frac{\partial \psi}{\partial x} = \frac{\psi(i+1,n) - \psi(i-1,n)}{2\Delta x} - \frac{\partial^3 \psi}{\partial x^3}\frac{\Delta x^2}{3!} + \cdots = \frac{\psi(i+1,n) - \psi(i-1,n)}{2\Delta x} + o(\Delta x^2) \tag{B.5}$$

$$\frac{\partial^2 \psi}{\partial x^2} = \frac{\psi(i+1,n) - 2\psi(i,n) + \psi(i-1,n)}{(\Delta x)^2} + o(\Delta x^2) \tag{B.6}$$

where $\psi(i,n)$ refers to the function value at the grid point i for time layer n, as shown in Figure B.1.

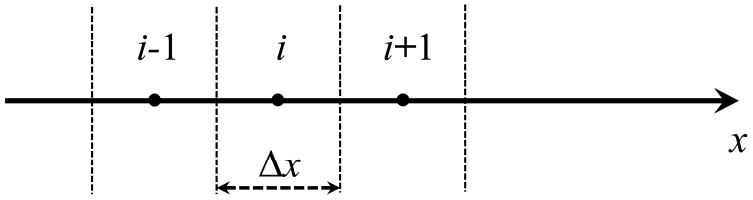

Figure B.1 The one dimensional discretization grid.

Based on Equation (B.5) and Equation (B.6), the pressure gradient at point $P(i, j)$ in the x and y directions can be obtained explicitly from the values of the surrounding points at the same time and the corresponding point at the time layer (n+1), as shown in Figure B.2:

$$\frac{\Delta p_x}{\Delta x} = \frac{p_{i,j} - p_{i-1,j}}{\Delta x} = -\rho\left(\frac{u_{i,j}^{n+1} - u_{i,j}^{n}}{\Delta t} + u_{i,j}\frac{u_{i+1,j} - u_{i-1,j}}{2\Delta x} + v_{i,j}\frac{u_{i,j+1} - u_{i,j-1}}{2\Delta y}\right) + \mu\left(\frac{u_{i+1,j} - 2u_{i,j} + u_{i-1,j}}{(\Delta x)^2} + \frac{u_{i,j+1} - 2u_{i,j} + u_{i,j-1}}{(\Delta y)^2}\right) \tag{B.7}$$

$$\frac{\Delta p_y}{\Delta y} = \frac{p_{i,j} - p_{i,j-1}}{\Delta y} = -\rho\left(\frac{v_{i,j}^{n+1} - v_{i,j}^{n}}{\Delta t} + u_{i,j}\frac{v_{i+1,j} - v_{i-1,j}}{2\Delta x} + v_{i,j}\frac{v_{i,j+1} - v_{i,j-1}}{2\Delta y}\right) + \mu\left(\frac{v_{i+1,j} - 2v_{i,j} + v_{i-1,j}}{(\Delta x)^2} + \frac{v_{i,j+1} - 2v_{i,j} + v_{i,j-1}}{(\Delta y)^2}\right) \tag{B.8}$$

Substituting the PIV velocity data to Equation (B.7) and Equation (B.8), the pressure drop between two grid points along the x and y directions in the flow field can be obtained. Since only the liquid in the drop was seeded with tracer particles, there were no velocity data for the area outside the drop.

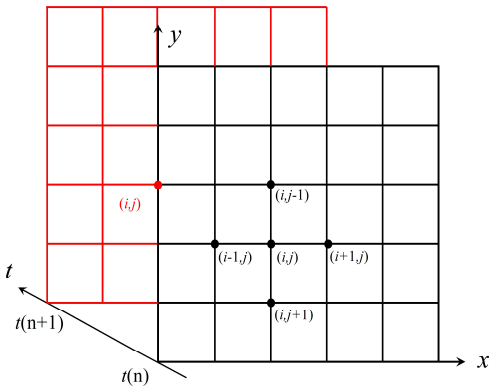

Figure B.2 2D computational grids at times t(n) and t(n+1).

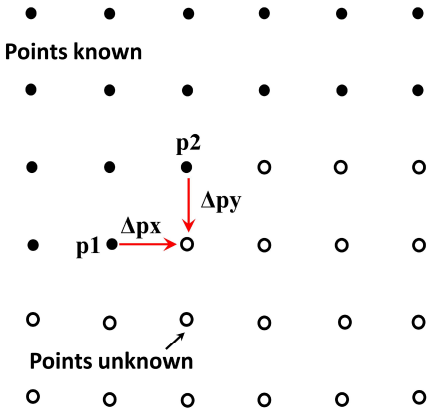

Figure B.3 Strategy for integration of pressure.

Equation (B.7) and Equation (B.8) only give the pressure gradient between two grid points in x and y directions respectively. To find the pressure value at a particular point the following integration was carried out:

$$p = \frac{1}{2}\left[(p_1 + \Delta p_x) + (p_2 + \Delta p_y)\right] \tag{B.9}$$

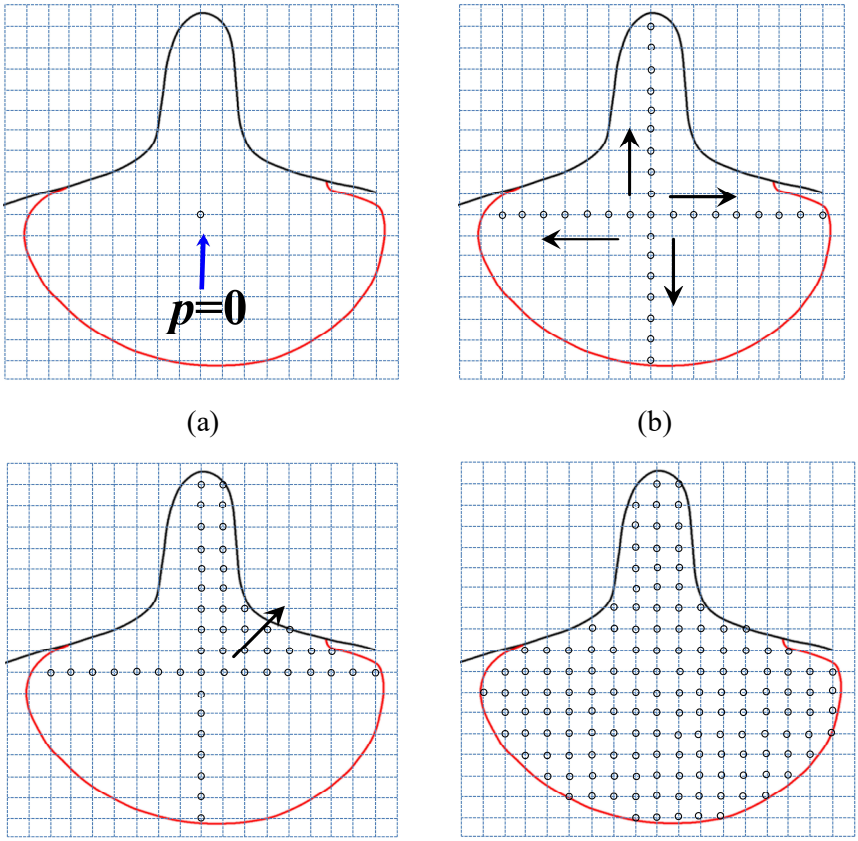

Figure B.4 Schematic of the integration scheme in the coalescing drop; the circles represent the grid points with known pressure.

Prior to the integration, the boundary conditions should be defined. This is challenging as the interface shape changes constantly during coalescence. In addition, the absolute pressure in the drop is not known. To initialize the integration, the pressure at a certain point in the grid was set to 0 as a reference (see Figure B.4(a)). Then the pressure values of the points at the same column and row as the reference point were calculated as shown in Figure B.4(b). At last the pressure values at the other areas of the drop were obtained according to Equation (B.9), where p_1 and p_2 refer to the known pressures of the grid points along the x and y directions, and p indicates the pressure of an unknown point, as shown in Figure B.3. The pressure fields in the coalescing drop for different experimental conditions is discussed in Section 5.6.

The calculation was conducted in Matlab R2018b, the coding is shown below:

```
%%%%%%%%%%%%%%%%%%%%%%%%%%%%%%%%%%%%%%%%%%%%%%%%%%%%%%%%%%%%%%%%%%%%%%%%%%%%
%  This program calculates the pressure distribution inside the
coalescing droplet based on the 2D-PIV velocity data and plot the
pressure filed into contour map.
%%%%%%%%%%%%%%%%%%%%%%%%%%%%%%%%%%%%%%%%%%%%%%%%%%%%%%%%%%%%%%%%%%%%%%%%%%%%
% Define variables
% dt -- the time step;
% dx -- the space step along x axis;
% dy -- the space step along y axis;
% CF -- the calibration factor;
% rou -- the density of the droplet liquid;
% miu -- the viscosity of the droplet liquid;
% DATA1 - The matrix that contains the velocity data and
% the corresponding locations at time step of (t-1);
% DATA2 - The matrix that contains the velocity data and
% the corresponding locations at time step of (t);
% xf -- the x coordinate of the velocity matrix at time step (t-1);
% yf -- the y coordinate of the velocity matrix at time step (t-1);
% uf -- the horizontal velocity along the x at time step (t-1);
% vf -- the vertical velocity along the y at time step (t-1);
% xl -- the x coordinate of the velocity matrix at time step (t);
% yl -- the y coordinate of the velocity matrix at time step (t);
% ul -- the horizontal velocity along the x at time step (t);
% vl -- the vertical velocity along the y at time step (t);

%%%%%%%%%%%%%%%%%%%%%%%%%%%%%%%%%%%%%%%%%%%%%%%%%%%%%%%%%%%%%%%%%%%%%%%%%%%%
clear all;
close all;
clc;

%%%%%%%%%%%%%%%%%%%%%%%%%%%%%%%%%%%%%%%%%%%%%%%%
%Input the properties of the fluids;
rou=1080;
miu=2.599e-3;

%%%%%%%%%%%%%%%%%%%%%%%%%%%%%%%%%%%%%%%%%%%%%%%%
```

```
% Initialize the time step and special step, in the experimental the
high-speed camera at a frequency of 5400fps was used; the calibration
factor is 1mm to 178 pixels.
dt=1/5400;%s
CF=1/178;
dx=CF*16/1000;
dy=CF*16/1000;

%%%%%%%%%%%%%%%%%%%%%%%%%%%%%%%%%%%%%%%%%%%%%%%%
% Load the 2D-PIV velocity data at time step of (t-1);
[fnom,fchemin]=uigetfile('*.jvc','filename jvc');
              cd(fchemin);
              rep=dir(['*.jvc']);
              fin=size(rep);
filename1=rep(1).name;
DATA1=load(filename1);
% Load the 2D-PIV velocity data at time step of (t);
filename2=rep(2).name;
DATA2=load(filename2);
DATA1=DATA1',DATA2=DATA2';

%%%%%%%%%%%%%%%%%%%%%%%%%%%%%%%%%%%%%%%%%%%%%%%%
%Assign data to make sure the velocity and location matrix matches the
corrdinate of the droplet shape
[xf,yf,uf,vf,noxf,noyf]=assignment_JVC(DATA1);
[xl,yl,ul,vl,noxl,noyl]=assignment_JVC(DATA2);
% Unify the unit
uf=0.001*uf*CF/dt; % m/s;
vf=0.001*vf*CF/dt; % m/s;
ul=0.001*ul*CF/dt; % m/s;
vl=0.001*vl*CF/dt; % m/s;

%%%%%%%%%%%%%%%%%%%%%%%%%%%%%%%%%%%%%%%%%%%%%%%%
% Load the matrix containing the information of the drop shape.
load('08-143.mat')
yis(47:67)=yi(28:-1:8);
xis(47:67)=xi(28:-1:8);
% As the image is enlarged for the convineient of the PIV post-
processing, the coordinates need to be re-adjusted.
xis=xis+138;
yis=yis-138;
xi=xi+138;
yi=yi-138;
% Smooth the lines showing the drop surface and the phase interface
zf = smooth(xis,yis,1,'rloess')
zf=1024-zf;
% Set the date corresponding to the area outside the droplet to be 0.
bw=roipoly(xf,yf,uf,xis,zf);
  uf=bw.*uf;
  vf=bw.*vf;
  ul=bw.*ul;
  vl=bw.*vl;
  uf(uf==0)=NaN;
  vf(vf==0)=NaN;

%%%%%%%%%%%%%%%%%%%%%%%%%%%%%%%%%%%%%%%%%%%%%%%%
% Calculate the pressure gradient dpx along the horizontal direction
x, as well as the dpy along the vertical direction y. The direct
```

```
differential method is applied.
for i=2:1:72
    for j=2:1:72
        dpx=dx*(-rou*((ul(i,j)-uf(i,j))/dt+uf(i,j)*(uf(i+1,j)-uf(i-
1,j))/(2*dx)+vf(i,j)*(uf(i,j+1)-uf(i,j-1))/(2*dy))+miu*(((uf(i+1,j)-
2*uf(i,j)+uf(i-1,j))/(dx^2))+(uf(i,j+1)-2*uf(i,j)+uf(i,j-1))/(dy^2)));
        dpy=dx*(-rou*((vl(i,j)-vf(i,j))/dt+vf(i,j)*(vf(i+1,j)-vf(i-
1,j))/(2*dx)+vf(i,j)*(vf(i,j+1)-vf(i,j-1))/(2*dy))+miu*(((vf(i+1,j)-
2*vf(i,j)+vf(i-1,j))/(dx^2))+(vf(i,j+1)-2*vf(i,j)+vf(i,j-1))/(dy^2)));
% Store the pressure information in to two matrixes representing the
dpx and dpy.
        H(i-1,j-1)=dpx;
        J(i-1,j-1)=dpy;
    end
end;

%%%%%%%%%%%%%%%%%%%%%%%%%%%%%%%%%%%%%%%%%%%%%%%
P=zeros(71,71)*nan;
% Initialize the integral by set one point to be 0; In this case the
% center point is(36,33), which can be slightly different in other
cases.
P(36,33)=0;
% Calculate the pressure frame as shown in Figure B.4(b)
for j=32:-1:10;
    P(36,j)=P(36,j+1)-H(36,j)*dx;
end
for j=34:1:53
    P(36,j)=P(36,j-1)+H(36,j-1)*dx;
end
for i=35:-1:19
    P(i,33)=P(i+1,33)-J(i,33)*dy;
end
for i=37:1:56
    P(i,33)=P(i-1,33)+J(i-1,33)*dy;
end
% Calculate the relative pressure drop based on the data acquired
before
% up-right
for i=35:-1:19
    for j=34:1:53
    P(i,j)=0.5*(P(i,j-1)+H(i,j-1)*dx+P(i+1,j)-J(i,j)*dy);
    end
end
% down-right
for i=37:1:56;
    for j=34:1:53;
        P(i,j)=0.5*(P(i,j-1)+H(i,j-1)*dx+P(i-1,j)+J(i-1,j)*dy);
    end
end
%down-left
for i=37:1:56;
    for j=32:-1:10;
        P(i,j)=0.5*(P(i,j+1)-H(i,j)*dx+P(i-1,j)+J(i-1,j)*dy);
    end
end
% up-left
    for i=35:-1:19;
        for j=32:-1:10;
```

```
      P(i,j)=0.5*(P(i,j+1)-H(i,j)*dx+P(i+1,j)-J(i,j)*dy);
        end
    end

%%%%%%%%%%%%%%%%%%%%%%%%%%%%%%%%%%%%%%%%%%%%
% plot the pressure drop
bw1=bw(2:72,2:72);
P=bw1.*P;
smooth(P);
xf=xf*CF;
yf=yf*CF;
% Plot the contour of the pressure field
[f1,g1]=contourf(xf(2:72,2:72),yf(2:72,2:72),P,[-0.005:0.0001:0.005])
caxis([-0.005,0.005]);
colormap(jet);
set(g1,'Linecolor','none')
h = colorbar;
set(h,'FontName','Times New Roman','FontSize',46)
get(h,'position')
set(h,'position',[0.730 0.15 0.05 0.72])
h.TickLabels = (-0.005:0.001:0.005)
hold on;
% Plot the streamlines
ss=streamslice(xf(2:72,2:72),yf(2:72,2:72),uf(2:72,2:72),vf(2:72,2:72
),[6])
set(ss, 'Color', [1 1 1],'Linewidth',1.3)

%%%%%%%%%%%%%%%%%%%%%%%%%%%%%%%%%%%%%%%%%%%%
% Plot the boundaries of the drop surface and the phase interface.
hold on
Dropsurface=plot(xis(1:46)*CF,zf(1:46)*CF,'k-')
hold on
Dropsurface2=plot(xis(47:end)*CF,zf(47:end)*CF,'k--')
hold on
Interface1=plot(xi(1:8)*CF,(1024-yi(1:8))*CF,'k-')
hold on
Interface2=plot(xi(29:end-3)*CF,(1024-yi(29:end-3))*CF,'k-')
axis([1.2 5.2 1.8 5.8]);
axis square;

%%%%%%%%%%%%%%%%%%%%%%%%%%%%%%%%%%%%%%%%%%%%
% Set units and the structure of the image
set(gca,'XTicklabel',[],'YTicklabel',[],'box','on')
set(gca,'position',[0.001,0.15,0.72,0.72] )
%%%%%%%%%%%%%%%%%%%%%%%%%%%%%%%%%%%%%%%%%%%%%%%%%%%%%%%%%%%%%%%%%%%%%%%%%%%
```

Appendix C: Acceleration of drops on the moving interface

The acceleration of the drop is attributed to the drag force from the surrounding liquid and the force from-the interface on the bottom of the drop. As shown in Figure C.1, in the 'inner' region I, where the drop bottom is very close to the interface, the flow pattern is different from that in the 'external' region II. The drag forces on the drop surface will also be different in these two regions. The drag force on a sphere which is fully submerged in oil with a relative speed Δv is estimated by (Nakayama, 2018):

$$F_{oil} = C_d \frac{\pi D_v^2 \rho_{oil} (\Delta v)^2}{8} \tag{C.1}$$

where C_d is the drag coefficient, D_v is the vertical diameter of the drop and Δv is the velocity of the oil phase relative to the drop. From the numerical simulations (discussed in Appendix B), the average velocity of the oil phase surrounding the drop was found to be approximately half of the interface velocity. The corresponding Reynolds number $Re=\rho D_v \Delta v/\mu$ is almost 50 at the beginning of the impact period when the velocity difference between the drop and the interface is large (Figure 7.3). When the drop reaches the speed of the surrounding liquid, the Re is reduced to about 0.02. According to (Dijkhuizen et al., 2010), the drag coefficient C_d for drops can be calculated from Equation (C.2), which is valid both in the Stokes region as well as at higher Re.

$$C_d = \frac{16}{Re}\left(1 + \frac{2}{1 + \frac{16}{Re} + \frac{3.315}{\sqrt{Re}}}\right) \tag{C.2}$$

Since only part of the drop is affected by the surrounding oil phase in the 'external' region II, a correction factor $\beta = \frac{2}{5}\left(2 + \frac{D_v - b}{D_h}\right)$, which depends on the drop geometry, needs to be introduced in to take this into account (Hale and Akers, 2016). As shown in Figure C.1 , b is the minor axis of the bottom of the drop.

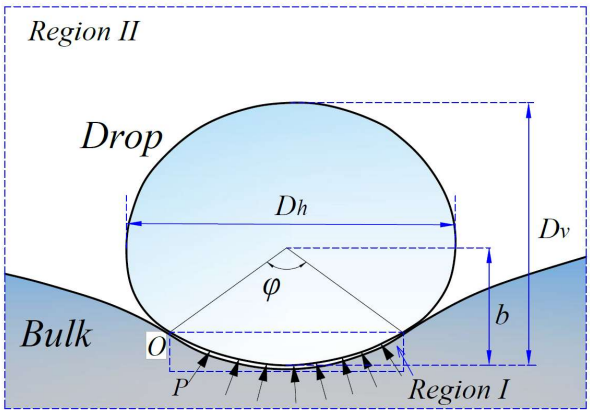

Figure C.1 Defined variables of the drop geometries on the deformed interface.

In the 'inner region' I, the shear force on the drop bottom surface is expressed as $\tau = \mu\frac{\partial u}{\partial h}$, where h is the film thickness, which is around 0.1 mm at the impact period. According to Sreenivas et al. (1999), a linear variation of the velocity is considered across the film region. The tangential velocity along the bulk interface u_b is considered equal to the final velocity of the drop, which is found from Figure 7.3. The velocity along the drop bottom surface is taken equal to 0, because no inner circulation in the drop was observed at this stage. The tangential shear force is thus estimated by integrating the shear stress along the bottom surface in Region I.

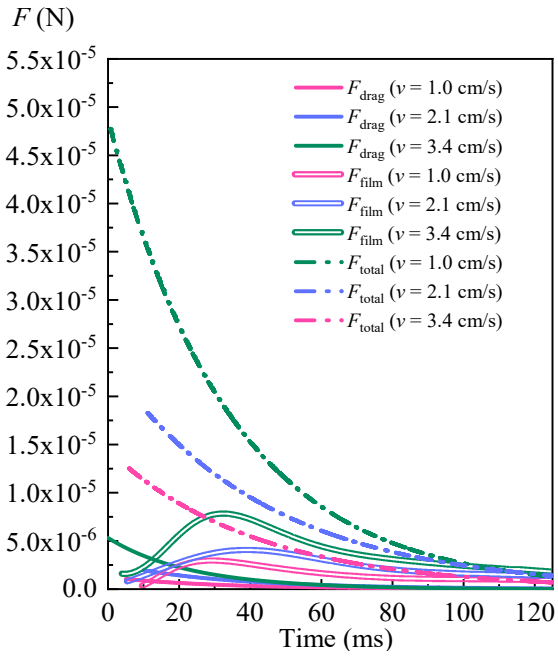

Figure C.2 the variations of the total force F_{total} that the drops acquire for the acceleration, the estimated drag force F_{drag} from the surrounding liquids and the tangential force F_{film} from the film at the bottom of the drop

The variations of the total force F_{total} required to accelerate the drop (which is calculated from Figure 7.3), the drag force from the surrounding liquid, F_{drag}, in Region II and the shear force in the thin film, F_{film}. in Region I at the initial stages are shown in Figure C.2. As can be seen, the shear force F_{film} from the film in the inner Region I contributes more than the drag force F_{drag} from the surrounding oil in most of the time. At the beginning (t < 15 ms), the relative velocity between the drop and the surrounding liquid is large, while the film area is small and the drag force F_{drag} is comparable to F_{film}. Afterwards, the drag force, $F_{drag,}$ decreases as the relative velocity between the drop and the surrounding liquid diminishes rapidly, while the shear force, F_{film}, in the film is increasing as its length increases. After a transition point, the shear force F_{film} decreases as the film region starts to shrink. The figure reveals that the combined F_{drag} and F_{film} forces are less than the force required to accelerate the drop, especially at the initial stages of drop rest, before t = 30 ms. It is believed that the Laplace force due to the deformation of the interface and the uneven distribution of the flow induced lubrication pressure in the trapped oil film generate a horizontal force that also contributes to the acceleration of the drop.

Appendix D: Estimation of the pressure in the trapped film for a stationary drop

The flow in the thin film trapped between the stationary drop and the bottom interface in Section 7.3 is simulated with ANSYS Fluent 19.2. As described in Section 7.3, the drop shape and the film thickness do not change during the whole process, which is regarded as steady state. The Reynolds number $Re = \rho uh/\mu$ in the thin trapped film is much lower than 1. Sawaguchi et al. (2019) and the lubrication theory can be applied. However, to get more accurate results, the inertial term is not ignored and in the simulation the full Navier-Stokes are considered. A two dimensional simulation is carried out, where the steady state shape of the drop and of the local film thickness are extracted from the experimental measurements. In the simulations it is assumed that the whole drop is surrounded by the oil phase and the nozzle is omitted. This is justified because in the level of the nozzle the oil velocity is close to zero and the effect of the nozzle on the flow field in the film region is expected to be negligible. As shown in Figure D.1 the drop is located at 50D away from both the inlet and the outlet to avoid ends effects. A relatively coarse mesh was set in region A near the inlet and the outlet. A refined mesh was used in the drop region B with a smooth transition to region A. The mesh in the film, whose thickness is around 50 μm, is further refined to 80 nodes across the film height to improve the simulation accuracy. In the simulations, both the drop surface and the interface are considered as boundaries with tangential velocities equal to those measured experimentally, as shown in Figure 7.8(c). For the interface a velocity of 2 cm/s was used. The calculations were carried out at atmospheric pressure and the simulated pressure distribution in the film is shown in Figure D.2.

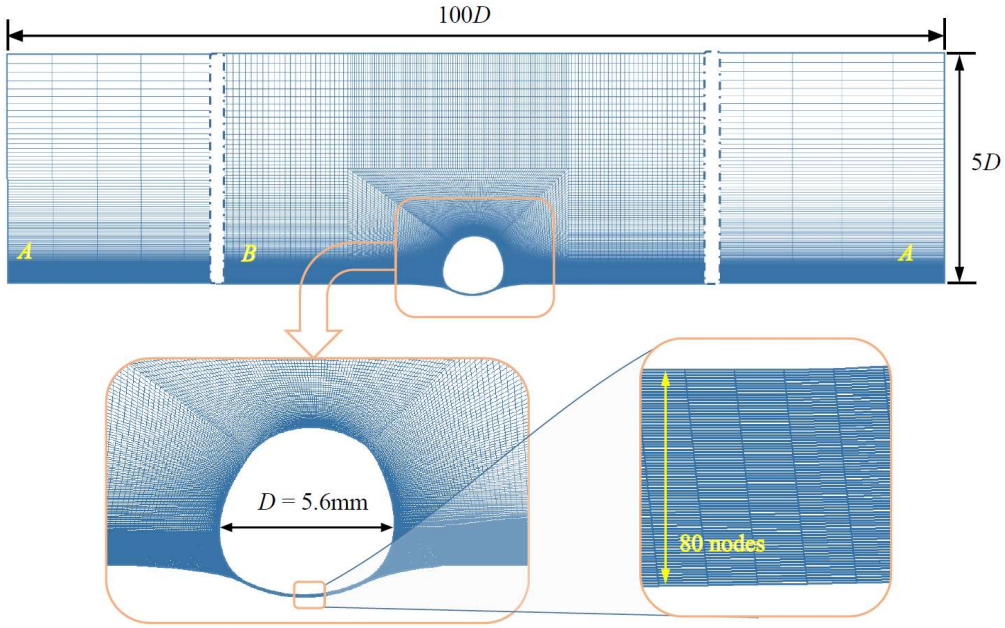

Figure D.1 Computational domain and details of the grid used around the drop and in the film region (total cells 128053).

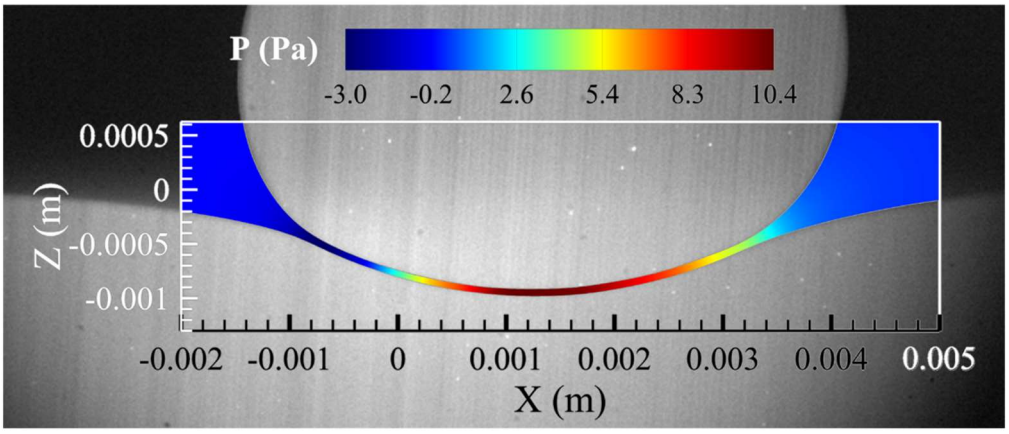

Figure D.2 Contours of the pressure field (Pa) in the trapped film and in the surrounding area.

Scientific output

Research Journals:

- Dong T, Weheliye W H, Angeli P. Laser induced fluorescence studies on the distribution of surfactants during drop/interface coalescence[J]. Physics of Fluids, 2019, 31(1): 012106.
- Dong T, Weheliye W H, Chausset P, et al. An experimental study on the drop/interface partial coalescence with surfactants[J]. Physics of Fluids, 2017, 29(10): 102101.
- Weheliye W H, Dong T, Angeli P. On the effect of surfactants on drop coalescence at liquid/liquid interfaces[J]. Chemical Engineering Science, 2017, 161: 215-227.
- Dong T, Wang F, Weheliye W H, Angeli P. Surfing of drops on moving liquid-liquid interfaces [J]. Journal of Fluid Mechanics.2019 (Under review)

Invited and Selected Talks:

- 71th APS Division of Fluid Dynamics, Atlanta, USA (November 2018);
- 70th APS Division of Fluid Dynamics, Denver, USA (November 2017);
- TMF Consortium, Imperial College London, UK (September 2017);
- AICHE Annual Meeting, San Francisco, USA (November 2016);
- UK ChemEngDay 2016, Bath, UK (March 2016).

Peer Review:

- Reviewer of the journal of Physics of Fluids;
- Reviewer of the journal of IEEE Access.

References

AARTS, D. G. & LEKKERKERKER, H. N. 2008. Droplet coalescence: drainage, film rupture and neck growth in ultralow interfacial tension systems. *Journal of fluid mechanics,* 606**,** 275-294.

AARTS, D. G., LEKKERKERKER, H. N., GUO, H., WEGDAM, G. H. & BONN, D. 2005. Hydrodynamics of droplet coalescence. *Physical review letters,* 95**,** 164503.

ANDRADE, B., SONG, Z., LI, J., ZIMMERMAN, S. C., CHENG, J., MOORE, J. S., HARRIS, K. & KATZ, J. S. 2015. New frontiers for encapsulation in the chemical industry. *ACS applied materials & interfaces,* 7**,** 6359-6368.

ANILKUMAR, A., LEE, C. & WANG, T. 1991. Surface-tension-induced mixing following coalescence of initially stationary drops. *Physics of Fluids A: Fluid Dynamics,* 3**,** 2587-2591.

ARYAFAR, H. & KAVEHPOUR, H. 2006. Drop coalescence through planar surfaces. *Physics of Fluids,* 18**,** 072105.

ARYAFAR, H. & KAVEHPOUR, H. 2008. Hydrodynamic instabilities of viscous coalescing droplets. *Physical Review E,* 78**,** 037302.

ASSOCIATION, G. P. 1963. *Physical properties of glycerine and its solutions*, Glycerine Producers' Association.

BAN, T., KAWAIZUMI, F., NII, S. & TAKAHASHI, K. 2000. Study of drop coalescence behavior for liquid–liquid extraction operation. *Chemical engineering science,* 55**,** 5385-5391.

BENMEKHBI, M., SIMON, S. & SJÖBLOM, J. 2014. Dynamic and rheological properties of span 80 at liquid–liquid interfaces. *Journal of Dispersion Science and Technology,* 35**,** 765-776.

BHAT, P. P., APPATHURAI, S., HARRIS, M. T., PASQUALI, M., MCKINLEY, G. H.

& BASARAN, O. A. 2010. Formation of beads-on-a-string structures during break-up of viscoelastic filaments. *Nature Physics,* 6**,** 625.

BLANCHETTE, F. & BIGIONI, T. P. 2006a. Partial coalescence of drops at liquid interfaces. *Nature Physics,* 2**,** 254.

BLANCHETTE, F. & BIGIONI, T. P. 2006b. Partial coalescence of drops at liquid interfaces. *Nature Physics,* 2**,** 254-257.

BLANCHETTE, F., MESSIO, L. & BUSH, J. W. 2009. The influence of surface tension gradients on drop coalescence. *Physics of fluids,* 21**,** 072107.

BŁAWZDZIEWICZ, J., CRISTINI, V. & LOEWENBERG, M. 1999. Near-contact motion of surfactant-covered spherical drops: ionic surfactant. *Journal of colloid and interface science,* 211**,** 355-366.

BRENNER, H. 2013. *Interfacial transport processes and rheology*, Elsevier.

BURRILL, K. & WOODS, D. 1973a. Film shapes for deformable drops at liquid-liquid interfaces. II. The mechanisms of film drainage. *Journal of Colloid and Interface Science,* 42**,** 15-34.

BURRILL, K. & WOODS, D. 1973b. Film shapes for deformable drops at liquid-liquid interfaces. III. Drop rest-times. *Journal of Colloid and Interface Science,* 42**,** 35-51.

CASTREJÓN-PITA, J. R., MUÑOZ-SÁNCHEZ, B. N., HUTCHINGS, I. M. & CASTREJÓN-PITA, A. 2016. Droplet impact onto moving liquids. *Journal of Fluid Mechanics,* 809**,** 716-725.

CHAN, D. Y., KLASEBOER, E. & MANICA, R. 2011. Film drainage and coalescence between deformable drops and bubbles. *Soft Matter,* 7**,** 2235-2264.

CHARLES, G. E. & MASON, S. G. 1960a. The coalescence of liquid drops with flat liquid/liquid interfaces. *Journal of Colloid Science,* 15**,** 236-267.

CHARLES, G. E. & MASON, S. G. 1960b. The mechanism of partial coalescence of liquid drops at liquid/liquid interfaces. *Journal of Colloid Science,* 15**,** 105-122.

CHEN, H., ZHAO, Y., LI, J., GUO, M., WAN, J., WEITZ, D. A. & STONE, H. A. 2011. Reactions in double emulsions by flow-controlled coalescence of encapsulated drops. *Lab on a Chip,* 11**,** 2312-2315.

CHEN, J.-D. 1985. A model of coalescence between two equal-sized spherical drops or bubbles. *Journal of colloid and interface science,* 107**,** 209-220.

CHEN, J. D., HAHN, P. S. & SLATTERY, J. 1984. Coalescence time for a small drop or bubble at a fluid-fluid interface. *AIChE journal,* 30**,** 622-630.

CHEN, X., MANDRE, S. & FENG, J. J. 2006. Partial coalescence between a drop and a liquid-liquid interface. *Physics of Fluids,* 18**,** 051705.

CHESTERS, A. K. & BAZHLEKOV, I. B. 2000. Effect of insoluble surfactants on drainage and rupture of a film between drops interacting under a constant force. *Journal of colloid and interface science,* 230**,** 229-243.

CHI, B. & LEAL, L. 1989. A theoretical study of the motion of a viscous drop toward a fluid interface at low Reynolds number. *Journal of Fluid Mechanics,* 201**,** 123-146.

CHINAUD, M., VOULGAROPOULOS, V. & ANGELI, P. 2016. Surfactant effects on the coalescence of a drop in a Hele-Shaw cell. *Physical Review E,* 94**,** 033101.

COUDER, Y., FORT, E., GAUTIER, C.-H. & BOUDAOUD, A. 2005. From bouncing to floating: noncoalescence of drops on a fluid bath. *Physical review letters,* 94**,** 177801.

CRISTINI, V., BŁAWZDZIEWICZ, J. & LOEWENBERG, M. 1998. Near-contact motion of surfactant-covered spherical drops. *Journal of Fluid Mechanics,* 366**,** 259-287.

DAI, B. & LEAL, L. G. 2008. The mechanism of surfactant effects on drop coalescence. *Physics of Fluids,* 20**,** 040802.

DAMIANO, A. P., BRUN, P.-T., HARRIS, D. M., GALEANO-RIOS, C. A. & BUSH, J. W. 2016. Surface topography measurements of the bouncing droplet experiment. *Experiments in Fluids,* 57**,** 163.

DAVANLOU, A. 2016. The Role of Liquid Properties on Lifetime of Levitated Droplets. *Langmuir,* 32**,** 9736-42.

DAVIS, D., DRANSFIELD, P. & TAN, A. The Stable Floating Liquid Droplet Phenomenon. 7th Australasian Conference on Hydraulics and Fluid Mechanics

1980: Preprints of Papers, 1980. Institution of Engineers, Australia, 451.

DAVIS, R. H., SCHONBERG, J. A. & RALLISON, J. M. 1989. The lubrication force between two viscous drops. *Physics of Fluids A: Fluid Dynamics,* 1**,** 77-81.

DELL'AVERSANA, P., BANAVAR, J. R. & KOPLIK, J. 1996. Suppression of coalescence by shear and temperature gradients. *Physics of Fluids,* 8**,** 15-28.

DENG, N.-N., WANG, W., JU, X.-J., XIE, R. & CHU, L.-Y. 2016. Spontaneous transfer of droplets across microfluidic laminar interfaces. *Lab on a Chip,* 16**,** 4326-4332.

DIJKHUIZEN, W., ROGHAIR, I., ANNALAND, M. V. S. & KUIPERS, J. 2010. DNS of gas bubbles behaviour using an improved 3D front tracking model—Drag force on isolated bubbles and comparison with experiments. *Chemical Engineering Science,* 65**,** 1415-1426.

DING, H., LI, E., ZHANG, F., SUI, Y., SPELT, P. D. & THORODDSEN, S. T. 2012. Propagation of capillary waves and ejection of small droplets in rapid droplet spreading. *Journal of Fluid Mechanics,* 697**,** 92-114.

DONG, T., WEHELIYE, W. H. & ANGELI, P. 2019. Laser induced fluorescence studies on the distribution of surfactants during drop/interface coalescence. *Physics of Fluids,* 31**,** 012106.

DONG, T., WEHELIYE, W. H., CHAUSSET, P. & ANGELI, P. 2017. An experimental study on the drop/interface partial coalescence with surfactants. *Physics of Fluids,* 29**,** 102101.

DOOLEY, B. S., WARNCKE, A. E., GHARIB, M. & TRYGGVASON, G. 1997. Vortex ring generation due to the coalescence of a water drop at a free surface. *Experiments in fluids,* 22**,** 369-374.

DREHER, T., GLASS, J., O'CONNOR, A. & STEVENS, G. 1999. Effect of rheology on coalescence rates and emulsion stability. *AIChE Journal,* 45**,** 1182-1190.

DUCHEMIN, L., LISTER, J. & LANGE, U. 2005. Static shapes of levitated viscous drops. *Journal of Fluid Mechanics,* 533**,** 161-170.

EASTOE, J. & DALTON, J. 2000. Dynamic surface tension and adsorption mechanisms of surfactants at the air–water interface. *Advances in colloid and interface science,* 85**,** 103-144.

EGGERS, J., LISTER, J. R. & STONE, H. A. 1999. Coalescence of liquid drops. *Journal of Fluid Mechanics,* 401**,** 293-310.

ERI, A. & OKUMURA, K. 2010. Bursting of a thin film in a confined geometry: Rimless and constant-velocity dewetting. *Physical Review E,* 82**,** 030601.

ESMAILIZADEH, L. & MESLER, R. 1986. Bubble entrainment with drops. *Journal of colloid and interface science,* 110**,** 561-574.

FALLEST, D. W., LICHTENBERGER, A. M., FOX, C. J. & DANIELS, K. E. 2010. Fluorescent visualization of a spreading surfactant. *New Journal of Physics,* 12**,** 073029.

FARHADI, H., RIAHI, S., AYATOLLAHI, S. & AHMADI, H. 2016. Experimental study of nanoparticle-surfactant-stabilized CO2 foam: Stability and mobility control. *Chemical Engineering Research and Design,* 111**,** 449-460.

FATHI, S., DICKENS, P. & FOUCHAL, F. 2010. Regimes of droplet train impact on a moving surface in an additive manufacturing process. *Journal of Materials Processing Technology,* 210**,** 550-559.

GAUTHIER, A., BIRD, J. C., CLANET, C. & QUÉRÉ, D. 2016. Aerodynamic Leidenfrost effect. *Physical Review Fluids,* 1**,** 084002.

GERI, M., KESHAVARZ, B., MCKINLEY, G. H. & BUSH, J. W. 2017. Thermal delay of drop coalescence. *Journal of Fluid Mechanics,* 833.

GHAEMI, S., RAGNI, D. & SCARANO, F. 2012. PIV-based pressure fluctuations in the turbulent boundary layer. *Experiments in fluids,* 53**,** 1823-1840.

GHOSH, P. & JUVEKAR, V. 2002. Analysis of the drop rest phenomenon. *Chemical Engineering Research and Design,* 80**,** 715-728.

GILET, T., MULLENERS, K., LECOMTE, J.-P., VANDEWALLE, N. & DORBOLO, S. 2007. Critical parameters for the partial coalescence of a droplet. *Physical Review E,* 75**,** 036303.

GILLESPIE, T. & RIDEAL, E. K. 1956. The coalescence of drops at an oil-water interface. *Transactions of the Faraday Society,* 52**,** 173-183.

GIRIBABU, K. & GHOSH, P. 2007. Adsorption of nonionic surfactants at fluid–fluid interfaces: importance in the coalescence of bubbles and drops. *Chemical*

engineering science, 62**,** 3057-3067.

HAHN, P. S., CHEN, J. D. & SLATTERY, J. 1985. Effects of London-van der Waals forces on the thinning and rupture of a dimpled liquid film as a small drop or bubble approaches a fluid-fluid interface. *AIChE journal,* 31**,** 2026-2038.

HALDAR, K., CHAKRABORTY, S. & CHAKRABORTY, S. 2018. Influence of Marangoni stress on the variation in number of coalescence cascade stages. *The Canadian Journal of Chemical Engineering*.

HALE, J. & AKERS, C. 2016. Deceleration of droplets that glide along the free surface of a bath. *Journal of Fluid Mechanics,* 803**,** 313-331.

HAMROCK, B. J., SCHMID, S. R. & JACOBSON, B. O. 2004. *Fundamentals of fluid film lubrication*, CRC press.

HAN, R., ZHANG, A.-M., LI, S. & ZONG, Z. 2018. Experimental and numerical study of the effects of a wall on the coalescence and collapse of bubble pairs. *Physics of Fluids,* 30**,** 042107.

HODGSON, T. & LEE, J. 1969. The effect of surfactants on the coalescence of a drop at an interface I. *Journal of Colloid and Interface Science,* 30**,** 94-108.

HODGSON, T. & WOODS, D. 1969. The effect of surfactants on the coalescence of a drop at an interface. II. *Journal of Colloid and Interface Science,* 30**,** 429-446.

HOSOKAWA, S., MASUKURA, Y., HAYASHI, K. & TOMIYAMA, A. 2017. Experimental evaluation of Marangoni stress and surfactant concentration at interface of contaminated single spherical drop using spatiotemporal filter velocimetry. *International Journal of Multiphase Flow,* 97**,** 157-167.

HOSOKAWA, S., MORIYAMA, S., TOMIYAMA, A. & TAKADA, N. 2003. PIV measurement of pressure distributions about single bubbles. *Journal of nuclear science and technology,* 40**,** 754-762.

JEELANI, S. & HARTLAND, S. 1994. Effect of interfacial mobility on thin film drainage. *Journal of colloid and interface science,* 164**,** 296-308.

JEFFREYS, G. & HAWKSLEY, J. 1965. Coalescence of liquid droplets in two-

component–two-phase systems: Part I. Effect of physical properties on the rate of coalescence. *AIChE Journal,* 11**,** 413-417.

JEONG, J. & HUSSAIN, F. 1995. On the identification of a vortex. *Journal of fluid mechanics,* 285**,** 69-94.

JIN, H., WANG, W., LIU, F., YU, Z., CHANG, H., LI, K. & GONG, J. 2017. Roles of interfacial dynamics in the interaction behaviours between deformable oil droplets. *International Journal of Multiphase Flow,* 94**,** 44-52.

JOSE, B. M. & CUBAUD, T. 2012. Droplet arrangement and coalescence in diverging/converging microchannels. *Microfluidics and nanofluidics,* 12**,** 687-696.

JOYE, J. L., HIRASAKI, G. J. & MILLER, C. A. 1992. Dimple formation and behavior during axisymmetrical foam film drainage. *Langmuir,* 8**,** 3083-3092.

KAVEHPOUR, H. P. 2015. Coalescence of drops. *Annual Review of Fluid Mechanics,* 47**,** 245-268.

KIM, J. & LONGMIRE, E. K. 2009. Investigation of binary drop rebound and coalescence in liquids using dual-field PIV technique. *Experiments in fluids,* 47**,** 263-278.

KINOSHITA, C., TENG, H. & MASUTANI, S. 1994. A study of the instability of liquid jets and comparison with Tomotika's analysis. *International journal of multiphase flow,* 20**,** 523-533.

KLASEBOER, E., CHEVAILLIER, J. P., GOURDON, C. & MASBERNAT, O. 2000. Film drainage between colliding drops at constant approach velocity: experiments and modeling. *Journal of colloid and interface science,* 229**,** 274-285.

KLEMASZEWSKI, J., DAS, K. & KINSELLA, J. 1992. Formation and coalescence stability of emulsions stabilized by different milk proteins. *Journal of food science,* 57**,** 366-371.

KLYUZHIN, I. S., IENNA, F., ROEDER, B., WEXLER, A. & POLLACK, G. H. 2010. Persisting water droplets on water surfaces. *The Journal of Physical Chemistry*

B, 114**,** 14020-14027.

LANG, S. B. & WILKE, C. 1971. A hydrodynamic mechanism for the coalescence of liquid drops. II. Experimental studies. *Industrial & Engineering Chemistry Fundamentals,* 10**,** 341-352.

LANGEVIN, D. 2015. Bubble coalescence in pure liquids and in surfactant solutions. *Current opinion in colloid & interface science,* 20**,** 92-97.

LHUISSIER, H., TAGAWA, Y., TRAN, T. & SUN, C. 2013. Levitation of a drop over a moving surface. *Journal of Fluid Mechanics,* 733.

LIU, X. & KATZ, J. 2006. Instantaneous pressure and material acceleration measurements using a four-exposure PIV system. *Experiments in fluids,* 41**,** 227.

LU, J. & CORVALAN, C. M. 2012. Coalescence of viscous drops with surfactants. *Chemical engineering science,* 78**,** 9-13.

MACKAY, G. & MASON, S. 1963. The gravity approach and coalescence of fluid drops at liquid interfaces. *The Canadian Journal of Chemical Engineering,* 41**,** 203-212.

MAHAJAN, L. 1930. Liquid drops on the same liquid surface. *Nature,* 126**,** 761.

MAR, A. & MASON, S. 1968. Coalescence in three-phase fluid systems. *Kolloid-Zeitschrift und Zeitschrift für Polymere,* 224**,** 161-172.

MARANGONI, C. 1865. *Sull'espansione delle goccie d'un liquido galleggianti sulla superfice di altro liquido*.

MARTIN, D. W. & BLANCHETTE, F. 2015. Simulations of surfactant effects on the dynamics of coalescing drops and bubbles. *Physics of Fluids,* 27**,** 012103.

MASON, S., MAY, K. & HARTLAND, S. 1995. Drop size and concentration profile determination in petroleum emulsion separation. *Colloids and Surfaces A: Physicochemical and engineering aspects,* 96**,** 85-92.

MCCLURE, J. & YARUSEVYCH, S. 2017. Optimization of planar PIV-based pressure estimates in laminar and turbulent wakes. *Experiments in Fluids,* 58**,** 62.

MENCHACA-ROCHA, A., MARTINEZ-DAVALOS, A., NUNEZ, R., POPINET, S. & ZALESKI, S. 2001. Coalescence of liquid drops by surface tension. *Physical Review E,* 63**,** 046309.

MILTON, J. R. 2004. Surfactants and interfacial phenomena. *John Wiley&Sons, NewYork*.

MOHAMED-KASSIM, Z. & LONGMIRE, E. K. 2004. Drop coalescence through a liquid/liquid interface. *Physics of Fluids,* 16**,** 2170-2181.

MOLÁČEK, J. & BUSH, J. W. 2013. Drops walking on a vibrating bath: towards a hydrodynamic pilot-wave theory. *Journal of Fluid Mechanics,* 727**,** 612-647.

MOROKUMA, T. & UTAKA, Y. 2016. Variation of the liquid film thickness distribution between contacting twin air bubbles during the coalescence process in water and ethanol pools. *International Journal of Heat and Mass Transfer,* 98**,** 96-107.

MURANO, M. & OKUMURA, K. 2018. Bursting dynamics of viscous film without circular symmetry: The effect of confinement. *Physical Review Fluids,* 3**,** 031601.

NAKAYAMA, Y. 2018. *Introduction to fluid mechanics*, Butterworth-Heinemann.

NAPOLITANO, L., MONTI, R. & RUSSO, G. 1986. Marangoni convection in one- and two-liquids floating zones. *Naturwissenschaften,* 73**,** 352-355.

NASH, J. J., SPICER, P. T. & ERK, K. A. 2018. Controllable internal mixing in coalescing droplets induced by the solutal Marangoni convection of surfactants with distinct headgroup architectures. *Journal of colloid and interface science,* 529**,** 224-233.

NIELSEN, L. E., WALL, R. & ADAMS, G. 1958. Coalescence of liquid drops at oil-water interfaces. *Journal of Colloid Science,* 13**,** 441-458.

NIKOLOV, A. D. & WASAN, D. T. 1995. Effects of surfactant on multiple stepwise coalescence of single drops at liquid-liquid interfaces. *Industrial & engineering chemistry research,* 34**,** 3653-3661.

NOWAK, E., KOVALCHUK, N. M., CHE, Z. & SIMMONS, M. J. 2016. Effect of surfactant concentration and viscosity of outer phase during the coalescence of a surfactant-laden drop with a surfactant-free drop. *Colloids and Surfaces A: Physicochemical and Engineering Aspects,* 505**,** 124-131.

NOWAK, E., XIE, Z., KOVALCHUK, N. M., MATAR, O. K. & SIMMONS, M. J.

2017. Bulk advection and interfacial flows in the binary coalescence of surfactant-laden and surfactant-free drops. *Soft matter,* 13**,** 4616-4628.

OLDENZIEL, G., DELFOS, R. & WESTERWEEL, J. 2012. Measurements of liquid film thickness for a droplet at a two-fluid interface. *Physics of Fluids,* 24**,** 022106.

ORTIZ-DUEÑAS, C., KIM, J. & LONGMIRE, E. K. 2010. Investigation of liquid–liquid drop coalescence using tomographic PIV. *Experiments in Fluids,* 49**,** 111-129.

PAULSEN, J. D., BURTON, J. C. & NAGEL, S. R. 2011. Viscous to inertial crossover in liquid drop coalescence. *Physical Review Letters,* 106**,** 114501.

PIRAT, C., LEBON, L., FRULEUX, A., ROCHE, J.-S. & LIMAT, L. 2010. Gyroscopic instability of a drop trapped inside an inclined circular hydraulic jump. *Physical review letters,* 105**,** 084503.

PRINCEN, H. 1963. Shape of a fluid drop at a liquid-liquid interface. *Journal of Colloid Science,* 18**,** 178-195.

PUCCI, G., HARRIS, D. M. & BUSH, J. W. 2015. Partial coalescence of soap bubbles. *Physics of Fluids,* 27**,** 061704.

PUCCI, G., HARRIS, D. M., FARIA, L. M. & BUSH, J. W. 2018. Walking droplets interacting with single and double slits. *Journal of Fluid Mechanics,* 835**,** 1136-1156.

RAES, F., VAN DINGENEN, R., VIGNATI, E., WILSON, J., PUTAUD, J.-P., SEINFELD, J. H. & ADAMS, P. 2000. Formation and cycling of aerosols in the global troposphere. *Atmospheric environment,* 34**,** 4215-4240.

RAVERA, F., FERRARI, M. & LIGGIERI, L. 2000. Adsorption and partitioning of surfactants in liquid–liquid systems. *Advances in Colloid and Interface Science,* 88**,** 129-177.

RAY, B., BISWAS, G. & SHARMA, A. 2010. Generation of secondary droplets in coalescence of a drop at a liquid–liquid interface. *Journal of Fluid Mechanics,* 655**,** 72-104.

REYNOLDS, O. 1881. On drops floating on the surface of water. *Chem. News,* 44**,** 211.

ROMMEL, W., BLASS, E. & MEON, W. 1993. Plate separators for dispersed liquid—liquid systems: The role of partial coalescence. *Chemical engineering science,* 48**,** 1735-1743.

SÁENZ, P. J., CRISTEA-PLATON, T. & BUSH, J. W. 2018. Statistical projection effects in a hydrodynamic pilot-wave system. *Nature Physics,* 14**,** 315.

SAN LEE, J., PARK, S. J., LEE, J. H., WEON, B. M., FEZZAA, K. & JE, J. H. 2015. Origin and dynamics of vortex rings in drop splashing. *Nature communications,* 6**,** 8187.

SAVINO, R., PATERNA, D. & LAPPA, M. 2003. Marangoni flotation of liquid droplets. *Journal of Fluid Mechanics,* 479**,** 307-326.

SAWAGUCHI, E., MATSUDA, A., HAMA, K., SAITO, M. & TAGAWA, Y. 2019. Droplet levitation over a moving wall with a steady air film. *Journal of Fluid Mechanics,* 862**,** 261-282.

SCHERER, G. W. 1984. Viscous sintering of a bimodal pore-size distribution. *Journal of the American Ceramic Society,* 67**,** 709-715.

SHAH, S. K., BHATTARAI, A. & CHATTERJEE, S. K. 2013. Applications of surfactants in modern science and technology. *Prof. Dr. Devendra Adhikari Department of Physics, Mahendra Morang Adarsha Multiple Campus Tribhuvan University, Biratnagar, Nepal Email: adksbdev@ yahoo. com***,** 147.

SHEN, F., LI, Y., LIU, Z. & LI, X. 2017. Study of flow behaviors of droplet merging and splitting in microchannels using Micro-PIV measurement. *Microfluidics and nanofluidics,* 21**,** 66.

SMITH, M. K. & NEITZEL, G. P. 2006. Multiscale modelling in the numerical computation of isothermal non-wetting. *Journal of Fluid Mechanics,* 554**,** 67-83.

SOMWANSHI, P. M., MURALIDHAR, K. & KHANDEKAR, S. 2018. Coalescence dynamics of sessile and pendant liquid drops placed on a hydrophobic surface. *Physics of Fluids,* 30**,** 092103.

SREENIVAS, K., DE, P. & ARAKERI, J. H. 1999. Levitation of a drop over a film flow.

Journal of Fluid Mechanics, 380**,** 297-307.

STANCIK, E. J., KOUHKAN, M. & FULLER, G. G. 2004. Coalescence of particle-laden fluid interfaces. *Langmuir,* 20**,** 90-94.

STRICKLAND, S. L., SHEARER, M. & DANIELS, K. E. 2015. Spatiotemporal measurement of surfactant distribution on gravity–capillary waves. *Journal of Fluid Mechanics,* 777**,** 523-543.

SWANSON, E. R., STRICKLAND, S. L., SHEARER, M. & DANIELS, K. E. 2015. Surfactant spreading on a thin liquid film: reconciling models and experiments. *Journal of Engineering Mathematics,* 94**,** 63-79.

TCHOLAKOVA, S., DENKOV, N. D., IVANOV, I. B. & CAMPBELL, B. 2006. Coalescence stability of emulsions containing globular milk proteins. *Advances in colloid and interface science,* 123**,** 259-293.

THORODDSEN, S., TAKEHARA, K. & ETOH, T. 2005. The coalescence speed of a pendent and a sessile drop. *Journal of Fluid Mechanics,* 527**,** 85-114.

THORODDSEN, S. T. & TAKEHARA, K. 2000. The coalescence cascade of a drop. *Physics of Fluids,* 12**,** 1265-1267.

TRONCHIN, T., DAVID, L. & FARCY, A. 2015. Loads and pressure evaluation of the flow around a flapping wing from instantaneous 3D velocity measurements. *Experiments in Fluids,* 56**,** 7.

VAN CAPELLEVEEN, B. F., KOLDEWEIJ, R. B., LOHSE, D. & VISSER, C. W. 2017. On the universality of Marangoni-driven spreading along liquid-liquid interfaces. *preprint*.

VAN OUDHEUSDEN, B. 2013. PIV-based pressure measurement. *Measurement Science and Technology,* 24**,** 032001.

VENKATARAMAN, P., TANG, J., FRENKEL, E., MCPHERSON, G. L., HE, J., RAGHAVAN, S. R., KOLESNICHENKO, V., BOSE, A. & JOHN, V. T. 2013. Attachment of a hydrophobically modified biopolymer at the oil–water interface in the treatment of oil spills. *ACS applied materials & interfaces,* 5**,** 3572-3580.

VIOLATO, D., MOORE, P. & SCARANO, F. 2011. Lagrangian and Eulerian pressure field evaluation of rod-airfoil flow from time-resolved tomographic PIV.

Experiments in fluids, 50**,** 1057-1070.

VOULGAROPOULOS, V. 2018. *Dynamics of spatially evolving dispersed flows.* UCL (University College London).

WAGONER, B. W., THETE, S. S. & BASARAN, O. A. 2018. A new experimental method based on volume measurement for determining axial scaling during breakup of drops and liquid threads. *Physics of Fluids,* 30**,** 082102.

WALKER, J. 1978. Drops of liquid can be made to oat on the liquid. *Scientific American*.

WANG, L., GAO, Y., LI, J., SUBIRADE, M., SONG, Y. & LIANG, L. 2016a. Effect of resveratrol or ascorbic acid on the stability of α-tocopherol in O/W emulsions stabilized by whey protein isolate: Simultaneous encapsulation of the vitamin and the protective antioxidant. *Food chemistry,* 196**,** 466-474.

WANG, L., ZHANG, G., WU, H., YANG, J. & ZHU, Y. 2016b. Note: A top-view optical approach for observing the coalescence of liquid drops. *Review of Scientific Instruments,* 87**,** 026103.

WASAN, D. T. 1992. Interfacial transport processes and rheology. *Chemical Engineering Education***,** 104.

WEHELIYE, W. H., DONG, T. & ANGELI, P. 2017. On the effect of surfactants on drop coalescence at liquid/liquid interfaces. *Chemical Engineering Science,* 161**,** 215-227.

WEISS, D. A. & YARIN, A. L. 1999. Single drop impact onto liquid films: neck distortion, jetting, tiny bubble entrainment, and crown formation. *Journal of Fluid Mechanics,* 385**,** 229-254.

WEIß, M. 2004. *Surfactant Adsorption and Marangoni Flow in Liquid Jets.* Doctor, UNIVERSITY OF OXFORD.

XU, J., ZHANG, Y., CHEN, H., WANG, P., XIE, Z., YAO, Y., YAN, Y. & ZHANG, J. 2013. Effect of surfactant headgroups on the oil/water interface: An interfacial tension measurement and simulation study. *Journal of Molecular Structure,* 1052**,** 50-56.

YANG, F., TCHOUKOV, P., QIAO, P., MA, X., PENSINI, E., DABROS, T., CZARNECKI, J. & XU, Z. 2018. Studying demulsification mechanisms of

water-in-crude oil emulsions using a modified thin liquid film technique. *Colloids and Surfaces A: Physicochemical and Engineering Aspects,* 540**,** 215-223.

YEO, L. Y., MATAR, O. K., DE ORTIZ, E. S. P. & HEWITT, G. F. 2001. The dynamics of Marangoni-driven local film drainage between two drops. *Journal of colloid and interface science,* 241**,** 233-247.

YEO, L. Y., MATAR, O. K., DE ORTIZ, E. S. P. & HEWITT, G. F. 2003. Film drainage between two surfactant-coated drops colliding at constant approach velocity. *Journal of colloid and interface science,* 257**,** 93-107.

YIANTSIOS, S. G. & DAVIS, R. H. 1990. On the buoyancy-driven motion of a drop towards a rigid surface or a deformable interface. *Journal of Fluid Mechanics,* 217**,** 547-573.

YUE, P., ZHOU, C. & FENG, J. J. 2006. A computational study of the coalescence between a drop and an interface in Newtonian and viscoelastic fluids. *Physics of Fluids,* 18**,** 102102.

ZHANG, F., LI, E. & THORODDSEN, S. T. 2009. Satellite formation during coalescence of unequal size drops. *Physical review letters,* 102**,** 104502.

ZHANG, F., THORAVAL, M.-J., THORODDSEN, S. T. & TABOREK, P. 2015. Partial coalescence from bubbles to drops. *Journal of Fluid Mechanics,* 782**,** 209-239.